Online ISSN 2716-9650
Print ISSN 2676-5837

Volume 3, Jun. 30, 2021

Journal of
Composites and Compounds

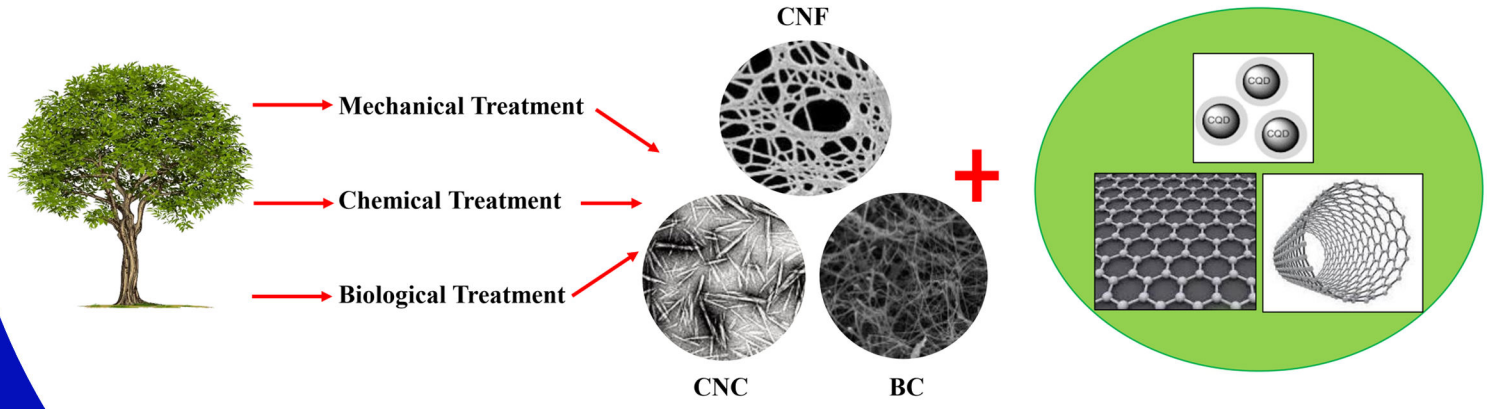

Editor-in-Chief: Prof. Dr. Hassan Karimi-Maleh

www.JOURCC.com

Journal of
Composites and Compounds

Online ISSN 2716-9650
Print ISSN 2676-5837
Jun. 30, 2021
Volume 3
No. 7

Available online at www.jourcc.com

Karoon St., Tehran, Iran

+982166897182

Journal of
Composites and Compounds
Online ISSN 2716-9650
Print ISSN 2676-5837
Jun. 30, 2021
Volume 3
No. 7

Table of contents

Functionalized $NiFe_2O_4$/mesopore silica anchored to guanidine nanocomposite as a catalyst for synthesis of 4H-chromenes under ultrasonic irradiation 84

Effects of Mg and MgO Nanoparticles on Microstructural and Mechanical Properties of Aluminum Matrix Composite Prepared via Mechanical Alloying 91

Effect of austenitic stainless steel cladding on the high-temperature oxidation resistance of Ferritic 2.25Cr-1Mo (Grade 22) steel using SMAW process 99

Electrodeposition of Nickel matrix composite coatings via various Boride particles: A review 106

Application of nanocellulose composites in the environmental engineering: A review 114

Application of Polyoxometalate-based composites for sensor systems: A review 129

Application of carbon allotropes composites for targeted cancer therapy drugs: A review 140

Available online at www.jourcc.com

Karoon St., Tehran, Iran
+982166897182

Available online at www.jourcc.com

Journal homepage: www.JOURCC.com

Journal of Composites and Compounds

Functionalized $NiFe_2O_4$/mesopore silica anchored to guanidine nanocomposite as a catalyst for synthesis of 4H-chromenes under ultrasonic irradiation

Somaye Mohammadi [a]*, *Zeinab Mohammadi* [a]

[a] *Department of Organic Chemistry, Faculty of Chemistry, University of Shahrekord, Shahrekord, 87317-51167, Iran*

ABSTRACT

A synergetic effect of nanocatalyst and ultrasonic irradiation was examined for the synthesis of 4H-chromenes from benzaldehyde, cyclohexanone, and malononitrile. It was observed this contributory improved the reaction that was used for the synthesis of the highly pure products in short reaction times and highest yields. The nanocomposite includes the guanidine anchored on to magnetic $NiFe_2O_4$ nanoparticles were used as the active base nanocatalyst for the sonication synthesis of 4H-chromenes compounds. The product was separated with simple filtration and purify with recrystallization by ethanol solvent. After completing the reaction, a nanocatalyst was collected and reused in 6 runs of model reaction. This nanocomposite has a magnetic core and a very active base surface area shell. The nanocatalyst was provided by the simple technique and identified by using FT-IR spectrum, scanning electron microscopy (SEM), X-ray diffraction (XRD), vibrating sample magnetometer (VSM), and Brunauer–Emmett–Teller (BET). This nanocomposite was used for the synthesized various derivatives of 4H-chromenes under ultrasonic irradiation. The organic products were identified by FT-IR and 1H-NMR.

Peer review under responsibility of jourcc

ARTICLE INFORMATION

Article history:
Received 4 June 2021
Received in revised form 22 June 2021
Accepted 27 June 2021

Keywords:
4H-Chromene
Cyclohexanone
Malononitrile
Ultrasonic mesopore silica

1. Introduction

Recently mesoporous silica spheres include magnetic metal nanoparticles, have an attractive idea for chemistry researchers [1-3]. These nanocomposites have active surfaces area for use in various sciences. This nanostructure has the potential for use as the nanocatalyst [4-6], sensors [7, 8], nanoreactors [9], and drug delivery processes [10], gas filtration [11], and also as nano-sized quantum materials [12]. The large surface area of mesoporous silica was used in optical coatings and catalytic processes [13]. The bulk mesophase [14, 15] was managed the ratio between silica-to-surfactant and silica/surfactant self-assembly formation of cubic, hexagonal, and lamellar shape [16]. Recently, the heterogeneous nanocomposite was used in organic reaction to synthesis of different organic products [17, 18].

The chromenes compounds have notable biological attributes, [19-21] such as anticancer [22], antibacterial [23], anticonvulsant [24], antimicrobial [25], anti-influenza [26], antimalarial [27], and anti-virus activities [28]. Tetrahydro-4H-chromenes were used for the cure of counting Huntington's disease [29] neurodegenerative illnesses [30], Alzheimer's disease [31], Parkinson's disease [32], and schizophrenia [33]. The usual reaction for synthesis tetrahydro-4H-chromene is the Michael addition in the presence of a base catalyst. Numerous multi-component reactions have been determined for the synthesis of various tetrahydro-4H-chromenes derivatives via the condensation of an aldehyde, malononitrile, and cyclic ketone at the presence of different inorganic and organic catalysts [33, 34].

Ultrasonic is the sound waves belonging to the group of mechanical waves, which included frequencies higher than the audible frequency of humans (20k Hz) [35, 36]. The piezoelectric influence has been used to provide ultrasonic waves since the 1880 s [37, 38]. Ultrasonic waves were invented with development in the technology of ceramic materials [39], for example, quartz, [40] lead zirconate barium titanate, and lead titanate [41, 42], the ultrasonic technique has progressively grown to be considered encouraging, green, and novel technology that can be replaced or help traditional chemical processing [43, 44].

Following the previously reported [45-47], in this research, it was reported a clean synthesis of 4H-chromenes derivatives from cyclohexanone, different benzaldehyde, and malononitrile under ultrasonic irradiation at the presence of the $NiFe_2O_4$/mesopore silica anchored to guanidine nanocomposite as the base catalyst.

* *Corresponding author: Somaye Mohammadi; E-mail: mohamadi_s65@yahoo.com, Tel: 98-31-55912388, Fax: 983155912397*

https://doi.org/10.52547/jcc.3.2.1

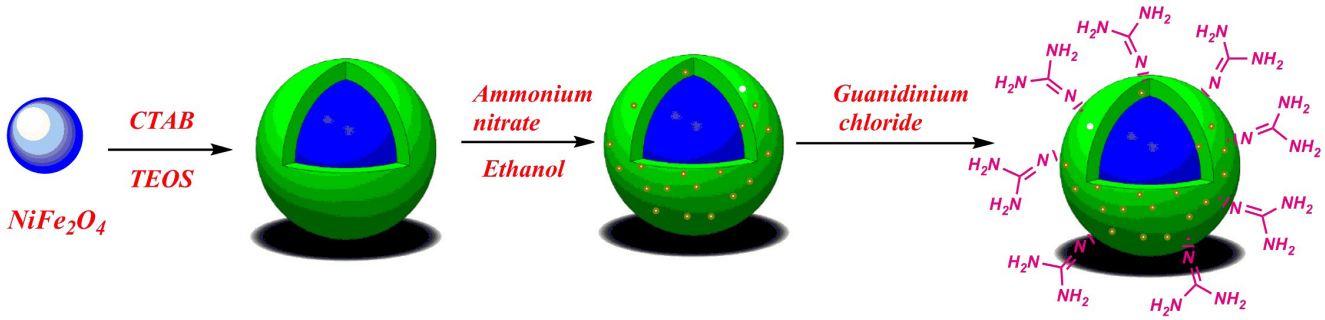

Scheme. 1. Synthesis of $NiFe_2O_4$/mesopore silica anchored to guanidine nanocomposite.

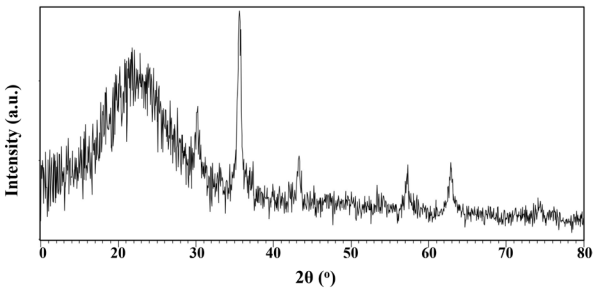

Fig. 1. XRD spectra of $NiFe_2O_4$@mesopore silica@ guanidine.

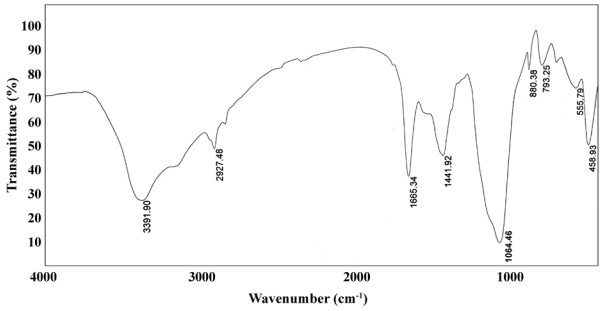

Fig. 2. The spectra of FT-IR of $NiFe_2O_4$@mesopore silica@ guanidine.

2. Experimental procedures

2.1. Materials and instruments

All the solvents and starting materials that used in the reaction include benzaldehyde derivatives (97%-99%), cyclohexanone (98%), malononitrile (99%), and ethanol (99%), cetyltrimethylammonium bromide (CTAB) (100%), tetraethyl orthosilicate (TEOS) (97%), sodium hydroxide (NaOH) (99%), were provided from Sigma, ferric (III) chloride ($FeCl_3$) (97%), nickel (II) chloride ($NiCl_2$) (98%), and sodium bicarbonate (95%), were obtained from Sinopharm Chemical. The organic products were recognized with ^1H NMR, FT-IR, and ^{13}C NMR analyses. The 1H NMR analysis was reported in $CDCl_3$ solvents using Bruker DRX-400 spectrometer, and the internal reference is tetramethylsilane. FT-IR spectra were reported with a Perkin-Elmer 550 spectrometers in the range of 400–4000 cm^{-1}. The crystal structure of nanocomposite (XRD) registered with (CuKa, radiation, λ = 0.154056 nm) that worked with a 15-kV accelerating voltage at the speed of 2° min−1 starting from 10° to 80°(2z.Theta;), for determined the morphology and size of nanocomposite used of Electron Microscope (FE-SEM) and EDX with Zeiss Scanning Electron with a 15-kV accelerating voltage. The surface areas and the size of pore in the nanocomposite illustrated by BET analysis with nitrogen adsorption in −196 °C using Tri-Star 3020 Micrometrics analyzer. The magnetic properties of nanocomposite were measured by a vibrating sample magnetometer (VSM), the VSM curves were recorded by PPMS-9 T at 300 K. The TGA was recorded in an air atmosphere by a 10 °C/min rate.

using the METLER-810 analyzer.

2.2. General procedure for preparation of nano magnetic $NiFe_2O_4$

The nickel ferrite nanoparticles were provided during a sol-gel method [29]. To the accomplishment, the chemical formula $NiFe_2O_4$, 40 ml $FeCl_3$ 6 H_2O (4 M) was stirred with 40 ml $NiCl_2$ $2H_2O$ (2 M). Then, 1.5 g citric acid monohydrate was added ($C_6H_8O_7$, H_2O) to the reaction mixture. The pH of the mixture increased to 7.0 added a little ammonia-water (NH_3-H_2O) to the reactions. The solution was heated to dry the water at 85°C and production of the brown colored gel. At the end of the method, the product was dry at 800 oC to 3h.

2.3. Synthesis of $NiFe_2O_4$@ mesopore silica

To provide an active base nanocatalyst, 5 mL NaOH 1 M, and 0.65 g of CTAB were dissolved in 100 mL deionized water and heated the mixture to 35 min at 100 °C. Then 0.1 g of $NiFe_2O_4$ nanocomposite was dispersed in 60 ml ethanol under sonicate irradiation. The obtained solution added to the reaction mixture. 2 ml TEOS was added to the reaction mixture two times after 15 and 40 min, the reaction mixture stirred at room temperature for 15 h at the end of the reaction the product collected by centrifuge and washed three times with water and ethanol, and dried at 70 °C for 24 h. The surfactant was removed from the nanocomposite by dispersed the product in ethanol (100 mL) and ammonium nitrate (50 mg) and stirred at 80 °C for 5 h. The product was separated by the centrifuge and dried at 100 °C for overnight.

2.4. Synthesis of $NiFe_2O_4$/mesopore silica anchored to guanidine nanocomposite

50.0 mg of $NiFe_2O_4$@mesopore silica was dispersed under ultrasonic irradiation in 10.0 mL toluene solvent for 30 min. Then 5mmol guanidinium chloride, 5 mmol 3-chloropropyltrimethoxysilane, and 2.5 mmol sodium bicarbonate in 10 mL dry toluene added to the reaction mixture then refluxed for 32 h. Then, the final product was separated by centrifuge and washed with water and ethanol. The product was dried at 80 °C under a nitrogen atmosphere (Scheme 1).

2.5. General multicomponent procedure for synthesis of 4H-chromene

4H-chromenes derivatives were synthesized in the three-component reaction. In this reaction, 1 mmol of malononitrile was reacted by 1 mmol of benzaldehyde at the presence of 10 mg of nanocatalyst. The reaction was followed under ultrasonic irradiation on the ethanol

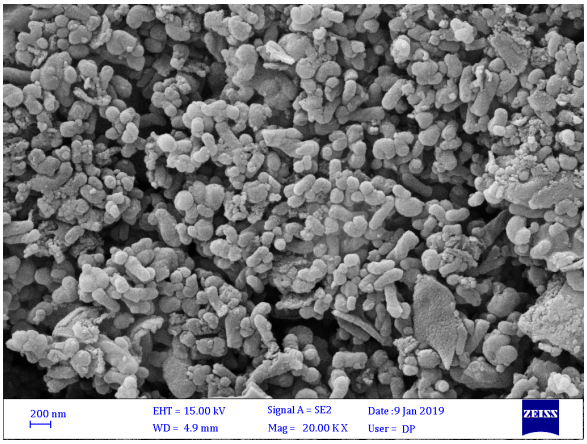

Fig. 3. FE-SEM image of $NiFe_2O_4$@mesopore silica@ guanidine.

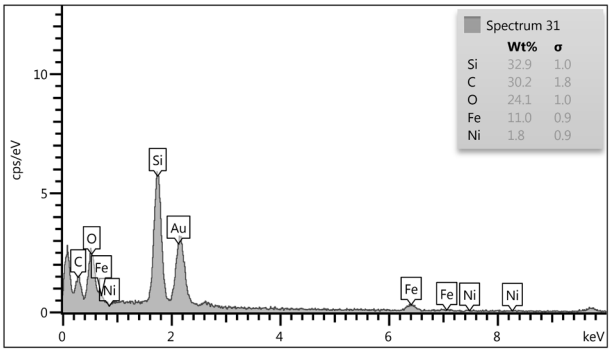

Fig. 5. EDS curves for $NiFe_2O_4$@mesopore silica@ guanidine.

solvent. After 5 min 1 mmol cyclohexanone was added to the reaction mixture, and the process was followed by thin-layer chromatography. The final product was separated with simple filtration and purification by recrystallization in the ethanol solvent. The final product identifies by the melting point, FT-IR, and ^{1}H NMR spectra (^{1}HNMR and FT-IR data were placed in SI files).

3. Result and discussion

3.1. Preparation and characterization

The $NiFe_2O_4$ nanoparticles were synthesized and functionalized by mesopore silica and guanidine. At first, $NiFe_2O_4$ was provided by the sol-gel method [48]. The obtained $NiFe_2O_4$ was reacted by CTAB, NaOH, and TEOS at ambient temperature to $NiFe_2O_4$ @ mesopore silica. The obtained magnetic nanocomposites reacted by guanidine under the refluxed condition to $NiFe_2O_4$@mesopore silica@ guanidine base nanocatalyst. The nanocomposite was distinguished by various analyses

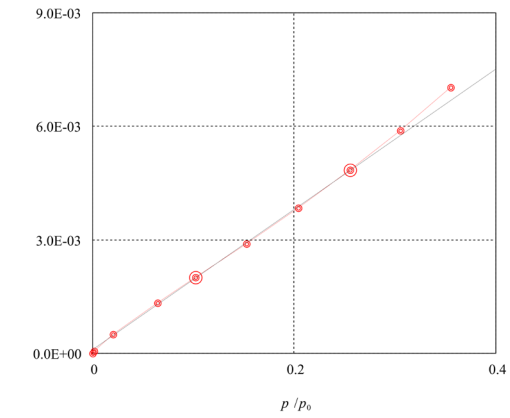

Fig. 4. BET curves for $NiFe_2O_4$@mesopore silica@ guanidine.

such as; SEM, EDX, XRD, FT-IR, BET, and VSM.

The XRD models were recorded of the crystal structure of $NiFe_2O_4$@ mesopore silica@ guanidine displayed in Fig. 1. The XRD pattern in Fig 1 shows the peaks (miller indices) in 30° (220), 37° (222), 45° (400), 58° (511), 62° (440) and 73°(533), regular XRD pattern of JCPDS card that due to the crystal structure of$NiFe_2O_4$ and the sharp peak in 22° due to amorphous mesopore silica.

Effective functionalization of the $NiFe_2O_4$@mesopore silica@ guanidine catalyst can be explained through FT-IR spectra (Fig. 2). According to the FT-IR spectrum of the nanocomposite, the presence of a peak around 458 cm^{-1} showed stretching vibration of Ni-O bonding; the peak of Fe-O looked near the 793 cm^{-1}; the NH^2 stretching bond displayed near 3391 cm^{-1}, and the peak of the Si-O stretching bond appeared around 1084 cm^{-1}.

The morphology and size of the nanocomposite were defined by the scanning electron microscopy analysis. The FE-SEM images of the $NiFe_2O_4$@mesopore silica@ guanidine (Fig. 3) shown the extremely uniform morphology for the nanocomposite. Moreover, the average particle size of $NiFe_2O_4$@mesopore silica@ guanidine was 77-85 nm.

The surface area and pore volume diameter of $NiFe_2O_4$@mesopore silica@ guanidine were defined using the Brunauer–Emmett–Teller (BET) technique. According to the acquired curve, the measurement of surface area was equal to 233 m_2g_{-1}, total pore volume 0.121 cm^3g^{-1} (Fig. 4).

Also, to characterize the percent of each element in the nanocomposite, it was studied elemental the energy-dispersive X-ray (EDS) spectrum. The EDS curve showed the percent of O, Si, Fe, Ni, and C were 24.1%, 32.9%, 1.8%, and 30.2`%, respectively (Fig. 5).

Thermogravimetric analysis (TGA) curves (Fig. 6) of $NiFe_2O_4$@ mesopore silica@ guanidine shows that losses of 60 percent of weight under 800 °C in the models are due to the release of adsorbed water, solvent, and organic materials.

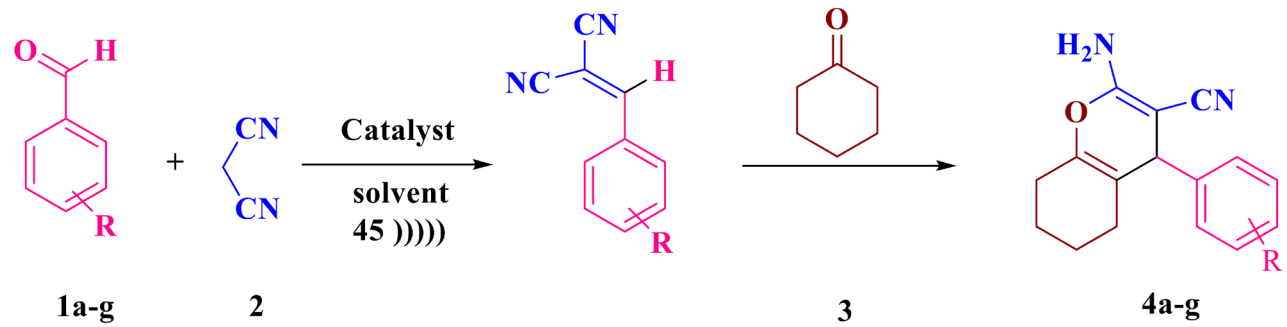

Scheme. 2. Synthesis of various derivatives of 4H-chromene in the presence of $NiFe_2O_4$/mesopore silica/guanidine nanocatalyst.

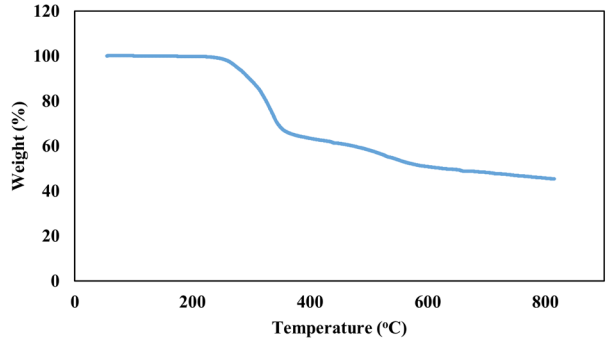

Fig. 6. TGA curves for $NiFe_2O_4$@mesopore silica@ guanidine.

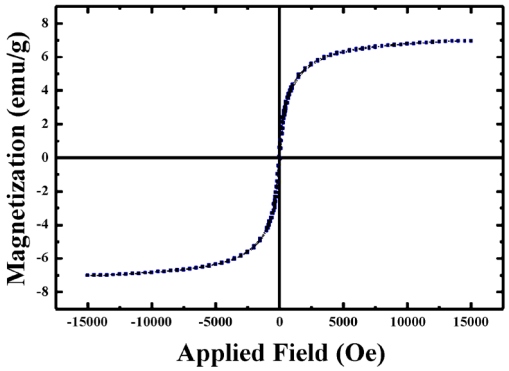

Fig. 7. FVSM curves for $NiFe_2O_4$@mesopore silica@ guanidine.

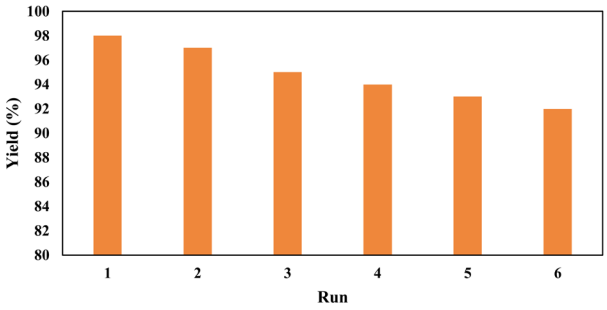

Fig. 8. The recyclability of $NiFe_2O_4$/mesopore silica/guanidine nanocatalyst in six runs.

Table 1.
Investigation of catalyst, catalyst amount in ethanol solvents for the synthesis of 4H-chromenes [a]

Entry	Catalyst	Catalyst amount (mg)	Time (h)	Yield [b] (%)
1	Et_3N	10	3.5	40
2	MgO	10	2.5	70
3	Morpholine	10	0.95	70
4	Guanidine	10	0.75	75
5	$NiFe_2O_4$/mesopore silica/guanidine	10	0.75	88
6	$NiFe_2O_4$/mesopore silica/guanidine	10	0.16	98
7	$NiFe_2O_4$/mesopore silica/guanidine	5	0.16	83
8	$NiFe_2O_4$/mesopore silica/guanidine	15	0.16	90

[a] Reaction conditions: benzaldehyde (1 mmol), malononitrile (2 mmol), cyclohexanone (1 mmol), 5 ml solvent.
[b] Isolated yield

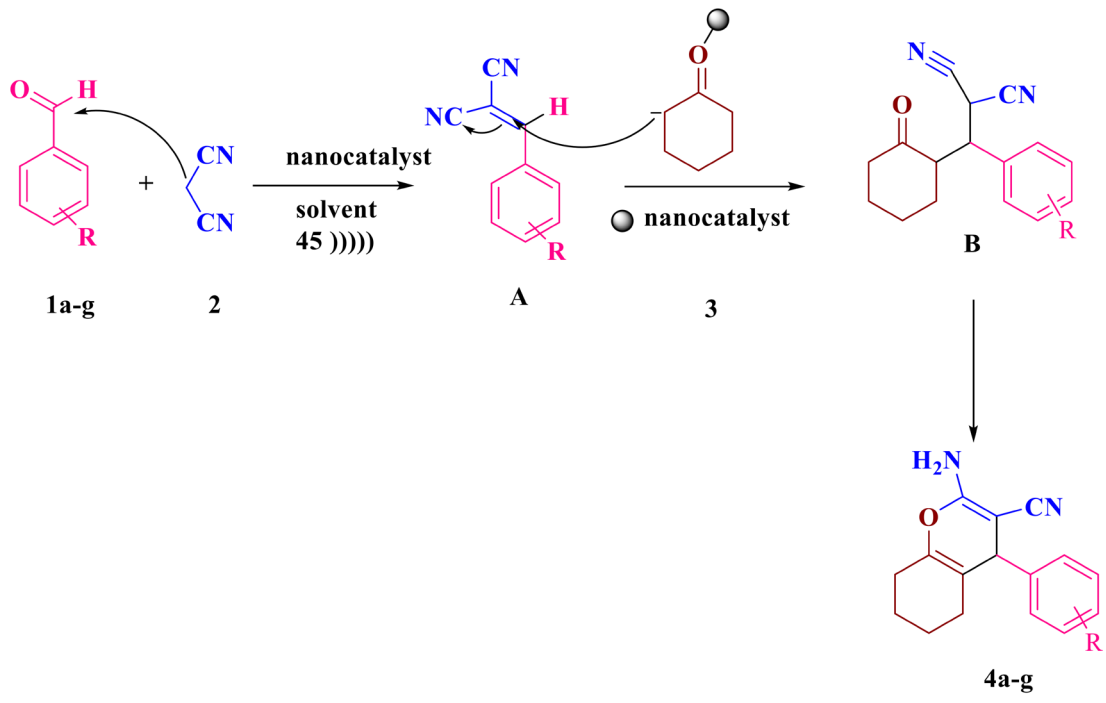

Scheme. 3. Proposed reaction mechanism for the Synthesis of 4H-choromene.

Table 2.
Investigation of solvent for the synthesis of 4H-chromenes [a]

Entry	Solvent	T °C	Time (h)	Yield [b] (%)
1	Acetonitrile	25	0.75	10
2	Chloroform	25	0.92	0
3	Ethanol	75	0.16	98
4	Methanol	25	0.75	90

[a] Reaction conditions: benzaldehyde (1 mmol), malononitrile (2 mmol), cyclohexanone (1 mmol), 5 ml solvent.
[b] Isolated yield

The magnetic properties of $NiFe_2O_4$@mesopore silica@ guanidine nanocomposite were recorded by the vibrating sample magnetometry (VSM) spectra of the nanocomposite. The magnetization curve of nanocomposite shown superparamagnetic properties (Fig. 7).

According to the TGA and EDX analyzed, the percent of organic materials was 60%, and mesopore silica around 30%. So, the percent of $NiFe_2O_4$ is around 10% in the nanocatalyst structure. Because the low percent of $NiFe_2O_4$ and covered with two-layer of mesopore silica and guanidine compound. The MS of the catalyst was decreased, but it has superparamagnetic properties and adsorbed with an external magnet.

The synthetic reaction of 4H-chromenes from benzaldehyde, cyclohexanone, and malononitrile was optimized by various solvents, catalysts, and temperatures.

The reaction was studied by utilizing different catalysts such as morpholine, Et_3N, MgO, and $NiFe_2O_4$/mesopore silica/guanidine in the ethanol solvents. The results of the study were exhibited in Table 1.

The results were displayed $NiFe_2O_4$/mesopore silica/guanidine (Table 1, Entry 5) and have the best yields of product in the short reaction time. The model reaction was tested in different solvents and the result showed in Table 2.

Table 3.
Several Power for the ultrasonic multicomponent reaction for synthesis of bis-ortho-aminocarbonitrile tetrahydronaphthalene 4a [a]

Entry	Power (W)	Time (min)	Yield [b] (%)
1	Silent	180	20
2	30	60	82
3	35	50	85
4	40	35	90
5	45	10	98
6	50	30	96

[a] Reaction conditions: Benzaldehyde (1 mmol), Cyclohexanone (1 mmol), Malononitrile (1 mmol), 5 ml Solvent.
[b] Isolated yield

Ultrasound irradiation was constructed as the motive energy for the improved yield of 4H-chromenes, that due to the increased temperature correlated to the production of hot spots. While the reaction was carried out without sonic irradiation in low yield and long reaction time (Table 3, entry 1). The best power for the reaction was acquired 45 W based on product yield and reaction time (Table 3, entry 5).

After optimization of the model reaction for the synthesis of 4h-chromene (4a-g), 1 mmol of benzaldehyde (1a-g), 1 mmol of malononitrile **(2)**, and 1mmol of cyclohexanone (3) were mixed in ethanol solvent and 5 mg NiFe2O4/mesopore silica/guanidine added to the mixture as the base nanocatalyst. The reaction was done under 45 power ultrasonic irradiation (Scheme 2) (Table 4).

The mechanism of the reaction for the production of 4H-chromenes

Table 4.
Synthesis of various derivatives of 4h-chromene in the presence of $NiFe_2O_4$/mesopore silica/guanidine nanocatalyst [a]

4a-l [a], yield % [b], Time (min)		
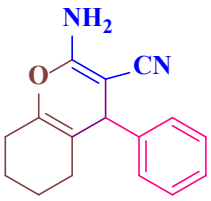 **4a: X= H, Y= H, 98, 10**	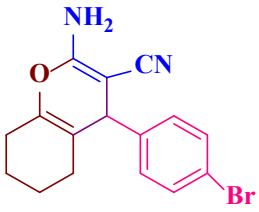 **4b: X= Br, Y= H, 95, 15**	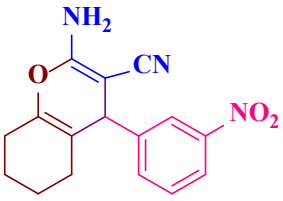 **4c: X= NO_2, Y= H, 96, 16**
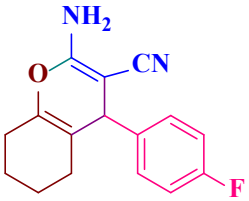 **4d: X= F, Y= H, 92, 17**	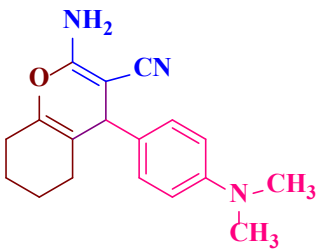 **4e: X= N,N dimethyl, Y= H, 93, 20**	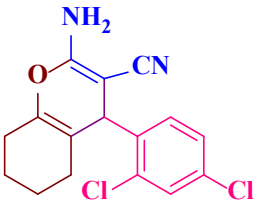 **4f: X=2,4 dichloro, Y= H, 91, 18**
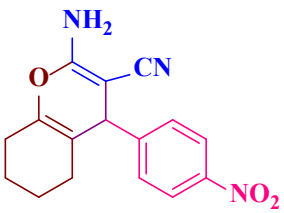 **4g: X= NO_2, Y= H, 94, 19**	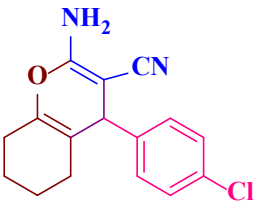 **4h: X= Cl, Y= H, 92, 17**	

[a] Reaction conditions: benzaldehyde (1 mmol), cyclohexanone (1 mmol), malononitrile (1 mmol), 0.1mmol nanocatalyst (5 mg), ethanol solvent (5ml), 45 power ultrasonic irradiation.
[b] Isolated yield

Table 5.
Comparisons of literatures reported catalyst with this work for synthesis compound 4a

Entry	Catalyst	Loading	Time (min)	Yield (%)	Method	Ref.
1	Morpholine	0.1 mmol	30	90	Reflux	[48]
2	$CaMgFe_2O_4$	0.1 mmol	20	92	r.t	[47]
3	$CoFe_2O_4$/lamellar mesopore silica/melamine	10 Mg	20	93	r.t	[31]
4	$NiFe_2O_4$/mesopore silica/guanidine	10 Mg	10	98	Ultrasound	This work

included various steps, at the first step, benzaldehyde and malononitrile reacted under Michael addition and formation the intermediate A under the nanomagnetic base $NiFe_2O_4$/mesopore silica/guanidine nanocatalyst. Then the cyclohexanone under condensation reaction joins to the intermediate A and formation intermediate B. The process followed by a cyclization reaction, the 4H-chromene (4a) compounds synthesis by absorption of the hydrogen, and double bonds rearrangement (Scheme 3).

3.2. Catalytic comparisons

To display the efficiency and influence of new methods for the synthesis of 4H-chromene derivatives, the obtained results were compared with the other methods, catalysts, and conditions (Table 5). As can be seen, the present study with different methods for added the starting material, nanocatalyst, and using ultrasonic irradiation is superior in yield of pure products and short reaction times.

3.3. Reusability

The reusability and nanocomposite are important advantages for commercial utilization. The reusability of $NiFe_2O_4$/mesopore silica/ guanidine nanocatalyst, was tested in six runs of the model reaction, and the results reported in Fig 8.

4. Conclusion

In this study, it was functionalized the $NiFe_2O_4$/mesopore silica with the guanidine compound. The mesopore silica has a large area for functionalization on the surface and pore. The reaction of benzaldehyde, malononitrile, and cyclohexanone as the model reaction was selected for examined the catalyst activity. The 4H-chromene was synthesized by used $NiFe_2O_4$/mesopore silica/ guanidine as a nanocatalyst in the excellent yields and short reaction times. The nanocomposite identified by FT-IR, SEM, XRD, VSM, BET techniques, and the organic products recognize by the melting point, ^{1}H NMR, and FT-IR analyses.

Supporting Information

Experimental details, copies of ^{1}H and FT-IR and of products is available free of charge via the Internet at

Acknowledgments

The authors are grateful to University of shahrekord for supporting this work by Grant No. 159148/92.

REFERENCES

[1] I.I. Slowing, B.G. Trewyn, S. Giri, V.Y. Lin, Mesoporous silica nanoparticles for drug delivery and biosensing applications, Advanced Functional Materials 17(8) (2007) 1225-1236.
[2] S.-H. Wu, C.-Y. Mou, H.-P. Lin, Synthesis of mesoporous silica nanoparticles, Chemical Society Reviews 42(9) (2013) 3862-3875.
[3] Z. Li, J.C. Barnes, A. Bosoy, J.F. Stoddart, J.I. Zink, Mesoporous silica nanoparticles in biomedical applications, Chemical Society Reviews 41(7) (2012) 2590-2605.
[4] S. Egodawatte, A. Datt, E.A. Burns, S.C. Larsen, Chemical insight into the adsorption of chromium (III) on iron oxide/mesoporous silica nanocomposites, Langmuir 31(27) (2015) 7553-7562.
[5] R.R. Castillo, M. Vallet-Regí, Functional mesoporous silica nanocomposites: biomedical applications and biosafety, International journal of molecular sciences 20(4) (2019) 929.
[6] L. Wei, N. Hu, Y. Zhang, Synthesis of polymer—mesoporous silica nanocomposites, Materials 3(7) (2010) 4066-4079.
[7] P. Xu, H. Yu, X. Li, Functionalized mesoporous silica for microgravimetric sensing of trace chemical vapors, Analytical chemistry 83(9) (2011) 3448-3454.
[8] M. Gao, J. Zeng, K. Liang, D. Zhao, B. Kong, Interfacial Assembly of Mesoporous Silica-Based Optical Heterostructures for Sensing Applications, Advanced Functional Materials 30(9) (2020) 1906950.
[9] R. Nechikkattu, C.-S. Ha, Temperature-responsive mesoporous silica nanoreactor with polymer gatings immobilized surface via a 'grafting-to'approach as peroxidase-like catalyst, Microporous and Mesoporous Materials 306 (2020) 110472.
[10] F.-C. Lin, J.I. Zink, Probing the local nanoscale heating mechanism of a magnetic core in mesoporous silica drug-delivery nanoparticles using fluorescence depolarization, Journal of the American Chemical Society 142(11) (2020) 5212-5220.
[11] A.F. Zarandi, H. Shirkhanloo, P. Paydar, A novel method based on functionalized bimodal mesoporous silica nanoparticles for efficient removal of lead aerosols pollution from air by solid-liquid gas-phase extraction, Journal of Environmental Health Science and Engineering 18(1) (2020) 177-188.
[12] W. Wang, Y. Chen, A. Chen, X. Ma, Composite particles with dendritic mesoporous-silica cores and nano-sized CeO_2 shells and their application to abrasives in chemical mechanical polishing, Materials Chemistry and Physics 240 (2020) 122279.
[13] S. Mohammadi, H. Naeimi, Synthesis of novel bis-spirooxindoles catalyzed by magnetic cobalt ferrite encapsulated MCM-41@ MgO as a solid base, Current Organic Synthesis (2020).
[14] A. Kazemzadeh, M.A. Meshkat, H. Kazemzadeh, M. Moradi, R. Bahrami, R. Pouriamanesh, Preparation of graphene nanolayers through surfactant-assisted pure shear milling method, Journal of Composites and Compounds 1(1) (2019) 22-26.
[15] S. Eskandarinezhad, R. Khosravi, M. Amarzadeh, P. Mondal, F.J.C. Magalhães Filho, Application of different Nanocatalysts in industrial effluent treatment: A review, Journal of Composites and Compounds 3(6) (2021) 43-56.
[16] Y. Wang, J. He, Y. Shi, Y. Zhang, Structure-dependent adsorptive or photocatalytic performances of solid and hollow dendritic mesoporous silica & titania nanospheres, Microporous and Mesoporous Materials 305 (2020) 110326.
[17] Q. Yu, T. Deng, F.-C. Lin, B. Zhang, J.I. Zink, Supramolecular assemblies of heterogeneous mesoporous silica nanoparticles to co-deliver antimicrobial peptides and antibiotics for synergistic eradication of pathogenic biofilms, ACS nano 14(5) (2020) 5926-5937.
[18] J.S. Schulze, J. Migenda, M. Becker, S.M. Schuler, R.C. Wende, P.R. Schreiner, B.M. Smarsly, TEMPO-functionalized mesoporous silica particles as heterogeneous oxidation catalysts in flow, Journal of Materials Chemistry A 8(7) (2020) 4107-4117.
[19] B. Van Gemert, Benzo and naphthopyrans (chromenes), Organic photochromic and thermochromic compounds, Springer 2002, pp. 111-140.
[20] R. Pratap, V.J. Ram, Natural and synthetic chromenes, fused chromenes, and versatility of dihydrobenzo [h] chromenes in organic synthesis, Chemical reviews 114(20) (2014) 10476-10526.
[21] M. Costa, T.A. Dias, A. Brito, F. Proença, Biological importance of structurally diversified chromenes, European journal of medicinal chemistry 123 (2016) 487-507.
[22] S.A. Patil, J. Wang, X.S. Li, J. Chen, T.S. Jones, A. Hosni-Ahmed, R. Patil, W.L. Seibel, W. Li, D.D. Miller, New substituted 4H-chromenes as anticancer agents, Bioorganic & medicinal chemistry letters 22(13) (2012) 4458-4461.
[23] A.M. El-Saghier, M.B. Naili, B.K. Rammash, N.A. Saleh, K.M. Kreddan, Synthesis and antibacterial activity of some new fused chromenes, Arkivoc 16 (2007) 83-91.
[24] V.T. Angelova, Y. Voynikov, P. Andreeva-Gateva, S. Surcheva, N. Vassilev, T. Pencheva, J. Tchekalarova, In vitro and in silico evaluation of chromene based aroyl hydrazones as anticonvulsant agents, Medicinal Chemistry Research 26(9) (2017) 1884-1896.
[25] N.M. Sabry, H.M. Mohamed, E.S.A. Khattab, S.S. Motlaq, A.M. El-Agrody, Synthesis of 4H-chromene, coumarin, 12H-chromeno [2, 3-d] pyrimidine deriva-

tives and some of their antimicrobial and cytotoxicity activities, European journal of medicinal chemistry 46(2) (2011) 765-772.
[26] O.S. Patrusheva, V.V. Zarubaev, A.A. Shtro, Y.R. Orshanskaya, S.A. Boldyrev, I.V. Ilyina, S.Y. Kurbakova, D.V. Korchagina, K.P. Volcho, N.F. Salakhutdinov, Anti-influenza activity of monoterpene-derived substituted hexahydro-2H-chromenes, Bioorganic & medicinal chemistry 24(21) (2016) 5158-5161.
[27] A. Parthiban, J. Muthukumaran, A. Manhas, K. Srivastava, R. Krishna, H.S.P. Rao, Synthesis, in vitro and in silico antimalarial activity of 7-chloroquinoline and 4H-chromene conjugates, Bioorganic & medicinal chemistry letters 25(20) (2015) 4657-4663.
[28] K. Takao, H. Yahagi, Y. Uesawa, Y. Sugita, 3-(E)-Styryl-2H-chromene derivatives as potent and selective monoamine oxidase B inhibitors, Bioorganic chemistry 77 (2018) 436-442.
[29] M. Amirnejad, M.R. Naimi-Jamal, H. Tourani, H. Ghafuri, A facile solvent-free one-pot three-component method for the synthesis of 2-amino-4H-pyrans and tetrahydro-4H-chromenes at ambient temperature, Monatshefte für Chemie-Chemical Monthly 144(8) (2013) 1219-1225.
[30] S. Rostamnia, A. Nuri, H. Xin, A. Pourjavadi, S.H. Hosseini, Water dispersed magnetic nanoparticles (H_2O-DMNPs) of γ-Fe_2O_3 for multicomponent coupling reactions: a green, single-pot technique for the synthesis of tetrahydro-4H-chromenes and hexahydroquinoline carboxylates, Tetrahedron Letters 54(26) (2013) 3344-3347.
[31] S. Mohammadi, H. Naeimi, Functionalized $CoFe_2O_4$/lamellar mesopore silica anchored to melamine nanocomposite as a novel catalyst for synthesis of 4H-chromenes under mild conditions, Applied Organometallic Chemistry 34(6) (2020) e5630.
[32] L.N. Nasirmahale, F. Shirini, H. Tajik, O.G. Jolodar, Efficient Synthesis of 5-Oxo-5, 6, 7, 8-Tetrahydro-4H-Chromenes Assisted by Poly (4-Vinylpyridine), Polycyclic Aromatic Compounds (2018).
[33] R. Pourhasan-Kisomi, F. Shirini, M. Golshekan, Introduction of organic/inorganic Fe_3O_4@ MCM-41@ Zr-piperazine magnetite nanocatalyst for the promotion of the synthesis of tetrahydro-4H-chromene and pyrano [2, 3-d] pyrimidinone derivatives, Applied Organometallic Chemistry 32(7) (2018) e4371.
[34] J.M. Khurana, B. Nand, P. Saluja, 1, 8-Diazabicyclo [5.4. 0] undec-7-ene: A Highly Efficient Catalyst for One-Pot Synthesis of Substituted Tetrahydro-4H-chromenes, Tetrahydro [b] pyrans, Pyrano [d] pyrimidines, and 4H-Pyrans in Aqueous Medium, Journal of Heterocyclic Chemistry 51(3) (2014) 618-624.
[35] I. Hua, M.R. Hoffmann, Optimization of ultrasonic irradiation as an advanced oxidation technology, Environmental Science & Technology 31(8) (1997) 2237-2243.
[36] S.-i. Umemura, C.A. Cain, K. Katakura, Ultrasonic irradiation system, Google Patents, 1989.
[37] A. Kotronarou, G. Mills, M.R. Hoffmann, Ultrasonic irradiation of p-nitrophenol in aqueous solution, the journal of physical chemistry 95(9) (1991) 3630-3638.
[38] L. Saunders, J. Perrin, D. Gammack, Ultrasonic irradiation of some phospholipid sols, Journal of Pharmacy and Pharmacology 14(1) (1962) 567-572.
[39] F. Sharifianjazi, H. Pakseresht Amir, M. Shahedi Asl, A. Esmaeilkhanian, H. Nargesi khoramabadi, H. Won Jang, M. Shokouhimehr, Hydroxyapatite consolidated by zirconia: applications for dental implant, Journal of Composites and Compounds 2(2) (2020).
[40] X. Wang, J. Song, J. Liu, Z.L. Wang, Direct-current nanogenerator driven by ultrasonic waves, Science 316(5821) (2007) 102-105.
[41] J. Daraei, Production and characterization of PCL (Polycaprolactone) coated TCP/nanoBG composite scaffolds by sponge foam method for orthopedic applications, Journal of Composites and Compounds 2(2) (2020) 44-49.
[42] E. Asadi, A.F. Chimeh, S. Hosseini, S. Rahimi, B. Sarkhosh, L. Bazli, R. Bashiri, A.H.V. Tahmorsati, A review of clinical applications of graphene quantum dot-based composites, Journal of Composites and Compounds 1(1) (2019) 31-40.
[43] D.L. White, Amplification of ultrasonic waves in piezoelectric semiconductors, Journal of Applied Physics 33(8) (1962) 2547-2554.
[44] M.J. Lowe, Matrix techniques for modeling ultrasonic waves in multilayered media, IEEE transactions on ultrasonics, ferroelectrics, and frequency control 42(4) (1995) 525-542.
[45] K.A. Nelson, R.D. Miller, D. Lutz, M. Fayer, Optical generation of tunable ultrasonic waves, Journal of Applied Physics 53(2) (1982) 1144-1149.
[46] S. Mohammadi, H. Naeimi, A synergetic effect of sonication with yolk-shell nanocatalyst for green synthesis of spirooxindoles, Green Chemistry Letters and Reviews 14(2) (2021) 344-356.
[47] H.K. Mohammadi, K.K. Kalantari, S.S. Naeimi, M. Pouretezad, E. Shokri, M. Tafazoli, M. Dastjerdi, L. Kardooni, Immediate and delayed effects of forearm kinesio taping on grip strength, Iranian Red Crescent Medical Journal 16(8) (2014).
[48] H. Naeimi, S. Mohammadi, Synthesis of 1H-Isochromenes, 4H-Chromenes and Orthoaminocarbonitrile Tetrahydronaphthalenes by $CaMgFe_2O_4$ Base Nanocatalyst, ChemistrySelect 5(8) (2020) 2627-2633.

Available online at www.jourcc.com

Journal homepage: www.JOURCC.com

Journal of Composites and Compounds

Effects of Mg and MgO Nanoparticles on Microstructural and Mechanical Properties of Aluminum Matrix Composite Prepared via Mechanical Alloying

Behnam Nazerian Khozani [a], Aliasghar Abuchenari [a]*

[a] *Department of Material Science and Engineering, Shahid Bahonar University of Kerman, Kerman, Iran*

A B S T R A C T

Aluminum-based composites reinforced with ceramic particles have been used for many applications because of their high hardness, good wear resistance, low weight, and low thermal expansion coefficient. The Al-MgO/Mg composite was prepared in the present study. The effects of milling time and amounts of initial Mg and MgO were studied on the properties of the composite. The milled powder mixtures were subsequently analyzed by the XRD and SEM tests. Crystal sizes and internal strains were calculated using XRD data and the Williamson-Hall equation. The hardness of samples was measured by the Vickers method. The results showed that the lattice parameter significantly increased by increasing the amount of Mg. During the milling, the crystallite size, and simultaneously internal strain and hardness increased by increasing amounts of Mg and MgO. The results also showed that the effects of Mg on the composite properties were higher than MgO particles.

Peer review under responsibility of jourcc

A R T I C L E I N F O R M A T I O N

Article history:
Received 31 May 2021
Received in revised form 12 June 2021
Accepted 27 June 2021

Keywords:
Composite
Mechanical alloying
Mg and MgO particles
Hardness
Sintering

1. Introduction

Metal matrix composites (MMCs) are now widely used in modern engineering applications due to their superior mechanical properties such as fracture toughness, specific stiffness to weight ratio, impact and high creep resistance, and high oxidation and corrosion resistance compared to conventional materials. MMCs with various matrix metals, such as copper, aluminum, nickel, and iron, are reinforced with various ceramics particles, such as MgO, TiC, Al_2O_3, and SiC, to increase strength through multiple strengthening mechanisms at room temperature. These include the fabrication of thermal dislocations due to a mismatch in the composite thermal expansion coefficients and the addition of refinement crystallite to the matrix microstructure [1-3].

There is an increasing demand for aluminum matrix composites reinforced with nano-ceramic particles. Because of its excellent combination of properties, such as high stiffness, low density, reasonable wear, controlled thermal expansion coefficient, and corrosion resistance, it is currently used in various applications, including aerospace and the automobile industry. Several parts are used in tribological systems in many application sectors, requiring friction performance and improved wear of these composites, thus, the addition of graphite particulates is required to improve machinability and wear resistance [4-6].

Squeeze casting, stir casting, liquid metal infiltration, powder metallurgy, mechanical alloying, and spray decomposition are some of the techniques used to make MMCs [7, 8]. In addition, mechanical alloying/milling has proved to be a successful method for improving reinforcement distribution throughout the matrix [9, 10].

Some studies have shown that reinforcements, such as SiC particles and other particles, can be successfully incorporated into an aluminum matrix using the MA technique. In addition, the refinement of sub-grain size and the uniform distribution of reinforcement have improved the properties of composites [9, 11, 12]. Moreover, nanocomposite powders made by Al-alloy powders and mechanical alloying of ceramic particles can be employed to make composites with better characteristics. Additionally, reducing the inter-particle spacing and incorporating ultrafine particles, such as nanoparticles, into the matrix improves mechanical properties significantly [13, 14].

Fine particles, on the other hand, have a higher tendency to agglomerate together. As a result, the optimum particle size, amount of reinforcement, and processing parameters should be determined for each technique and matrix [15, 16]. MgO is a better choice for reinforcement because of its high melting point (Tm = 2800 C), compressive strength, hardness, and excellent thermodynamic stability [17, 18].

According to Azhar et al., the addition of MgO particles improved the mechanical properties [19]. In addition, Abdizadeh et al. [20] demonstrated that adding fine MgO particles to Zirconia Toughened Alumina (ZTA) improved wear performance by 50% and increased hardness. Vickers hardness decreases and increases with coarser and finer MgO particle sizes, respectively, when using ZTA. Thus, the hardness of the composite specimens increases as MgO increases, while the resistance

* *Corresponding author: Aliasghar Abuchenari; E-mail: aliab596@yahoo.com*
https://doi.org/10.52547/jcc.3.2.2

decreases [21]. Aluminum alloy (A356.1) matrix composites reinforced with nanoparticle MgO were fabricated using the stir casting method by Ansary yar et al. [22]. According to the findings, the composites with 1.5 vol. % reinforcement particles fabricated at 850 °C had a homogeneous microstructure and improved mechanical properties.

This research aims to investigate the impact of MgO and Mg nanoparticle content on mechanical properties and the microstructure of Al-MgO/Mg composites made by mechanical alloying, along with the effect of MgO and Mg content on the crystal parameters.

2. Materials and methods

2.1. Materials

Pure aluminum powder (99 wt%), pure magnesium powder (99 wt%), and pure magnesium oxide powder (98 wt%) were purchased from Khorasan Powder Metallurgy Co. (Mashhad, Iran). The particle sizes of Al, MgO, and Mg powder were 25, 120, and 136 μm, respectively.

2.2. Composite preparation

Aluminum metal matrix composites were prepared by a mechanical alloying technique. In the first step, the pure aluminum powder reinforced with 5 wt% of MgO powder was produced by ball milling with the following parameters: ball-to-powder weight ratio: 20:1, ball diameter: 1 and 2 cm, ball material: AISI 420 quenched stainless steel, and speed 250 rpm. Ethanol 3% (wt.) was added to control the process. The argon atmosphere was also used as a control gas. Then, pure aluminum powder with a constant content of MgO powder (5 wt%) was reinforced with 10 and 15 wt% of Mg powder. In the last step, pure aluminum powder with a constant content of Mg powder (10 wt%) was reinforced with 10 and 15 wt% of MgO powder. The powder was cold-pressed (pressure: 25.4 MPa) in a steel mold. The compressed samples were then sintered in a furnace (Shenyang GE Furnace Co. LTD, Shenyang, China) with argon atmosphere at 400°C for 45 min. These samples were produced to investigate the effects of MgO and Mg on the microstructure and mechanical properties of the metal matrix composite. The sample balls were milled for 5, 10, 20, and 40 h because the time was necessary to complete the mechanical alloying process. Finally, the composites were obtained with these compounds: Al-5MgO, Al-5MgO/10Mg, Al-5MgO/15Mg, Al-10MgO/10Mg, and Al-15MgO/10Mg.

2.3. Characterization and testing

The composites were subjected to the X-Ray diffraction (XRD) analysis. Crystalline phases were identified using X'Pert HighScore software (2.2b) equipped with the PCPDFWIN database.

Crystallite size and lattice-strain were determined by the Hall-Williamson method [23]:

$$\beta\cos\theta = 2\varepsilon\sin\theta + \frac{0.9\lambda}{D}$$

where "B" is broadening due to crystallite size and lattice strain, is strain, "θ" is the 'Bragg's angle, "λ" is the wavelength of the incident X-ray beam in nm, and "D" is crystalline size. Lattice strains were identified by Sigma Plot software.

Equation 3-2 [24] also determines lattice parameters:

$$a = \frac{\lambda\sqrt{h^2+k^2+l^2}}{2\sin\theta}$$

The lattice parameters were determined for (2 2 0), (3 1 1), and (2 2 2) and the extrapolation function method.

The microstructure of the samples was analyzed by a Scanning Electron Microscope (SEM, JEOL JSM-5800 LV) with energy-dispersive

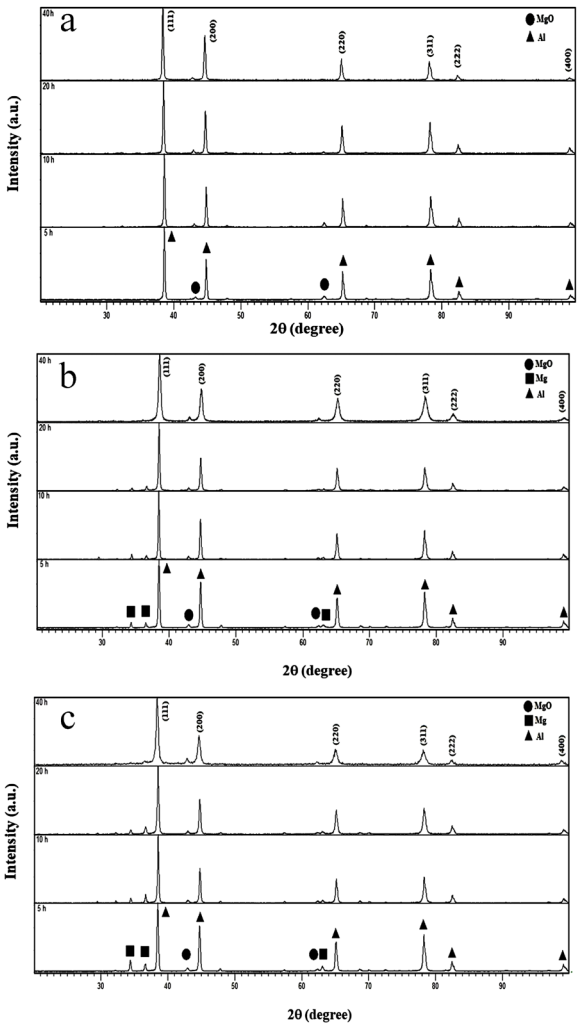

Fig. 1. X-ray diffraction pattern of composites in various times of ball milling. a) Al-5MgO composite, b) Al-5MgO/10Mg composite, and c) Al-5MgO/15Mg composite. .

X-ray spectroscopy (EDX) at an operating voltage of 20 kV, and the particle size was determined with Image Tools software. The hardness of the composites was evaluated by the Micro–Vickers hardness tester (Struers, Durmin20). The mean of five measurements was recorded in various regions of the polished samples. The applied load and the time of loading were 250 mN and 5s, respectively.

3. Results and discussion

3.1. XRD analysis

Figure 1 shows the X-ray diffraction pattern of the prepared composites with various amounts of Mg nanoparticles. Figure 1-a shows the XRD pattern of the Al-5MgO composite at various times of ball milling. Aluminum peaks with a high height and low width with an FCC crystal structure, as well as MgO peaks, can be seen in the first 5 h. The aluminum peaks become wider and their height decreases as the milling time increases to 40 h. In addition, the non-displacement of aluminum peaks is observed during milling, and the peaks related to MgO in the diffraction pattern of the powder mixture are shortened over time while studying the diffraction angle of aluminum peaks.

There is no solid solution formed because MgO particles do not enter the aluminum lattice. The peak of MgO particles does not disappear because they do not dissolve in the aluminum lattice. However, as milling time increases, the size of magnesium oxide particles decreases below microns, causing them to appear less intense on the XRD. The mech-

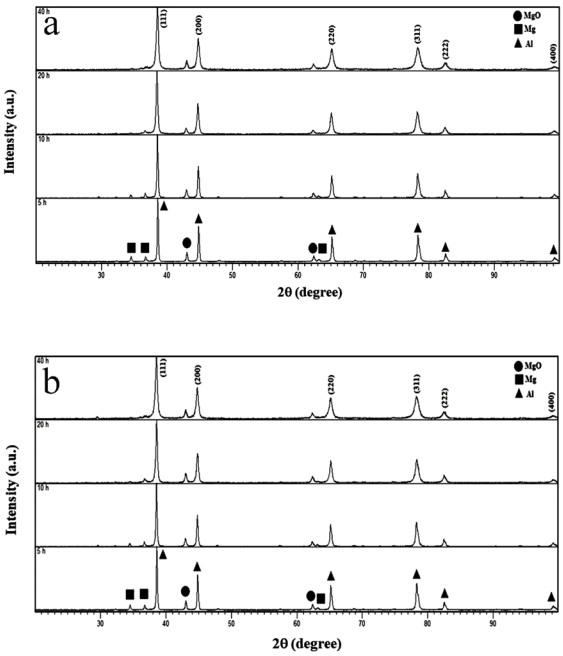

Fig. 2. X-ray diffraction pattern of composites at various times of ball milling. a) Al-10MgO/10Mg composite and b) Al-15MgO/10Mg composite.

anism is that magnesium oxide particles crush and distribute the underlying powder among the aluminum particles, changing its behavior. High-energy collisions of bullet-powder-bullet and bullet-powder-container create many crystal defects in the milling process, such as borders, misalignments, and voids, which increase over time. The ground lattice parameter does not increase because magnesium oxide particles enter the aluminum field, implying no diffusion mechanism [24, 25].

Figures 1-b and 1-c show the XRD patterns of Al-5MgO/10Mg and Al-5MgO/15Mg composites at various ball milling times. All peaks related to aluminum with FCC crystal structure, magnesium with HCP crystal structure, and magnesium oxide peaks can be seen for both samples in the first 5 h. The intensity of magnesium peaks gradually decreased with increasing milling time from 5 to 20 h but did not completely disappear. The magnesium peak was completely disappeared after 40 h of milling, leaving only the aluminum peaks with FCC structures and magnesium oxide. Aluminum peaks also shifted towards lower diffraction angles. Clearer small Mg peaks are seen in the dispersion pattern of the primary powders in the mixture containing 15% by weight of magnesium (Fig. 1-c) and fade away over milling time, indicating that the magnesium particles in the aluminum field are dissolved during the mechanical alloying process. The formation of solid-aluminum-magnesium supersaturated solution with FCC structure in mechanical alloying of powdered aluminum and magnesium has been reported by Gubicza [26], Umbrajkar [27], Scudino [28], Singh [29], Aqeeli [30, 31], and Youssef [32]. The absence of peaks in XRD patterns related to compounds between aluminum and magnesium, on the other hand, could be a reason for magnesium solubility in aluminum. These findings, combined with previous findings, show the formation of (Al(Mg)ss) without the formation of metal-metal compounds of up to 30% of magnesium atoms. It is in agreement with [27-29, 31, 33] that the solubility of the alloying elements, the presence of stress in the microstructure, and crystallite shrinkage have all been blamed for the increase in the width of the aluminum peaks [34].

According to the examination, the intensity of the aluminum peaks decreased and their width increased during milling in all three samples. The figures also show that as the magnesium percentage increases, the peaks become wider and their intensity decreases, indicating an increase in the lattice strain and a decrease in the crystallite size with the increased magnesium content.

Figure 2 shows the XRD pattern of the prepared composites with various amounts of MgO nanoparticles. Figure 2 (a and b) shows the XRD patterns of Al-10MgO/10Mg and Al-15MgO/10Mg composites at various times of ball milling.

The XRD pattern variations of these two samples are approximately similar to that of the Al 5MgO/10Mg sample. As the milling time increases, the peak intensity of magnesium with an HCP structure also decreases and gradually disappears. It is also observed that as the milling time increases, the aluminum peaks become wider and their intensity decreases. Finally, aluminum peaks with the FCC structure and magnesium oxide are seen after 40 h of milling. It is also observed that the peaks become wider and their height decreases with increasing the milling time, which indicates an increase in the lattice strain and a decrease in the crystallite size with increasing the milling time [33].

3.2. Crystallite size and lattice characteristics

Graphs of crystallite size, lattice strain, and lattice parameter size in terms of milling time for different chemical compounds are shown in Figure 3 (a-c). Figure 3-a shows the crystallite size diagram in terms of milling time for different chemical compositions, indicating that the crystallite size decreases with increasing milling time. The process of reducing the crystallite size to 40 h is nearly identical with the addition of magnesium and the increased milling time. Crystallite size decreases on a steep slope in the early stages of milling, and milling is then done at a slower rate, between 20 and 40 h. Al-5MgO, for example, reduces the crystallite size to 54 nm when the milling time is increased to 40 h. The figure also shows that the decrease in crystallite size becomes more significant as magnesium increases up to 15% by weight after 40 h of milling. Al/5MgO composite powder reduces the crystallite size of this composite from 54 to 26 nm. The crystallite size decreases by a significant slope when magnesium oxide is added to Al-(5-15) MgO/10Mg composites and the fine-crystallite decreases at a much slower rate when the milling time is increased from 5 to 20 h. The crystallite size of all three samples became nearly identical in 40 h, ranging from 32 to 37 nm. It is clear from this graph that the effect of various amounts of MgO is less than that of Mg. In general, as milling time increases, severe plastic deformation in powder particles increases crystalline defects such as spot defects, misplacements, and so on [35-37].

The presence of crystal defects increases the system energy and increases the lattice strain. To compensate for the effect mentioned above, the system misplaces sub-crystallites with a less energetic arrangement, and eventually, the sub-crystallites become the main crystallites due to the mechanical work by rotating the sub-crystallites and sliding the crystallite boundaries, which causes micro-crystallinity and the formation of a nanocrystalline structure during the mechanical alloying process [26, 35, 36, 38].

Figure 3-b shows the lattice strain diagram in terms of milling time for various chemical compounds, depicting an increase in the Al-5MgO sample lattice strain at a relatively constant rate. However, the lattice strain increases more sharply as the amount of magnesium increases with decreasing crystallite size, and the rate of increase in lattice strain decreases over time. The figure also shows that as the magnesium level rises, the lattice strain rises significantly. On the other hand, it is clear from the two forms that increasing magnesium oxide by 10 and 15 wt. % does not significantly change the crystallite size or the Al-MgO/10Mg composite lattice strain. On the other hand, magnesium oxide particles are hard particles that, when placed between ground phase particles, cause a local strain around them, increasing dislocation density, thereby speeding up the fine-crystallite process. However, the effect of magnesium on the crystallite size and lattice strain is greater than that of the

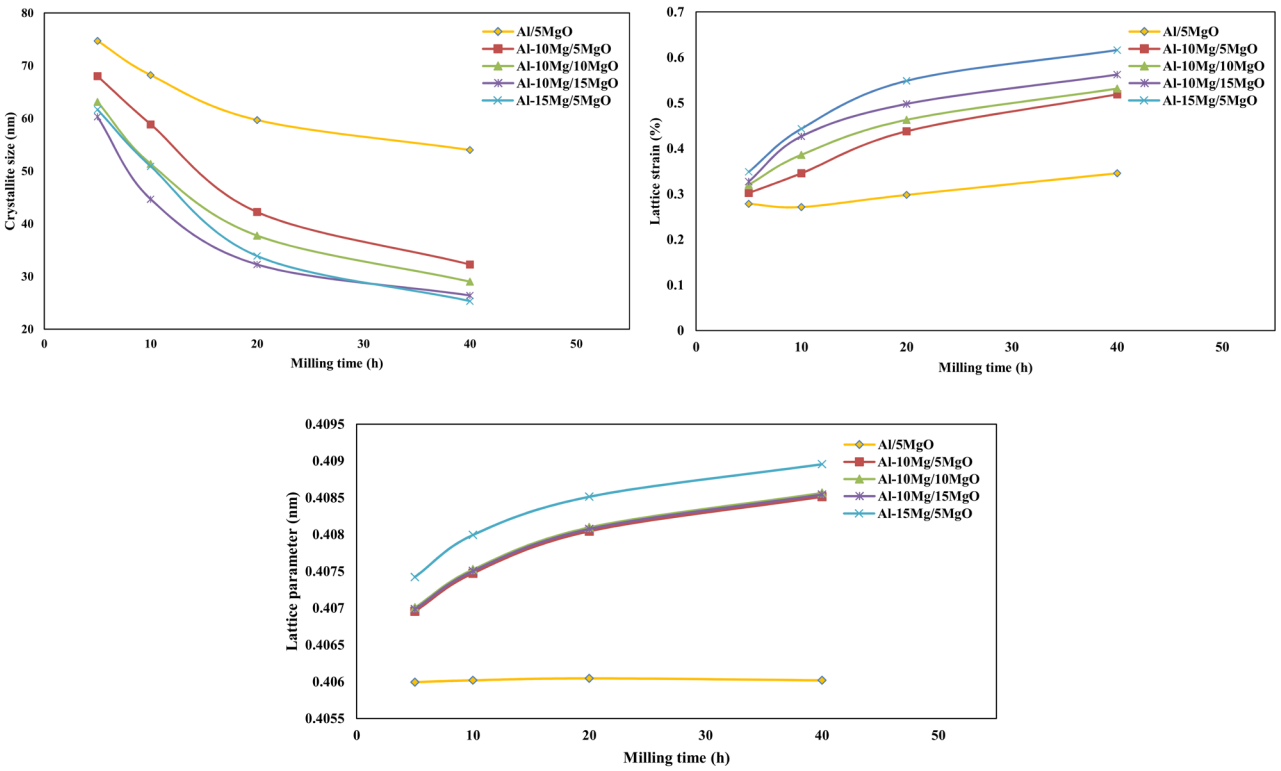

Fig. 3. The variations of composites according to ball milling times. a) Crystallite size variations, b) lattice strain variation, and c) lattice parameter variation.

magnesium oxide percentage.

Different mechanisms of MgO and Mg for increasing dislocation density can be attributed to this phenomenon. For example, MgO particles cause local strain around them and increase dislocation density by crushing and dispersing among aluminum particles, whereas Mg dissolving in aluminum causes hard work in the background powder particles and increases dislocation density during milling time. Of course, increasing the amount of magnesium oxide and crushing it, and increasing the local strain and dislocation density both accelerate the dissolution of magnesium in the aluminum field [4, 15]. Similarly, the increasing effect of Al_2O_3 reinforcing particles by 5, 10, and 15 wt.% on the microstructure of Al-10Mg/Al_2O_3 composites were reported in a study by Safari [39]. Their findings revealed that increasing the number of Al_2O_3 particles did not result in a significant decrease in crystallite size or an increase in the lattice strain.

Figure 3-c shows the size of the lattice parameter in milling time for different percentages of magnesium and magnesium oxide. The crystallite parameter for the Al-5MgO sample has a constant value with increasing the milling time, as shown in the figure. The figure also shows that as the magnesium increases, the lattice parameter increases significantly. For Al-(5-15)MgO/10Mg composites, changes in the lattice parameters with the addition of magnesium oxide are not noticeable over time and have an almost constant trend for all three samples. Because of the saturation of soluble magnesium in aluminum at the start of milling, the increase of the aluminum lattice parameter with milling time is faster than for long periods. Therefore, the more magnesium in the powder mixture, the more changes in the aluminum lattice parameter happen, and the number of magnesium atoms increases in the aluminum field. In general, the increase in solid solubility of magnesium in aluminum during mechanical alloying is attributed to the formation of a nanocrystalline structure and the creation of a large volume fraction of crystallite boundaries [40]. The results of Gubicza [41], Youssef [40], and Scudino [42] also show an increase in the lattice parameter in aluminum-magnesium alloys with increasing magnesium content and milling time. According to Figure 3, the amplifier phase does not affect the lattice parameter because magnesium oxide does not enter the aluminum lattice. In addition, no solid solution is formed, and local strain in the aluminum field only increases by crushing and distribution in the aluminum field; besides, dislocation density causes the peak height to be shortened [43].

3.3. Microstructure analysis

The SEM images of the Al-5MgO composite powder milled at various times are shown in Figures 4(a-d). The SEM image of the sample ground for 5 h shows that the particles are severely deformed and form a flat, flaky morphology due to the impact of the soft ground powder on the pellets and the particle mill. The difference in crystallite size is very noticeable at this time. Some particles are small while others are quite large. The particles flatten and flake as the milling time is increased to 10 and 20 h, indicating the cold welding process and the flexibility of the aluminum powder. Finally, dislocation density in the particles increases after 40 h of milling and significant deformation of the powder particles, resulting in increased work hardening and brittleness in the powder particles [44].

Magnesium oxide particles are also used as reinforcements in the joints of welded metal particles, increasing the substrate hardness even more. Because of the brittleness of powder particles, they are broken by increasing their hard work, thereby decreasing the size of the powder particles. The morphology of the flat state becomes almost coaxial with the breaking of plate powder particles and the absence of cold welding, but a stable state is not created in the powder particles.

The SEM images of the Al-5MgO/10Mg and Al-5MgO/15Mg powder samples, milled at different times, are shown in Figures 5 and 6. Due to collisions between the powder particles and the particle mill container after 5 h of milling, they became wider in these samples with the addition of magnesium.

Due to the dominance of the cold welding process, the particle size

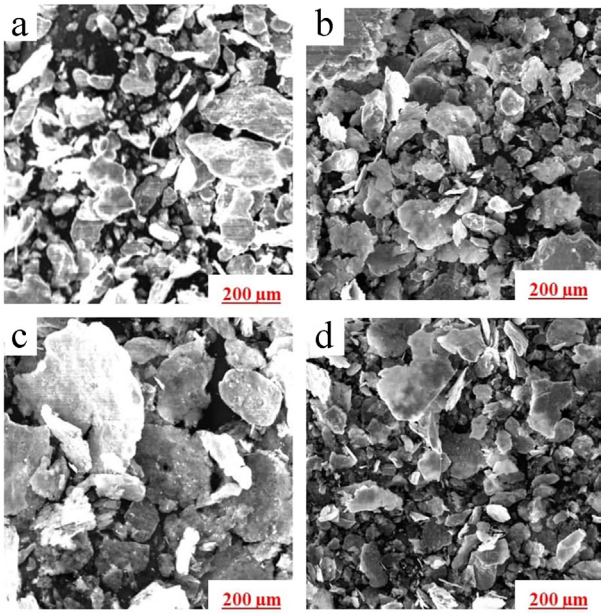

Fig. 4. SEM image of Al-5MgO sample after (a) 5, (b) 10, (c) 20, and (d) 40 h of milling.

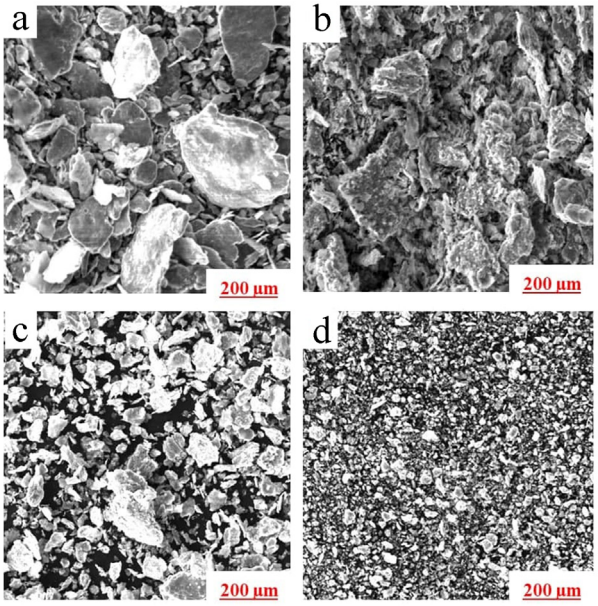

Fig. 5. SEM image of Al-5MgO/10Mg sample after (a) 5 (b) 10 (c) 20 (d) 40 hours of milling.

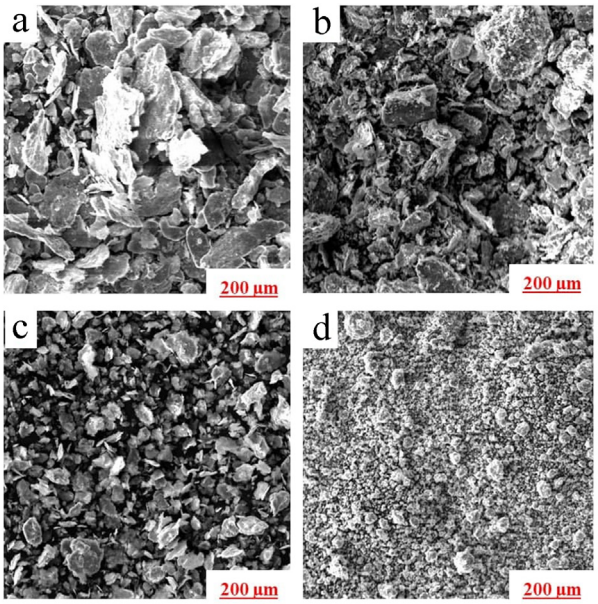

Fig. 6. SEM image of the Al-5MgO/15Mg15 sample after (a) 5 (b) 10 (c) 20 (d) 40 hours of milling.

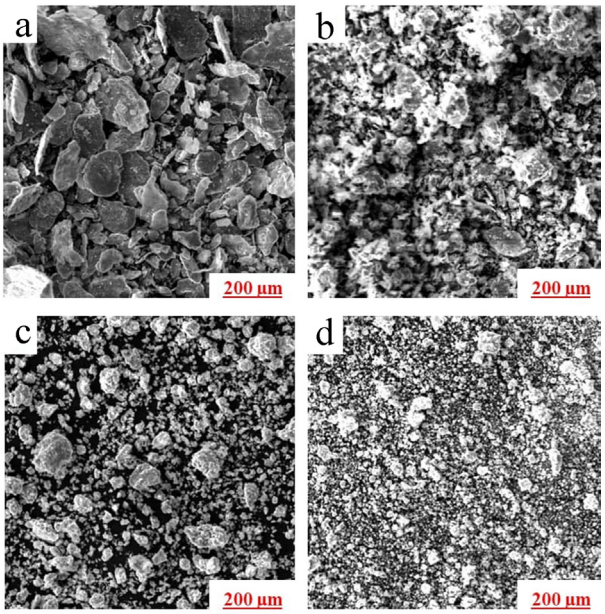

Fig. 7. SEM image of Al-10MgO/10Mg sample after (a) 5 (b) 10 (c) 20 (d) 40 hours of milling.

increases as the milling time increases to 10 h, resulting in a layered morphology of the powder particles. The structure of the layers disappears as the milling time increases from 10 to 20 h, and they are prone to failure due to the hard work created in the powder. The powders become finer, and the particle size distribution becomes more uniform as the failure process takes precedence over the cold welding process. Finally, a completely coaxial morphology with fine particles and a uniform particle size distribution is formed after 40 h of milling. Therefore, both the penetration of magnesium into the aluminum lattice and the hard work in the powder particles increases with the increase in magnesium. After 40 h of milling, the mechanical milling process is accelerated and the powder particles are in a stable state [45].

SEM images of powdered Al-10MgO/10Mg and Al-15MgO/10Mg samples taken at various times (Figs. 7 and 8) clearly show that their morphology follows a similar pattern to that of the Al-5MgO/10Mg composite using the same procedure. In addition, all three samples had a completely coaxial morphology with fine particles and a uniform particle size distribution after 40 h of milling.

Figure 9 depicts particle size with various compositions and milling times. The average particle size of Al-5MgO composite powder increases to 59 microns with an increase in milling time of up to 20 h due to the predominance of the cold-welding process. Then, it decreases to 47 microns after 40 h of milling due to the predominance of the fracture process. The average powder particle size for Al-5MgO/10Mg composite powder increases to 46 microns after 10 h and then it rapidly decreases with increasing time to 20 h. The particle size of the powder decreases at a slower rate of up to 13 microns between 20 and 40 h.

The same process can be seen in the Al-5MgO/15Mg composite powder sample, which has a particle size of 42 microns after 10 h but decreases to 9 microns after 40 h. It is also known that both the maximum particle size of the powder and the time required to achieve that size decrease as magnesium intensity increases, implying that magnesium speeds up the mechanical milling process. Finally, the steady-state, i.e., the balance between the two processes of cold-welding and failure in the powder particles is not achieved and the particle size decrease trend continues after 40 h of milling. As a result, the milling operation must be

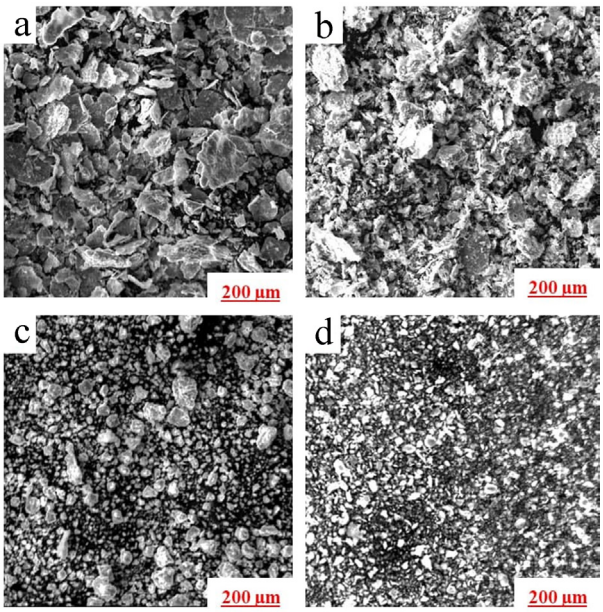

Fig. 8. SEM image of Al-15MgO/10Mg sample after (a) 5 (b) 10 (c) 20 (d) 40 hours of milling.

carried out over a longer period to achieve a stable state.

The particle size changes of Al-(5-15)MgO/10Mg composite powders follow a nearly identical pattern in this diagram, and the maximum particle size decreases with the addition of magnesium oxide. It is also known that as the amount of magnesium increases in the powder, the particle size of the powder decreases so does the time it takes to reach the maximum particle fineness. The amount of magnesium has also been found to reduce the maximum particle size. Consequently, the effect of increasing magnesium is more pronounced than that of increasing magnesium oxide, as shown in this graph. This phenomenon can be explained by the different effects of MgO and Mg on the behavior of powders. MgO particles change the behavior of the powder by crushing and dispersing it among the aluminum particles, whereas Mg dissolving in the aluminum background during milling changes the behavior of the composite powder [15, 45].

3.4. hardness test

Figure 10-a shows changes in the microhardness of composite powders with milling time before heat treatment. As the magnesium level rises, the hardness level rises as well. It is also known that an increase in magnesium has a greater effect on the hardness of the samples than that in magnesium oxide. With an increase in the milling time of up to 40 h, the microhardness of Al-5MgO composite powder increases with a relatively constant trend of up to 165 V. Increasing the milling time to 40 h causes more hard work in the ground powder particles and leads to the breaking of brittle and large MgO particles and even the distribution of the particles in the aluminum field. This increases dislocation density, increasing the hard work on the powder particles even more.

The hardness of the Al-5MgO composite increases significantly by are adding 10% and 15% magnesium, to the point where the microhardness values of the Al-5MgO/10Mg and Al-5MgO/15Mg composite samples increase to 208 and 236, respectively. The increase in microhardness of up to 20 h is attributed to magnesium dissolution in the aluminum field, as well as an increase in dislocation density and hard work in the powder particles.

The solubility of magnesium in the field of aluminum increases as the percentage of magnesium increases, and so does the work hardening and dislocation density. On the other hand, increasing both the percentage of magnesium and the milling time by more than 20 h causes the dislocation density to increase, dynamic recovery to occur, and hardening speed to decrease due to increased work hardening. The formation of a solid solution (Al(Mg)ss) and the intensification of hardness due to the presence of soluble magnesium in the aluminum are two mechanisms by which magnesium increases hardness. Figure 10 shows that while increasing the percentage of MgO to 10 and 15 wt.% causes a slight increase in hardness, it is not significant. Al-10MgO/10Mg and Al-15MgO/10Mg composites have microhardness values of 215 and 220 Vickers after 40 h, respectively. The different mechanisms of the two for increasing hardness are attributed to the low effect of magnesium oxide particles on magnesium [15, 45, 46]. Figure 10-b shows changes in the microhardness of composite powders with milling time after heat treatment. After sintering, the hardness of all samples decreases, with the magnesium-free sample having the lowest hardness, indicating the occurrence of the recovery and recrystallization processes, lowering the work hardness of the powder particles. For example, without magnesium, hardness drops by about 30%, while increases of 10% and 15% by weight result in hardness drops of about 16 and 9%, respectively. The hardness of the sample without magnesium decreases as recovery and recrystallization processes occur, and the hardness reduction levels were about 11 and 10%, respectively, when magnesium oxide was increased by 10% and 15% by weight.

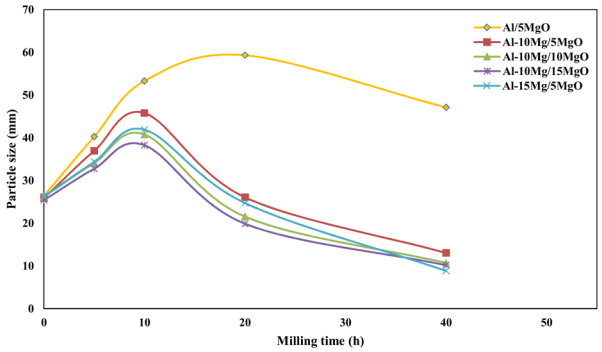

Fig. 9. Changes in particle size according to various compositions and milling times.

Despite the recovery and recrystallization processes, two factors prevented the reduction of hardness in the magnesium-containing sample. First, it slows down the game, but it also makes it more difficult. On the other hand, as the number of magnesium oxide particles increases, the amount of work required increases, causing these particles to decrease and, as a result, the dislocation density to rise. The penetration process is accelerated, and the probability of magnesium dissolving increases in the aluminum field, which increases the hardness of the samples and compensates for the decrease in post-sintering hardness by increasing the dislocation density during sintering [20].

4. Conclusions

At different milling times, adding magnesium to Al/MgO composite powder reduces crystallite size and increases composite lattice strain. Magnesium is dissolved into aluminum and forms an aluminum-magnesium supersaturated solid solution (Al (Mg) ss) when magnesium is added to the Al/MgO composite powder, increasing the composite lattice parameter. In Al/5MgO composite powder, increasing the magnesium percentage leads to a coaxial morphology with finer particle size and more uniform distribution. The increase in the amount of dissolved magnesium in the aluminum field and the change in its mechanical behavior are the causes of these changes. Before sintering, the hardness of the samples increases as milling time and magnesium increase. The hardness drops after the sintering process in the sample without magnesium

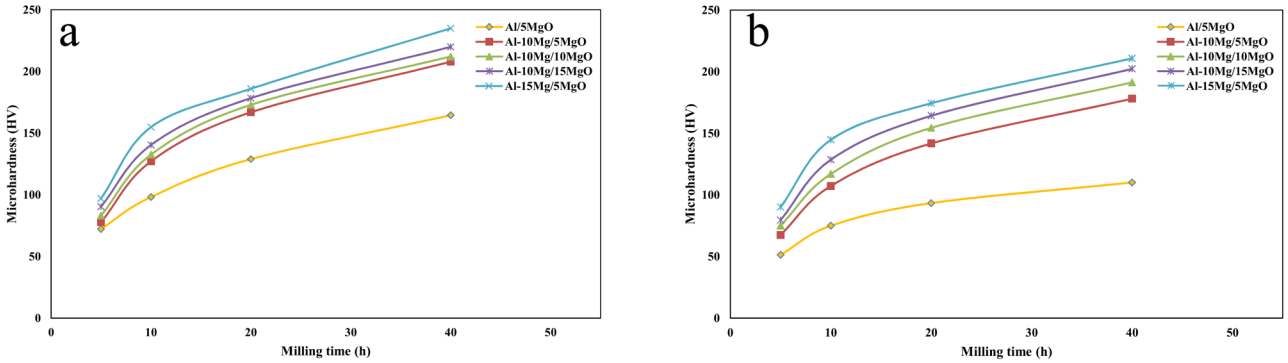

Fig. 10. a) Micro-hardness changes of different powder samples according to pre sintering milling time b) Micro-hardness changes of different powder samples according to post sintering milling time (at 400 °C for 45 minutes).

due to the recovery and recrystallization processes. As the magnesium content increases, the soluble magnesium in the recovery and recrystallization processes slows down and eventually stops, reducing the hardness drop. The effect of increasing magnesium oxide on decreasing crystallite size, increasing underlying lattice strain, morphological changes, powder particle size, and sample hardness (before and after sintering) is more negligible than increasing magnesium.

REFERENCES

[1] S. Bahl, Fiber reinforced metal matrix composites-a review, Materials Today: Proceedings 39 (2021) 317-323.
[2] K.U. Kainer, Basics of metal matrix composites, Metal Matrix Composites (2006) 1-54.
[3] N. Manikandan, K. Balasubramanian, D. Palanisamy, P. Gopal, D. Arulkirubakaran, J. Binoj, Machinability analysis and ANFIS modelling on advanced machining of hybrid metal matrix composites for aerospace applications, Materials and Manufacturing Processes 34(16) (2019) 1866-1881.
[4] S.S. Irhayyim, H.S. Hammood, A.D. Mahdi, Mechanical and wear properties of hybrid aluminum matrix composite reinforced with graphite and nano MgO particles prepared by powder metallurgy technique, AIMS Mater Sci 7 (2020) 103-115.
[5] R. Casati, Aluminum matrix composites reinforced with alumina nanoparticles, Springer2016.
[6] M. Tayyebi, D. Rahmatabadi, R. Hashemi, Review of mechanical and microstructural properties of aluminum matrix composites reinforced with ceramic particles produced by SPD processes, Journal of Science and Technology of Composites 5(4) (2019) 583-594.
[7] M.N. Ervina Efzan, N. Siti Syazwani, M.M.A. Al Bakri, Fabrication method of aluminum matrix composite (AMCs): a review, Key Engineering Materials, Trans Tech Publ, 2016, pp. 102-110.
[8] A.K. Sharma, R. Bhandari, C. Pinca-Bretotean, A systematic overview on fabrication aspects and methods of aluminum metal matrix composites, Materials Today: Proceedings (2021).
[9] C.-Z. Nie, J.-J. Gu, J.-L. Liu, D. Zhang, Production of boron carbide reinforced 2024 aluminum matrix composites by mechanical alloying, Materials Transactions 48(5) (2007) 990-995.
[10] K.R. Cardoso, B.d.S. Izaias, L.d.S. Vieira, A.M. Bepe, Mechanical alloying and spark plasma sintering of AlCrCuFeZn high entropy alloy, Materials Science and Technology 36(17) (2020) 1861-1869.
[11] M. Adamiak, Mechanical alloying for fabrication of aluminium matrix composite powders with Ti-Al intermetallics reinforcement, Journal of Achievements in Materials and Manufacturing Engineering 31(2) (2008) 191-196.
[12] D. ŞİMŞEK, İ. SİMSEK, D. ÖZYÜREK, Production and Characterization of Al-SiC Composites by Mechanical Milling, Bitlis Eren Üniversitesi Fen Bilimleri Dergisi 8(1) (2019) 227-233.
[13] R. Pandiyarajan, M. Prabakaran, T. Rajkumar, K.V. Kumar, R. Manikandan, Metallurgical and mechanical properties of SiC/B_4C reinforced with aluminum composites synthesized by mechanical alloying, Materials Today: Proceedings 37 (2021) 1794-1798.
[14] H. Arik, Effect of mechanical alloying process on mechanical properties of α-Si_3N_4 reinforced aluminum-based composite materials, Materials & Design 29(9) (2008) 1856-1861.
[15] A.A. Yar, M. Montazerian, H. Abdizadeh, H. Baharvandi, Microstructure and mechanical properties of aluminum alloy matrix composite reinforced with nano-particle MgO, Journal of Alloys and Compounds 484(1-2) (2009) 400-404.
[16] V. Chak, H. Chattopadhyay, T. Dora, A review on fabrication methods, reinforcements and mechanical properties of aluminum matrix composites, Journal of Manufacturing Processes 56 (2020) 1059-1074.
[17] K.J. Joshua, S. Vijay, D.P. Selvaraj, P. Ramkumar, Influence of MgO particles on microstructural and mechanical behaviour of AA7068 metal matrix composites, IOP Conference Series: Materials Science and Engineering, IOP Publishing, 2017, p. 012011.
[18] H. Abdizadeh, P. Vajargah, M. Baghchesara, Fabrication of MgO nanoparticulates reinforced aluminum matrix composites using stir-casting method, Kovove Mater. 53 (2015) 319-326.
[19] A.Z.A. Azhar, H. Mohamad, M.M. Ratnam, Z.A. Ahmad, The effects of MgO addition on microstructure, mechanical properties and wear performance of zirconia-toughened alumina cutting inserts, Journal of alloys and compounds 497(1-2) (2010) 316-320.
[20] H. Abdizadeh, R. Ebrahimifard, M.A. Baghchesara, Investigation of microstructure and mechanical properties of nano MgO reinforced Al composites manufactured by stir casting and powder metallurgy methods: A comparative study, Composites Part B: Engineering 56 (2014) 217-221.
[21] M. Em Pul, R. Calin, F. Gül, Investigation of abrasion in Al–MgO metal matrix composites, Materials Research Bulletin 60 (2014) 634-639.
[22] A.A. Yar, M. Montazerian, H. Abdizadeh, H.R. Baharvandi, Microstructure and mechanical properties of aluminum alloy matrix composite reinforced with nano-particle MgO, Journal of Alloys and Compounds 484(1) (2009) 400-404.
[23] G. Williamson, W. Hall, X-ray line broadening from filed aluminium and wolfram, Acta metallurgica 1(1) (1953) 22-31.
[24] R. Wahab, S. Ansari, M.A. Dar, Y.S. Kim, H.S. Shin, Synthesis of magnesium oxide nanoparticles by sol-gel process, Materials Science Forum, Trans Tech Publ, 2007, pp. 983-986.
[25] M.A. Baghchesara, H. Abdizadeh, Microstructural and mechanical properties of nanometric magnesium oxide particulate-reinforced aluminum matrix composites produced by powder metallurgy method, Journal of mechanical science and technology 26(2) (2012) 367-372.
[26] J. Gubicza, M. Kassem, G. Ribárik, T. Ungár, The microstructure of mechanically alloyed Al–Mg determined by X-ray diffraction peak profile analysis, Materials Science and Engineering: A 372(1-2) (2004) 115-122.
[27] S.M. Umbrajkar, M. Schoenitz, S.R. Jones, E.L. Dreizin, Effect of temperature on synthesis and properties of aluminum–magnesium mechanical alloys, Journal of Alloys and Compounds 402(1) (2005) 70-77.
[28] S. Scudino, M. Sakaliyska, K.B. Surreddi, J. Eckert, Mechanical alloying and milling of Al–Mg alloys, Journal of Alloys and Compounds 483(1) (2009) 2-7.
[29] D. Singh, C. Suryanarayana, L. Mertus, R.H. Chen, Extended homogeneity range of intermetallic phases in mechanically alloyed Mg–Al alloys, Intermetallics 11(4) (2003) 373-376.
[30] N. Al-Aqeeli, G. Mendoza-Suarez, A. Labrie, R.A.L. Drew, Phase evolution of Mg–Al–Zr nanophase alloys prepared by mechanical alloying, Journal of Alloys and Compounds 400(1) (2005) 96-99.
[31] N. Al-Aqeeli, G. Mendoza-Suarez, C. Suryanarayana, R.A.L. Drew, Development of new Al-based nanocomposites by mechanical alloying, Materials Science and Engineering: A 480(1) (2008) 392-396.
[32] K.M. Youssef, R.O. Scattergood, K. Linga Murty, C.C. Koch, Ultratough

nanocrystalline copper with a narrow grain size distribution, Applied physics letters 85(6) (2004) 929-931.
[33] A. Wagih, Mechanical properties of Al–Mg/Al_2O_3 nanocomposite powder produced by mechanical alloying, Advanced Powder Technology 26(1) (2015) 253-258.
[34] B.D. Cullity, Elements of X-ray Diffraction, Addison-Wesley Publishing1956.
[35] C. Suryanarayana, N. Grant, A Practical Approach Plenum Press, New York (1998).
[36] Y. Saberi, S.M. Zebarjad, G.H. Akbari, On the role of nano-size SiC on lattice strain and grain size of Al/SiC nanocomposite, Journal of Alloys and Compounds 484(1) (2009) 637-640.
[37] C. Suryanarayana, Mechanical alloying and milling, Progress in materials science 46(1-2) (2001) 1-184.
[38] F.L. Zhang, C.Y. Wang, M. Zhu, Nanostructured WC/Co composite powder prepared by high energy ball milling, Scripta Materialia 49(11) (2003) 1123-1128.
[39] J. Safari, M.D. Chermahini, G. Akbari, The effect of Mg content on microstructure and mechanical properties of Al–xMg/5Al_2O_3 nanocomposite prepared by mechanical alloying, Powder technology 234 (2013) 7-12.
[40] K. Youssef, R. Scattergood, K. Murty, C. Koch, Nanocrystalline Al–Mg alloy with ultrahigh strength and good ductility, Scripta materialia 54(2) (2006) 251-256.
[41] J. Gubicza, M. Kassem, G. Ribárik, T. Ungár, The microstructure of mechanically alloyed Al–Mg determined by X-ray diffraction peak profile analysis, Materials Science and Engineering: A 372(1) (2004) 115-122.
[42] S. Scudino, M. Sakaliyska, K.B. Surreddi, J. Eckert, Mechanical alloying and milling of Al–Mg alloys, Journal of Alloys and Compounds 483(1-2) (2009) 2-7.
[43] F. Tarasi, M. Medraj, A. Dolatabadi, J. Oberste-Berghaus, C. Moreau, Amorphous and crystalline phase formation during suspension plasma spraying of the alumina–zirconia composite, Journal of the European Ceramic Society 31(15) (2011) 2903-2913.
[44] A. Simchi, S. Kamrani, S.M. Seyed Reihani, WITHDRAWN: Processing of Al-SiC nanocomposite powder by high-energy ball milling, Journal of Materials Processing Technology (2007).
[45] M.A. Baghchesara, H. Abdizadeh, H.R. Baharvandi, Effects of MgO nano particles on microstructural and mechanical properties of aluminum matrix composite prepared via powder metallurgy route, International Journal of Modern Physics: Conference Series, World Scientific, 2012, pp. 607-614.
[46] V.K. Dwivedi, S.P. Dwivedi, R. Yadav, Effect of heat treatment process on microstructure and mechanical behaviour of Al/MgO composite material, Advances in Materials and Processing Technologies (2020) 1-10.

Available online at www.jourcc.com

Journal homepage: www.JOURCC.com

Journal of Composites and Compounds

Effect of austenitic stainless steel cladding on the high-temperature oxidation resistance of ferritic 2.25Cr-1Mo (Grade 22) steel using the SMAW process

Hassan Jafarikhorami [a]*

[a] *Department of Materials, Science and Research Branch, Islamic Azad University, Tehran, Iran*

A B S T R A C T

The high-temperature oxidation resistance of low alloy steel affected by the cladding of austenitic stainless steel has been investigated in this study. For this purpose, Shielded Metal Arc Welding (SMAW) technique was used to prepare a proper layer of AISI347 on the surface of ferritic steels. The microstructure and morphology properties of the alloys were examined using transmission electron microscopy (TEM), scanning electron microscopy (SEM), and Energy Dispersive X-Ray Analysis (EDX) techniques. Results demonstrated that the construction of oxide shells on the surface of non-modified ferritic steel was responsible for its low resistance in contrast to the oxidation at high-temperature conditions. The oxidation screening of coated and uncoated samples with tuning time at constant temperature showed the increased oxidizing intensity of both materials. Conversely, with tuning temperature from 850 to 950 oC at a constant time, an abnormal increase was observed in oxidation intensity. The corresponding k_ps of the uncoated sample was determinate 1.27708×10^{-8}, 3.267×10^{-8}, and the corresponding k_ps of coated material was determinate 54.5×10^{-10}, 6.6×10^{-10}. The performed investigation proved that the formation of oxidized compact needle microstructures in the resulting alloy is the reason for the extraordinarily oxidizing resistance of austenitic stainless steel.

Peer review under responsibility of jourcc

A R T I C L E I N F O R M A T I O N

Article history:
Received 31 May 2021
Received in revised form 15 June 2021
Accepted 28 December 2021

Keywords:
Ferritic steels
Cr-Mo steel
SMAW technique
austenitic steel
Corrosion resistance
Oxidation

1. Introduction

1. Introduction

The alloy of 2.25Cr-1Mo (ASTM Grade 22) is low-alloy ferritic-bainitic steel. This was developed for high-temperature applications and is also being applied primarily in the current systems of energy generation [1], properly considered as an alternative material for pressure containers of nuclear power plants (NPPs) at high-temperature conditions [2-4]. The radiation resistance [5, 6], high-temperature creep [7], welding [8, 9], and the microstructure [8] of 2.25Cr–1Mo steel have been widely investigated during the last three decades. Additionally, some researchers are keen on the wearing and corrosion of this material and have performed several explorations [10, 11]. Recently, Wang et al. have studied the tangential fretting wear of 2.25Cr–1Mo steel and the effect of 2.25Cr–1Mo steel wear behavior at high temperatures [10, 12].

Having enough stability, mechanical properties, and ease of fabrication are additional requirements. Stability, requires corrosion and oxidation resistance, microstructural stability, and resistance to graphitization that is a requisite for creep resistance. The thermal efficiency in power generation relies on operating temperatures, thus there has been, and remains, a constant striving to find material technologies that enable higher operating temperatures. This is the case in applications such as turbine materials and the operating temperatures of heat exchangers and pipes. In a typical application, Grade 22 steel is applied for superheater tubing and filler metal for joining steam piping because of its good creep-rupture strength [13, 14] and radiation resistance [15-17] as mentioned above.

Bainitic alloys have been developed to prepare analogous creep properties, with excellent weldability, but they will be more susceptible to oxidation. Since the 1990s, the focus of the development of power plant steels has been on higher chromium alloys that provide increased oxidation resistance, while minimally reduces its ductility [18].

The steam generated by boilers passes through the superheater tubes to produce superheated steam. The superheater tubes are frequently subjected to failures due to corrosion-related issues. The materials of superheater tubes are selected for a specific design life in a complex situation involving high temperature, pressure, and corrosive environment. The 2.25Cr-1.0Mo low-alloy steel is one of the most common materials used for the construction of super heater tubes due to its high-temperature mechanical strength and great corrosion resistance. However, as a result of improper operation conditions such as temperature runaway or inadequate corrosion mitigation, superheater tubes are susceptible to failure mechanisms such as oxygen pitting [19, 20], creep [21, 22], thermal fatigue [22, 23], temper embrittlement [24], and stress corrosion

* *Corresponding author: Hassan Jafarikhorami; E-mail: jafarikhorami@gmail.com*
https://doi.org/10.52547/jcc.3.2.3

Fig. 1. The images of a plate; (a) primary plate (before creption), (b) plate after creption, and (c) polished creptsample.

cracking (SCC) [25, 26]. Stress corrosion cracking occurs when tensile stress, corrosive environment, and susceptible material exist at the same time. In boilers built with carbon and low-alloy steel tubes, oxygen and sodium hydroxide are corrosive agents that can cause SCC failures [27]. Research works have indicated that induced pits due to poor water treatment may act as stress concentrators for the initiation of the cracks [28].

In welded tubes, a strength mismatch between weld deposit and base metal due to great hardenability of 2.25Cr-1.0Mo steel increases cracking occurrence in the tube weldment [28]. Therefore, post-weld heat treatment of weld in 2.25Cr-1.0Mo tubes, in addition to reducing residual stress, is necessary to minimize strength and hardness mismatch by the reduction of weldment hardness [29].

Furthermore, studies have demonstrated that the use of more corrosion-resistant materials, including stainless steel, effectively limits the boiler equipment corrosion, helping the lifetime duration of boilers. However, this is expensive, and interesting aims are to provide a cost-effective substitute to the application of cheaper materials, such as Fe-2.25Cr-1Mo (as low-alloy steel) and high-temperature operations. To make this possible while maintaining a reasonable lifetime of the boiler equipment, it is necessary to understand the underlying mechanisms of the rapid corrosion of low-alloy steels necessitating a better understanding of the effect of existing corrosive species. There are a few essays that closely investigate the influence of some elements such as chlorine-containing composites, particularly alkali chlorides [30], on high-temperature corrosion of low-alloy steels [31], pure iron [32], and stainless steels [33].

In addition, while it is well-known that oxygen-released compounds cause oxidation and corrosion in all these materials, the underlying mechanisms of this element are still under discussion. Herein, we aim to study the effect of austenitic stainless steel cladding on the high-temperature oxidation resistance of ferritic 2.25Cr-1Mo (Grade 22) steel, which has not been studied so far. For this purpose, the SMAW technique was applied to prepare a suitable layer of AISI347 over the surface of ferritic steels. The microstructure and morphology properties were examined in the resulted alloys.

2. Materials and methods

2.1. Materials

The material used in this study is 20 plates of ASTM A387 Grade 22 steel (Table 1), prepared with equal dimensions (40×30×10 mm). Austenitic steel (E347-16) purchased from Methrod Co. (the UK) was employed as the coating metal SMAW was used to clad austenitic steel over each Fe-Cr-Mo plate.

Table 1.
Chemical composition of the consumed steel as a substrate

%Mo	%Cr	%Si	%S	%P	%Mn	%C
0.99	2.32	0.45	0.03	0.028	0.4	0.13

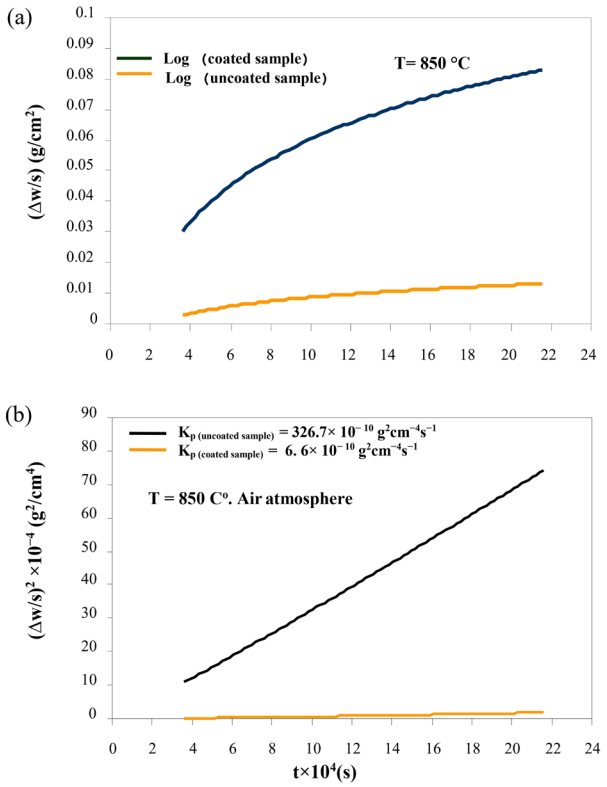

Fig. 2. Air oxidation weight gains of the uncoated and coated samples oxidized at 850 °C; (a) weight gain against time and (b) squared weight gain against time.

2.2. Sample preparation

The crept specimens were sectioned on the upper surface of 10 samples, to comparison 10 others plates without crepitation. Note that none of the samples had obvious necking regions and the samples were extracted in such a way to examine the surface parallel to the loading axis, as shown schematically in Figure 1.

The extracted samples were polished in multiple stages using a diamond paste (3-μm solution, followed by 1-μm solution) and colloidal silica (15-nm solution) before the hardness measurements.

2.3. Characterization

To investigate and identify the type and number of induced oxide phases on the surface of the samples in the oxidation test, the XRD analysis was used using the PAN Analytical instrument (Model X'Pert PROMPD, the Netherlands). The growth of oxide layers depends on the ability of oxygen to penetrate and the morphology of the primary oxide shells. The morphology of the detected shells on the oxidation effect was studied by a SEM (JEOL model JSM-6610LV, Japan) equipped with EDS of Oxford instrument facility (model number 51-ADD0013).

3. Results and discussions

3.1. Oxidation kinetics

The weight gain of the samples per unit area (Δw/s) versus time (t) is shown in Figure 2a. This exhibits the results of tThermogravimetric analyses of steels containing 2.25 Cr-1Mo (AISI A387) as the substrate steel (uncoated) and austenitic stainless steel AISI 347 as the coated steel coated at 850 °C inside the furnace for 60 h.

For the comparison of weight increase of uncoated and coated samples (Fig 2a), the weight gain of coated samples was almost uniform and low, contrary to the uncoated samples. On the other hand, uncoated sam-

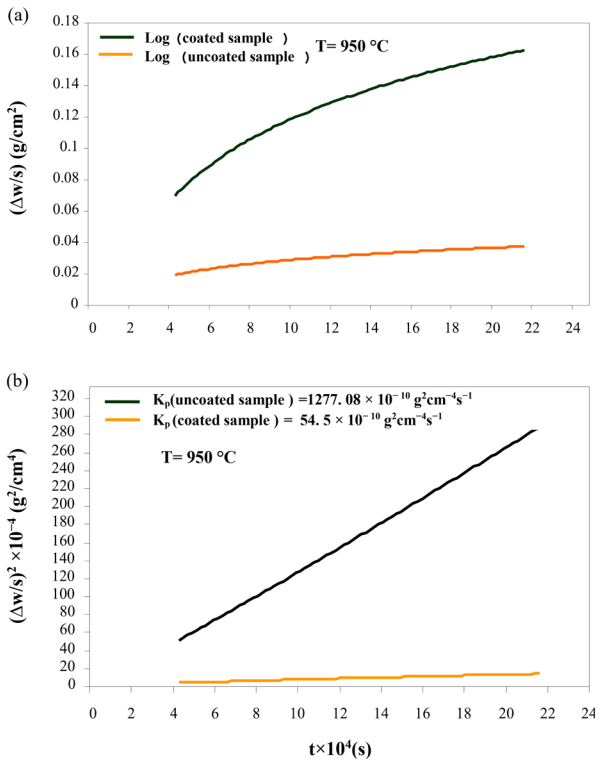

Fig. 3. Air oxidation weight gains of the uncoated and coated samples oxidized at 950 °C; (a) weight gain against time and (b) squared weight gain against time.

ples have a significant weight increase due to the high rate of oxidation. Fig 2b shows the ratio of $(\Delta w/s)^2$ to the times for coated and uncoated samples at 850 °C.

In most cases, there is a linear relationship between the ratio $(\Delta w/s)^2$ and (t), which indicates the parabolic law corresponding to Eq. 1"

$$(\Delta w/s)^2 = K_p . t \quad (1)$$

where "w" is the weight gain of the samples, "s" is the area, and "t" is time. The parabolic relationship indicates that the growth of oxide shells is a function of diffusion, and "K_p" as a coefficient for the growth rate of Cr oxide is proportional to the penetration of oxygen. The "K_p" coefficients for coated and uncoated samples at the tested temperatures are given in Table 2.

By comparing Figure 2a and 3a, it seems that increasing the temperature from 850 °C to 950 °C has little effect on the growth rate of the oxides and the increase in weights of the uncoated and the coated samples relative to each other. However Fig 3a depicts a large difference between the weight increase of coated and uncoated samples. Fig 3b also shows a ratio of $(\Delta w/s)^2$ for coated and uncoated samples at 950 °C. Although in the thermogravimetric analysis of samples at two applied temperatures, the effect of temperature is not very considerable, in comparison to Figures 2b and 3b, there is a remarkable difference in the ratio of $(\Delta w/s)^2$. This means that the growth rate of oxide layers in uncoated samples at 950 °C is much higher than that at 850 °C, but the growth rate does not change considerably in coated samples.

Fig. 4 shows a comparison of a ratio of $(\Delta w/s)^2$ for coated samples at both 850 and 950 °C. At 850 °C the ratio of $(\Delta w/s)^2$ increased linearly,

Table 2.
K_p coefficients at the tested temperatures

Temperature (°C)	AISI347	2.25Cr-1Mo
850	6.6 ×10−10	3.267 × 10−8
950	54.5×10−10	1.27708 × 10−8

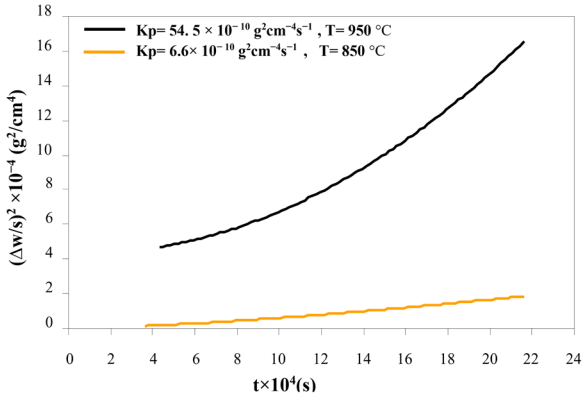

Fig. 4. Comparison of squared weight gain of samples per unit time for coated samples at 850 and 950 °C.

while it was almost curved at 950 °C, and did not change markedly in comparison with the uncoated samples. Persdotter et al [30] investigated the oxidation of Fe-2.25Cr-1Mo in presence of KCl(s) at 400 °C and crack formation and its influence on oxidation kinetics. Their results show slow parabolic kinetics recorded by TGA, which indicates that the oxide growth is diffusion-controlled in good agreement with previous studies [31, 34, 35]. The difference in parabolic rate constant between iron and Fe-2.25Cr-1Mo observed in their study indicates that the presence of chromium, detected in the inward growing spinel, has an important influence on the overall growth rate at 400 °C.

3.2. Surface morphology examination

SEM images with a magnification of 15000x were also used to compare the morphology of the oxides. As mentioned in the previous sections, the test variables were time and temperature. To study the morphology of surface oxides for both uncoated and coated samples, the times of 10 h and 60 h were selected at both temperatures of 850 and 950 °C.

Figure 5 (a and b) shows the SEM images of the uncoated sample, which was placed in a normal atmosphere furnace at 850 °C for 10 h and 60 h. As expected, there are iron-rich phases on the oxidized surface of the uncoated sample. The types of these phases will be specified by XRD analysis in the next section.

Figur 5a clearly defines the block-shaped surface oxides. Open spaces between oxide blocks are the best place for oxygen to penetrate the substrates and this will increase the oxidation rate in uncoated samples. This will cause the oxide shells formed during servicing of these steels at high temperatures to easily accelerate oxidation from the separated surface. Moreover, peeling off the oxide blocks will reduce the thickness of the relevant sheet and thus reduce the service time of the part.

Figure 5b also shows the SEM image of the uncoated sample kept in the furnace at 850 °C at a maximum time of 60 h. At a constant temperature, increasing the oxidation time will certainly lead to the growth of oxidative shells which is understood by examining and observing Figure 5 (a and b). The growth of oxide blocks was oberved with increasing time from 10 h to 60 h, and their compaction decreased compared to 10 h. Figure 5 (a and b) is presented to investigate the effect of time on the morphology of surface oxides.

To study the effect of temperature, it was necessary to take pictures of samples that were oxidized at 950°C in proportion to 10 and 60 h.

Figure 5c shows the SEM image of a sample placed in a furnace at 950 °C for 10 h. Comparing Figure 5 a and c, the effect of temperature is well visible. Increasing the temperature will increase the growth rate of oxide layers and shells. On the other hand, comparing Fig 5a and c reveals that the growth rate of oxide layers is almost the same. Increasing both the temperature and the oxidation time will lead to a decrease

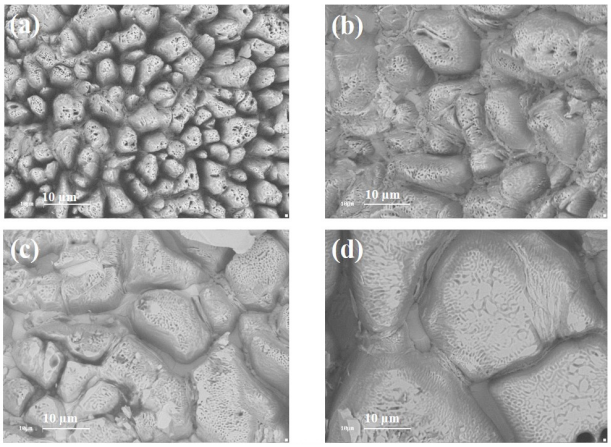

Fig. 5. SEM image of uncoated sample, oxidized in (a) T = 850 °C, t = 10 h (15000x), (b) T = 850 °C, t = 60 h (15000x), (c) T = 950 °C, t = 10 h (15000x), and (d) T = 950 °C t = 60 h (15000x).

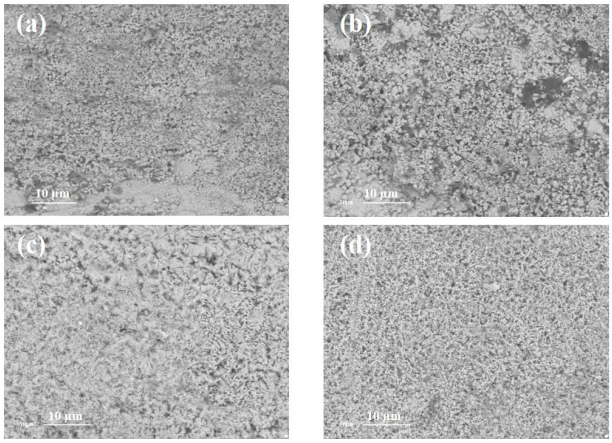

Fig. 6. SEM image of the coated sample, oxidized in (a) T = 850 °C, t = 10 h (15000x), (b) T = 850 °C, t = 60 h (15000x), (c) T = 950 °C, t = 10 h (15000x), and (d) T = 950 °C, t = 60 h (15000x).

in the height of block-shaped oxides, which will sometimes increase the adhesion of the oxide shells. Jagadeeswara Rao et al. [36] studied atmospheric air oxidation of 9Cr-1Mo steel and found that as increasing the time of oxidation to 50 h increased the size of the oxide globules, yielding two different morphologies of platelet and globules.

Unlike uncoated samples whose surface morphology was in the form of block-shaped oxides, the morphology of the oxides in coated samples is needle-shaped and compact in structure. Figure 6 (a and b) show the SEM images of the coated samples, which were placed in an oven at 850 °C for 10 h and 60 h. As can be seen from Fig 6a, the needle-shaped oxides are observed in coated samples. The compactness of these needle-shaped oxide layers is considered to be the most important reason for increasing oxidation resistance because it has made it difficult for oxygen to penetrate the underlying layers and this has reduced the oxidation rate in coated samples. Similarly, to investigate the effect of oxidation time on coated samples, a comparison was made between SEM images at longer times. Figure 6b shows the SEM image of the coated sample, kept in an oven at 850 °C for 60 h. Comparing Fig 5a and b, it seems that increasing the oxidation time did not have much effect on the surface morphology of the samples at a constant temperature. The only effect that will increase over time is a slight increase in the weight of the samples due to oxidation. Figure 6 (c and d) shows the SEM images of a sample placed in a furnace at 950 °C for 10 h and 60 h to investigate the effect of increasing the temperature from 850 °C to 950 °C on the morphology of surface oxides.

Increasing the temperature led to an increase in the number of oxide needles per unit area. In other words, due to the formation of compressed oxide needles, the weight gain rate of coated samples significantly declined compared to uncoated samples in the same conditions and compared to a sample placed in the furnace at 850 °C for 10 h. The needles did not grow but became more compact. On the other hand, increasing the time from 10 to 60 h at 950 °C will make the oxide needles more compact, which will create a stronger barrier against oxygen penetration and thus reduce the oxidation rate at high temperatures.

According to the result of the EDX analysis, the peaks indicate iron-rich oxide phases, with the difference that the intensity of these peaks is relatively higher than previous peaks, which confirms the increase in the percentage of oxide phases. EDX analysis also shows the presence of Cr-rich phases along with iron-rich phases. In the next section, the types of phases formed on the surface of coated samples will be fully discussed based on XRD analysis. Unlike uncoated samples, EDX analysis in coated samples did not differ much between the obtained peaks. This means that the thickness of the needle-shaped layers was not very large, but the increase in time and temperature caused the compression of the oxide layers.

3.3. Phase analysis

As shown in the previous section and according to the relevant SEM images, only the growth of the initial phases was observed that occurred in the first stage of the experiment, i.e. at 10 h and 850 °C. For this reason, the samples were subjected to an XRD test by applying both the maximum temperature and oxidation test time. Among the uncoated samples, a sample was selected that was exposed to a temperature of 950 °C for 60 h. Figure 7a shows the XRD analysis image of the uncoated sample, which along with the obtained results, can prove with certainty that the iron-rich phases will include the oxidative phases of Fe_2O_3, Fe_3O_4, and FeO. Also, some Fe-Cr-O compound in the form of FeCr2O4 is present in the formed oxide shells due to the presence of Cr in the substrate steel. In contrast, the XRD analysis was performed to investigate the type and number of phases formed on the surface of coated samples from a sample that was in the oven at 950 °C for 60 h. Fig 7b shows the XRD analysis image of this sample.

As shown in Figure 7b, the phases that formed in the coated samples were Cr_2O_3, Fe_2O_3, and some of the oxide phases of CrO_2. CrO_2 oxide will usually form at temperatures above 1100 °C, which will reduce the oxidation resistance due to the porosity of the oxide-shaped needle

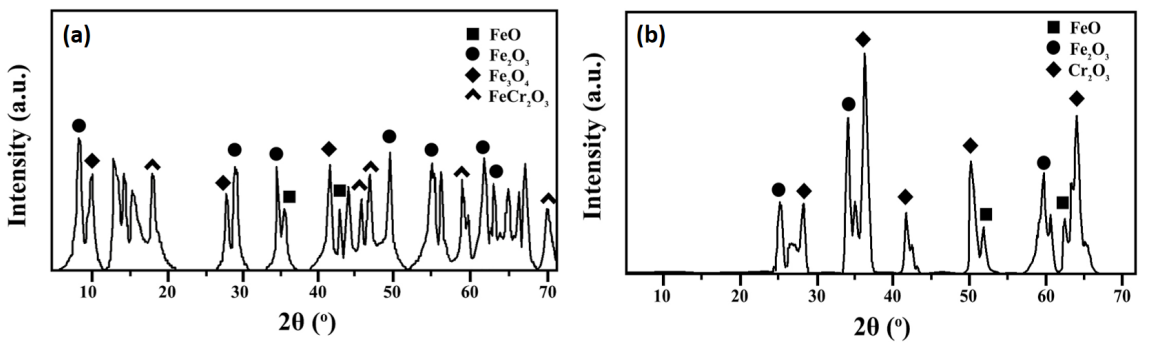

Fig. 7. XRD analysis images of (a) uncoated and (b) coated samples oxidized at T = 950 °C, t = 60 h.

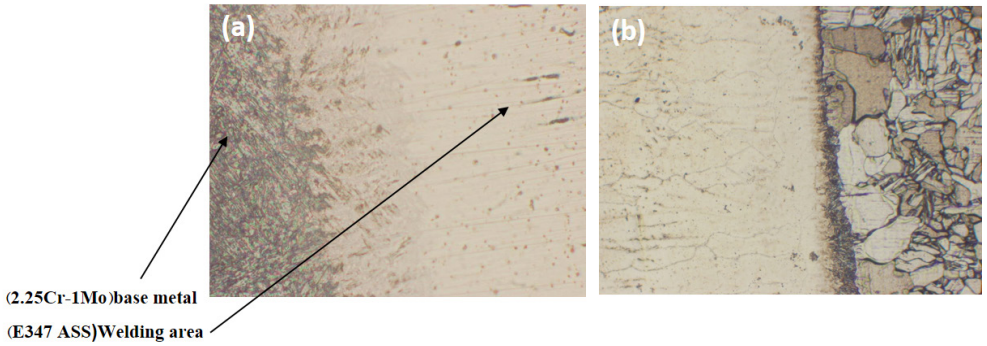

Fig. 8. Metallographic images of (a) the weld affected area and (b) the area affected by welding after the oxidation test at T= 850 °C, t = 10 h (x200).

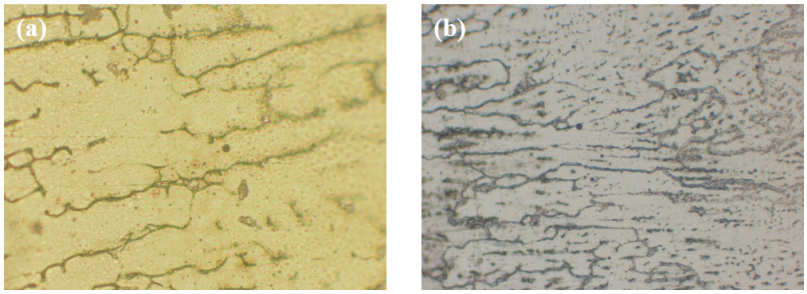

Fig. 9. Metallographic images of (a) the welding area and (b) the weld zone after oxidation at T = 850 °C, t = 10 h (x200).

shells. Creating any porosity will increase the possibility of oxygen penetration and thus increase the rate of oxidation. In this sample, some of this free phase was formed due to storage at 950 °C for a long time (60 h), but it had little effect on reducing oxidation resistance due to a low temperature in this experiment. Earlier studies show that the oxidation of ferritic steels can result in the formation of a multi-layered oxide scale on the surface consisting of Fe_2O_3, Fe_3O_4, and FeO [37, 38].

3.4. Microstructural degradation of weldments

To study the microstructure of the weldments, it was necessary to first prepare the cross-section of the samples and then sand and polish them. For this purpose, sanding numbers of 120, 240, 280, 360, 400, 600, 800, and 1000 were used, respectively, for pre-prepared sections. Then, images of the coated samples were taken with a light microscope before and after the oxidation test.

In this section, an attempt is made to provide a brief and useful explanation of the effects of oxidation time and temperature on the area affected by welding and the welding area, along with the relevant metallographic images. Figure 8a shows a metallographic image of the weld affected area at 200x magnification before any oxidation test. As a result of welding in an area as narrow as 60 µm, it has changed and is out of coaxial state.

Figure 8b shows a metallographic image of a welding-affected area after an oxidation test at 850 °C for 10 h. As can be seen in Figure 8 (a and b), storage at 850 °C will reduce the size of the area affected by welding. On the other hand, the base metal grains have returned to their original state, i.e. coaxial grains due to the infiltration phenomenon.

Figure 9a shows a metallographic image of the weld zone before the oxidation test and after welding. Unlike the affected area, the oxidation test had little effect on the weld area. Since the weld metal contains between 5 and 10% ferrite, storage at this temperature and time has only resulted in partial cohesion of the ferrite veins, which have grown somewhat during the oxidation test. Figure 9b shows a metallographic image of a boiling point exposed to 850 °C for 10 h.

The effect of time was investigated on the area affected by welding and the welding area. Figure 9b shows the metallographic images of the weld area oxidized at 850 °C for 10-60 h. According to Figure 10 (a and b), increasing the oxidation time at a constant temperature will not have a significant effect on the microstructure of the weld area. Figure 10 (c and b) also shows the metallographic image of the weld zone subjected to oxidation at 850 °C for 10 and 60 h. In this case, the increase in time did not affect the welding area.

The effect of temperature was investigated on the area affected by welding and the boiling area.

The effect of temperature increase will be much greater than time. Figure 11 shows a metallographic image of a weld-affected area that was subjected to oxidation at 850 and 950 °C for 60 h. Comparing Figure 11a and b will conclude that increasing the temperature from 850 to 950 °C leads to the growth of central coaxial grains and the base metal, and the area and width of the affected area are reduced by boiling. Figure 11 (c and d) shows the metallography of the weld zone, which was subjected to oxidation at 850 and 950 °C for 60 h. Unlike the area affected by welding and the base metal, the increase in temperature did not have much effect on the metallographic structure of the weld area.

Table 3.
Chemical composition of the uncoated and coated samples obtained from the EDS analysis

Sample	O	Fe	Cr	Mo
Uncoated oxidized sample at T = 850°C, t = 10h	63.74	25.50	6.36	4.40
coated oxidized sample at T = 850°C, t = 10h	58	27	8.70	6.30

4. Conclusions

Forming a protective layer of cream on the surface of stainless steel will have a significant effect on protection against corrosion and oxidation at high temperatures. Suitable for various applications, stainless steels are widely used, especially in pipelines, pressure vessels, and heat exchangers, whose application temperature can reach up to 1100 °C. Due to the lower cost and the lower thermal expansion coefficient of ferritic steels, such as one containing 2.25Cr-1Mo, than austenitic stainless steels, these steels will be a suitable alternative. Because of the need to apply higher temperatures, on the other hand, the use of austenitic stainless steel coating seems a logical method due to the formation of a

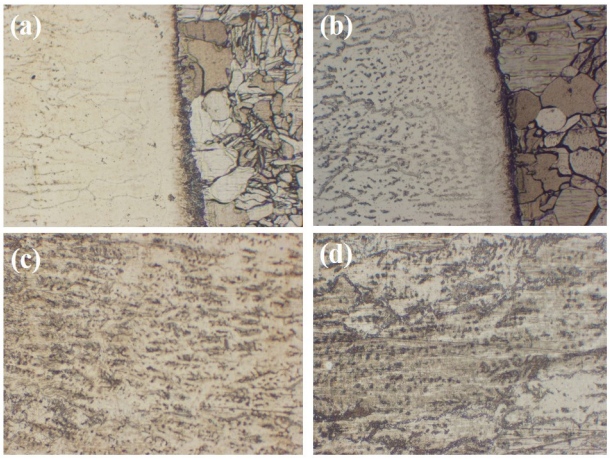

Fig. 10. The metallographic image of the weld affected area lasted (a) 10 h and (b) 60 h at 850 °C (x200), and metallographic image of the welding area during (c) 10 h and (d) 60 h at 850 °C (x200).

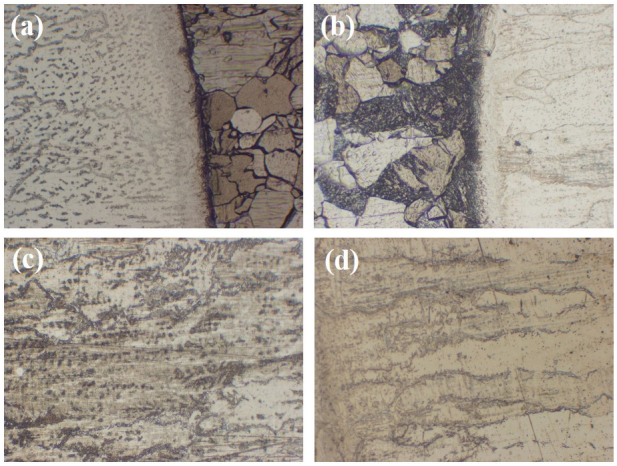

Fig. 11. Metallographic image of the affected area for 60 h at (a) 850 °C and (b) 950 °C (x200) and metallographic image of the welding area for (a) 60 h at 850 °C and (b) 950 °C (x200).

protective layer of Cr. In this study, the effect of 347 austenitic stainless steel coating was investigated on the oxidation behavior of steel containing 2.25Cr-1Mo at a high temperature, along with analyzing the mechanism of formation of protective oxide layers. The findings showed that the stainless steel coating reduced the intensity of oxidation, especially at 950 °C. Examination of the morphology of oxide layers shows the structure of coaxial oxide shells in uncoated samples and compressed oxide needles in coated samples. At both temperatures, the oxidation intensity increased with increasing time at a constant temperature, while an abnormal increase in oxidation intensity was observed at a constant time with increasing the temperature from 850 to 950 °C. Uncoated samples at 850 and 950 °C had oxidation constants of (Kp) of 3.267×10^{-8} and 1.27708×10^{-8}, respectively, and those for coated samples were 6.6×10^{-10} and 54.5×10^{-10} at 850 and 950 °C, respectively. Studies have shown that the oxidation resistance of austenitic stainless steel is due to the formation of oxidized compact needles.

REFERENCES

[1] F. Masuyama, Advances in creep damage/life assessment technology for creep strength enhanced ferritic steels, Procedia Engineering 55 (2013) 591-598.
[2] O. Muránsky, H. Zhu, S.-L. Lim, K. Short, J. Cairney, M. Drew, On the evolution of mechanical properties and microstructure of ferritic-bainitic (FB) 2.25 Cr-1Mo (Grade 22) steel during high-temperature creep, Materialia 9 (2020) 100513.
[3] S. Zinkle, Advanced irradiation-resistant materials for Generation IV nuclear reactors, Structural Materials for Generation IV Nuclear Reactors, Elsevier2017, pp. 569-594.
[4] D. Blagoeva, L. Debarberis, M. Jong, P. Ten Pierick, Stability of ferritic steel to higher doses: Survey of reactor pressure vessel steel data and comparison with candidate materials for future nuclear systems, International Journal of Pressure Vessels and Piping 122 (2014) 1-5.
[5] J. Calaf Chica, P.M. Bravo Díez, M. Preciado Calzada, A new prediction method for the ultimate tensile strength of steel alloys with small punch test, Materials 11(9) (2018) 1491.
[6] J. Bulloch, A study concerning material fracture toughness and some small punch test data for low alloy steels, Engineering failure analysis 11(4) (2004) 635-653.
[7] M.T. Whittaker, B. Wilshire, Advanced procedures for long-term creep data prediction for 2.25 chromium steels, Metallurgical and Materials Transactions A 44(1) (2013) 136-153.
[8] S. Ren, S. Li, Y. Wang, D. Deng, N. Ma, Finite element analysis of residual stress in 2.25 Cr-1Mo steel pipe during welding and heat treatment process, Journal of Manufacturing Processes 47 (2019) 110-118.
[9] A. Elrefaey, Y. Javadi, J.A. Francis, M.D. Callaghan, A.J. Leonard, Evolution of microstructure and toughness in 2.25 Cr-1Mo steel welds, International Journal of Pressure Vessels and Piping 165 (2018) 20-28.
[10] X.-d. Chen, L.-w. Wang, L.-y. Yang, R. Tang, Y.-q. Yu, Z.-b. Cai, Investigation on the impact wear behavior of 2.25 Cr–1Mo steel at elevated temperature, Wear (2021) 203740.
[11] R. Sahoo, B. Jha, T. Sahoo, S. Mantry, Effect of microstructural degradation on solid particle erosion behavior of 2.25 Cr-1Mo steel, Tribology Transactions 57(4) (2014) 679-689.
[12] X.-D. Chen, L.-W. Wang, L.-Y. Yang, R. Tang, Z.-B. Cai, Effects of Temperature on the Fretting Wear Behavior of 2.25 Cr-1Mo Tubes against Gr_5C_{12} Rods, Materials 13(15) (2020) 3388.
[13] M. Whittaker, B. Wilshire, Long term creep life prediction for Grade 22 (2·25Cr—1Mo) steels, Materials science and technology 27(3) (2011) 642-647.
[14] K. Maruyama, K. Sawada, J. Koike, H. Sato, K. Yagi, Examination of deformation mechanism maps in 2.25 Cr—1Mo steel by creep tests at strain rates of 10^{-11} to 10^{-6} s^{-1}, Materials Science and Engineering: A 224(1-2) (1997) 166-172.
[15] R. Klueh, A.T. Nelson, Ferritic/martensitic steels for next-generation reactors, Journal of Nuclear Materials 371(1-3) (2007) 37-52.
[16] H. Bhadeshia, A. Strang, D. Gooch, Ferritic power plant steels: remanent life assessment and approach to equilibrium, International materials reviews 43(2) (1998) 45-69.
[17] S.C. Deevi, Advanced Intermetallic Iron Aluminide Coatings for High Temperature Applications, Progress in Materials Science (2020) 100769.
[18] S. Dépinoy, C. Toffolon-Masclet, S. Urvoy, J. Roubaud, B. Marini, F. Roch, E. Kozeschnik, A.-F. Gourgues-Lorenzon, Carbide precipitation in 2.25 Cr-1 Mo bainitic steel: effect of heating and isothermal tempering conditions, Metallurgical and Materials Transactions A 48(5) (2017) 2164-2178.
[19] K. Ranjbar, Failure analysis of boiler cold and hot reheater tubes, Engineering Failure Analysis 14(4) (2007) 620-625.
[20] A. Heyes, Oxygen pitting failure of a bagasse boiler tube, Engineering Failure Analysis 8(2) (2001) 123-131.
[21] A. Saha, H. Roy, Failure investigation of a secondary super heater tube in a 140 MW thermal power plant, Case studies in engineering failure analysis 8 (2017) 57-60.
[22] A. Alvino, D. Lega, F. Giacobbe, V. Mazzocchi, A. Rinaldi, Damage characterization in two reformer heater tubes after nearly 10 years of service at different operative and maintenance conditions, Engineering Failure Analysis 17(7-8) (2010) 1526-1541.
[23] A. Usman, A.N. Khan, Failure analysis of heat exchanger tubes, Engineering Failure Analysis 15(1-2) (2008) 118-128.
[24] Z. PENG, W. REN, C. YANG, F. CHEN, H. LIU, F. PENG, Q. MEI, Relationship between the evolution of phase parameters of grain boundary $M_{23}C_6$ and embrittlement of HR_3C super-heater tubes in service, Acta Metall Sin 51(11) (2015) 1325-1332.
[25] C.A. Duarte, E. Espejo, J.C. Martinez, Failure analysis of the wall tubes of a water-tube boiler, Engineering Failure Analysis 79 (2017) 704-713.
[26] S. Xu, C. Wang, W. Wang, Failure analysis of stress corrosion cracking in heat exchanger tubes during start-up operation, Engineering Failure Analysis 51 (2015) 1-8.
[27] J.J. Aumuller, V.A. Carucci, Determination of Service Life for Undamaged and Damaged Delayed Coker Drums, ASME 2016 Pressure Vessels and Piping Conference, American Society of Mechanical Engineers Digital Collection, 2016.
[28] A. Ahmadi, M. shayegani Akmal, A. Pasha, S. Yareie, Failure analysis of cracked 2.25 Cr–1.0 Mo steel tubes of an oil refinery boiler, Engineering Failure

Analysis 110 (2020) 104435.
[29] M. Nakano, T. Tanaka, M. Abe, M. Nakatani, H. Terasaki, Improvement of Low-Temperature Toughness in Weld Metal Made of 9Cr-1Mo-V Steel by GTAW Method, Pressure Vessels and Piping Conference, American Society of Mechanical Engineers, 2019, p. V06BT06A005.
[30] A. Persdotter, M. Sattari, E. Larsson, M.O. Ogaz, J. Liske, T. Jonsson, Oxidation of Fe-2.25 Cr-1Mo in presence of KCl (s) at 400° C–Crack formation and its influence on oxidation kinetics, Corrosion Science 163 (2020) 108234.
[31] M.A. Olivas-Ogaz, J. Eklund, A. Persdotter, M. Sattari, J. Liske, J.-E. Svensson, T. Jonsson, The Influence of Oxide-Scale Microstructure on KCl (s)-Induced Corrosion of Low-Alloyed Steel at 400 C, Oxidation of Metals 91(3) (2019) 291-310.
[32] H. Ma, C. Zhou, L. Wang, High temperature corrosion of pure Fe, Cr and Fe–Cr binary alloys in O_2 containing trace KCl vapour at 750° C, Corrosion Science 51(8) (2009) 1861-1867.
[33] J. Sui, J. Lehmusto, M. Bergelin, M. Hupa, The effects of KCl, NaCl and K_2CO_3 on the high-temperature oxidation onset of sanicro 28 steel, Oxidation of metals 85(5-6) (2016) 565-598.
[34] N. Folkeson, T. Jonsson, M. Halvarsson, L.G. Johansson, J.E. Svensson, The influence of small amounts of KCl (s) on the high temperature corrosion of a Fe-2.25 Cr-1Mo steel at 400 and 500° C, Materials and Corrosion 62(7) (2011) 606-615.
[35] T. Jonsson, N. Folkeson, J.-E. Svensson, L.-G. Johansson, M. Halvarsson, An ESEM in situ investigation of initial stages of the KCl induced high temperature corrosion of a Fe–2.25 Cr–1Mo steel at 400 C, Corrosion Science 53(6) (2011) 2233-2246.
[36] C.J. Rao, S. Ningshen, J. Philip, Atmospheric air oxidation of 9Cr-1Mo steel: Depth profiling of oxide layers using glow discharge optical emission spectrometry, Spectrochimica Acta Part B: Atomic Spectroscopy 172 (2020) 105973.
[37] S.B. Ranganath, C.D. Wick, B.R. Ramachandran, Role of Structure and Oxidation States in the Passivation of Stainless Steel by Chromium, group 29 (2019) 33.
[38] M. Weiser, R.J. Chater, B.A. Shollock, S. Virtanen, Transport mechanisms during the high-temperature oxidation of ternary γ/γ′ Co-base model alloys, NPJ Materials Degradation 3(1) (2019) 1-11.

Available online at www.jourcc.com

Journal homepage: www.JOURCC.com

Journal of Composites and Compounds

Electrodeposition of Nickel matrix composite coatings via various Boride particles: A review

Alireza Dordsheikh Torkamani [a], *Mohammad Velashjerdi* [b]*, *Aqeel Abbas* [c], *Mohammad Bolourchi* [a], *Pabitra Maji* [d]

[a] *School of Metallurgy and Materials Engineering, Iran University of Science and Technology (IUST), Tehran, Iran*
[b] *Department of Materials Science and Engineering, Faculty of Engineering, Arak University, Arak, Iran*
[c] *Department of Materials science and Engineering, National Taiwan University, Taiwan, China*
[d] *Department of Mechanical Engineering, NIT Agartala, India, 799046*

ABSTRACT

Composite electrodeposition or Electroplating is a process primarily applied in the industry through which metal substrates are coated with an additional phase, such as low-thickness films of a range of metals. Lately, the advent of coating based on metal matrix through deposition has been vital because the superior hardness has more improved wear and corrosion resistance than alloy-based or pure coatings of metal. Nickel is an engineering material, which has been broadly utilized for metal matrix applications. This paper summarizes recent research on the electrodeposition of nickel matrix composite coatings with borides ceramic particles. Some of these particles are ZrB_2, BN, TiB_2, Ni_3B, CrB_2, etc. in the nickel matrix. In addition, the most important results achieved in the field of these composite coatings were collected in this review.

Peer review under responsibility of jourcc

ARTICLE INFORMATION

Article history:
Received 27 May 2021
Received in revised form 10 June 2021
Accepted 25 June 2021

Keywords:
Electroplating
Composite coatings
Nickel matrix
Borides

Table of contents

1. Introduction 106
2. Nickel matrix composite coatings 107
3. The principles of the electrodeposition method for coating 107
4. Essential components of Borides particles 108
5. Electrodeposition of Nickel matrix composite coatings via Boride particles 108
5.1. Electrodeposition of Nickel matrix composite coatings via ZrB_2 particles 109
5.2. Electrodeposition of Nickel matrix composite coatings via TiB_2 particles 109
5.3. Electrodeposition of Nickel matrix composite coatings via BN particles 110
5.4. Electrodeposition of Nickel matrix composite coatings via another boride particles 110
6. Conclusions 111

1. Introduction

Metal matrix composite coatings produced via deposit have become more significant in latest years because of their high hardness, corrosion, and wear resistance than pristine metal or alloy coatings [1]. These characteristics are primarily determined by individual composition phases of a composite covering and, as a result, the distribution and quantity of co-deposited grains, which are influenced by several method variables, considering electrolyte composition, grains properties, and supplied current [2-4]. Nickel is a widely used metal matrix because it is an engineering material. Because of their high anti-wear and hardness characteristics, nickel-matrix composites are gaining popularity for potential engineering applications [5-7].

In comparison to mechanical and thermal methods for preparing composite layers, such as metal spraying, powder metallurgy, and vacuum deposition, or nitriding, such as magnetron sputtering, electrodeposition offers a great and versatile path to the realization of detection coatings of composites (i.e., materials with far more than one phase) comprising particles distributed in a metal matrix [8-10]. The electroly-

* *Corresponding author: Mohammad Velashjerdi; E-mail: mm.velashjerdi@gmail.com*
https://doi.org/10.52547/jcc.3.2.4

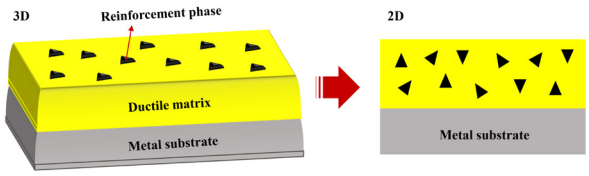

Fig. 1. The schematic of MMC coating on the metal substrate.

sis conditions (presence of additives, the content of the electrolyte bath, pH, electrolyte agitation, and temperature), current circumstances (the kind of enforced current and current density values), and the characteristic of the reinforcing grains (size, concentration, surface characteristics, and the type of distribution in the bath) are all factors that can affect the electrodeposition process and, therefore, the microstructure of the composite coating [11-13].

Composite electrodeposition is the process of incorporating second-step grains into the metallic composition during the electrodeposition process. Solid lubricants (graphite, PTFE, BaF_2, MoS_2), nitrides (AlN, TiN, Si_3N_4, and BN), carbides (B_4C and SiC), nanowires, flakes, whiskers, nanorods, nanotubes, and diamond are some of these particles [14-16]. The inclusion of small particles as the second step increases the surface hardness, corrosion resistance, wear resistance, and rising temperature inertness of composite coatings [17]. These characteristics are primarily determined by each matrix phase of a composite coating, as well as the quantity and dispersion of co-deposited grains, which are controlled by some process factors including particle properties, electrolyte composition, and supplied current [18, 19].

Composite plating was originally recorded in the United States in 1928 in a research of a Cu-graphite covering for such an automotive bearing [20]. The topic saw significant advancements in the 1960s and 1970s, especially in Europe, due to fondness in the diversity of probable coatings, the search for wear-resistant coatings, and the mechanism of particle co-deposition appropriate for rising automotive and aerospace engineering. Strong ceramic grains in beneficial engineering metal composites to realize Co or Ni layers containing, nitrides, or borides, carbides, such as WC or SiC, have received a lot of attention in the literature during this time [21].

Electrodeposited Ni_3B coatings are a relatively new research topic that has received a lot of attention in recent years [22, 23]. Ni-Ni_3B coatings are used successfully in a variety of industries, including automotive, chemical, and electronics [24]. The TiB_2 is a good anti-corrosive material and has excellent wear resistance and mechanical properties. Electrodeposition approaches have only been used in a few studies to incorporate TiB_2 particles into the nickel matrix. Because of their extreme melting point, high hardness, chemical inertness, and oxidation resistance, coatings are based on Ni-TiB_2. The research expressed that electrodeposition of nickel matrix composite coatings via boride particles showed improved properties compared to other coatings [25, 26].

In this study, we review principles of composite plating, nickel matrix composite coatings, and electrodeposition of these coatings via boride particles such as Ni_3B, ZrB_2, CrB_2, BN, and TiB_2. The results obtained from the publications can help to select the promotional materials in various industries.

2. Nickel matrix composite coatings

Metal matrix composite (MMC) is extensively used for strengthening engineering and substrate repair metal components as it combines the high strength and hardness of the ceramic phase with the good hardness of the matrix. MMCs can be made of a variety of materials, including Be, Ti, Mg, Fe, Ni, Al, and Co [27-29]. The Ni-based MMC covering, which is discussed in the next section, is one of the most interesting and challenging metal matrices covering. Figure 1 shows the schematic of MMC coating on the metal substrate.

Nickel and its alloys have several advantages over other alloys, including corrosion resistance, wear resistance, and hardness. For this reason, industry and scientists are interested in using it in a composite coating matrix to improve magnetic properties, increase wear and corrosion resistance, and repair parts [30, 31]. Ni-based composite coatings have excellent high adhesive, and corrosion resistance, high bonding strength, and abrasive wear resistance making them useful in the industry [32-34]. Cutting tools, turbine blades, plungers and rollers, extruders, rolling mill rolls, rods, and piston heads, and wearing plates, for example, all benefit from Ni-based coatings. Vityaz et al. (1993) [35] published the first paper on Ni-based composite coating. They looked at the properties of a plasma coating of a tauboride-containing NiCrBTi alloy with 5–35 wt% TiC sprayed in the air, underwater, and vacuum. As a result, the Ni-based composite was further investigated, and many papers have been published on the subject.

In recent years, the electrodeposition of Ni coating has accounted for nearly 12% of global Ni consumption. The most common application of electroplated Ni coating is for decorative purposes [30]. Ni deposits are used in industry for a variety of purposes, including improving corrosion and wear resistance, changing the dimensions of small pieces, repairing eroded metals, improving magnetic properties, producing organic coatings, or preparing the substrate surface for glazing, and more [36]. An electrodeposition process can produce a Ni-based alloy and a Ni-based composite coating in addition to pure Ni coating. Sensor, electronic, optic industries, and communication all use this type of coating [37, 38].

3. The principles of the electrodeposition method for coating

Electrodeposition, also known as electroplating, is a method of depositing a coating on a substrate that is immersed in an electrolyte via electrolysis. This can be done in a high-temperature merged metal salt (melded salt electroplating) or in a room-temperature aqueous medium (aqueous solution electroplating). The major flaw of this method is its inability to achieve uniform thickness.

Aside from that, the important substrate surface preparation and the evaluation of hydrogen ions are its drawbacks [39-41]. Electroplating is commonly used for decorative coatings as well as low-level corrosion and wear resistance. Deposition of high-temperature resistant, ceramic and biological coatings can also be produced by raising the potential difference in the cells [42-44].

The following steps can be used to describe the process of particle integration in the metal matrix during electrodeposition: 1) particles move from the solution bulk to the metal surface, 2) particle adsorption on the electrode surface (interaction), and 3) particle embedding in the metal matrix as it grows. Guglielmi [45] presented the first model to account for the electrodeposition of metal reinforced with particles. According to this mechanism, the electrodeposition process is divided into two parts. To begin, van der Waals forces weakly adsorb particles on the cathode site, as a result of which there is a high level of surface covering as seen by the Langmuir adsorption isotherm. Second, under the effect of the supplied electric field, the particles are forcefully adsorbed on the surface and into the developing metal matrix by Coulomb forces. Figure 2 shows the schematic of several stages of strong and poor fixation adsorption arbitrarily on the electrode surface.

Celis [46] suggested a five-step model to explain the electrodepo-

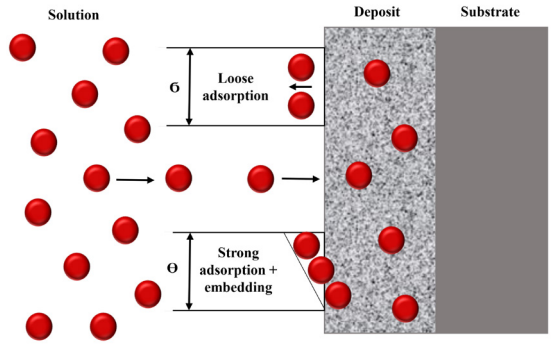

Fig. 2. The schematic of the process of co-deposition according to the Guglielmi model.

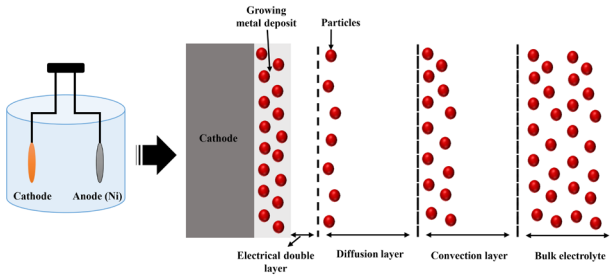

Fig. 3. The schematic procedure for co-electrodepositing unsolvable particles into a developing metal matrix to form a metal composite covering.

sition process: 1) the grains are surrounded by an ionic atmosphere, 2) particle mass movement to the hydrodynamic boundary layer via convection, 3) particles diffuse to the cathode surface by a diffusional mass movement, 4) electroactive ions and free ions are adsorbed on the grains here on the cathode, and 5) electro-reduction of adsorbed ions with particle integration into the expanding metal.

According to the Kurosaki model, mechanical agitation is used to move dispersed particles to the Helmholtz double layer in the prime stage [47]. In this model, electrophoresis is used to transfer charged particles to the cathode from a significant potential gradient. By the Coulomb attraction between adsorbed anions and particles on the cathode, the cathode surface has particles deposited on it in the third phase and incorporated into the developing metal layer [47].

Other models [20, 48] have been proposed, but additional research is needed to account for particle characteristics (composition, crystallinity, size, and so on) and operating electrodeposition parameters [48-50]. Figure 3 summarizes the most important procedure concerned with the particle electroplating into a metallic matrix in growth. .

4. Essential components of Borides particles

Boron compounds are well valued due to features such as high Young's modulus, high hardness, and low density; nevertheless, their application is limited due to low fracture toughness, poor inter ability, and low wettability with most metals [51, 52]. To have a significant trend on B-based compositions, it is critical to identify the most practical synthesis method for the fabrication of B components. One of such methods is electroplating, which is applied to coat materials with a film of various metals. Despite the well-known useful properties of borides, such as hardness, supporting the metallic under-layer from wear, little research has been carried out on borides electrodeposition, and this area is still widely unknown. Possibly, the first methodical study was performed by Andrieux and Weiss (1940) [53]. Although this study led to more electro-synthesis process than electroplating, it illustrated that a lot of binary compounds could be fabricated through electrochemical methods by molten salts. Particularly, the compounds of molybdenum and tungsten were fabricated through electrolysis from molten salts of anti-monides, sulfides, arsenides, carbides, and borides. The composition of the bath was normally composed of alkali metal borate-fluoride combinations, which are great solvents for the tungsten and molybdenum oxides [53].

Kellner [54] investigated the impacts of a range of factors affecting the purity and quality of plated boron to improve the process. To produce a smooth, hard, and adherent deposit, he discovered that compounds based on oxygen, such as B_2O_3, should be strictly eliminated from the melt. His solvent was a 1:1 mixture of LiF-KF, with boron added as BF_3 (g). The electroactive species is BF_4^- shown in equation (1), and the gas is very soluble. The temperature was 700 °C. A three-electron reduction was confirmed by electrochemical and mass balance studies:

$$BF_4^- + 3e = B + 4F^- \quad (1)$$

TiB_2 has received the most attention out of all the refractory borides. This is due to its excellent resistance to oxidation (even at 1000 °C), corrosion, and erosion in high-temperature concentrated brines, and the adhesion of coating and substrate. By adding BF_3 to this melt, Kellner et al. [55] followed Kellner's research on boron plating from FLINAK. Titanium was included, but it was most likely converted to its fluoride type. The probable reactions at the cathode are shown in Equation (2):

$$\begin{aligned} &2BF_4^- + 6e = 2B + 8F^- \\ &TiF_6^{3-} + 3e = Ti + 6F^- \\ &\hline \\ &2BF_4^- + TiF_6^{3-} + 9e = TiB_2 + 14F^- \end{aligned} \quad (2)$$

Some of the research done is focused on the functional features of plating, created to prevent corrosion in valves and pipes employed to transport high-temperature, geothermal brines. As a result, only the overall reactions were given, despite the plating processes being cautiously examined and the characteristics of the coating being explored [53, 56, 57].

5. Electrodeposition of Nickel matrix composite coatings via Boride particles

Coatings with adequate hardness and wear resistance are usually deposited on devices that are employed for harsh forming, cutting, and casting usages, wherever the process situations generally lead to elevated temperatures, enhanced mechanical loads, and increased wear [58-60]. Coatings consisting of hard Cr are noted due to their excellent corrosion and wear resistance; however, materials such as carbon-based materials, boride, oxides, carbides, and nitrides are also widely utilized in fabricating hard coatings because of their superior tribological and mechanical characteristics [61-64]. Despite having a promising mix of features that has drawn the attention of a growing number of researchers, the industrial applicability of boride-based thin films remains limited. The fact that the related bulk phases display promising features, such as chemical stability and high hardness, has sparked interest in boride coatings [65, 66]. In addition, wonderful oxidation resistance and chemical stability in harsh conditions are the recurrent characteristics of these materials [61].

A nickel-boron alloy layer can be created on the surface of a solid substrate, such as plastic or metal, using an electroless NiB coating technique [67]. Rajagopal et al. [68] discussed the composite coatings of Ni-B received by an electroplating process and electroless-based deposition from a bath of borohydride. The deposits of nickel created via chemical reduction and sodium borohydride are compounds of boron

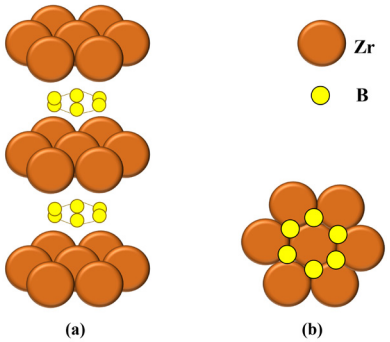

Fig. 4. The schematic of ZrB_2 structural projection: a) 3D view and b) top view.

and nickel. The resistivity of heat-treated Ni-B composite coatings to electricity was almost similar to that of the electroplated nickel (about 10 Ωm). Electroplated and electroless composite coatings of Ni-B had corrosion resistance greater than electroplated nickel because of soaking in NaCl solution. Individual electroplated and electroless Ni-B composite coatings once heated to 400 °C present the most superior corrosion resistance to the Ni-B coatings that were plated in advance. The mentioned phenomenon results in the existence of the Ni_2B and Ni_3B phases, which could decrease the current density of local corrosion. Indeed, there was no mark of corrosion on the deposits of heat-treated Ni-B when being soaked about 100 h, while corrosion marks were ascertained for electroplated nickel with the same thickness (10 μm) after 20 h of the immersion test. The resistance of heat-treated, at 400 °C, composite coatings of electroless and electroplated Ni-B to abrasion is $3 \times 10^{-4}\frac{mm^3}{hr}$ vs. $25 \times 10^{-4}\frac{mm^3}{hr}$ for a plated nickel. Further investigation revealed that the tensile properties and hardness of the electroplated Ni-B composite were larger than the as-deposited electroless composite of Ni-B. The superior characteristics of electroplated composites of Ni-B to electroless Ni-B coatings make it clear that electroplating could be a suitable approach for producing Ni-B composites [68].

5.1. Electrodeposition of Nickel matrix composite coatings via ZrB_2 particles

Zirconium diboride (ZrB_2) has a highly covalent refractory and hexagonal crystal shape ceramic material. It is a rare ceramic with strong thermal and electrical conductivities shared with isostructural titanium diboride and hafnium diboride. As shown in Figure 4, this system comprises layers of boron (B) atoms in two-dimensional graphite-like plates in sp^2 hybridization with hexagonal close-packed (hcp) Zr arrays alternating [69].

ZrB_2 structure includes Zr–Zr metallic connections, B–B covalent linkages, and Zr–B covalent/ionic bonds. Zr–Zr bonds have strong electrical and thermal conductivities due to the existence of free electrons, which increase the hardness, stiffness, and chemical inertness properties of B–B bonds. The melting point of ZrB_2 is raised due to the strong Zr–B bonds. In addition to its high melting point, ZrB_2 has several unique properties, including high-temperature retention strength and slags, chemical inertness to molten metals, corrosion and erosion resistance in harsh environments, high thermal and electrical conductivities, low thermal expansion coefficient, and excellent thermal shock resistance. ZrB_2 has also been shown to be resistant to plasma arcs and sparks [70-72].

Buichi ISE et al. [73] examined Ni-ZrB_2 composite coatings electrodeposited from Watt's bath in which ZrB_2 particles were present. According to the results, the optimum plating condition for maximizing ZrB_2 content was identified at 5 $\frac{A}{dm^2}$ and 900 rpm. The co-deposition rate of ZrB_2 particles is dependent on the plating current density and plating solution stirring rate. In the range of 10-20 $\frac{mg}{cm^2}$, a linear association was discovered between ZrB_2 content and the amount of deposited Ni-ZrB_2 composite.

Mellors and Senderoff [74] showed that electrolysis of the melt containing Flinak[1] 80 w/o (weight percent) – ZrF_4 8 w/o – B_2O_3 12 w/o in a graphite crucible 750 °C produced a smooth, dark-colored deposit at 100% cathode current efficiency, based on the assumption of 10 $\frac{F}{mol}$ of ZrB_2. The anode and the cathode were zirconium and a nickel strip, respectively. On raising the temperature to 800 °C, a bright, coherent plate was obtained (at 100% cathode current efficiency) that was re-identified as ZrB_2. It will be noticed that there exists a considerable diffusion layer between the nickel substrate and ZrB_2. The mentioned layer is a nickel boride, from which zirconium is absent. By the same token, nickel is absent from the ZrB_2 deposit. This indicates that some boron diffuses into nickel from the initially deposited ZrB_2, resulting in a deposit at the interface having a B: Zr ratio slightly less than 2. The electron probe analysis indicates that the intermediate layer is, in all probability, Ni_3B, and it is thought that the presence of this material contributes to the adherence of ZrB_2 to the substrate.

Huang et al. [75] showed that certain compounds (e.g. TiC, ZrB_2, and TiB_2) were recognized for possessing adequate thermal and electrical conductivities as well as hardness. It was shown that hard particles with electrical conductivity could impact the stability of electroless nickel plating bath in a way that TiB_2 and ZrB_2 had significant and the least important effects, respectively. Moreover, this boride ZrB_2 is stable at high temperatures and resistant to molten metals, molten salts, and atmospheric oxidation, rendering it an appropriate material for protection applications in harsh conditions.

5.2. Electrodeposition of Nickel matrix composite coatings via TiB_2 particles

A high melting point (3225 °C), high-temperature strength, high thermal conductivities, hardness, and wear resistance are all characteristics of titanium diboride (TiB_2)-based materials. As a result, they are excellent for cutting tools, electrode materials, and wear-resistant coatings that require extreme environmental conditions and service temperatures of more than 2000 °C. Because monolithic TiB_2 has a poor oxidation resistance over 1000 °C, additives have been employed to improve its oxidation behavior at high temperatures [76-78].

Gyawali et al. [79] fabricated Ni-TiB_2 coatings by pulse electrodeposition techniques from nickel sulfamate bath containing dispersed submicron TiB_2 particles. The results showed a greater Vickers' microhardness of around 690 HV in the composite coating fabricated from TiB_2 particles in the electrolyte. This level of microhardness is around three times greater than that of the pure nickel coating (230 HV). Moreover, composite coatings have illustrated a positive shift in corrosion potential of E_{corr} = -0.2692 V compared with that of nickel, which is equal to -0.3117 V. The presence of an extended passive section together with a positive charge of corrosion potential for the composite coatings can be associated with the variety in the crystal structure of the nickel matrix and modified grain size, as well as implemented TiB_2 particles that probably behaved as an interior physical barrier against the development of corrosion, therefore, enhancing the polarization resistance of the composite layer.

To increase the performance of Ni-TiB_2-Dy_2O_3 composite coatings, Liu et al. [80] employed TiB_2 and Dy_2O_3 as co-deposited particles. Electrodeposition of a hexadecyl pyridinium bromide and nickel cetyltrimethylammonium bromide solution containing TiB_2 and Dy_2O_3 particles yielded Ni-TiB_2-Dy_2O_3 composite coatings. According to the findings, wear losses of mass of Ni-TiB_2-Dy_2O_3 matrix coatings were 9

1. "Flinak" is the acronym for the eutectic composition of KF-LiF-NaF that melts at 454 °C. Its composition in mole per cent is 46.5 LiF, 11.5 NaF, and 42.0 KF.

and 1.57 times smaller than pristine Ni and Ni-TiB_2 composite coatings, respectively. The friction coefficients of pristine Ni, Ni-TiB_2-Dy_2O_3, and Ni-TiB_2 composite coatings were 0.723, 0.619, and 0.815, respectively. Among the three coatings, Ni-TiB_2-Dy_2O_3 composite coatings had the lowest friction coefficient.

Gyawali et al. [81] used electrodeposition to create Ni–W–TiB_2 composite coatings on the copper substrate. The Vickers micro-hardness of Ni-W-TiB_2 composite coatings was much higher than pure Ni and Ni-W alloy coatings, along with enhanced wear and coefficient of friction in the Ni-W-TiB_2 composite coating. Adhesive wear is significant in pure Ni and Ni-W coatings, whereas abrasive wear is observed in Ni-W-TiB_2 composite coatings. The scratch resistance of the composite coating was better than pure nickel and Ni-W coatings. W alloying and TiB_2 inclusion into the nickel matrix affected the scratch resistance of the composite coating.

5.3. Electrodeposition of Nickel matrix composite coatings via BN particles

Boron nitride (BN) is a boron-nitrogen refractory substance with the chemical formula BN that is thermally and chemically resistant. It appears in a variety of crystalline forms that are isoelectronic to a carbon lattice with a comparable structure. BN ceramics have long been employed as parts of high-temperature equipment due to their superior chemical and thermal stability. Nanotechnology could benefit from BN [82, 83]. Because of their wear resistance and high hardness, Ni-BN composites are significant for a variety of applications. The metal matrix particle measurement is unaffected by BN particles [84, 85].

Pompei et al. [5] electrodeposited nickel–boron nitride (Ni–BN) composites from a sulfate bath containing up to 10 $\frac{g}{l}$ of dispersed boron nitride particles. The surfactants in the plating solution improve the micro-hardness of the deposit, from 280 to about 400 HV. The improvement in micro-hardness of the composite coating can be because of (a) the dispersive strengthening effect of h-BN, (b) inhibited crystalline growth by h-BN nano-sheets in the coatings in the electrodeposition procedure, thereby refining nickel crystallites, and (c) hindering the movement of dislocations and the sliding of grain boundary by h-BN nano-sheets. Besides, the results clarify the improvement of corrosion protection by h-BN reinforcement in the nickel matrix.

Tripathi et al. [86] investigated Ni-Fe alloy matrix nanocomposite coatings containing uniformly dispersed 24 wt. % BN particles. The results showed that the hardness levels of as-deposited and heat-treated nanocomposite coatings were significantly higher than that of the substrate. A correlation between crystallite size and strain with hardness was worked out in their research.

Li et al. [87] investigated the pulse electrodeposition of functionally graded (FG) Ni-W/BN(h) nanocomposite coatings with varying BN(h) nanoparticle content along with the thickness. The findings demonstrated that the content of BN(h) nanoparticles and tungsten grew to various degrees as the frequency or duty cycle was reduced along with the four-layer structure. In addition, FG Ni-W/BN(h) coatings had much better wear resistance and microhardness than uniform Ni-W/BN(h) coatings. Furthermore, the presence of more BN(h) nanoparticles in the deposits improved the corrosion resistance in FG coatings.

5.4. Electrodeposition of Nickel matrix composite coatings via another boride particles

As with many other transition metal borides, chromium diboride (CrB_2) is an inorganic compound that is exceedingly strong and hard

Table 1.
Bath elements of Ni-B alloy matrix composite coatings

Composite coatings	Boron source and content ($\frac{g}{l}$)	Nickel source and content ($\frac{g}{l}$)	Particle type, content ($\frac{g}{l}$)	Results	Ref.
Ni-B/CeO_2	DMAB*, 3	$NiSO_4.6H_2O$-240 $NiCl_2.H_2O$-45	CeO_2, 15	The surface roughness, hardness, modulus of elasticity, and corrosion behavior of Ni-B corrosion improved with the addition of CeO_2.	[95]
Ni-B/TiO_2	DMAB, 3	$NiSO_4.6H_2O$-250 $NiCl_2.H_2O$-40	TiO_2, 50	When compared to NiB coating, Ni-B/TiO_2 coating has a better surface hardness, wear resistance, and resistance to corrosion.	[96]
duplex Ni–B–TiO_2/ Ni	DMAB, 3	$NiSO_4.6H_2O$-250 $NiCl_2.H_2O$-40	TiO_2, 50	This coating showed high hardness and good corrosion resistance properties.	[97]
Ni-B/Al_2O_3	DMAB, 3	$NiSO_4.6H_2O$-240 $NiCl_2.H_2O$-45	Al_2O_3, 15	The surface roughness, hardness, modulus of elasticity, and corrosion behavior are significantly improved with the addition of Al_2O_3 in Ni–B coating.	[98]
Ni-B/La_2O_3	DMAB, 5	$NiSO_4.6H_2O$-280	La_2O_3, 5-10	The thermal stability of metastable Ni-B coatings improved with the addition of La_2O_3.	[99]
Ni-B/V_2O_5- ZrO_2	DMAB, 3	$NiSO_4.6H_2O$-240 $NiCl_2.H_2O$-45	V_2O_5-ZrO_2, 0.75+0.75	The Ni-B coating's hardness, surface roughness, and modulus of elasticity are almost 70-170 percent higher.	[100]
Ni-B/Fe_2O_3	DMAB, 3	$NiSO_4.6H_2O$-240 $NiCl_2.H_2O$-45	Fe_2O_3, 15	The results showed a 52% improvement in hardness and good corrosion protection in Ni-B coating with Fe_2O_3.	[101]
Ni- B/Diamond	TMAB †, 3	$NiSO_4.6H_2O$-240 $NiCl_2.H_2O$-45	Diamond, 5-50	Extremely high hardness is obtained with the addition of diamond.	[102]
Ni-B/Y_2O_3	DMAB, 3	$NiSO_4.6H_2O$-240 $NiCl_2.H_2O$-45	Y_2O_3, 9	The superior thermal stability and improvement of mechanical and anti-corrosion properties (73.6%) are obtained with the addition of Y_2O_3 on Ni-B coating.	[103]
Ni-B/TiC-Y_2O_3	DMAB, 3	$NiSO_4.6H_2O$-240 $NiCl_2.H_2O$-45	Y_2O_3, 9 and TiC, 15	The findings showed adding TiC-Y_2O_3 to Ni-B coating improves surface roughness, wear, and corrosion resistance (30%).	[104]

* DMAB: Dimethylamine borane
† TMAB: Trimethylamine borane

and transmits electricity and heat similar to many metallic alloys, with a high melting point [88]. Nozdrin et al. [89] studied the features of the electrical deposition of nickel-based composite coatings, which contain CrB_2 nano-powder as a strengthening phase. With the existence of the nano-dispersed phase, the maximum limit of the working density of the electrolyte current is 1.0 $\frac{KA}{m^2}$, which is greater than that for achieving nickel coatings in this electrolyte (0.5 $\frac{KA}{m^2}$). The micro-hardness of the Ni-CrB_2 nanocomposite is recognized by the quantity of the CrB_2 nanoparticles. The coating obtained at cathode current densities of 0.1, 0.5, and 1.0 $\frac{KA}{m^2}$ have micro-hardness values of 2.86, 3.29, and 4.44 GPa, respectively, which are higher than those obtained for the nickel matrix at j_c=0.5 $\frac{KA}{m^2}$ by a factor of 1.41, 1.62, and 2.19.

Rare earth oxides (such as CeO_2) exhibit exceptional properties in MMC coatings, preventing cracks, defects, and pores. Compared to pure Ni coatings, it can also improve corrosion resistance [90, 91]. On the substrate of steel, Wang et al. [92] utilized pulsed electrodeposition to produce Ni-W-B composites containing CeO_2 nanoparticles. The results showed that pulse co-deposition of Ni, W, B, and CeO_2 nanoparticles resulted in Ni-W-B/CeO_2 composites with increased micro-hardness and superior wear resistance after being heat-treated at 400 °C for 1 h. The as-deposited alloy exhibited a maximum surface hardness of 636 HV, a deposition rate of 0.0281 $\frac{mm}{h}$ at a frequency of 1000 Hz, a pulsation duty circle of 10%, and a pulse-estimated average density of 10 $\frac{A}{dm^2}$. The formed composites were largely amorphous and somewhat crystalline, and the crystallization tendency was enhanced when they were exposed to 400 °C. The refinement of the development and grain structures of microstructures were aided by lowering. The pulsed switching frequency was reduced from 75% to 10%. Pulse electrodeposition was used to reduce the crystal sizes of the composites.

Among the numerous ceramic particles, boron carbide (B_4C) particles are one of the most promising reinforcing particles because they have unique physical-mechanical characteristics that make them ideal for abrasive grit and wear-resistant components.

Using pulsed electrodeposition, He et al. [93] created a Ni–W–B_4C MMC coating with only the 2$\frac{g}{l}$$B_4C$ concentration. According to the findings, applying B_4C nanoparticles to the Ni-W alloy substantially enhanced the micro-hardness and substrate morphology of matrix coating. Ni-W-B_4C nanocomposite has a substantially higher corrosion resistance than Ni-W alloy deposits.

Table 1 presents the elements of the composite coating bath and the Ni-B matrix. The dimension of the strengthening element could be in the range of micron or nano. Table 1 demonstrates that a variety of oxides, nitrides, carbides, nitrides, and oxides are employed as reinforcing elements, and even though the size of particles is quite paramount; some studies present no results regarding the sizes of the strengthening inert particles [94].

6. Conclusions

The composite coating based on Ni, which is a very effective method, may be used to modify the surface of components. Since surface engineering can be described as a novel approach, it is still in the early stages of development. According to a review of the literature, the Ni-based MMC coating gives the area a very high strength, which improves wear resistance.

The presence of Ni also demonstrates good corrosion resistance. However, the review shows that only Ni alloy or Ni coatings are not as effective as Ni-based composite coatings. Plasma spraying, thermal, chemical, and physical vapor deposition have all been considered as methods for preparing nanocomposite materials. When compared to other electrodeposition methods, precision management, uniform deposition, low energy needs, low cost in producing wide-area samples, great versatility, reproducibility, ability to coat complex component configurations, waste reduction, and increased efficiency are only some of the benefits. A wide range of particles have been used in nickel matrix electrodeposits, including oxides such as SiO_2, TiO_2, Al_2O_3, SnO_2, ZrO_2, CeO_2, and Cr_2O_3, carbides such as WC, SiC, and TiC nitrides such as carbon nanotubes and BN, Si_3N_4, and so on. Boride ceramic particles have recently been used in a variety of MMCs. The results of mechanical properties, wear, and corrosion in these composites show that boride particles have a significant impact on improving these properties.

This study examines Ni-based composite coatings, the concept of electrodeposition methods, the behavior of boride particles in composites, and the literature on nickel matrix composite coatings reinforced with boride ceramics particles. Furthermore, it appears that further studies are required in this sector to fully understand the behavior of various boride particles in Ni-based composite coatings.

REFERENCES

[1] M. Sabzi, S.H.M. Anijdan, M. Roghani Zadeh, M. Farzam, The effect of heat treatment on corrosion behaviour of Ni–P–3 gr/lit Cu nano-composite coating, Canadian metallurgical quarterly 57(3) (2018) 350-357.

[2] L. Xiaozhen, L. Xin, Y. Aibing, W. Huang, Preparation and tribological performance of electrodeposited Ni-TiB_2-Dy_2O_3 composite coatings, Journal of Rare Earths 27(3) (2009) 480-485.

[3] S. Kumar, R. Singh, M. Hashmi, Metal matrix composite: a methodological review, Advances in Materials and Processing Technologies 6(1) (2020) 13-24.

[4] A.S. Perna, A. Viscusi, A. Astarita, L. Boccarusso, L. Carrino, M. Durante, R. Sansone, Manufacturing of a metal matrix composite coating on a polymer matrix composite through cold gas dynamic spray technique, Journal of Materials Engineering and Performance 28(6) (2019) 3211-3219.

[5] E. Pompei, L. Magagnin, N. Lecis, P.L. Cavallotti, Electrodeposition of nickel–BN composite coatings, Electrochimica Acta 54(9) (2009) 2571-2574.

[6] M. Sabzi, S.H. Mousavi Anijdan, Microstructural analysis and optical properties evaluation of sol-gel heterostructured NiO-TiO_2 film used for solar panels, Ceramics International 45(3) (2019) 3250-3255.

[7] M. Sabzi, S.M. Dezfuli, Z. Balak, Crystalline texture evolution, control of the tribocorrosion behavior, and significant enhancement of the abrasion properties of a Ni-P nanocomposite coating enhanced by zirconia nanoparticles, International Journal of Minerals, Metallurgy, and Materials 26(8) (2019) 1020-1030.

[8] F. Walsh, C. Ponce de Leon, A review of the electrodeposition of metal matrix composite coatings by inclusion of particles in a metal layer: an established and diversifying technology, Transactions of the IMF 92(2) (2014) 83-98.

[9] F.C. Walsh, S. Wang, N. Zhou, The electrodeposition of composite coatings: Diversity, applications and challenges, Current Opinion in Electrochemistry 20 (2020) 8-19.

[10] Z. Mahidashti, M. Aliofkhazraei, N. Lotfi, Review of nickel-based electrodeposited tribo-coatings, Transactions of the Indian Institute of Metals 71(2) (2018) 257-295.

[11] J.M. Costa, A.F. de Almeida Neto, Electrodeposition of nickel-tungsten alloys under ultrasonic waves: Impact of ultrasound intensity on the anticorrosive properties, Ultrasonics Sonochemistry 73 (2021) 105495.

[12] K.K. Maniam, S. Paul, A Review on the Electrodeposition of Aluminum and Aluminum Alloys in Ionic Liquids, Coatings 11(1) (2021) 80.

[13] H. Gül, F. Kılıç, M. Uysal, S. Aslan, A. Alp, H. Akbulut, Effect of particle concentration on the structure and tribological properties of submicron particle SiC reinforced Ni metal matrix composite (MMC) coatings produced by electrodeposition, Applied Surface Science 258(10) (2012) 4260-4267.

[14] C. Zhao, Y. Zhou, X. Xing, S. Liu, X. Ren, Q. Yang, Precipitation stability and micro-property of (Nb, Ti) C carbides in MMC coating, Journal of Alloys and Compounds 763 (2018) 670-678.

[15] C. Feng, V. Guipont, M. Jeandin, O. Amsellem, F. Pauchet, R. Saenger, S. Bucher, C. Iacob, B_4C/Ni composite coatings prepared by cold spray of blended or CVD-coated powders, Journal of thermal spray technology 21(3-4) (2012) 561-570.

[16] N.K. Bhoi, H. Singh, S. Pratap, Developments in the aluminum metal matrix composites reinforced by micro/nano particles–a review, Journal of Composite Materials 54(6) (2020) 813-833.

[17] D.K. Sharma, D. Mahant, G. Upadhyay, Manufacturing of metal matrix composites: A state of review, Materials Today: Proceedings 26 (2020) 506-519.

[18] D. Mercier, J.-F. Vanhumbeeck, M. Caruso, X.V. Eynde, M. Febvre, Micro-

structural and mechanical characterisation of electroplated nickel matrix composite coatings, Surface Engineering 35(2) (2019) 177-188.
[19] L. Singh, B. Singh, K.K. Saxena, Manufacturing techniques for metal matrix composites (MMC): an overview, Advances in Materials and Processing Technologies 6(2) (2020) 441-457.
[20] J. Fransaer, J.-P. Celis, J. Roos, Analysis of the electrolytic codeposition of non-brownian particles with metals, Journal of the Electrochemical Society 139(2) (1992) 413.
[21] K. Helle, F. Walsh, Electrodeposition of composite layers consisting of inert inclusions in a metal matrix, Transactions of the IMF 75(2) (1997) 53-58.
[22] S. Ahmadiyeh, A. Rasooli, M.G. Hosseini, Preparation of Pulse Electrodeposited Ni-B Coating with RSM Software and Evaluation of Its Microhardness and Electrochemical Behavior, Metallurgical and Materials Transactions A (2020) 1-13.
[23] Q. Barati, S.M.M. Hadavi, Electroless Ni-B and Composite Coatings: A Critical Review on Formation mechanism, Properties, Applications and Future trends, Surfaces and Interfaces (2020) 100702.
[24] E. Ünal, A. Yaşar, İ.H. Karahan, A review of electrodeposited composite coatings with Ni–B alloy matrix, Materials Research Express 6(9) (2019) 092004.
[25] Y. Wang, W. Zhang, D. Chen, X. Liu, W. Hu, L. Liu, J. Yan, X. Xiong, High temperature friction and wear performance of TiB_2-50Ni composite coating sprayed by HVOF technique, Surface and Coatings Technology 407 (2021) 126766.
[26] Z. Huang, Y. Zhou, T. Nguyen, Study of nickel matrix composite coatings deposited from electroless plating bath loaded with TiB_2, ZrB_2 and TiC particles for improved wear and corrosion resistance, Surface and Coatings Technology 364 (2019) 323-329.
[27] A. Kelly, C.H. Zweben, Comprehensive composite materials, Elsevier2000.
[28] P. Maji, S.K. Ghosh, R.K. Nath, R. Karmakar, Microstructural, mechanical and wear characteristics of aluminum matrix composites fabricated by friction stir processing, Journal of the Brazilian Society of Mechanical Sciences and Engineering 42(4) (2020) 1-24.
[29] Y. Hu, W. Cong, A review on laser deposition-additive manufacturing of ceramics and ceramic reinforced metal matrix composites, Ceramics International 44(17) (2018) 20599-20612.
[30] V. Torabinejad, M. Aliofkhazraei, S. Assareh, M. Allahyarzadeh, A.S. Rouhaghdam, Electrodeposition of Ni-Fe alloys, composites, and nano coatings–A review, Journal of Alloys and Compounds 691 (2017) 841-859.
[31] A. Karimzadeh, M. Aliofkhazraei, F.C. Walsh, A review of electrodeposited Ni-Co alloy and composite coatings: Microstructure, properties and applications, Surface and Coatings Technology 372 (2019) 463-498.
[32] J.F. Flores, A. Neville, N. Kapur, A. Gnanavelu, An experimental study of the erosion–corrosion behavior of plasma transferred arc MMCs, Wear 267(1) (2009) 213-222.
[33] D. Chaliampalias, G. Vourlias, E. Pavlidou, S. Skolianos, K. Chrissafis, G. Stergioudis, Comparative examination of the microstructure and high temperature oxidation performance of NiCrBSi flame sprayed and pack cementation coatings, Applied Surface Science 255(6) (2009) 3605-3612.
[34] S.M. Anijdan, M. Sabzi, M.R. Zadeh, M. Farzam, The influence of pH, rotating speed and Cu content reinforcement nano-particles on wear/corrosion response of Ni-P-Cu nano-composite coatings, Tribology international 127 (2018) 108-121.
[35] P. Vityaz, A. Verstak, T. Talako, S. Sobolevskiy, E. Lugscheider, P. Jokiel, G. Beckschulte, K. Yuschenko, G. Pursche, Processing and investigation of tauboride-containing NiCrBTi-TiC plasma coatings, Materials Science and Engineering: A 168(1) (1993) 61-66.
[36] M. Schlesinger, M. Paunovic, Modern Electroplating, John Willey & Sons, INC (NY, 2000) (2000).
[37] J. Huiming, S. Jiang, L. Zhang, Structural characterization and corrosive property of Ni-P/CeO_2 composite coating, Journal of Rare Earths 27(1) (2009) 109-113.
[38] S. Singkammo, A. Wisitsoraat, C. Sriprachuabwong, A. Tuantranont, S. Phanichphant, C. Liewhiran, Electrolytically exfoliated graphene-loaded flame-made Ni-doped SnO_2 composite film for acetone sensing, ACS applied materials & interfaces 7(5) (2015) 3077-3092.
[39] J.R. Davis, Surface engineering for corrosion and wear resistance, ASM international2001.
[40] H.J. Biswal, P.R. Vundavilli, A. Gupta, Perspective—Electrodeposition of Graphene Reinforced Metal Matrix Composites for Enhanced Mechanical and Physical Properties: A Review, Journal of the Electrochemical Society (2020).
[41] A. Davydov, V. Volgin, Template electrodeposition of metals. Review, Russian Journal of Electrochemistry 52(9) (2016) 806-831.
[42] B. Fotovvati, N. Namdari, A. Dehghanghadikolaei, On coating techniques for surface protection: A review, Journal of Manufacturing and Materials processing 3(1) (2019) 28.
[43] R. Karmakar, P. Maji, S.K. Ghosh, A Review on the Nickel Based Metal Matrix Composite Coating, Metals and Materials International (2020) 1-13.
[44] A. Lelevic, F.C. Walsh, Electrodeposition of NiP alloy coatings: a review, Surface and Coatings Technology 369 (2019) 198-220.
[45] N. Guglielmi, Kinetics of the deposition of inert particles from electrolytic baths, Journal of the Electrochemical Society 119(8) (1972) 1009.
[46] J.-P. Celis, J. Roos, C. Buelens, A mathematical model for the electrolytic codeposition of particles with a metallic matrix, Journal of the Electrochemical Society 134(6) (1987) 1402.
[47] Y. Kurosaki, M. Shiozaki, K. Higashine, M. Sumimoto, Effect of oxide shape on magnetic properties of semiprocessed nonoriented electrical steel sheets, ISIJ international 39(6) (1999) 607-613.
[48] Y.H. Ahmad, A. Mohamed, Electrodeposition of nanostructured nickel-ceramic composite coatings: a review, (2014).
[49] G. Munday, J. Hogan, A. McDonald, On the microstructure-dependency of mechanical properties and failure of low-pressure cold-sprayed tungsten carbide-nickel metal matrix composite coatings, Surface and Coatings Technology 396 (2020) 125947.
[50] N. Aboudzadeh, C. Dehghanian, M.A. Shokrgozar, Effect of electrodeposition parameters and substrate on morphology of Si-HA coating, Surface and Coatings Technology 375 (2019) 341-351.
[51] M. Saeedi Heydari, H.R. Baharvandi, S.R. Allahkaram, Electroless nickel-boron coating on B_4C-Nano TiB_2 composite powders, International Journal of Refractory Metals and Hard Materials 76 (2018) 58-71.
[52] K.K. Raj, M. Annaiah, T. Gangadhar, V. Girija, Evaluation of mechanical properties of A390 reinforced with boron carbide MMC, AIP Conference Proceedings, AIP Publishing LLC, 2020, p. 030019.
[53] K.H. Stern, Electrodeposition of refractory compounds from molten salts—borides, carbides and silicides, Metallurgical and Ceramic Protective Coatings, Springer1996, pp. 54-73.
[54] J.D. Kellner, Electrodeposition of coherent boron, Journal of the Electrochemical Society 120(6) (1973) 713.
[55] J.D. Kellner, W.J. Croft, L.A. Shepard, Titanium Diboride Electrodeposited Coatings, ARMY MATERIALS AND MECHANICS RESEARCH CENTER WATERTOWN MA, 1977.
[56] T. Nallusamy, High-temperature stability of titanium boride reinforced alumina-silicon carbide based composite, Silicon 13 (2021) 1087-1095.
[57] A.N. Zadiranov, M.Y. Malkova, R. Abu-Nijim, Production of nickel composite materials reinforced with ultrafine powders, Journal of Chemical Technology and Metallurgy 55(3) (2020) 608-613.
[58] M. Tkadletz, N. Schalk, R. Daniel, J. Keckes, C. Czettl, C. Mitterer, Advanced characterization methods for wear resistant hard coatings: a review on recent progress, Surface and Coatings Technology 285 (2016) 31-46.
[59] V.M. Gopinath, S. Arulvel, A review on the steels, alloys/high entropy alloys, composites and coatings used in high temperature wear applications, Materials Today: Proceedings 43 (2021) 817-823.
[60] V. Tseluikin, On the structure and properties of composite electrochemical coatings. A Review, Protection of Metals and Physical Chemistry of Surfaces 52(2) (2016) 254-266.
[61] A. Lelevic, F.C. Walsh, Electrodeposition of NiP composite coatings: A review, Surface and Coatings Technology 378 (2019) 124803.
[62] J. Luo, Y. Meng, T. Shao, Q. Zhao, Advanced tribology: proceedings of CIST2008 & ITS-IFToMM2008, Springer Science & Business Media2010.
[63] C.V. Kumar, B. Kandasubramanian, Advances in ablative composites of carbon based materials: A review, Industrial & Engineering Chemistry Research 58(51) (2019) 22663-22701.
[64] C. Mitterer, Borides in thin film technology, Journal of solid state chemistry 133(1) (1997) 279-291.
[65] V.I. Matkovich, G.-. Samsonov, P. Hagenmuller, Boron and refractory borides, Springer1977.
[66] D. Santana, G. Koga, W. Wolf, I. Bataev, A. Ruktuev, C. Bolfarini, C. Kiminami, W. Botta, A. Jorge Jr, Wear-resistant boride reinforced steel coatings produced by non-vacuum electron beam cladding, Surface and Coatings Technology 386 (2020) 125466.
[67] A. Tozar, İ.H. Karahan, Effect of octylphenyl ether group nonionic surfactant on the electrodepositon of the hexagonal boron nitride reinforced Ni-B matrix composite coatings, Surface and Coatings Technology 381 (2020) 125131.
[68] I. Rajagopal, Electroless and electrodeposition of nickel boron composites, Bulletin of Materials Science 5(3) (1983) 323-331.
[69] S.C. Zhang, G.E. Hilmas, W.G. Fahrenholtz, Mechanical properties of sintered ZrB_2–SiC ceramics, Journal of the European Ceramic Society 31(5) (2011)

893-901.
[70] J. Sonber, A. Suri, Synthesis and consolidation of zirconium diboride, Advances in Applied Ceramics 110(6) (2011) 321-334.
[71] S.-Q. Guo, Densification of ZrB_2-based composites and their mechanical and physical properties: a review, Journal of the European Ceramic Society 29(6) (2009) 995-1011.
[72] M.S. Asl, B. Nayebi, Z. Ahmadi, M.J. Zamharir, M. Shokouhimehr, Effects of carbon additives on the properties of ZrB_2–based composites: a review, Ceramics International 44(7) (2018) 7334-7348.
[73] B. ISE, S. MEGURO, Content of ZrB_2 in the Ni-ZrB_2 Composite Layer Electrodeposited by Dispersion Plating, Denki Kagaku oyobi Kogyo Butsuri Kagaku 61(2) (1993) 212-217.
[74] G.W. Mellors, S. Senderoff, Electrodeposition of Coherent Coatings of Refractory Metals, Journal of The Electrochemical Society 118(2) (1971) 220.
[75] Z.H. Huang, Y.J. Zhou, T.T. Nguyen, Study of nickel matrix composite coatings deposited from electroless plating bath loaded with TiB_2, ZrB_2 and TiC particles for improved wear and corrosion resistance, Surface and Coatings Technology 364 (2019) 323-329.
[76] B.R. Golla, T. Bhandari, A. Mukhopadhyay, B. Basu, Titanium Diboride, Ultra-High Temperature Ceramics2014, pp. 316-360.
[77] Y.L. Krutskii, N.Y. Cherkasova, T. Gudyma, O. Netskina, T. Krutskaya, Diborides of Some Transition Metals: Properties, Application and Production. Review. Part 1. Titanium and Vanadium Diborides, Steel in Translation 51(2) (2021) 93-106.
[78] D.S. Prakash, N.D. Raja, Investigation of tensile strength, hardness and wear of titanium diboride reinforced AA6061 composite, Materials Today: Proceedings (2021).
[79] G. Gyawali, S.H. Cho, S.W. Lee, Electrodeposition and characterization of Ni-TiB_2 composite coatings, Metals and Materials International 19(1) (2013) 113-118.
[80] X. Liu, X. Li, A. Yu, W. Huang, Preparation and tribological performance of electrodeposited Ni-TiB_2-Dy_2O_3 composite coatings, Journal of Rare Earths 27(3) (2009) 480-485.
[81] G. Gyawali, K. Tripathi, B. Joshi, S.W. Lee, Mechanical and tribological properties of Ni-W-TiB_2 composite coatings, Journal of Alloys and Compounds 721 (2017) 757-763.
[82] V. Sharma, H.L. Kagdada, P.K. Jha, P. Śpiewak, K.J. Kurzydłowski, Thermal transport properties of boron nitride based materials: A review, Renewable and Sustainable Energy Reviews 120 (2020) 109622.
[83] S. Yu, X. Wang, H. Pang, R. Zhang, W. Song, D. Fu, T. Hayat, X. Wang, Boron nitride-based materials for the removal of pollutants from aqueous solutions: a review, Chemical Engineering Journal 333 (2018) 343-360.
[84] G.R. Bapu, Characteristics of Ni-BN electrocomposites, Plating and surface finishing 82(7) (1995) 70-73.
[85] S. Ranganatha, T. Venkatesha, Fabrication and anticorrosion performance of Ni–P–BN nanocomposite coatings on mild steel, Surface Engineering and Applied Electrochemistry 53(5) (2017) 449-455.
[86] M.K. Tripathi, D. Singh, V. Singh, Electrodeposition of Ni-Fe/BN nano-composite coatings from a non-aqueous bath and their characterization, Int. J. of Electrochemical Science 8 (2013) 3454-3471.
[87] H. Li, Y. He, T. He, D. Qing, F. Luo, Y. Fan, X. Chen, Ni-W/BN(h) electrodeposited nanocomposite coating with functionally graded microstructure, Journal of Alloys and Compounds 704 (2017) 32-43.
[88] L.R. Jordan, A.J. Betts, K.L. Dahm, P.A. Dearnley, G.A. Wright, Corrosion and passivation mechanism of chromium diboride coatings on stainless steel, Corrosion science 47(5) (2005) 1085-1096.
[89] I. Nozdrin, G. Galevskii, M. Terent'eva, V. Rudneva, Features of electrodeposition of "nickel-chromium diboride nanopowder" composite coatings, Russian Journal of Non-Ferrous Metals 54(5) (2013) 383-387.
[90] C. Wu, M. Ma, W. Liu, M. Zhong, H. Zhang, W. Zhang, Effects of rare earth oxide on the nucleation of carbide particles in laser cladded MMCp coating, Pacific International Conference on Applications of Lasers and Optics, Laser Institute of America, 2008, pp. 488-493.
[91] H. Zhuang, Q. Zhang, D. Zhang, Microstructure and Tribological Properties of Ni-Based Laser-Clad Coatings by Rare Earth Modification, Journal of Thermal Spray Technology (2021) 1-22.
[92] J. Wang, R. Xu, Y. Zhang, Study on characteristics of Ni-W-B composites containing CeO_2 nano-particles prepared by pulse electrodeposition, Journal of Rare Earths 30(1) (2012) 43-47.
[93] T. He, Y. He, H. Li, Z. Su, Y. Fan, Z. He, Fabrication of Ni-W-B4C composite coatings and evaluation of its micro-hardness and corrosion resistance properties, Ceramics International 44(8) (2018) 9188-9193.
[94] L. Xiaozhen, L. Yifan, S. Lingling, S. Xiaowen, Preparation and performance of electrodeposited Ni-TiB_2-Sm_2O_3 composite coatings, Journal of Rare Earths 28 (2010) 97-101.
[95] R. Shakoor, R. Kahraman, U.S. Waware, Y. Wang, W. Gao, Synthesis and properties of electrodeposited Ni–B–CeO_2 composite coatings, Materials & Design 59 (2014) 421-429.
[96] Y. Wang, S.-J. Wang, X. Shu, W. Gao, W. Lu, B. Yan, Preparation and property of sol-enhanced Ni–B–TiO_2 nano-composite coatings, Journal of Alloys and Compounds 617 (2014) 472-478.
[97] S.-J. Wang, Y. Wang, X. Shu, S. Tay, W. Gao, R.A. Shakoor, R. Kahraman, Preparation and property of duplex Ni–B–TiO_2/Ni nano-composite coatings, International Journal of Modern Physics B 29(10n11) (2015) 1540022.
[98] Shakoor, R., et al., Properties of electrodeposited Ni–B–Al2O3 composite coatings. Materials & Design, 2014. 64: p. 127-135.
[99] D. Zhang, X. Cui, G. Jin, Z. Cai, M. Dong, Thermal stability of Ni-B/La_2O_3 coatings by electro-brush plating technique, Surface and Coatings Technology 349 (2018) 1042-1047.
[100] U.S. Waware, A. Hamouda, A.K. Pradhan, Effect of codeposition of mixed nanoparticles (V_2O_5 and ZrO_2) on the structure and properties of Ni-B nanocomposite coating, Journal of Alloys and Compounds 752 (2018) 253-259.
[101] S. Waware, N. Wasekar, Manufacture and properties of Ni–B–Fe_2O_3 composite nano-coatings by electrodeposition, Journal of Material Sciences & Engineering 6(6) (2017).
[102] H. Ogihara, A. Hara, K. Miyamoto, N.K. Shrestha, T. Kaneda, S. Ito, T. Saji, Synthesis of super hard Ni–B/diamond composite coatings by wet processes, Chemical communications 46(3) (2010) 442-444.
[103] R.A. Shakoor, U.S. Waware, K. Ali, R. Kahraman, A. Popelka, M.M. Yusuf, A. Hasan, Novel Electrodeposited Ni-B/Y_2O_3 Composite Coatings with Improved Properties, Coatings 7(10) (2017) 161.
[104] B. Li, W. Zhang, T. Mei, Y. Miao, Fabrication of Ni–B/TiC–Y_2O_3 nanocomposites by one-step electrodeposition at different duty cycle and evaluation of structural, surface and performance as protective coating, Journal of Alloys and Compounds 823 (2020) 153888.

Available online at www.jourcc.com

Journal homepage: www.JOURCC.com

Journal of Composites and Compounds

Application of nanocellulose composites in the environmental engineering as a catalyst, flocculants, and energy storages: a review

Mario Pagliaro [a], Rosaria Ciriminna [a], Mohammad Yusuf [b], Sara Eskandarinezhad [c], Irshad Ahmad Wani [d], Mina Ghahremani [e], Zahra Rezaei Nezhad [f]*

[a] *Istituto per lo Studio dei Materiali Nanostrutturati, CNR, via U. La Malfa 153, 90146 Palermo, Italy*
[b] *Department of Chemical Engineering, Universiti Teknologi PETRONAS, Bandar Seri Iskandar, 32610, Malaysia*
[c] *Department of Mining and Metallurgy, Yazd University, Yazd, Iran*
[d] *Postgraduate Department of Chemistry, Govt. Degree College Bhadarwah, University of Jammu, Jammu and Kashmir, India, 182222*
[e] *Faculty of Chemistry, Institute for Advanced Studies in Basic Sciences (IASBS), Gava Zang, PO Box 45195-1159, Zanjan, Iran*
[f] *Department of Physical Chemistry, Faculty of Chemistry, Shahid Beheshti University, Tehran, Iran*

ABSTRACT

Nanocellulose, the most promising bionanomaterial, is obtained either from the degradation of natural polymers or by the activity of bacteria and microorganisms. These biomaterials present various advantages, including full recyclability, biodegradability, and lack of harmful effects on the human body and environment. Furthermore, nanocelluloses are candidates to fabricate thin transparent layers, fibers, hydrogels, and aerogels due to their remarkable optical, thermal, and mechanical behaviors, including high crystallinity, Young's modulus, and porosity content. These exceptional properties present the superb potential of these materials for the device of environmentally engineered tenable products. This paper presents an outline of the contemporary nanocellulose research works as well as details and information on the nanocellulose materials, especially the synthesis process of composites, along with the areas in which these materials can be utilized, such as energy, flocculant, pollution sensors, and catalysts, to respond to the rising requests of these materials.

Peer review under responsibility of jourcc

ARTICLE INFORMATION

Article history:
Received 31 May 2021
Received in revised form 9 June 2021
Accepted 28 June 2021

Keywords:
Nanocellulose
Composite
Energy
Flocculant
Pollution sensors
catalysts

Table of contents

1. Introduction 114
2. Nanocellulose 115
2.1. Cellulose nanofibers (CNF) 116
2.2. Cellulose nanocrystals (CNC) 117
2.3. Bacterial cellulose (BC) 117
3. Synthesis of nanocellulose composites 117
3.1. Nanocellulose−Nanocarbon Composites 118
3.2. Nanocellulose−Organic Polymer Matrixes 119
3.3. Nanocellulose−Inorganic Nanoparticle Composites 119
4. Application of nanocellulose composites in the environmental engineering 119
4.1. Application of nanocellulose composite in the catalysts 119
4.2. Application of nanocellulose composite in the pollutant sensors 120
4.3. Application of nanocellulose composite in the flocculant 121
4.4. Application of nanocellulose composite in the energy fields 122
5. Conclusions and future insights 123

1. Introduction

In a report named "Global Nanocellulose Fiber Market Report" published by Research Insights in 2020, it has been anticipated that the price of nanocellulose on the market will have reached $2.712 billion by 2025, with an expansion rate of 18.80% per year through 2018 and 2025 [1]. Nevertheless, achieving this significant economic rise of nanocellulose

* *Corresponding author: Sara Eskandarinezhad; E-mail: s.eskandari.nezhad@gmail.com*
https://doi.org/10.52547/jcc.3.2.5

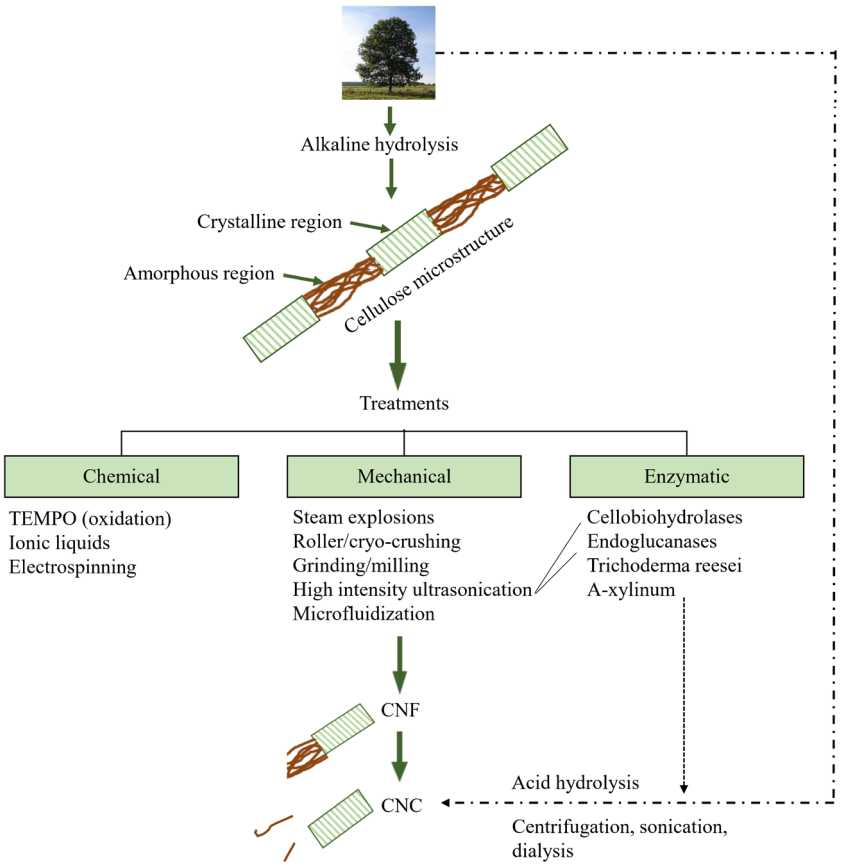

Fig. 1. The schematic of the CNFs from wood fibers using chemical and mechanical approaches.

materials largely depends on the production (e.g., the evolution of techniques, considering environmental matters), commerce and advertising (e.g., public approval, market penetration, cot managing), and human health matters, for example when applied in nutriment and biomedical industries) [2, 3]. At this time, only a handful number of companies have effectively taken nanocellulose materials and their valuable derivatives on the market. Nanocellulose materials are applied in several areas of our life due to their superior optical, mechanical, and thermal behaviors and characteristics. Despite that, to produce these materials on a commercial scale, their technical issues and high costs are still a challenge needing to be tackled. Regarding power supply and environmental aspects, nanocellulose is a source of recoverable energy, which is plentiful in terms of source variation and availability in nature. The advent of nanocellulose-based materials can save energy, solve environmental issues, and foster economic advances [4, 5].

During the past years, nanocellulose has exhibited convenient performance in a variety of applications such as paper production [6], the treatment of water [7]; and sewage [8], biomedicine technology [9, 10], and energy extraction [11]. Ranby et al. [12]; and Turbak et al. [13], first mentioned different types of nanocellulose in their articles to discuss scientific theoretical concepts and report new cellulose products, namely cellulose microfibril (CMF), cellulose nanocrystal (CNC), and micro fibrillated cellulose (MFC). Decades after that, active companies are currently producing nanocellulose with a range of size distribution and structures of nanoparticles [14].

The major content of the usual paper is cellulose, which has much larger diameters than nanocellulose (normally <10 nm) that presents unique properties, including great mechanical strength, high surface area, and limited scattering of the visible light. Both the decomposition of the cellulose pulp of plants and bacterial activity have been used to extract nanocellulose. These materials are employed for fabricating thin translucent layers, fibers, hydrogels, and aerogels, exhibiting superior optical, thermal, and mechanical behaviors. These substrates act as an appropriate matrix or conveyor for inorganic nanoparticles, which results in the production of nanocomposites. Additionally, cellulose-based nanocomposites are easily attained through the direct combination of highly hydrophilic or hydrophobic nanocellulose derivatives with organic and inorganic substances. In principle, the abovementioned properties coupled to full biodegradability, recyclability, and lack of toxicity make these composites appropriate for application in a vast array of industrial fields [15, 16].

From the viewpoint of an environmentalist, nanocomposites based on nanocellulose, are promising materials for applications such as filtration of potable water [17], catalytic decomposition of organic-based contaminants [18, 19], spilled oil absorbents of water [20], and observing aquatic pathogens, and organic-based pollutants [21], and advanced energy conversion appliances [22]. In this review, the research scope focuses on the nanocellulose, chiefly nanocellulose-based nanocomposite, their synthesis procedures and their application in environmental-related science and engineering. In addition, the increasing and broadening demands to these materials and perhaps guide environmentalists and engineers interested in identifying new materials for handling current environmental issues is discussed in this review.

2. Nanocellulose

As nanotechnology has developed, nanocellulose-based materials have increasingly attracted the attention of scientists and scholars. Nanocellulose is a term used to explain nanomaterials based on cellulose with a minimum of one dimension, length, width, or breadth on the nanometric scale [23]. Nanocellulose is identical to the smallest constitutional component of the cellulose-based biomass of different organisms [24,

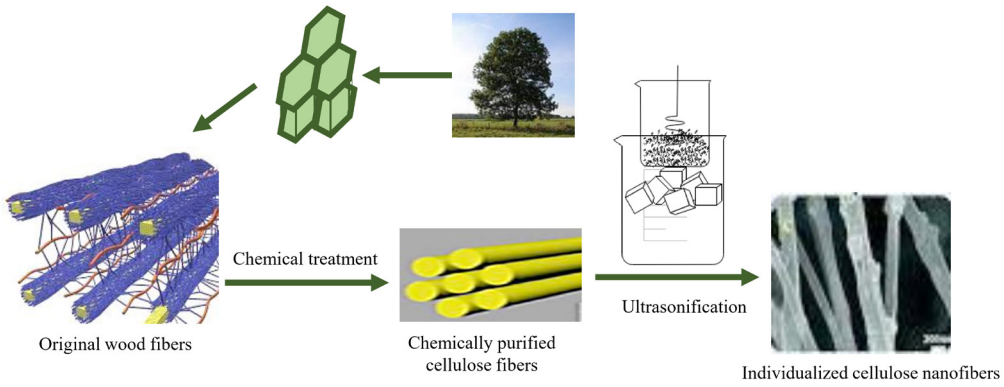

Fig. 2. Conventional methods used for obtaining CNC particles.

25]. The structure of nanocellulose is rod-shaped and rigid, with rod dimensions varying from 1 to 100 nm and 10 to 100 nm in diameter and length, respectively. Due to the abundance and bio-based nature of these materials, they are obtainable from several natural sources such as marine invertebrate animals, plant biomass, and algae. In addition, nanocellulose can be fabricated using some *Acetobacter* types of cellulose bacterial by the bio-based synthesis method [26]. The chemistry of nanocellulose is made up of a biopolymer in which d-glucoanhydropyranose units are repeated and linked by an ester bond (β1→4) [27].

Similar to cellulose, nanocellulose presents an intrinsic chemical structure with ample hydroxyl groups and a specific quantity of aldehyde together with carboxyl groups to provide superior performance. Nanocellulose exhibits considerable properties, such as large surface area, active functional groups, high mechanical strength, and high crystallinity, due to its nanostructure, providing a large variety of applications in different fields [5, 28].

Conventionally, nanocellulose is obtained by two top-down and bottom-up technique, and the former involves mechanical, chemical, and enzymatic treatment of lignocellulosic fibers. For instance, agricultural biomass, including cotton fibers, ramie, hemp, and wood using a highly intensified ultrasonication approach into their respective fundamental nanofibrils with diameters inferior to 6 nm [29, 30]. Brown (1886) [31]; stated that a bottom-up method using fermentation of low molecular weight sugars and the *Acetobacter* types of bacterial cellulose could be employed to synthesize the fibers of nanocellulose or microbial cellulose.

These techniques, either used individually or successively, could obtain the desired structure and morphology [32]. The nanocellulosic materials are classified into three main subcategories based on their isolation methods. These categories include (1) cellulose nanocrystals (CNCs), also known as nanocrystalline celluloses (NCCs), nanocellulose whiskers (CNWs), and rod-like cellulose microcrystals, normally prepared from lignocellulosic materials and acid hydrolysis for removing non-crystalline cellulose from the cellulose nanocrystals with a rod structure (2). Nanofibers of cellulose (CNFs/NFCs), also named microfibrillated cellulose (MFC), nanofibrils, and microfibrils, are produced through mechanical methods or accompanied by enzymatic and chemical pretreatment methods for defibrillation of cellulose fibers. (3) Bacterial cellulose (BC), also known as bacterial nanocellulose (BNC), microbial cellulose, and biocellulose are commonly synthesized from various types of the Acetobacteraceae (Fig. 1) [33, 34].

Similar to other nanoparticles, such as carbon nanotubes (CNTs), nano-clay, and carbon black, various techniques have been used to characterize nanocellulose and its suspensions to study its surface chemistry, thermal stability, storage modulus, fiber length and width, fiber aspect ratio, complex viscosity, viscosity, aggregation degree, and crystallinity before its applications in different areas. The most commonplace methods widely applied for the investigation and characterization of the behavior and characteristics of synthesized nanocellulose are X-ray photoelectron spectroscopy, differential scanning calorimetry, dynamic light scattering, dynamic mechanical analysis (DMA), zeta potential, scanning transmission electron microscopy (STEM), atomic force microscopy (AFM), X-ray powder diffraction (XRD), Fourier transforms infrared spectroscopy (FTIR), transmission electron microscopy (TEM), scanning electron microscopy (SEM), and thermogravimetric analysis (TGA) [35, 36].

2.1. Cellulose nanofibers (CNF)

Cellulose nanofiber (CNF), also called nanofibrous cellulose, nanofibrillar cellulose, and nanofibrillated cellulose (NFC), is characterized by its distinctive structure made up of a bundle of stretched cellulose chain molecules with cellulose nanofibrils together with repeating crystalline and amorphous regions [37-39]. NFC is composed of a mass of stretched nanofibers of cellulose. The cellulose chains possess a large surface area and are twisted and flexible. NFCs are different from CNCs in that they are composed of many amorphous domains and soft, long chains with widths and lengths often to a few hundred nanometers and several micrometers, respectively [40, 41]. Before converting the fibers to CNF, a vigorous mechanical disintegration should be exerted to the cell wall of the plant because of the sophisticated cellulose fiber structure. The fiber diameter is generally from 10 to 100 nm, dependent on the disintegration force [37, 38].

Various researches have focused on the CNF extraction from cellulose-based sources, including rice straw, oil palm biomass, flax, wood pulp, bamboo, cotton, hemp, and kenaf [42, 43]. The most important approaches for deriving CNFs from cellulose fibers are mechanical treatment such as milling, grinding, homogenization, chemical treatment, such as TEMPO oxidation, and a combined process of both chemical and mechanical treatments [44, 45]. Mechanical treatments are primarily used among all the treatment procedures. Figure 1 shows the cellulose nanofibers from wood fibers using chemical and mechanical approaches. In general, nanofibrillated cellulose defibrillation requires intense mechanical treatment processes such as grinding, microfluidization, cryo crushing, high-pressure homogenization, high-intensity ultrasonication, and a combination of two or three treatment processes [27, 42].

Unlike biological methods, including enzymatic treatments, chemical treatment is based on alkali treatments [46, 47]. Many researchers have applied the integration of these approaches to achieve the desired product. Similar to CNCs, the basic properties of NFCs change according to the source of raw material and the utilized extraction process. Employing a variety of treatment approaches results in significant variations of the shape, fibrillation degree, morphology, and properties of NFCs. A study performed by Desmaisons et al. has evolved an index of quality based on eight alternative criteria for measuring different reported NFCs

[48, 49].

2.2. Cellulose nanocrystals (CNC)

CNCs, also recognized as nanowhiskers, have a prolonged crystalline rod-like shape with superior rigidity to NFC due to greater removal of the amorphous domains. The typical crystallinity degree for a CNC varies from 54 to 88% [50, 51]. The source of CNC extraction is widespread, which includes garlic peel and cloves, *Posidonia oceanica*, wheat straw, coconut husk fibers, soy hulls, mulberry bark, banana rachis, pineapple leaf, grape skin, bagasse, rice straw, and sugarcane bagasse [52]. Various methods are employed for extracting relatively pure CNCs from the cell wall [23, 53]. Other methods such as high-intensity ultrasonication of microcrystalline celluloses (MCCs), microwave-assisted hydrolysis, acid hydrolysis, steam explosion, chemical pulping, and mechanical pulping (of wood) are also used to produce CNCs [54, 55]. Sulfuric acid hydrolysis or heat-controlled approaches present extraction processes, which are widely used for producing CNC [56, 57]. The intensive acid hydrolysis of cellulose fibers occurs through handling acid concentration, time, agitation, and temperature. This method results in the selective hydrolysis of non-crystalline cellulose domains and provides the CNCs with high crystallinity [27, 44]. Figure 2 shows conventional methods used for obtaining cellulose nanocrystal particles.

Along with acid hydrolysis, enzymatic hydrolysis and high-intensity sonication are alternative promising environmentally-friendly methods used to produce CNCs, which have gained much attention through the recent decades. As the high-intensity sonication takes away both the crystalline and amorphous regions of cellulose, this method is nonselective and results in the extraction of CNCs with lower crystallinity [58, 59]. It has also been declared that successive alkaline solution treatments at altered concentrations accompanied with mechanical treatments lead to the release of a significant quantity of nanocellulose with diameters ranging between 5 and 20 nm [60, 61]. Scientific reports also introduce other promising mechanical extraction processes, including waring blending, microfluidizer, grinding, and high-pressure homogenization [27, 62].

The properties of the extracted CNCs, such as the crystallinity degree, morphology, aspect ratio, and dimensional dispersity, are dependent on the conditions of reaction and the source of cellulose used [63]. It is known that the production of CNCs by sulfuric acid provides improved thermal stability, which is linked to the sulfate attachment on the surface of CNCs [64, 65]. Nevertheless, sulfuric acid utilization presents some disadvantages, including corrosion due to economic acid recovery, the presence of sulfate groups, and the dumping of a considerable quantity of salt obtained from the neutralization process of acid [66]. CNCs demonstrate various extraordinary properties, including superior strength, large surface area, high-magnetic response, and excellent crystallinity index [67].

The dimensions of CNC rods, also called whiskers, vary between 3 and 50 nm and 50 and 500 nm in width and length, respectively. CNCs present high elastic modulus (20−50 GPa) [68], high axial stiffness (105−168 GPa) [69], excellent tensile strength (~9 GPa) [70], superior thermal stability (~260 °C) [71], large aspect ratio (~10−70) [72], limited thermal expansion coefficient (~0.1 ppm/K) [73], low density (1.5−1.6 g/ cm3) [74], lyotropic liquid crystalline behavior, and shear-thinning property [49, 75, 76].

Combining CNCs with other synthetic or natural polymers results in the emergence of functional composites. Bilodeau [77] and Kalia [78] have discussed various methods to produce CNC composites. Moreover, surface modification methods can change the self-assembly behavior of CNCs in suspensions and control their interfacial characteristics in composites. CNCs provide composites with improved mechanical behavior, decreased density, and increased surface area.

2.3. Bacterial cellulose (BC)

Bacterial cellulose nano-fibers (BCNFs) have a three-dimensional (3D) network of nanofibers and are derived from aerobic bacteria acting as an extracellular polysaccharide membrane by a bottom-up method [79, 80]. Bacterial cellulose (BC) presents a similar molecular formula to that of plants; however, it has a distinctive 3D micro-and nano-porous structure, which gives it excellent purity, increased polymerization degree, appropriate crystallinity (70–80%), great water content (90%), and proper thermal and mechanical stability [81, 82]. Nevertheless, BC costs significantly due to the utilization of expensive carbon sources and is not favorable in economic production [82, 83].

The lack of specific functional groups, aside from alcohol, and polymers, including pectin, lignin, and hemicellulose in BC, is the major distinction between BC and plant-derived CNFs [84]. Thus, BC is superior to other types of CNFs due to its good purity in the form of CNF, high crystallinity of about 80-90%, and great water-absorbing capacity [38, 85]. Bacterial nanocellulose (BNC) is made using cultivating bacteria in a water-based culture media, including nitrogen sources, carbon, phosphate, and glucose for a few days. Altering cultivation conditions, such as nutrient source, the ratio of oxygen, the type of bacterial strain, cultivation in a bioreactor, and incubation time, can modify the structure and behavior of BNC tubes [86-89]. Recent systematic studies have shown the influence of cultivation conditions on the BNC tubes and their properties [88]. *Gluconacetobacter xylinus CGMCC No. 1186* was covered with fructose or glucose in bioreactors with a silicon tube. Studies have shown that fructose use improves the nanocellulose yield. Moreover, reactor variation results in altering the amount of dissolved oxygen and the structure of the achieved nanocellulose tubes [49].

Gatenholm and Klemm [90] have shown that a usual BC production process typically requires two weeks for cellulose production. Moreover, nanocellulose derived from BC presents superior crystallinity to nanocellulose produced from plants [91]. During several decades, the sources of cellulose production have largely changed. Until now, cellulose derivatives from some common bacterial types, including *Acetobacter xylinum (Gluconacetobacter xylinus or Komagataeibacter medellinensis*) and *Gluconacetobacter medellinensis*, have been studied due to their promising function as adsorbent, catalyst, and membrane [92]. Adsorbents, catalysts, and aerogel membranes based on BCs have been used for removing copper, lead, and dye, as well as the distillation of the membrane [93-95]. Overall, BC production aims to tackle the issues regarding its fermentation procedure, which demands novel low-cost culture mediums to enable BC production during decreased and limited times [38, 96].

Besides having the Youn's modulus of 78 GPa, reports have shown that BNC has an excellent capacity for holding water and a molecular weight of a maximum of 8000 Da [97]. BNCs are promising functional materials in application such as scaffolds and have excellent mechanical, optical, and magnetic properties -for example, the impregnation of in-situ Fe3O4 nanoparticles for processing bacterial nanocellulose with magnetic properties or in the fabrication of ferromagnetic cobalt ferrite nanoparticles [98, 99] because of their inferior apparent density and large surface area [49, 100].

BNC is a suitable candidate for applications, such as implants and tissue engineering scaffolds, due to its simple processing for removing hemicellulose and lignin contaminants [49, 101, 102].

3. Synthesis of nanocellulose composites

The increasing necessity for biomaterials in industrial areas replaces traditional materials based on petrol. Nanocellulose has been combined with various materials ranging from either pure or composite ones [103].

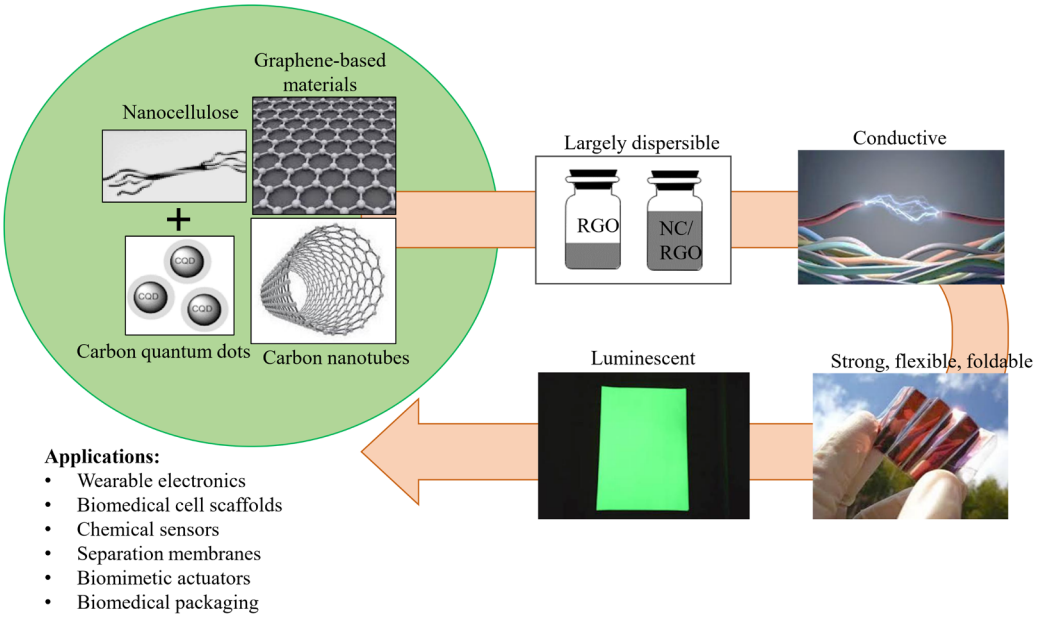

Fig. 3. The composite of nanocarbon and nanocellulose besides a few application areas and properties of these composites.

Nanocellulose provides a forum for implementing various materials on a nanometric scale owing to its large surface area, great porosity content, and excellent mechanical strength. Nanocomposites based on nanocellulose present mixed properties of the nanocellulose structure and the implemented nanomaterial with cooperative behavior [104]. Three main methods are generally used to implement nanomaterials into nanocellulose form, namely 1) adding and forming the implemented nanomaterial directly into a dispersed nanocellulose, 2) using BC membranes to form implemented nanomaterial inside the nanocellulose network, and 3) forming a layer of implemented nanomaterial directly on the surficial area of nanocellolose. Several implemented nanomaterials, including metallic nanoparticles (e.g. Pd, Ag, Au, Ag, Ni, CuO, and TiO_2), as well as mineral-based nanomaterials (montmorillonite, SiO_2, and $CaCO_3$), and carbon-based nanomaterials (e.g. graphene and carbon nanotubes) are used to be implemented in nanocellulose materials. In terms of the utilization areas of the nanocomposites of nanocellulose, their use in environmental-related functions such as energy production, sensors, catalysts, and antibacterial materials are of great importance and consideration [49].

3.1. Nanocellulose−Nanocarbon Composites

Nanocellulose is merged with graphene-based materials, quantum dots of carbon, and nanotubes of carbon nanotubes, all of which are nanocarbons, giving practical characteristics to nanocellulose material (Fig. 3). Therefore, nanocellulose presents appealing characteristics such as biodegradability, biocompatibility, high mechanical strength, and non-toxicity, making them useful for applications in clothing due to being flexible, rigid, smoothly textured, reparability, and high deformation [105]. As a result, the general function of nanocellulose is to sustain nanocarbons, materials with demanding processing because of their high chance of forming aggregates. Composites of nanocellulose and nanocarbon present superior mechanical strength to those of polymer and nanocarbon [106]. Nanocellulose costs are higher than carbon-based nanotubes and graphene-derived materials. Using nanocarbons as dopants in the nanocellulose structure results in a limit of infiltration, which can provide electrical conductivity to the structure for lower prices than the pure nanocarbon. For producing composites of cellulose and nanocarbon, chemical approaches, such as surface modification, have been used to enhance the solubility of cellulose [107]; however, it is also feasible to generate stability for dispersions without the employment of those methods. The advantageous interactions between the nanocellulose and nanocarbon reduce the chance of aggregation for the two materials [49, 108].

Applying the composites of nanocarbon and nanocellulose demands materials with excellent mechanical properties, biocompatibility, and electrical conduction. Separating nanocarbon into graphene-based materials, carbon nanotubes, and carbon quantum dots demonstrates the utilization area of composite materials [109, 110].

Nanotubes of carbon present elevated electrical and thermal conductivities, superb mechanical properties, excellent stability, and great aspect ratios. Adding these nanotubes improves the composites' mechanical strength and provides it with conductivity providing the presence of that an adequate quantity of connections. As cellulose and carbon nanotubes present great connections, they are known as natural companions [111]. The composite of cellulose and carbon nanotube has gained much interest in the areas of conductive papers [112-114] and fibers as well as wearable electronics [115], and aerogel [116], which has been only investigated in one study. Pure carbon nanotubes are likely to envelop cellulose fibers, resulting in the generation of a castable paper pulp presenting homogeneous electrical conductivity if made through a standard paper production process [115]. This composite paper illustrates the intervention of electromagnetics, which presents more efficient protection than circuit boards fabricated by printing metals. In addition, the addition of CNTs into cellulose leads to the enhancement of the stiffness and tensile strength of paper, which consequently creates a flexible and robust product. It is investigated that the ductility improvement owes to possessing long entangled and short components together: the nanocrystals of cellulose act as an inhabitant of the CNT aggregation and protect connections of the wide structure of nanotube [107]. Composites of carbon nanotube and cellulose are utilized as supercapacitor electrodes, biomimetic actuators, and biosensors by providing scaffolds with properties such as self-standing, lightweight, and foldability for titania [117] and polyaniline [49, 118].

Graphene presents special behaviors in terms of electronic carriage and electrocatalytic operations. Composites of cellulose and graphene are greatly porous and possess superb shape maintenance. These composites are used as sensitive and selective sensors of solvents, which

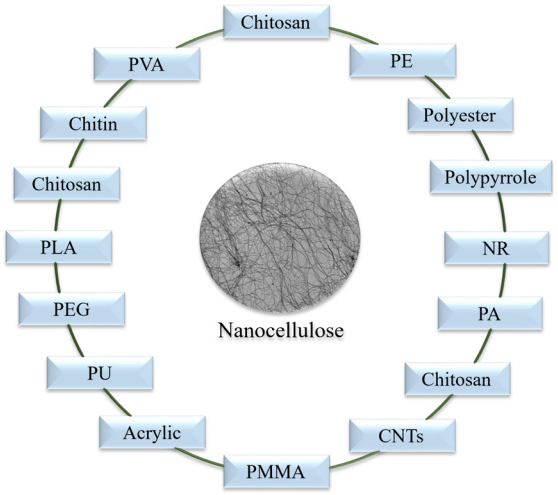

Fig. 4. A diagram of the latest studies on the composites of nanocellulose organic polymer.

operate based on observing capacitance change during adsorption [119]. According to the relative change of capacitance, the absorption of n-hexene, chloroform, toluene, ethanol, and acetone can be identified from each other [49].

3.2. Nanocellulose−Organic Polymer Matrixes

Nanocellulose in the form of fibers is largely used to strengthen polymer composites. Many studies have extensively investigated the function of the interphase layer on mechanical strength. Hydrogen bonding of parallel chains situated between the cellulose and crystalline areas provides the assemblage. Provided that a force efficiently conveys to the tough reinforcing domain, the elasticity modulus of the composite is the same as that of arbitrarily-oriented hard CNC because of the structure and the large surface area of the composites [49, 120].

Composites of nanocellulose and organic polymers have a sophisticated structure of high mechanical strength, intermolecular and intramolecular hydrogen bonds, and the capability of presenting a stiff, tight, and strong structure. Several polymeric matrixes, including epoxy resins [121], polyurethane [122], polystyrene-co-butadiene [123], polyethylene oxide-co-epichlorohydrin [124], polyvinyl acetate [125], and polystyrene-co-butyl acrylate [126], have been strengthened by nanocellulose. These organic composites are fabricated with the aid of a range of approaches, such as impregnation of the solution [127], hot pressing, freeze-drying, [128], and compression molding [129], among which casting is widely employed [130-132]. The latest studies on the composites of nanocellulose organic polymer, besides their application areas, are illustrated in Figure 4.

Two varieties of approaches are generally used for producing cellulose-based composites: (1) the two-stage approach, which involves cellulosic solution achieved through the full dissolution of a cellulose portion that is strengthened by substitutional cellulose, and (2) the one-stage approach through which an incomplete dissolution of cellulose generates a matrix domain sedentary nearby the residual fiber center [49, 133].

The optical, mechanical, and thermal properties can be improved with the implementation of nanocellulose in the polymeric matrix. For instance, Tan et al. [134] recently fabricated a uniform cellulose fiber dispersion in coatings of waterborne acrylic that presented enhanced transparency and characteristics. The coatings made of composite demonstrated the utmost increase of 500% in elastic modulus, doubled hardness, and a decrease in abrasion loss by 35% compared to the properties of the pure coating. To produce high-quality materials, nanocellulose reinforcements have been used with thermoplastic (polyethylene oxide (PEO), polylactic acid (PLA), polyvinyl alcohol (PPA), polypropylene carbonate (PPC), polypropylene (PP), and polyethylene (PE)) and thermoset (polyurethane and epoxy) polymers.

3.3. Nanocellulose−Inorganic Nanoparticle Composites

Owing to the cooperative result of the mixed chemical and physical interactions between the inorganic and organic elements, hybrid organic-inorganic nanomaterials usually present enhanced physicochemical properties such as optical, mechanical, and thermal properties, together with conductivity [120, 134]. Novel materials have been introduced due to incorporating organic strengthening elements such as nanowhiskers and nanofibers of cellulose in a range of composite matrixes [49].

Hybrid composites of nanocellulose and inorganic materials are widely prepared by atomic layer deposition, dispersion of doping casting ionic liquid/cellulose, layer-by-layer deposition, and liquid phase deposition. Hybrid composites of metal nanoparticle and nanocellulose are typically synthesized through reduction by either an extraneous agent, a reduction functional group implemented on the superficial area of nanocellulose, or the inherent reduction of the hydroxyl and aldehyde groups of nanocellulose [109]. In a remarkable study, mixing CNCs and Ag wire exposed to light resulted in the formation of small, catalytic Ag nanoparticles on the surface of CNCs. The light plays a crucial role in dissolving the Ag wire and provides a specific concentration of Ag^+ ions in the solution. Carbon−oxygen double bonds are the products of the hydroxyl group oxidation on the surface of CNC, while the silver is reduced on the exterior areas of CNC. Nanoparticles of ruthenium were fabricated through a mixture of the chemical oxidation and CNC surface, which are extremely challenging to fabricate from usual ruthenium(III) chloride ($RuCl_3$) [135].

4. Application of nanocellulose composites in the environmental engineering

Nanocellulose is a promising material in packing, electronics, optoelectronics, pharmaceutical materials, biomedical applications, nourishment, and cosmetic materials due to its several extraordinary benefits, including excellent water absorption, non-toxicity, maintenance, biocompatibility, and high mechanical strength. More importantly, nanocellulose separated from a range of biomass junks presents cost-effectivity relative to other raw materials. As a result, the advent of valuable produce through nanocellulose derived from biomass junk materials enhances the economic status and protects nature [136-138].

The nanocellulose-based materials prepared through the previously stated approaches possess characteristics such as recyclability, sustainability, and carbon neutrality [102]. As a result, their characteristics turn these materials into environmentally-friendly nanomaterial, which present a favorable function when employed in composites. Combining these materials with inorganic and organic substances results in the production of a composite, which can be extensively employed in optoelectronic, electronic, detection of human motion, packaging, and many other applications [103].

4.1. Application of nanocellulose composite in the catalysts

The use of nanocellulose composites is increasing for treating polluted water through the catalytic activity of organic contaminants [139]. Two types of implemented nanoparticles are applied for catalytic purposes, which are photocatalysts such as titanium dioxide (TiO_2) and precious metals including gold (Au), silver (Ag), and platinum (Pt). Generally, nanocellulose catalysts sustain the catalyst for prohibiting the aggregation of nanoparticles [15].

Combining microfiber carbons (MFCs) and TiO_2 nanoparticles would result in the formation of transparent and stiff thin layers. FTIR

results have presented that TiO_2-NPs and the surface of MFC interact electrostatically with each other. Increasing the amount of TiO_2 lowers both the mechanical strength and the transparency of the nanocomposite [140]. It is suggested that this nanocomposite may be applied for photocatalytic applications to decompose organically-based pollutants; however, this suggestion has not been clearly investigated here. There are some huge proofs regarding this suggestion in articles. To name a few, a study claimed that a nanocellulose-based aerogel was coated with a TiO_2 layer, with a thickness of 7 nm, through a chemical vapor deposition method. The pollutant was modeled with methylene blue, which was effectively decomposed afterward under UV light, suggesting that the material is promising for treating water [141]. Besides, the nanocomposite of TiO_2 and nanocellulose is an excellent photoswitch superabsorbent of water. The cellulose aerogel coated with TiO_2 presents hydrophobic behavior (contact angle of 140° for water). The UV irradiated nanocomposite shows super hydrophilic characteristics, and by keeping it in the dark, the composite becomes hydrophobic again [141]. The MFC aerogel coated with TiO_2 has the potential to be utilized for absorbing spilled oil from water as it has extremely lightweight and hydrophobic behavior, enabling it to suspend on the surface of the water and take in organic solvents up to almost 20-40 times of its weight [20].

Precious metals, including Pd, Pt, Ag, and Au, are widely used for catalytic activities. Nanocomposites of metal nanoparticles and nanocellulose are mainly fabricated through metal salts reduction when presented to nanocellulose. Various chemical materials, including hydroxyl groups of nanocellulose, Na_3citrate, sodium borohydride ($NaBH_4$), and hydrogen (H_2), are employed as reducing agents. In a study, Cirtiu et al. put a suspension of palladium chloride ($PdCl_2$) and NCC into an atmosphere of H_2 with a pressure of 4 bar for 2 h. This caused the Pd^{2+} to reduce to palladium nanoparticles (PdNPs) with a particle size of about 3.6 ± 0.8 nm. Cyclohexanone was formed as a product of phenol transformation through the hydrogenation activity of catalysts on the nanocomposite of PdNP and NCC. The mentioned reaction did not happen by synthesizing Pd nanoparticles without the presence of NCC. The outcomes and products are ascribed to PdNPs aggregation followed by a decrease in responsive surface area when there is a lack of the covering role of NCC [142].

Likewise, the production of dispersed AuNPs was supported using MFCs, which were oxidized by TEMPO. Through the synthesis process, the reduction of MFC surface covered with Au^{3+} occurred using $NaBH_4$ at ambient temperature, resulting in the formation of extremely dispersed AuNPs. The dispersion quality of AuNPs crystals was confirmed with the aid of TEM and selected area electron diffraction (SAED) data, which displayed convenient dispersion of crystals with a homogeneous diameter of 5 nm situated mainly along the fibers. The nanocomposite of AuNP and MFC demonstrates a UV-vis absorption spectrum, which is not as broad as those of the composite of AuNP and cellulose or the solution of AuNP, suggesting that the nanocomposite of AuNP and MFC includes lower aggregated Au nanoparticles. The author hypothesizes that the carboxylate groups of MFC stabilize Au nanoparticles and hinder the aggregation of Au nanoparticles. The nanocomposite of AuNP and MFC demonstrated high catalytic activity in 4-nitrophenol degradation. Nitroaromatic-based materials, undesired organic derivatives of pharmaceuticals, agrochemicals, and dyes, present toxicity [15, 143]. Thus, 4-nitrophenol is utilized mainly as an example for investigating the catalytic function of metal nanoparticles [143-145]. The nanocomposites of AuNP and MFC presented site time yields of more than 840 times higher than those of the traditional composites of AuNP and polymer [145]. An environmentally-friendly approach was introduced by Wu et al. to synthesize the nanocomposites of AuNP and NCC. The synthesis method was carried out at an ambient temperature, during which the sedentary reduction of Au^{3+} using NCC hydroxyl groups resulted in the formation of 30 nm-diameter AuNPs. Data from TEM confirmed the well-distribution of the AuNPs and indicated that the nanoparticles were not grown along the fibers of NCC. The resulted nanocomposites of AuNP and NCC were far more effective, up to 3 times than the AuNPs, without supporting through the degradation of 4-nitrophenol by catalysts because of the improved AuNPs dispersion [144].

Azetsu et al. [146] also studied the catalytic performance of Pd and Au bimetallic nanoparticles through cellulose MFCs, which were oxidized by TEMPO acting as a supporter. Because of the great carboxylate groups' density, which existed in the MFCs with concentrations of 1.0 wt% and 0.96 mmol/g (carboxylic acid (-COOH)), nanoparticles of hybridized Au–Pd, Pd, and Au with catalytic behavior and excellent dispersion were sedentarily produced on the surface of MFCs. The reduction agents of NaBH4 and the anchors of AuNP of carboxylate groups were employed in this method. A variety of NP and MFC nanocomposites have been compared regarding their catalytic activity for reducing 4-nitrophenol to 4-aminophenol. The site time yields of the reaction, including reduction and catalysts, were assessed through the absorbance change at 400 nm. The results demonstrated that the Au nanoparticles with a size of 4 nm, which were deposited on the MFCs, illustratde greater catalytic behavior than a condition in which the nanoparticles are deposited on other types of natural or synthetic polymers.

Nevertheless, greater catalytic activity in 4-nitrophenol reduction is assigned to the hybrid nanocomposite of Au–Pd NP and MFC (ratio of Au: Pd equal to 3:1). Some suggestions state that the improved catalytic performance may arise from the impacts of electronic mediated ligands. These effects of electronic-mediated ligands speed up the reactions of catalysts prompted by electronic interactions occurring between two metal nanoparticles concerning the single nanoparticles of metal.

Copper(II) oxide (CuO) nanoparticles are additionally employed as catalysts besides TiO_2 and precious metal nanoparticles. Through the 4-nitrophenol degradation by CuO-NP/NCC catalysts, the reduction of Cu^{2+} via $NaBH_4$ at room temperature occurred and resulted in the formation of CuO nanoparticles on the surficial area of NCC. The nanocomposites of CuO nanoparticles and NCC nanocomposites presented superior function for the degradation of 4-nitrophenol to CuO nanoparticles, which were supported by graphene or were not supported at all. This is due to the greater surface area of NCC and the immobility of CuO nanoparticles using NCC hydroxyl groups [143]. All the studied literature in this part declare that the deposition of metal nanoparticles on the porous NCC is random and the covering percentage of the surface of nanoparticles on NCC is limited. Therefore, Padalkar et al. suggested applying cetyltrimethylammonium bromide (CTAB) to enhance the covering percentage of the surface metal nanoparticles on NCC. The adsorption of CTAB on the surface of metal nanoparticles, through its cationic quaternary ammonium groups, could present interaction with hydroxyl groups that are high in electron levels as well as anionic groups on the NCC surface. In contrast with the synthesis condition in the absence of CTAB in which the metal nanoparticles formed on the surface of the TEM grid, the synthesis procedure with the use of CTAB resulted in the formation of metal nanoparticles along the fibrils [15].

4.2. Application of nanocellulose composite in the pollutant sensors

Composites of nanocellulose thin layers and phenolic resin have superior average shear strength (~9.6 MPa) to that of non-nanocellulose Cu-Cu joints (~4.7 MPa) [147, 148]. The thin composite layers based on bacterial nanocellulose presented considerably high elasticity modulus (28 GPa) compared with fibrillated kraft pulp composites because of a greater aspect ratio, purity, crystallinity, and homogeneous size [149].

Leal et al. [150] fabricated a composite film made up of cellulose nanocrystals via tapioca starch and glycerin as precursors. The prepared film of the composite showed an appropriate barrier of oxidation and mechanical performance. The penetrability of water vapor was 2.5-folds

lower, and the maximum stress was about twice the starch film with the absence of nanocellulose. The prepared film of composite demonstrated its promising performance in the food packaging industry.

In a study, a supercapacitor was made up of nanocellulose and CNTs with possessing the capacitance of 14.9-16.5 mF and series resistance of 74-155 Ω at a 1.8 cm^2 section. This illustrates far superior capacity for storing energy to the films of CNT films (10mF and 30Ω) with a great power density and extended life duration. The mentioned inexpensive products used as storage can be extensively applied in self-governing intelligence technology [151]. Nanocellulose composites are alternatively used in vehicle, aerospace, electrochemical cells, and sewage treatment industries [152].

Many scientists have evolved biosensors based on the nanocomposites of Au nanoparticles and nanocellulose [153]. In order to recognize chemicals with electrochemical routes, some researchers used the AuNP conductivity and the biocompatibility of BC through incorporating the nanocomposite into an electrode [154-156]. Zhang et al. [155] prepared nanocomposites of Au nanoparticles and BC for hydrogen peroxide (H_2O_2) sensors and glucose. At the first stage, ultrasonication was employed to disperse BC hydrogels in water, followed by the addition of polyethyleneimine (PEI) and $HAuCl_4$. During the next step, the compound was held at 60 °C when the formation of Au nanoparticles occurred on the nanocellulose surface with PEI acting as a linking and reducing agent. The addition of a variety of halides to the mixture changes the golden shell on the surface of nanocellulose. SEM images presented that adding chloride triggered a homogenous and even coating of Au nanoparticles, with a size of 9 nm, on the surface of the BC surface. The addition of bromide provides agglomerates of Au nanoparticles, which are greater in size and superior covering of Au nanoparticles on the surface of BC. Adding iodide provides submicron Au nanoparticles and an inferior covering of Au nanoparticles on the surface of BC. The nanocomposite of Au nanoparticles and BC obtained from this method was coated on a glassy carbon electrode (GCE) followed by being functionalized with myoglobin (MB), hemoglobin (HB), and horseradish peroxidase (HRP). The as-prepared AuNP/BC/MB/GCE, AuNP/BC/HB/GCE, and AuNP/BC/HRP/GCE were shown to present effective performance as sensors for H_2O_2 while AuNP/BC/HRP/GCE demonstrated the most effective function [154, 155]. At the same time, the composite of AuNP/BC/GCE functionalized with the glucoseoxidase (GOx), and HRP highlighted the best application as a sensor for glucose [156].

Au and Ag nanoparticles have been widely investigated by surface-enhanced Raman spectroscopy (SERS) [157-160]. The biosensors prepared based on this approach are employed in studying organic pollutants and aquatic pathogens. For instance, former research performed by our group observed two known aquatic protozoa, *Cryptosporidium parvum*, and *Giardia lamblia,* by a biosensor based on an immunogold. As directly applying the colloids of AuNP and AgNP is usually unsuitable in real-life circumstances, a flexible substrate based on SERS-like paper is suitable. Nanocellulose could be used to prepare films and papers to host nanoparticles activated by SERS. Despite that, the function of the nanocomposites of Au nanoparticles and nanocellulose or Ag nanoparticles and nanocellulose for SERS underlayers have been investigated only in a handful of researches [161, 162]. Marques et al. [162] prepared the nanocomposite of Ag nanoparticles and BC by in situ Ag^+ reductions using Na3citrate on the matrix of BC.

The produced substrate of Ag nanoparticle and BC presents the ability to recognize 2,2′-dithiodipyridine and thiosalicylic acid at concentrations of 10−4 M. The SERS spectra of the L-histidine, L-glutamin, and L-phenylalanine amino acids have been achieved using this substrate. Park et al. [161] also synthesized the nanocomposite of Au nanoparticle and BC to act as an underlayer for the detection of phenylacetic acid (PAA) and 4-fluorobenzenethiol (4-FBT) trace organic chemicals based on SERS. This method benefited from the 3D structure of BC. Deformation of the 3D nanocomposite of Au nanoparticle and BC rises from the drying process generates hot spots along the vertical direction, which causes far more Raman signals than conventional 2D SERS substrates. Au nanoparticles could alternatively be functionalized to obtain other aims than their direct application in the biosensors. Pinto et al. performed the deposition process of the nanoparticles of Au on BC via Au^{3+}–BC complex reduction using Na_3citrate. A uniform SiO_2 coating on the nanoparticles of Au was evolved for specifically separating the nanoparticles of Au. Using this method, the thickness of the SiO_2 shell on the nanoparticles of Au could be altered in the range of 15-100 nm, which has also been noticed in TEM results. The membranes of BC, which were functionalized using the nanoparticles of Au or Au–SiO_2, were fabricated afterward through layer-by-layer (LbL) deposition with the aid of PSS, poly(sodium 4-styrenesulfonate), PDDA, and poly(diallyldimethylammonium chloride). This study proposes that it is likely to curb the optical behavior of the nanocomposites of Au nanoparticles and BC via covering the Au nanoparticles with SiO_2 and by varying the constitution of the layers with the membranes of Au–SiO_2 nanoparticles and BC alongside Au nanoparticles and BC. One of the convenient utilization areas of this nanocomposite is a core-shell biosensor based on paper if long-run chemical and stability are of great importance [163]. Nanocomposites of Au nanoparticles and NCC can be used as a substrate for immobilizing enzymes. At the first step, Au nanoparticles are generated on the surface of NCC by reducing the $HAuCl_4$ using $NaBH_4$. Afterward, thioctic acid (Thc), including –SH and –COOH, bounds to the surface of Au nanoparticles and its carboxylic acid groups activated through N-hydroxysulfosuccinimide (NHS) and 1-ethyl-3-[3-(dimethylamino)propyl]carbodiimide (EDC). Eventually, the amino groups of the enzyme – cyclodextrin glycosyltransferase (CGTase) – make covalent bounds with the activated carboxylic acid groups on the surface of nanocomposites. The capacity of CGTase on the nanocomposites of Au nanoparticles and NCC for making bounds is 165 mgg^{-1} of NCC, and the CGTase presented high biocatalytic performance [164]. The significant amount of enzymes on the surface of this nanocomposite implies that it is useful for producing biosensors based on enzymes [15].

4.3. Application of the nanocellulose composite in the flocculant

Flocculants based on biopolymers including alginate, cellulose, tannins, and chitosan, have gained much attention. These materials are famous for their biodegradability, having a large specific surface area, and possessing nanometric dimensions [165, 166]. Generally, there are two types of natural polymer flocculants [167]. The first type includes natural polymers grafting to produce semi-natural flocculants such as polyacrylamide-grafted hydroxypropyl methylcellulose [168]. The second type is obtained via direct modification of natural polymers to produce enhanced natural flocculants, including dicarboxylic acid nanocellulose [169]. Studies regarding the utilization of nanocellulose chemicals for water are not enough as scientists' major consideration is on metal adsorption from thinned watery solution or photocatalysis as mentioned previously. One of the challenges regarding the utilization of CNCs as flocculants is agglomeration, which is because of the presence of hydrogen bond networks originating from the –OH groups on the surface of CNCs [170].

Nevertheless, the characteristics of CNC flocculants may alter by changing the –OH groups on the surface, thus, the appropriate quantity of –OH groups on the surface should be recognized for preparing a useful flocculant. Anionic surface groups, including hydroxy groups, are widely observed in nanocelluloses following the pulping process because of the plant cell wall components [171]. As a result, anionic nanocellulose and a range of inorganic minerals are typically negatively charged and weak in interactions. Furthermore, reports have stated that an anionic flocculation agent has inferior solubility in acid-based

solutions, hindering its functional use as a flocculant in the mentioned states [14].

A range of chemical pretreatments, including citric/hydrochloric acid hydrolysis [170], 2,2,6,6-tetramethylpiperidin-1-oxyl-mediated (or TEMPO-mediated) [172], aminoguanidinereacted wood celluloses [173], periodate-chlorite oxidation [171, 173], and carboxymethylation [171], have been employed to increase the density of anionic charge and bestow nanocellulose with cationic charges to extend its application. Nanocellulose adjustment for preparing cationic equivalents is significantly beneficial for removing anionic particles via molecular interactions occurring between different charges that lead to the aggregation of particles in applications such as wastewater treatment [14].

At this time, it is possible to functionalize nanocellulose for creating efficient flocculants through the subjection of hydrophobic, cationic, or anionic functional groups to the surface of nanocellulose by the neutralization of charge. The surface of cellulose, activated by –OH groups, stimulates effective nanocellulose functionalization, adds proper functionality, and provides largely efficient flocculants [174]. Furthermore, presenting functional groups to the cellulose can improve its interaction with various compounds to boost the polarity and hydrophilicity of the surface [14].

Suopajärvi et al. studied a range of functionalized nanocelluloses, including cationic and anionic dialdehyde, which have been used for flocculating wastewater. Their study outcome was hopeful, demonstrating that functionalized nanocellulose could be used as an agent for treating wastewater. Presenting anionic groups (e.g. carboxy) detaches the network of the nanocellulose surface groups through hydrogen bonding, which subsequently enhances the nanocellulose performance as an adsorbent [139]. For example, interval oxidation is used for implementing aldehyde groups by oxidizing surface groups of –OH and varying the carbonic structure of the glucopyranose ring [175]. The mentioned 2,3-dialdehyde cellulose aldehyde groups are facile to be subsequently transformed into different functional groups, such as imines, sulphonates, or carboxylic acids [171]. The application of anionic and cationic dialdehyde celluloses, obtained by aqueous interval oxidation, has been researched by Liimatainen et al. [176, 177] who demonstrated that the nanoparticles of anionic cellulose provided an improved flocculation function of kaolin compared with materials based on cationic dialdehyde cellulose.

Oxidizing nanocellulose using TEMPO in the presence of water with moderate conditions is an additional useful approach for adjusting nanocellulose in chemical ways for generating a significant number of charges. The mentioned approach effectively converts surface hydroxymethyl groups to their related types of carboxylic [172]. Then, a nocellulose aggregation can be hindered by negative charge groups presented on the surface of nanocellulose through repulsive forces. Chen et al. [178] presented NCC materials stabilized by electrostatic forces that could be prepared through a reaction including three steps: the oxidation of periodate, chlorite, and TEMPO. The researchers stated that periodate oxidation degraded cellulose, which could be limited through minimizing the oxidation of periodate and increasing the oxidation of TEMPO [14].

Many researchers have investigated the chemical and physical modification of the nanocellulose structure to enhance its behavior and characteristics. To name a few, Sun et al. [179] studied the influence of CNC application on the flocculation of Gram-negative bacteria (Pseudomonas aeruginosa PAO1). This research presented that the output of the bacteria-depleted flocculation relied on the form of the particles of cellulose colloids. Furthermore, the research demonstrated that particles having the form of a rod, which is normally seen in CNC, could greatly deplete colloids compared with particles with the form of a sphere. Moreover, the competence of the flocculation – flocculation of anionic microalgal cells - of CNCs increased by presenting imidazole and cationic pyridinium functional groups via the grafting method in comparison with that of typical polymer-based flocculants [174, 180]. All in all, many scientists have studied a range of methods for modifying nanocellulose to expand its usage in the industry [14].

4.4. Application of nanocellulose composite in energy fields

Lately, several studies have prepared appliances for storing energy with BNC [181]. Besides these apparatuses, numerous developments have also happened in the environment and technology [182-185]. BNC can be applied for strengthening materials or is being reinforced by additives based on its utilization. Recent studies have tried to fabricate advanced flexible BNC-based materials with no impact on their intrinsic characteristics [186]. Many researchers have investigated cellulose-based materials as a promising alternative. Many investigations have also been performed regarding applying a combination of BNC and CNTs [187]. The studies experimented with the electrochemical efficiency and function of BNC nanocomposite electrodes with their unique 3D porous structure, which makes them a promising material for storing usages [185]. The NFC is a valuable material for several applications, including printed electronics, electronic gadgets, sensors, and smart electronic materials. Its various properties and characteristics include mechanical strength, limited thermal expansion, transparency, inferior surface roughness, and ignorable surface roughness. In addition, NFC has been widely used in nanocomposite fabrication with amylopectin, polyurethane, styrene butyl acrylate, melamine-formaldehyde, and phenolic resin. [188-190]. The underlayers based on NFC are efficient in fabricating electronic gadgets for substituting conventional high-cost glass preparing methods. NFC has more enhanced heat transfer behavior than glass. Moreover, the transparency of NFC arises from its closely packed structure and a minor fiber space inhibits the scatter of light [191].

Nanocomposites of nanocellulose could be used in fabricating Li-ion batteries, solar cells, and fuel cells. Fuel cell function is to produce electricity from chemical energy. Fuel, normally H_2, oxidizes via catalytic activities at the anode while O_2 is reduced catalytically to H_2O at the cathode. Through an employed circuit, the electrons re transferred from the anode to the cathode. BC is a suitable underlayer to gather a considerable quantity of anode catalysts with nanometric size. By immersing the BC membrane in a solution with the ammonium hexachloropalladate concentration of 5 mM, precipitation of Pd nanoparticles forms in the BC membrane.

Nevertheless, immersing plant cellulose in hexachloropalladate solution does not lead to the formation of precipitates. With the aid of tapping mode AFM, it was found that the structure of plant cellulose was weaved closely together with organized fibers; however, the fibers of BC fibers had a tunnel-shaped structure, which was not as dense as the former one. Consequently, it is claimed that reducing groups inside their loose structure are responsible for the precipitation of Pd nanoparticles in BC. In a study, a native membrane of BC was subjected between the layers of the nanocomposites of PdNP and BC to be applied in a fuel cell as a membrane electrode assembly (MEA). The density of Pd in the cathode and anode membranes was 0.4 mg/cm^2 in dry weight conditions, while the MEA thickness was 150 μm. The oxidized H_2 was employed to the PdNP/BC anode, and the greatest current was around 0.26 mA, which presents that this nanocomposite is a promising one in applications for converting energy. The mentioned membrane of PdNP/BC demonstrates more benefits than alternative polyelectrolyte-based membranes because of its limited gas crossing and enhanced thermal stability [192].

Solar cells are used to generate electricity from solar energy. Due to the high mechanical strength, smoothness, and transparency of nanocellulose papers, they can be applied efficiently for producing the substrates of solar cells. Hu et al. [193] devised a solar cell with transparent papers

of nanocellulose using an indium-tin-oxide (ITO)-coated paper of nanocellulose, which was prepared via radio frequency magnetron sputtering with a target made up of 90% of In_2O_3 and 10% of SnO_2. Followed by the coating process, the transparent paper turned translucent. Afterward, the coated paper of nanocellulose underwent treatment by [6:6]-phenyl-C61-butyric acid methyl ester (PCBM), with poly(3-hexylthiophene) (P3HT) acting as a layer for absorbing light. The application of this transparent paper lengthened the light path inside the absorbent layer, which led to more absorption of sunlight. The fabricated solar cell presented an efficiency of 0.4% for power conversion, demonstrating the potential of nanocellulose papers to be applied in photovoltaic devices. Nonetheless, the short-circuit current and total power conversion efficiency (PCE) of the solar cell made from nanocellulose papers are inferior to those of the glassy solar cell due to the ITO sheet resistance on nanopaper, which is about 50–100 times more than that on glass.

Besides solar cells and fuel cells, nanocellulose can alternatively be employed in Li-ion batteries (LIBs), which are rechargeable energy storage appliances, very reputable, and are extensively applied in customer electronic devices. Nanocellulose papers make it possible to fabricate functional and flexible LIBs with a limited thickness. Jabbour et al. have thoroughly reviewed cellulose LIBs [194]. In this study, we discuss LIBs based on nanocellulose and their benefits. Some reports have shown the application of nanocelluloses for electrolyte, separator, and electrode in LIB cells [195-198]. Jabbour et al. prepared a flexible LIB anode based on graphite/MFC by performing vacuum drying on a slurry of graphite/MFC at 313 K for several hours. Besides the anode of graphite/MFC, the cell involved the electrolyte of diethyl carbonate and ethylene carbonate together with LiPF6 and a cathode of Li foil. The anode based on graphite/MFC presented the same charge/discharge capacity as the typical graphite/poly(vinylidene fluoride) (PVDF) plus suitable stability, illustrating that tenable MFCs could substitute the synthesized chemical PVdF to fabricating LIB anodes [199].

Hu et al. [200] also fabricated a nanocellulose paper combined with CNT, coated with Si (Si-nano paper) to be applied as a LIB electrode. Initially, the paper based on CNT/nanocellulose was fabricated through freeze-drying of the uniform mixture of a hydrogel from CNT/nanocellulose. The CNT implementation in the composites provides improved electrical conductivity. In the next step, the plasma-enhanced CVD (PECVD) approach was utilized to deposit a low-thickness Si-based coating on the paper of CNT/nanocellulose. In the final step, the cell was fabricated using Li metal foil, Si-nanopaper, and a Celgard 2250 separator immersed in an electrolyte involving LiPF6 in ethylene carbonate/diethyl carbonate. The fabricated Si-based nano paper presented a persistent capacity equal to 1200 mAh/g after 100 cycles of charge and discharge, which is more than three times higher than the theoretical capacity for a typical graphite-based anode. In addition, the flexible and significantly porous structure of the paper of CNT and nanocellulose, introducing plenty of housing locations for the expansion of the Si layer during lithiation, provides the Si-based nanopaper with enhanced stability.

Leijonmarck et al. [198] incorporated the MFC separator and electrode into a paper to fabricate a LIB cell with suitable flexibility. The desired cell was produced using successive vacuum filtering of the negative electrode suspension, which involved MFCs and graphite together with a separator suspension made up of MFCs and SiO_2 as well as the positive electrode suspension, containing MFCs and $LiFePO_4$ on a filtering paper. The dehydrated cell includes three layers mounted on each other as well as two outer electrodes and one centrally-positioned separator. This flexible paper-based battery possesses high strength and demonstrates appropriate capacity cycles of charge and discharge. The MFCs play a crucial role in bonding the parts and supplying a network with enough strength and flexibility for the LIB cell. Apart from nanocellulose application in separators or electrodes, they could be employed in electrolytes to strengthen and reinforce the device.

5. Conclusions and future insights

This study concisely investigated the late developments in the fabrication of nanomaterials based on nanocellulose and their prospective utilization in environment-related areas. The sources of nanocellulose are vast and inexpensive. The top-down cellulose pulp decomposition leads to the fabrication of highly thin nanofibers possessing diameters of 2–5 nm. These nanocelluloses present unique thermal, mechanical, and optical behaviors. Aerogel, fiber, film, and papers of nanocellulose fabricated through the bottom-up method present enough location to act as a powerful bearer for integrating implemented nanomaterials. The nanocomposites based on nanocellulose present several benefits, such as catalytic and antimicrobial activities, which enable the materials to be used in water treatment. Nanocellulose combined with Au nanoparticles could be a suitable SERS underlayer, provided that the size and loading of Au nanoparticles are improved. In addition, nanocellulose is utilized as a modern substrate for the fabrication of fuel cells, presenting promising usage in energy devices.

Over the following years, approaches for ameliorating the distribution and size of metal and other nanoparticles in nanocellulose underlayers regarding their utilization will gain much attention. Fine and well-dispersed nanoparticles are beneficial for catalyst areas, whereas large and aggregated metal nanoparticles present a better performance in the SERS area. The loading of nanoparticles is additionally pretty paramount in nanocomposites. Investigating the loading limitation and quantity is crucial for various nanoparticles in the matrix of nanocellulose and requires further study. Furthermore, incorporating inorganic material additives in the nanocellulose can change their durability. Consequently, studies have to try to extend the life of nanocomposites or refabricate them in order to turn them into durable materials. Nanocellulose nanocomposites are promising materials as a large number of researchers have searched for finding a low-cost and green material to fight against today's environment-related issues.

Until now, the majority of review studies have concentrated on only a distinctive kind of nanocellulose: aerogel sorbents, adsorbents, or a special kind of treatment for ecological recovery such as water treatment. The present review focuses on introducing an outline of the latest advances and future trends of a range of nanocelluloses applied in various fields of environmental recovery and treatment, such as previous outcomes, contemporary development, and future trends. The latest advances of nanocellulose employed as a membrane, flocculant, photocatalyst, or adsorbent for different utilizations in environment recovery and treatment are discussed thoroughly here.

This review emphasized studies and developments in the fields of NCC, NFC, and BNC. Future probable usage of these materials is varied, ranging from medication and biomedical areas to marketable commercial productions. Choosing the best nanocellulose for a specific application is demanding and vital. In the pharmaceutical and drug delivery fields, BNC is the best candidate. Nevertheless, the NFC is a perfect choice in areas such as rheology qualifiers and additives of composites, which require a larger amount of materials. On the other hand, NCC is ideal to be used in applications including the biomedical field, rheology qualifier of polymer composites, and interface stabilizers. Several studies performed by different researchers and companies have explored the production enhancement and commercial development of nanocellulose.

REFERENCES

[1] M.A. Markets, Nanocellulose Market Worth, 2019, p. 66.
[2] G. Chauve, J. Bras, Industrial point of view of nanocellulose materials and their

possible applications, HANDBOOK OF GREEN MATERIALS: 1 Bionanomaterials: separation processes, characterization and properties, World Scientific2014, pp. 233-252.
[3] K. Heise, E. Kontturi, Y. Allahverdiyeva, T. Tammelin, M.B. Linder, O. Ikkala, Nanocellulose: recent fundamental advances and emerging biological and biomimicking applications, Advanced Materials 33(3) (2021) 2004349.
[4] S. Yu, J. Sun, Y. Shi, Q. Wang, J. Wu, J. Liu, Nanocellulose from various biomass wastes: its preparation and potential usages towards the high value-added products, Environmental Science and Ecotechnology (2020) 100077.
[5] K. Dhali, M. Ghasemlou, F. Daver, P. Cass, B. Adhikari, A review of nanocellulose as a new material towards environmental sustainability, Science of the Total Environment (2021) 145871.
[6] E.C. Lengowski, E.A.B. Júnior, M.M.N. Kumode, M.E. Carneiro, K.G. Satyanarayana, Nanocellulose in the paper making, Sustainable polymer composites and nanocomposites, Springer2019, pp. 1027-1066.
[7] A. Mautner, Nanocellulose water treatment membranes and filters: a review, Polymer International 69(9) (2020) 741-751.
[8] R. Alsahli, Synthesis a new Membrane from the Nano-Cellulose Membrane and Nano-Ceramic Membrane in Bioreactor System into the Microbial Fuel Cell for Sewage Treatment by Algae, (2019).
[9] J. Liu, S. Willför, A. Mihranyan, On importance of impurities, potential leachables and extractables in algal nanocellulose for biomedical use, Carbohydrate Polymers 172 (2017) 11-19.
[10] E. Philip, A. Madhavan, B. AK, S. Raveendran, A. Pugazhendhi, E. Gnansounou, A. Pandey, Promising Eco-Friendly Biomaterials for Future Biomedicine: Cleaner Production and Applications of Nanocellulose, (2021).
[11] J.H. Kim, D. Lee, Y.H. Lee, W. Chen, S.Y. Lee, Nanocellulose for energy storage systems: beyond the limits of synthetic materials, Advanced Materials 31(20) (2019) 1804826.
[12] B. Ra nby, A. Banderet, L.G. Sillén, Aqueous Colloidal Solutions of Cellulose Micelles, Acta Chemica Scandinavica 3 (1949) 649-650.
[13] A.F. Turbak, F.W. Snyder, K.R. Sandberg, Microfibrillated cellulose, a new cellulose product: properties, uses, and commercial potential, J Appl Polym Sci Appl Polym Symp, 1983, pp. 815-827.
[14] K.P.Y. Shak, Y.L. Pang, S.K. Mah, Nanocellulose: Recent advances and its prospects in environmental remediation, Beilstein journal of nanotechnology 9(1) (2018) 2479-2498.
[15] H. Wei, K. Rodriguez, S. Renneckar, P.J. Vikesland, Environmental science and engineering applications of nanocellulose-based nanocomposites, Environmental Science: Nano 1(4) (2014) 302-316.
[16] D.A. Gopakumar, Y.B. Pottathara, K. Sabu, H.A. Khalil, Y. Grohens, S. Thomas, Nanocellulose-based aerogels for industrial applications, Industrial Applications of Nanomaterials, Elsevier2019, pp. 403-421.
[17] P.R. Sharma, S.K. Sharma, T. Lindström, B.S. Hsiao, Nanocellulose-Enabled Membranes for Water Purification: Perspectives, Advanced Sustainable Systems 4(5) (2020) 1900114.
[18] H. Lu, L. Zhang, J. Ma, N. Alam, X. Zhou, Y. Ni, Nano-cellulose/mof derived carbon doped CuO/Fe_3O_4 nanocomposite as high efficient catalyst for organic pollutant remedy, Nanomaterials 9(2) (2019) 277.
[19] E. Kalantari, M.A. Khalilzadeh, D. Zareyee, Effective Reduction of Cr (VI) and Organic Dyes Using Pd NPs/Fe_3O_4@ nanocellulose as a Recoverable Catalyst in Aqueous Media, Journal of Inorganic and Organometallic Polymers and Materials 31(1) (2021) 319-330.
[20] J.T. Korhonen, M. Kettunen, R.H. Ras, O. Ikkala, Hydrophobic nanocellulose aerogels as floating, sustainable, reusable, and recyclable oil absorbents, ACS applied materials & interfaces 3(6) (2011) 1813-1816.
[21] Z. Ma, P. Zhou, L. Zhang, Y. Zhong, X. Sui, B. Wang, Y. Ma, X. Feng, H. Xu, Z. Mao, A recyclable 3D gC_3N_4 based nanocellulose aerogel composite for photodegradation of organic pollutants, Cellulose 28(6) (2021) 3531-3547.
[22] R. Guo, L. Zhang, Y. Lu, X. Zhang, D. Yang, Research progress of nanocellulose for electrochemical energy storage: A review, Journal of Energy Chemistry (2020).
[23] D. Klemm, F. Kramer, S. Moritz, T. Lindström, M. Ankerfors, D. Gray, A. Dorris, Nanocelluloses: A New Family of Nature-Based Materials, Angewandte Chemie International Edition 50(24) (2011) 5438-5466.
[24] A.K. Bharimalla, S.P. Deshmukh, P.G. Patil, N. Vigneshwaran, Energy efficient manufacturing of nanocellulose by chemo-and bio-mechanical processes: a review, World Journal of Nano Science and Engineering 5(04) (2015) 204.
[25] S. Ahankari, P. Paliwal, A. Subhedar, H. Kargarzadeh, Recent Developments in Nanocellulose-Based Aerogels in Thermal Applications: A Review, ACS nano 15(3) (2021) 3849-3874.
[26] K.-Y. Lee, Y. Aitomäki, L.A. Berglund, K. Oksman, A. Bismarck, On the use of nanocellulose as reinforcement in polymer matrix composites, Composites Science and Technology 105 (2014) 15-27.
[27] N. Saba, M. Jawaid, 4 - Recent advances in nanocellulose-based polymer nanocomposites, in: M. Jawaid, S. Boufi, A.K. H.P.S (Eds.), Cellulose-Reinforced Nanofibre Composites, Woodhead Publishing2017, pp. 89-112.
[28] Y. Chu, Y. Sun, W. Wu, H. Xiao, Dispersion Properties of Nanocellulose: A Review, Carbohydrate Polymers (2020) 116892.
[29] C. Castro, R. Zuluaga, J.-L. Putaux, G. Caro, I. Mondragon, P. Gañán, Structural characterization of bacterial cellulose produced by Gluconacetobacter swingsii sp. from Colombian agroindustrial wastes, Carbohydrate Polymers 84(1) (2011) 96-102.
[30] K. De France, Z. Zeng, T. Wu, G. Nyström, Functional materials from nanocellulose: utilizing structure–property relationships in bottom-up fabrication, Advanced Materials (2020) 2000657.
[31] A.J. Brown, XIX.—The chemical action of pure cultivations of bacterium aceti, Journal of the Chemical Society, Transactions 49 (1886) 172-187.
[32] M.M. Ibrahim, T.Y. Fahmy, E.I. Salaheldin, F. Mobarak, M.A. Youssef, M.R. Mabrook, Synthesis of tosylated and trimethylsilylated methyl cellulose as pH-sensitive carrier matrix, Life Science Journal 1(12) (2015) 29-37.
[33] N. Lin, A. Dufresne, Nanocellulose in biomedicine: Current status and future prospect, European Polymer Journal 59 (2014) 302-325.
[34] S. Yu, J. Sun, Y. Shi, Q. Wang, J. Wu, J. Liu, Nanocellulose from various biomass wastes: Its preparation and potential usages towards the high value-added products, Environmental Science and Ecotechnology 5 (2021) 100077.
[35] K. Rajan, A. Djioleu, G. Kandhola, N. Labbé, J. Sakon, D.J. Carrier, J.-W. Kim, Investigating the effects of hemicellulose pre-extraction on the production and characterization of loblolly pine nanocellulose, Cellulose (2020) 1-14.
[36] B. Karl, Y. Alkhatib, U. Beekmann, T. Bellmann, G. Blume, F. Steiniger, J. Thamm, O. Werz, D. Kralisch, D. Fischer, Development and characterization of bacterial nanocellulose loaded with Boswellia serrata extract containing nanoemulsions as natural dressing for skin diseases, International Journal of Pharmaceutics 587 (2020) 119635.
[37] H. Kargarzadeh, M. Ioelovich, I. Ahmad, S. Thomas, A. Dufresne, Methods for Extraction of Nanocellulose from Various Sources, Handbook of Nanocellulose and Cellulose Nanocomposites2017, pp. 1-49.
[38] K.P.Y. Shak, Y.L. Pang, S.K. Mah, Nanocellulose: Recent advances and its prospects in environmental remediation, Beilstein Journal of Nanotechnology 9 (2018) 2479-2498.
[39] K.J. Nagarajan, N.R. Ramanujam, M.R. Sanjay, S. Siengchin, B. Surya Rajan, K. Sathick Basha, P. Madhu, G.R. Raghav, A comprehensive review on cellulose nanocrystals and cellulose nanofibers: Pretreatment, preparation, and characterization, Polymer Composites 42(4) (2021) 1588-1630.
[40] M.H. Hussin, D. Trache, C.T.H. Chuin, M.N. Fazita, M.M. Haafiz, M.S. Hossain, Extraction of cellulose nanofibers and their eco-friendly polymer composites, Sustainable polymer composites and nanocomposites, Springer2019, pp. 653-691.
[41] T. Willhammar, K. Daicho, D.N. Johnstone, K. Kobayashi, Y. Liu, P.A. Midgley, L. Bergström, T. Saito, Local crystallinity in twisted cellulose nanofibers, ACS nano 15(2) (2021) 2730-2737.
[42] D. Li, 8 Public-private partnership in the development of social entrepreneurship in mainland China, Social Entrepreneurship in the Greater China Region: Policy and Cases (2016) 126.
[43] J. Pennells, I.D. Godwin, N. Amiralian, D.J. Martin, Trends in the production of cellulose nanofibers from non-wood sources, Cellulose 27(2) (2020) 575-593.
[44] T. Abitbol, A. Rivkin, Y. Cao, Y. Nevo, E. Abraham, T. Ben-Shalom, S. Lapidot, O. Shoseyov, Nanocellulose, a tiny fiber with huge applications, Current Opinion in Biotechnology 39 (2016) 76-88.
[45] Y. Habibi, H. Chanzy, M.R. Vignon, TEMPO-mediated surface oxidation of cellulose whiskers, Cellulose 13(6) (2006) 679-687.
[46] S. Janardhnan, M.M. Sain, Isolation of cellulose microfibrils–an enzymatic approach, Bioresources 1(2) (2006) 176-188.
[47] G. Tonoli, E. Teixeira, A. Corrêa, J. Marconcini, L. Caixeta, M. Pereira-da-Silva, L. Mattoso, Cellulose micro/nanofibres from Eucalyptus kraft pulp: preparation and properties, Carbohydrate polymers 89(1) (2012) 80-88.
[48] J. Desmaisons, E. Boutonnet, M. Rueff, A. Dufresne, J. Bras, A new quality index for benchmarking of different cellulose nanofibrils, Carbohydrate polymers 174 (2017) 318-329.
[49] B. Thomas, M.C. Raj, A.K. B, R.M. H, J. Joy, A. Moores, G.L. Drisko, C. Sanchez, Nanocellulose, a Versatile Green Platform: From Biosources to Materials and Their Applications, Chemical Reviews 118(24) (2018) 11575-11625.
[50] M. Roman, Toxicity of cellulose nanocrystals: a review, Industrial Biotechnology 11(1) (2015) 25-33.
[51] L. Douard, J. Bras, T. Encinas, M. Belgacem, Natural acidic deep eutectic

solvent to obtain cellulose nanocrystals using the design of experience approach, Carbohydrate Polymers 252 (2021) 117136.
[52] F. Kallel, F. Bettaieb, R. Khiari, A. García, J. Bras, S.E. Chaabouni, Isolation and structural characterization of cellulose nanocrystals extracted from garlic straw residues, Industrial Crops and Products 87 (2016) 287-296.
[53] S. Lu, T. Ma, X. Hu, J. Zhao, X. Liao, Y. Song, X. Hu, Facile extraction and characterization of cellulose nanocrystals from agricultural waste sugarcane straw, Journal of the Science of Food and Agriculture (2021).
[54] M. Kunaver, A. Anžlovar, E. Žagar, The fast and effective isolation of nanocellulose from selected cellulosic feedstocks, Carbohydrate Polymers 148 (2016) 251-258.
[55] T. Kos, A. Anžlovar, M. Kunaver, M. Huskić, E. Žagar, Fast preparation of nanocrystalline cellulose by microwave-assisted hydrolysis, Cellulose 21(4) (2014) 2579-2585.
[56] R. Xiong, X. Zhang, D. Tian, Z. Zhou, C. Lu, Comparing microcrystalline with spherical nanocrystalline cellulose from waste cotton fabrics, Cellulose 19(4) (2012) 1189-1198.
[57] W. Bai, J. Holbery, K. Li, A technique for production of nanocrystalline cellulose with a narrow size distribution, Cellulose 16(3) (2009) 455-465.
[58] Y. Tang, X. Shen, J. Zhang, D. Guo, F. Kong, N. Zhang, Extraction of cellulose nano-crystals from old corrugated container fiber using phosphoric acid and enzymatic hydrolysis followed by sonication, Carbohydrate Polymers 125 (2015) 360-366.
[59] N. Pandi, S.H. Sonawane, K.A. Kishore, Synthesis of cellulose nanocrystals (CNCs) from cotton using ultrasound-assisted acid hydrolysis, Ultrasonics sonochemistry 70 (2021) 105353.
[60] K. Abe, S. Iwamoto, H. Yano, Obtaining Cellulose Nanofibers with a Uniform Width of 15 nm from Wood, Biomacromolecules 8(10) (2007) 3276-3278.
[61] P. Liu, B. Pang, S. Dechert, X.C. Zhang, L.B. Andreas, S. Fischer, F. Meyer, K. Zhang, Structure Selectivity of Alkaline Periodate Oxidation on Lignocellulose for Facile Isolation of Cellulose Nanocrystals, Angewandte Chemie 132(8) (2020) 3244-3251.
[62] A. Serpa, J. Velásquez-Cock, P. Gañán, C. Castro, L. Vélez, R. Zuluaga, Vegetable nanocellulose in food science: A review, Food Hydrocolloids 57 (2016) 178-186.
[63] T. Aziz, H. Fan, X. Zhang, F. Haq, A. Ullah, R. Ullah, F.U. Khan, M. Iqbal, Advance study of cellulose nanocrystals properties and applications, Journal of Polymers and the Environment 28(4) (2020) 1117-1128.
[64] M. Börjesson, K. Sahlin, D. Bernin, G. Westman, Increased thermal stability of nanocellulose composites by functionalization of the sulfate groups on cellulose nanocrystals with azetidinium ions, Journal of Applied Polymer Science 135(10) (2018) 45963.
[65] P.H.F. Pereira, H.L.O. Júnior, L.V. Coutinho, B. Duchemin, M.O.H. Cioffi, Obtaining cellulose nanocrystals from pineapple crown fibers by free-chlorite hydrolysis with sulfuric acid: physical, chemical and structural characterization, Cellulose 27(10) (2020) 5745-5756.
[66] Kusmono, R.F. Listyanda, M.W. Wildan, M.N. Ilman, Preparation and characterization of cellulose nanocrystal extracted from ramie fibers by sulfuric acid hydrolysis, Heliyon 6(11) (2020) e05486.
[67] M. Islam, L. Chen, J. Sisler, K. Tam, Cellulose nanocrystal (CNC)–inorganic hybrid systems: synthesis, properties and applications, Journal of Materials Chemistry B 6(6) (2018) 864-883.
[68] I. Usov, G. Nyström, J. Adamcik, S. Handschin, C. Schütz, A. Fall, L. Bergström, R. Mezzenga, Understanding nanocellulose chirality and structure–properties relationship at the single fibril level, Nature communications 6(1) (2015) 1-11.
[69] S. Camarero-Espinosa, D.J. Boday, C. Weder, E.J. Foster, Cellulose nanocrystal driven crystallization of poly (d, l-lactide) and improvement of the thermomechanical properties, Journal of Applied Polymer Science 132(10) (2015).
[70] J. Zhang, N. Luo, X. Zhang, L. Xu, J. Wu, J. Yu, J. He, J. Zhang, All-cellulose nanocomposites reinforced with in situ retained cellulose nanocrystals during selective dissolution of cellulose in an ionic liquid, ACS Sustainable Chemistry & Engineering 4(8) (2016) 4417-4423.
[71] L. Petersson, I. Kvien, K. Oksman, Structure and thermal properties of poly (lactic acid)/cellulose whiskers nanocomposite materials, Composites Science and Technology 67(11-12) (2007) 2535-2544.
[72] C. Ye, S.T. Malak, K. Hu, W. Wu, V.V. Tsukruk, Cellulose nanocrystal microcapsules as tunable cages for nano-and microparticles, Acs Nano 9(11) (2015) 10887-10895.
[73] T. Nishino, I. Matsuda, K. Hirao, All-Cellulose Composite, Macromolecules 37(20) (2004) 7683-7687.
[74] H. Liu, D. Liu, F. Yao, Q. Wu, Fabrication and properties of transparent polymethylmethacrylate/cellulose nanocrystals composites, Bioresource technology 101(14) (2010) 5685-92.
[75] S. Shafiei-Sabet, W.Y. Hamad, S.G. Hatzikiriakos, Rheology of nanocrystalline cellulose aqueous suspensions, Langmuir 28(49) (2012) 17124-33.
[76] E.E. Ureña-Benavides, G. Ao, V.A. Davis, C.L. Kitchens, Rheology and Phase Behavior of Lyotropic Cellulose Nanocrystal Suspensions, Macromolecules 44(22) (2011) 8990-8998.
[77] M. Bilodeau, R.J. Moon, A. Rudie, M. Bilodeau, Production and Applications of Cellulose Nanomaterials, Peachtree Corners, GA: Tappi Press.[Google Scholar] (2014).
[78] S. Kalia, A. Dufresne, B.M. Cherian, B.S. Kaith, L. Avérous, J. Njuguna, E. Nassiopoulos, Cellulose-Based Bio- and Nanocomposites: A Review, International Journal of Polymer Science 2011 (2011) 837875.
[79] W. Liu, H. Du, M. Zhang, K. Liu, H. Liu, H. Xie, X. Zhang, C. Si, Bacterial cellulose-based composite scaffolds for biomedical applications: a review, ACS Sustainable Chemistry & Engineering 8(20) (2020) 7536-7562.
[80] Z. Hussain, W. Sajjad, T. Khan, F. Wahid, Production of bacterial cellulose from industrial wastes: a review, Cellulose 26(5) (2019) 2895-2911.
[81] R.K. Mishra, A. Sabu, S.K. Tiwari, Materials chemistry and the futurist eco-friendly applications of nanocellulose: Status and prospect, Journal of Saudi Chemical Society 22(8) (2018) 949-978.
[82] S.M. Choi, E.J. Shin, The nanofication and functionalization of bacterial cellulose and its applications, Nanomaterials 10(3) (2020) 406.
[83] A. Vazquez, M.L. Foresti, P. Cerrutti, M. Galvagno, Bacterial Cellulose from Simple and Low Cost Production Media by Gluconacetobacter xylinus, Journal of Polymers and the Environment 21(2) (2013) 545-554.
[84] O. Nechyporchuk, M.N. Belgacem, J. Bras, Production of cellulose nanofibrils: A review of recent advances, Industrial Crops and Products 93 (2016) 2-25.
[85] N. Mahfoudhi, Nanocellulose as a novel nanostructured adsorbent for environmental remediation: a review, Cellulose v. 24(no. 3) (2017) pp. 1171-1197-2017 v.24 no.3.
[86] A. Bodin, H. Bäckdahl, H. Fink, L. Gustafsson, B. Risberg, P. Gatenholm, Influence of cultivation conditions on mechanical and morphological properties of bacterial cellulose tubes, Biotechnology and bioengineering 97(2) (2007) 425-34.
[87] H. Bäckdahl, B. Risberg, P. Gatenholm, Observations on bacterial cellulose tube formation for application as vascular graft, Materials Science and Engineering 31 (2011) 14-21.
[88] J. Tang, X. Li, L. Bao, L. Chen, F.F. Hong, Comparison of two types of bioreactors for synthesis of bacterial nanocellulose tubes as potential medical prostheses including artificial blood vessels, Journal of Chemical Technology & Biotechnology 92(6) (2017) 1218-1228.
[89] F.G. Blanco Parte, S.P. Santoso, C.-C. Chou, V. Verma, H.-T. Wang, S. Ismadji, K.-C. Cheng, Current progress on the production, modification, and applications of bacterial cellulose, Critical reviews in biotechnology 40(3) (2020) 397-414.
[90] P. Gatenholm, D. Klemm, Bacterial Nanocellulose as a Renewable Material for Biomedical Applications, Mrs Bulletin 35 (2010) 208-213.
[91] R. Jonas, L.F. Farah, Production and application of microbial cellulose, Polymer Degradation and Stability 59(1) (1998) 101-106.
[92] V. Revin, E. Liyas'kina, N. Sapunova, A. Bogatyreva, Isolation and characterization of the strains producing bacterial cellulose, Microbiology 89(1) (2020) 86-95.
[93] M.E. Leitch, C. Li, O. Ikkala, M.S. Mauter, G.V. Lowry, Bacterial Nanocellulose Aerogel Membranes: Novel High-Porosity Materials for Membrane Distillation, Environmental Science & Technology Letters 3(3) (2016) 85-91.
[94] C. Peng, T. Li, Y. Zou, C. Xiang, F. Xu, J. Zhang, L. Sun, Bacterial cellulose derived carbon as a support for catalytically active Co–B alloy for hydrolysis of sodium borohydride, International Journal of Hydrogen Energy 46(1) (2021) 666-675.
[95] T. Kamal, I. Ahmad, S.B. Khan, M. Ul-Islam, A.M. Asiri, Microwave assisted synthesis and carboxymethyl cellulose stabilized copper nanoparticles on bacterial cellulose nanofibers support for pollutants degradation, Journal of Polymers and the Environment 27(12) (2019) 2867-2877.
[96] A.F. Jozala, L.C. de Lencastre-Novaes, A.M. Lopes, V. de Carvalho Santos-Ebinuma, P.G. Mazzola, A. Pessoa, Jr., D. Grotto, M. Gerenutti, M.V. Chaud, Bacterial nanocellulose production and application: a 10-year overview, Applied microbiology and biotechnology 100(5) (2016) 2063-72.
[97] D. Klemm, D. Schumann, F. Kramer, N. Heßler, M. Hornung, H.-P. Schmauder, S. Marsch, Nanocelluloses as Innovative Polymers in Research and Application, in: D. Klemm (Ed.), Polysaccharides II, Springer Berlin Heidelberg, Berlin, Heidelberg, 2006, pp. 49-96.
[98] S.L. Arias, A.R. Shetty, A. Senpan, M. Echeverry-Rendón, L.M. Reece, J.P. Allain, Fabrication of a Functionalized Magnetic Bacterial Nanocellulose with Iron Oxide Nanoparticles, Journal of visualized experiments : JoVE (111) (2016).

[99] R.T. Olsson, M.A. Azizi Samir, G. Salazar-Alvarez, L. Belova, V. Ström, L.A. Berglund, O. Ikkala, J. Nogués, U.W. Gedde, Making flexible magnetic aerogels and stiff magnetic nanopaper using cellulose nanofibrils as templates, Nature nanotechnology 5(8) (2010) 584-8.
[100] L. Wang, C. Schütz, G. Salazar-Alvarez, M.-M. Titirici, Carbon aerogels from bacterial nanocellulose as anodes for lithium ion batteries, RSC Advances 4(34) (2014) 17549-17554.
[101] M.L. Hassan, A.P. Mathew, E.A. Hassan, N.A. El-Wakil, K. Oksman, Nanofibers from bagasse and rice straw: process optimization and properties, Wood Sci Technol 46(1-3) (2012) 193-205.
[102] M. Roman, A.P. Haring, T.J. Bertucio, The growing merits and dwindling limitations of bacterial cellulose-based tissue engineering scaffolds, Current Opinion in Chemical Engineering 24 (2019) 98-106.
[103] N. Yin, R. Du, F. Zhao, Y. Han, Z. Zhou, Characterization of antibacterial bacterial cellulose composite membranes modified with chitosan or chitooligosaccharide, Carbohydrate polymers 229 (2020) 115520.
[104] J. Huang, A. Dufresne, N. Lin, Nanocellulose: From fundamentals to advanced materials, John Wiley & Sons2019.
[105] S.S. Athukoralalage, R. Balu, N.K. Dutta, N. Roy Choudhury, 3D bioprinted nanocellulose-based hydrogels for tissue engineering applications: A brief review, Polymers 11(5) (2019) 898.
[106] R. Xiong, K. Hu, A.M. Grant, R. Ma, W. Xu, C. Lu, X. Zhang, V.V. Tsukruk, Ultrarobust Transparent Cellulose Nanocrystal-Graphene Membranes with High Electrical Conductivity, Advanced Materials 28(7) (2016) 1501-1509.
[107] Q. Meng, I. Manas-Zloczower, Carbon nanotubes enhanced cellulose nanocrystals films with tailorable electrical conductivity, Composites Science and Technology 120 (2015) 1-8.
[108] M.G. Adsul, D.A. Rey, D.V. Gokhale, Combined strategy for the dispersion/dissolution of single walled carbon nanotubes and cellulose in water, Journal of Materials Chemistry 21(7) (2011) 2054-2056.
[109] D. Trache, V.K. Thakur, Nanocellulose and Nanocarbons Based Hybrid Materials: Synthesis, Characterization and Applications, Multidisciplinary Digital Publishing Institute, 2020.
[110] D. Trache, A.F. Tarchoun, M. Derradji, T.S. Hamidon, N. Masruchin, N. Brosse, M.H. Hussin, Nanocellulose: From fundamentals to advanced applications, Frontiers in Chemistry 8 (2020).
[111] V. Durairaj, P. Li, T. Liljeström, N. Wester, J. Etula, I. Leppänen, Y. Ge, K.S. Kontturi, T. Tammelin, T. Laurila, Functionalized Nanocellulose/Multiwalled Carbon Nanotube Composites for Electrochemical Applications, ACS Applied Nano Materials (2021).
[112] B. Fugetsu, E. Sano, M. Sunada, Y. Sambongi, T. Shibuya, X. Wang, T. Hiraki, Electrical conductivity and electromagnetic interference shielding efficiency of carbon nanotube/cellulose composite paper, Carbon 46(9) (2008) 1256-1258.
[113] S. Yun, J. Kim, A bending electro-active paper actuator made by mixing multi-walled carbon nanotubes and cellulose, Smart Materials and Structures 16 (2007) 1471-1476.
[114] T. Oya, T. Ogino, Production of electrically conductive paper by adding carbon nanotubes, Carbon 46(1) (2008) 169-171.
[115] J. Zeng, L. Yan, Metal-free transparent luminescent cellulose films, Cellulose 22(1) (2015) 729-736.
[116] H. Qi, E. Mäder, J. Liu, Electrically conductive aerogels composed of cellulose and carbon nanotubes, Journal of Materials Chemistry A 1(34) (2013) 9714-9720.
[117] F. Wang, D. Li, Foldable and free-standing 3D network electrodes based on cellulose nanofibers, carbon nanotubes and elongated TiO_2 nanotubes, Materials Letters 158 (2015) 119-122.
[118] A. Jasim, M.W. Ullah, Z. Shi, X. Lin, G. Yang, Fabrication of bacterial cellulose/polyaniline/single-walled carbon nanotubes membrane for potential application as biosensor, Carbohydrate polymers 163 (2017) 62-69.
[119] A. Kafy, A. Akther, M.I.R. Shishir, J. Kim, Cellulose/graphene oxide composite for electrode materials of flexible energy devices, SPIE2017.
[120] G.L. Drisko, C. Sanchez, Hybridization in Materials Science – Evolution, Current State, and Future Aspirations, European Journal of Inorganic Chemistry 2012(32) (2012) 5097-5105.
[121] A. Lanna, M. Suklueng, C. Kasagepongsan, S. Suchat, Performance of novel engineered materials from epoxy resin with modified epoxidized natural rubber and nanocellulose or nanosilica, Advances in Polymer Technology 2020 (2020).
[122] P. Khadivi, M. Salami-Kalajahi, H. Roghani-Mamaqani, Evaluation of in vitro cytotoxicity and properties of polydimethylsiloxane-based polyurethane/crystalline nanocellulose bionanocomposites, Journal of Biomedical Materials Research Part A 107(8) (2019) 1771-1778.
[123] K.L. Dagnon, K. Shanmuganathan, C. Weder, S.J. Rowan, Water-Triggered Modulus Changes of Cellulose Nanofiber Nanocomposites with Hydrophobic Polymer Matrices, Macromolecules 45(11) (2012) 4707-4715.
[124] J.R. Capadona, K. Shanmuganathan, D.J. Tyler, S.J. Rowan, C. Weder, Stimuli-Responsive Polymer Nanocomposites Inspired by the Sea Cucumber Dermis, Science 319(5868) (2008) 1370-1374.
[125] A.E. Way, L. Hsu, K. Shanmuganathan, C. Weder, S.J. Rowan, pH-Responsive Cellulose Nanocrystal Gels and Nanocomposites, ACS Macro Letters 1(8) (2012) 1001-1006.
[126] V. Favier, H. Chanzy, J.Y. Cavaille, Polymer Nanocomposites Reinforced by Cellulose Whiskers, Macromolecules 28(18) (1995) 6365-6367.
[127] J. Cai, J. Chen, Q. Zhang, M. Lei, J. He, A. Xiao, C. Ma, S. Li, H. Xiong, Well-aligned cellulose nanofiber-reinforced polyvinyl alcohol composite film: Mechanical and optical properties, Carbohydrate polymers 140 (2016) 238-245.
[128] E. Robles, A.M. Salaberria, R. Herrera, S.C.M. Fernandes, J. Labidi, Self-bonded composite films based on cellulose nanofibers and chitin nanocrystals as antifungal materials, Carbohydrate polymers 144 (2016) 41-49.
[129] S. Wang, X. Zhang, X. Wu, C. Lu, Tailoring percolating conductive networks of natural rubber composites for flexible strain sensors via a cellulose nanocrystal templated assembly, Soft Matter 12(3) (2016) 845-852.
[130] C. Geng, X. Hu, G. Yang, Q. Zhang, F. Chen, Q. Fu, Mechanically reinforced chitosan/cellulose nanocrystals composites with good transparency and biocompatibility, Chinese Journal of Polymer Science 33 (2014) 61-69.
[131] B. Soni, E.B. Hassan, M.W. Schilling, B. Mahmoud, Transparent bionanocomposite films based on chitosan and TEMPO-oxidized cellulose nanofibers with enhanced mechanical and barrier properties, Carbohydrate Polymers 151 (2016) 779-789.
[132] N. Rescignano, E. Fortunati, S. Montesano, C. Emiliani, J.M. Kenny, S. Martino, I. Armentano, PVA bio-nanocomposites: a new take-off using cellulose nanocrystals and PLGA nanoparticles, Carbohydr Polym 99 (2014) 47-58.
[133] C. Amara, A. El Mahdi, R. Medimagh, K. Khwaldia, Nanocellulose-based composites for packaging applications, Current Opinion in Green and Sustainable Chemistry (2021) 100512.
[134] C. Sanchez, G.J.d.A.A. Soler-Illia, F. Ribot, T. Lalot, C.R. Mayer, V. Cabuil, Designed Hybrid Organic−Inorganic Nanocomposites from Functional Nanobuilding Blocks, Chemistry of Materials 13(10) (2001) 3061-3083.
[135] N. Meulendijks, M. Burghoorn, R. van Ee, M. Mourad, D. Mann, H. Keul, G. Bex, E. van Veldhoven, M. Verheijen, P. Buskens, Electrically conductive coatings consisting of Ag-decorated cellulose nanocrystals, Cellulose 24(5) (2017) 2191-2204.
[136] G. Yang, M.W. Ullah, S. Zhijun, Nanocellulose: Synthesis, Structure, Properties and Applications, World Scientific2021.
[137] L. Bacakova, J. Pajorova, M. Tomkova, R. Matejka, A. Broz, J. Stepanovska, S. Prazak, A. Skogberg, S. Siljander, P. Kallio, Applications of nanocellulose/nanocarbon composites: Focus on biotechnology and medicine, Nanomaterials 10(2) (2020) 196.
[138] L. Bacakova, J. Pajorova, M. Bacakova, A. Skogberg, P. Kallio, K. Kolarova, V. Svorcik, Versatile application of nanocellulose: From industry to skin tissue engineering and wound healing, Nanomaterials 9(2) (2019) 164.
[139] P. Jain, A.G. Bhavani, Nanocellulose-Based Materials for the Removal of Organic Toxicants and Antibacterial Applications, Nanocellulose and Its Composites for Water Treatment Applications (2021) 183.
[140] C. Schütz, J. Sort, Z. Bacsik, V. Oliynyk, E. Pellicer, A. Fall, L. Wågberg, L. Berglund, L. Bergström, G. Salazar-Alvarez, Hard and transparent films formed by nanocellulose–TiO_2 nanoparticle hybrids, PLoS One 7(10) (2012) e45828.
[141] M. Kettunen, R.J. Silvennoinen, N. Houbenov, A. Nykänen, J. Ruokolainen, J. Sainio, V. Pore, M. Kemell, M. Ankerfors, T. Lindström, Photoswitchable superabsorbency based on nanocellulose aerogels, Advanced Functional Materials 21(3) (2011) 510-517.
[142] C.M. Cirtiu, A.F. Dunlop-Briere, A. Moores, Cellulose nanocrystallites as an efficient support for nanoparticles of palladium: application for catalytic hydrogenation and Heck coupling under mild conditions, Green Chemistry 13(2) (2011) 288-291.
[143] Z. Zhou, C. Lu, X. Wu, X. Zhang, Cellulose nanocrystals as a novel support for CuO nanoparticles catalysts: facile synthesis and their application to 4-nitrophenol reduction, RSC advances 3(48) (2013) 26066-26073.
[144] X. Wu, C. Lu, Z. Zhou, G. Yuan, R. Xiong, X. Zhang, Green synthesis and formation mechanism of cellulose nanocrystal-supported gold nanoparticles with enhanced catalytic performance, Environmental Science: Nano 1(1) (2014) 71-79.
[145] H. Koga, E. Tokunaga, M. Hidaka, Y. Umemura, T. Saito, A. Isogai, T. Kitaoka, Topochemical synthesis and catalysis of metal nanoparticles exposed on crystalline cellulose nanofibers, Chemical communications 46(45) (2010) 8567-8569.
[146] A. Azetsu, H. Koga, A. Isogai, T. Kitaoka, Synthesis and catalytic features

of hybrid metal nanoparticles supported on cellulose nanofibers, Catalysts 1(1) (2011) 83-96.
[147] C.F. João, A.C. Baptista, I.M. Ferreira, J.C. Silva, J.P. Borges, Natural Nanofibres for Composite Applications, Fibrous and Textile Materials for Composite Applications, Springer2016, pp. 261-299.
[148] R. Gao, J. Shen, F. Xie, Y. Zuo, D. Wu, Effects of phenolic resin addition on the electrical conductivity and mechanical strength of nano-copper paste formed Cu-Cu joints, Journal of Electronic Materials 46(11) (2017) 6388-6394.
[149] A. Nakagaito, S. Iwamoto, H. Yano, Bacterial cellulose: the ultimate nano-scalar cellulose morphology for the production of high-strength composites, Applied Physics A 80(1) (2005) 93-97.
[150] I.L. Leal, Y.C. da Silva Rosa, J. da Silva Penha, P.R. Cruz Correia, P. da Silva Melo, D.H. Guimarães, J.D.V. Barbosa, J.I. Druzian, B.A.S. Machado, Development and application starch films: PBAT with additives for evaluating the shelf life of Tommy Atkins mango in the fresh-cut state, Journal of Applied Polymer Science 136(43) (2019) 48150.
[151] S. Tuukkanen, S. Lehtimäki, F. Jahangir, A.-P. Eskelinen, D. Lupo, S. Fransila, Printable and disposable supercapacitor from nanocellulose and carbon nanotubes, Proceedings of the 5th Electronics System-integration Technology Conference (ESTC), IEEE, 2014, pp. 1-6.
[152] D. Lasrado, S. Ahankari, K. Kar, Nanocellulose-based polymer composites for energy applications—A review, Journal of Applied Polymer Science 137(27) (2020) 48959.
[153] C. Liu, J. Dong, G.I. Waterhouse, Z. Cheng, S. Ai, Electrochemical immunosensor with nanocellulose-Au composite assisted multiple signal amplification for detection of avian leukosis virus subgroup J, Biosensors and Bioelectronics 101 (2018) 110-115.
[154] W. Wang, T.-J. Zhang, D.-W. Zhang, H.-Y. Li, Y.-R. Ma, L.-M. Qi, Y.-L. Zhou, X.-X. Zhang, Amperometric hydrogen peroxide biosensor based on the immobilization of heme proteins on gold nanoparticles–bacteria cellulose nanofibers nanocomposite, Talanta 84(1) (2011) 71-77.
[155] T. Zhang, W. Wang, D. Zhang, X. Zhang, Y. Ma, Y. Zhou, L. Qi, Biotemplated synthesis of gold nanoparticle–bacteria cellulose nanofiber nanocomposites and their application in biosensing, Advanced Functional Materials 20(7) (2010) 1152-1160.
[156] W. Wang, H.Y. Li, D.W. Zhang, J. Jiang, Y.R. Cui, S. Qiu, Y.L. Zhou, X.X. Zhang, Fabrication of bienzymatic glucose biosensor based on novel gold nanoparticles-bacteria cellulose nanofibers nanocomposite, Electroanalysis 22(21) (2010) 2543-2550.
[157] Y.H. Ngo, D. Li, G.P. Simon, G. Garnier, Effect of cationic polyacrylamides on the aggregation and SERS performance of gold nanoparticles-treated paper, Journal of colloid and interface science 392 (2013) 237-246.
[158] W. Leng, P.J. Vikesland, Nanoclustered gold honeycombs for surface-enhanced Raman scattering, Analytical chemistry 85(3) (2013) 1342-1349.
[159] X.-M. Qian, S.M. Nie, Single-molecule and single-nanoparticle SERS: from fundamental mechanisms to biomedical applications, Chemical Society Reviews 37(5) (2008) 912-920.
[160] Y. Wang, H. Wei, B. Li, W. Ren, S. Guo, S. Dong, E. Wang, SERS opens a new way in aptasensor for protein recognition with high sensitivity and selectivity, Chemical Communications (48) (2007) 5220-5222.
[161] M. Park, H. Chang, D.H. Jeong, J. Hyun, Spatial deformation of nanocellulose hydrogel enhances SERS, BioChip Journal 7(3) (2013) 234-241.
[162] P.A. Marques, H.I. Nogueira, R.J. Pinto, C.P. Neto, T. Trindade, Silver-bacterial cellulosic sponges as active SERS substrates, Journal of Raman Spectroscopy: An International Journal for Original Work in all Aspects of Raman Spectroscopy, Including Higher Order Processes, and also Brillouin and Rayleigh Scattering 39(4) (2008) 439-443.
[163] R.J. Pinto, P.A. Marques, M.A. Martins, C.P. Neto, T. Trindade, Electrostatic assembly and growth of gold nanoparticles in cellulosic fibres, Journal of colloid and interface science 312(2) (2007) 506-512.
[164] K.A. Mahmoud, K.B. Male, S. Hrapovic, J.H. Luong, Cellulose nanocrystal/gold nanoparticle composite as a matrix for enzyme immobilization, ACS applied materials & interfaces 1(7) (2009) 1383-1386.
[165] L. Van Haver, S. Nayar, Polyelectrolyte flocculants in harvesting microalgal biomass for food and feed applications, Algal Research 24 (2017) 167-180.
[166] P. Maćczak, H. Kaczmarek, M. Ziegler-Borowska, Recent Achievements in Polymer Bio-Based Flocculants for Water Treatment, Materials 13(18) (2020) 3951.
[167] H. Zhu, Y. Zhang, X. Yang, H. Liu, L. Shao, X. Zhang, J. Yao, One-step green synthesis of non-hazardous dicarboxyl cellulose flocculant and its flocculation activity evaluation, Journal of hazardous materials 296 (2015) 1-8.
[168] R. Das, S. Ghorai, S. Pal, Flocculation characteristics of polyacrylamide grafted hydroxypropyl methyl cellulose: An efficient biodegradable flocculant, Chemical engineering journal 229 (2013) 144-152.
[169] T. Suopajärvi, H. Liimatainen, O. Hormi, J. Niinimäki, Coagulation–flocculation treatment of municipal wastewater based on anionized nanocelluloses, Chemical Engineering Journal 231 (2013) 59-67.
[170] J. Ci, C. Cao, S. Kuga, J. Shen, M. Wu, Y. Huang, Improved performance of microbial fuel cell using esterified corncob cellulose nanofibers to fabricate air-cathode gas diffusion layer, ACS Sustainable Chemistry & Engineering 5(11) (2017) 9614-9618.
[171] H. Liimatainen, T. Suopajärvi, J. Sirviö, O. Hormi, J. Niinimäki, Fabrication of cationic cellulosic nanofibrils through aqueous quaternization pretreatment and their use in colloid aggregation, Carbohydrate polymers 103 (2014) 187-192.
[172] Y. Habibi, L.A. Lucia, O.J. Rojas, Cellulose nanocrystals: chemistry, self-assembly, and applications, Chemical reviews 110(6) (2010) 3479-3500.
[173] T. Suopajärvi, J.A. Sirviö, H. Liimatainen, Cationic nanocelluloses in dewatering of municipal activated sludge, Journal of environmental chemical engineering 5(1) (2017) 86-92.
[174] S. Eyley, D. Vandamme, S. Lama, G. Van den Mooter, K. Muylaert, W. Thielemans, CO_2 controlled flocculation of microalgae using pH responsive cellulose nanocrystals, Nanoscale 7(34) (2015) 14413-14421.
[175] R. Hartmann, J.A. Sirviö, R. Sliz, O. Laitinen, H. Liimatainen, A. Ämmälä, T. Fabritius, M. Illikainen, Interactions between aminated cellulose nanocrystals and quartz: adsorption and wettability studies, Colloids and Surfaces A: Physicochemical and Engineering Aspects 489 (2016) 207-215.
[176] H. Liimatainen, J. Sirviö, O. Sundman, M. Visanko, O. Hormi, J. Niinimäki, Flocculation performance of a cationic biopolymer derived from a cellulosic source in mild aqueous solution, Bioresource technology 102(20) (2011) 9626-9632.
[177] H. Liimatainen, J. Sirviö, O. Sundman, O. Hormi, J. Niinimäki, Use of nanoparticular and soluble anionic celluloses in coagulation-flocculation treatment of kaolin suspension, Water research 46(7) (2012) 2159-2166.
[178] D. Chen, T.G. van de Ven, Flocculation kinetics of precipitated calcium carbonate induced by electrosterically stabilized nanocrystalline cellulose, Colloids and Surfaces A: Physicochemical and Engineering Aspects 504 (2016) 11-17.
[179] X. Sun, C. Danumah, Y. Liu, Y. Boluk, Flocculation of bacteria by depletion interactions due to rod-shaped cellulose nanocrystals, Chemical engineering journal 198 (2012) 476-481.
[180] D. Vandamme, S. Eyley, G. Van den Mooter, K. Muylaert, W. Thielemans, Highly charged cellulose-based nanocrystals as flocculants for harvesting Chlorella vulgaris, Bioresource technology 194 (2015) 270-275.
[181] D. Klemm, B. Heublein, H.P. Fink, A. Bohn, Cellulose: fascinating biopolymer and sustainable raw material, Angewandte chemie international edition 44(22) (2005) 3358-3393.
[182] A.N. Aleshin, A.S. Berestennikov, P.S. Krylov, I.P. Shcherbakov, V.N. Petrov, I.N. Trapeznikova, R.I. Mamalimov, A.K. Khripunov, A.A. Tkachenko, Electrical and optical properties of bacterial cellulose films modified with conductive polymer PEDOT/PSS, Synthetic Metals 199 (2015) 147-151.
[183] L. Urbina, I. Algar, C. García-Astrain, N. Gabilondo, A. González, M. Corcuera, A. Eceiza, A. Retegi, Biodegradable composites with improved barrier properties and transparency from the impregnation of PLA to bacterial cellulose membranes, Journal of Applied Polymer Science 133(28) (2016).
[184] I. Chiulan, A.N. Frone, D.M. Panaitescu, C.A. Nicolae, R. Trusca, Surface properties, thermal, and mechanical characteristics of poly (vinyl alcohol)–starch-bacterial cellulose composite films, Journal of Applied Polymer Science 135(6) (2018) 45800.
[185] H. Luo, J. Dong, Y. Zhang, G. Li, R. Guo, G. Zuo, M. Ye, Z. Wang, Z. Yang, Y. Wan, Constructing 3D bacterial cellulose/graphene/polyaniline nanocomposites by novel layer-by-layer in situ culture toward mechanically robust and highly flexible freestanding electrodes for supercapacitors, Chemical Engineering Journal 334 (2018) 1148-1158.
[186] Y. Numata, H. Kono, M. Tsuji, K. Tajima, Structural and mechanical characterization of bacterial cellulose–polyethylene glycol diacrylate composite gels, Carbohydrate polymers 173 (2017) 67-76.
[187] S. Dutta, J. Kim, Y. Ide, J.H. Kim, M.S.A. Hossain, Y. Bando, Y. Yamauchi, K.C.-W. Wu, 3D network of cellulose-based energy storage devices and related emerging applications, Materials Horizons 4(4) (2017) 522-545.
[188] M.E. Malainine, M. Mahrouz, A. Dufresne, Thermoplastic nanocomposites based on cellulose microfibrils from Opuntia ficus-indica parenchyma cell, Composites Science and Technology 65(10) (2005) 1520-1526.
[189] A.N. Nakagaito, H. Yano, Novel high-strength biocomposites based on microfibrillated cellulose having nano-order-unit web-like network structure, Applied Physics A 80(1) (2005) 155-159.

[190] R. Masoodi, R. El-Hajjar, K. Pillai, R. Sabo, Mechanical characterization of cellulose nanofiber and bio-based epoxy composite, Materials & Design (1980-2015) 36 (2012) 570-576.
[191] A. Ramezani Kakroodi, S. Cheng, M. Sain, A. Asiri, Mechanical, thermal, and morphological properties of nanocomposites based on polyvinyl alcohol and cellulose nanofiber from Aloe vera rind, Journal of Nanomaterials 2014 (2014).
[192] B.R. Evans, H.M. O'Neill, V.P. Malyvanh, I. Lee, J. Woodward, Palladium-bacterial cellulose membranes for fuel cells, Biosensors and Bioelectronics 18(7) (2003) 917-923.
[193] L. Hu, G. Zheng, J. Yao, N. Liu, B. Weil, M. Eskilsson, E. Karabulut, Z. Ruan, S. Fan, J.T. Bloking, Transparent and conductive paper from nanocellulose.
[194] L. Jabbour, R. Bongiovanni, D. Chaussy, C. Gerbaldi, D. Beneventi, Cellulose-based Li-ion batteries: a review, Cellulose 20(4) (2013) 1523-1545.
[195] M. Schroers, A. Kokil, C. Weder, Solid polymer electrolytes based on nanocomposites of ethylene oxide–epichlorohydrin copolymers and cellulose whiskers, Journal of Applied Polymer Science 93(6) (2004) 2883-2888.
[196] F. Alloin, A. D'aprea, N. El Kissi, A. Dufresne, F. Bossard, Nanocomposite polymer electrolyte based on whisker or microfibrils polyoxyethylene nanocomposites, Electrochimica Acta 55(18) (2010) 5186-5194.
[197] A. Chiappone, J.R. Nair, C. Gerbaldi, L. Jabbour, R. Bongiovanni, E. Zeno, D. Beneventi, N. Penazzi, Microfibrillated cellulose as reinforcement for Li-ion battery polymer electrolytes with excellent mechanical stability, Journal of Power Sources 196(23) (2011) 10280-10288.
[198] S. Leijonmarck, A. Cornell, G. Lindbergh, L. Wågberg, Single-paper flexible Li-ion battery cells through a paper-making process based on nano-fibrillated cellulose, Journal of Materials Chemistry A 1(15) (2013) 4671-4677.
[199] L. Jabbour, C. Gerbaldi, D. Chaussy, E. Zeno, S. Bodoardo, D. Beneventi, Microfibrillated cellulose–graphite nanocomposites for highly flexible paper-like Li-ion battery electrodes, Journal of Materials Chemistry 20(35) (2010) 7344-7347.
[200] L. Hu, N. Liu, M. Eskilsson, G. Zheng, J. McDonough, L. Wågberg, Y. Cui, Silicon-conductive nanopaper for Li-ion batteries, Nano Energy 2(1) (2013) 138-145.derived carbon as a support for catalytically active Co–B alloy for hydrolysis of sodium borohydride, International Journal of Hydrogen Energy 46(1) (2021) 666-675.

Journal of Composites and Compounds 3 (2021) 129-139

Available online at www.jourcc.com

Journal homepage: www.JOURCC.com

Journal of Composites and Compounds

Application of polyoxometalate-based composites for sensor systems: A review

Hamid Khalilpour [a], *Parisa Shafiee* [b]*, *Amirhossein Darbandi* [c], *Mohammad Yusuf* [d], *Shirin Mahmoudi* [e], *Zahra Moazzami Goudarzi* [f], *Sadegh Mirzamohammadi* [g]

[a] *Department of Mining, Metallurgy and Materials Engineering, Université Laval, Québec, Canada*
[b] *Catalyst and Nano Material Research Laboratory (CNMRL), School of Chemical, Petroleum and Gas Engineering, Iran University of Science and Technology, Tehran, Iran*
[c] *Department of Mechanical Engineering, Payame Noor University, Tehran, Iran*
[d] *Department of Chemical Engineering, Universiti Teknologi PETRONAS, Bandar Seri Iskandar, 32610, Malaysia*
[e] *Semiconductor Department, Materials and Energy Research Center, Karaj, Iran*
[f] *Department of Chemical Engineering, Isfahan University of Technology, Isfahan, Iran*
[g] *Department of materials and Metallurgical Engineering, Technical and Vocational University (TVU), Tehran, Iran*

A B S T R A C T

Composites based on polyoxometalates (POMs) have been increasingly attracted by many researchers due to their multitudinous architectures and excellent redox activities as well as outstanding proton and electron transport capacities. Lately, much research has been done on POMs composited with well-porous framework materials (including ZIFs, MOFs) or conducting polymers, carbon quantum dot (CQD), graphene, carbon structures (e.g. carbon nanotubes (CNTs)), and metal nanoparticles (NPs). The results exhibited improved stability and enhanced electrochemical performances. Hence, developing POMs and POM-based composite materials (PCMs) has long been a topic of interest for chemical researchers. Herein, the properties and applications of pristine POMs, doped POMs, and composite-based POMs are reviewed in detail. The various compositions of POMs with sensing application such as POMs-nanocarbon composites (POMs-graphene composites and POMs-carbon nanotube composites), POMs-conductive polymer composites, and POMs-metal composites are also investigated in this review.

Peer review under responsibility of jourcc

A R T I C L E I N F O R M A T I O N

Article history:
Received 18 April 2021
Received in revised form 5 June 2021
Accepted 29 June 2021

Keywords:
Polyoxometalates
Composites
Framework materials
Electrochemical performances

Table of contents

1. Introduction 129
2. Principal properties of POMs 130
3. Insertion of dopant ions in POMs 132
4. POMs-based composites for sensor systems 133
4.1. POMs-nanocarbon composites 133
4.1.1. POMs-graphene composites 133
4.1.2. POMs-carbon nanotube composites 134
4.2. POMs-conductive polymer composites 135
4.3. POMs-metal composites 136
5. Conclusions and future insights 136

1. Introduction

Polyoxometalates (POMs) have an architecture made up of oxygen atoms and primary transition metals, such as Ta, Nb, W, V, and Mo in their maximum state of oxidation. Moreover, they significantly comprise different heteroatoms including As, Si, P, and Ge. It would be possible to distinguish between the molecular oxides of POMs and most metal oxides. They include diverse metal atoms that contain about 368 metal atoms as nuclearities into an individual cluster molecule reaching nanoparticles. Berzelius firstly reported synthesizing POM in the 19th

* *Corresponding author: Parisa Shafiee; E-mail: Parisashafiee603@gmail.com*
https://doi.org/10.52547/jcc.3.2.6

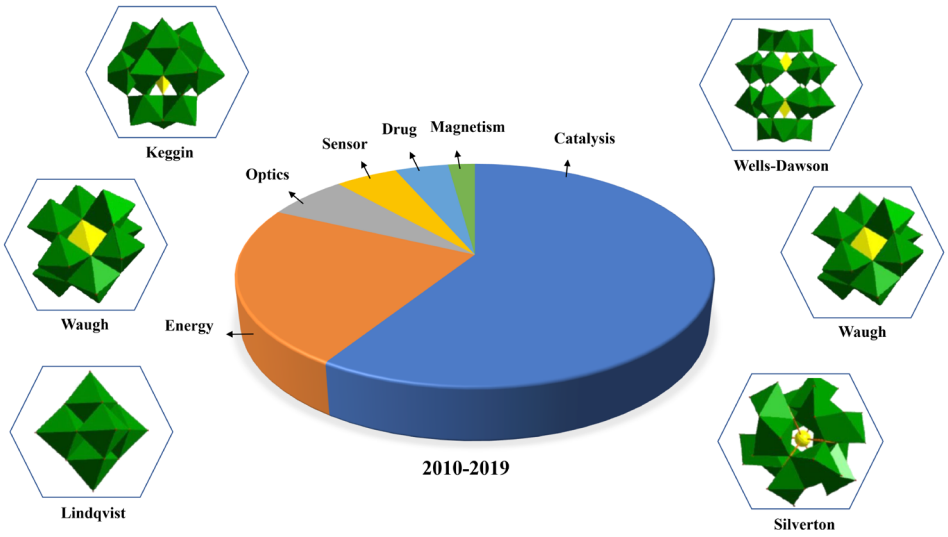

Fig. 1. Classical structure species of POMs and certain presented essential usages of POM-based structures in the recent decade.

century [1]. Besides, the oxoanions are occasionally assembled in a non-aqueous medium or a solid-state condition as in minerals. There are some properties to measure the stability of POMs in various solvents including aqueous/non-aqueous media lsuch as their ability to keep their structural properties and prevent declining or changing to other formations [2-5].

Many novel POM skeletons were uncovered, followed by the discovery of six classical systems such as Lindqvist, Dawson, Waugh, Keggin, Silverton, and Anderson (Fig. 1). Among the basic constructions of POMs, Dawson (X/M =2/18) and Keggin (X/M =1/12) are two main forms of POMs. Other complex structures are achieved by the accumulation of two or more Dawson or Keggin parts. The skeleton and composition of these forms of POMs depend on the employed methods and conditions. Some of the newly-generated POMs structures are ″sandwich″ type (a mix of the two lacunary entities of XW9 or X2W15 and H4XW15), ″crown″ or ″wheel″ type (a tetramer of the lacunary Dawson K12H2P2W12O48), and the ″banana″ type (two Keggin entities, XW9M3O40 or XW9M2M'O40 are linked to XW6O16) [6, 7].

Numerous types of POM compositions with more intriguing and diversified structures have been shown by self-assembly of purely inorganic construction blocks and/or network bridging functions of organic ligands and metal ions due to the high activities of lacunary POM building blocks. For example, POM composite materials containing TMs, rare-earth ions (RE) replaced POMs, organic ligand, and heterometallic modified POMs, have been widely employed [1, 8, 9].

Because of their excellent electron and proton transportations and unstable redox behaviors, individual particle magnet activity and optical capabilities are already reported in POM-based composite materials (PCMs) [10-13]. In multi-electron reduction processes, POMs are good electron reservoirs. As a result, they can be used in the electrochemical field. Proton conductivity is another remarkable property of PCMs, allowing them to be used in modern perspectives, such as proton-exchange membrane fuel cells [10, 11, 14]. POMs, on the other hand, have been discovered to play a key part in the extraordinary development of PCMs having greater efficiency and stability. PCMs are also being used to create neoteric smart structures for applications such as optics [10, 11, 14], pharmaceuticals [15-17], energy-related applications [18-20], sensors [21-23], and green catalysis [24-26] (Fig. 1).

POMs are appealing for amperometric sensor applications because of their ability to sustain reversible multi-electron redox processes. They are particularly useful for detecting redox-active agricultural and industrial contaminants, including iodate, hydrogen peroxide, chlorate, nitrate, and bromate. POMs-based composites and nanocarbon structures, including carbon nanotubes (CNTs) and graphene, have gained much attention due to mixing the excellent chemical activity of POMs with the fascinating electronic properties of nanocarbon structures (a high surface area associated with electrical conductivity), which make them appropriate candidates for catalytic, energy-storing, energy conversion, electronics, and molecular sensor applications [27-30].

As sensing applications are among the most paramount research topics in technology these days, this paper reviews the fundamental properties of pristine POMs, doped POMs, and composite-based POMs in detail. Furthermore, and more importantly, the various compositions of POMs with sensing applications, such as POMs-nanocarbon composites (POMs-graphene composites and POMs-carbon nanotube composites), POMs-conductive polymer composites, and POMs-metal composites are investigated, a topic that has not been thoroughly investigated in other studies to this extent. This review is likely to pave the way for novel methods to modify POM-based composites in sensing applications.

2. Principal properties of POMs

Marignac [31] successfully discovered the synthesis way of 1:12 silico-tungstic acid in 1864. In the 20th century, Rosenheim first began the systematic analysis of POMs and the study of their characteristics. POMs are significantly able to adapt with and deliver a special number of electrons without any change or decomposition in their construction. Isopolyanions (IPAs) and heteropolyanions (HPAs) are components of POMs and are repeatedly created into aqueous media [32-34]. Besides, the oxoanions are occasionally assembled in a non-aqueous medium or a solid state as in minerals. There are some properties to measure the stability of POMs in various solvents, including aqueous/non-aqueous media such as their ability to keep their structural properties and prevent declining or changing to other formations. Among the basic constructions of POMs, Dawson (X/M =2/18) and Keggin (X/M =1/12) are two main forms of POMs. Other complex structures are achieved by the accumulation of two or diverse Dawson or Keggin parts [35-37].

That kind of POM based on a Keggin is formed by adjusting several metal atoms (M = Mo, Ta, W, Nb, V) around an individual heteroatom (X = Ge, As, Si, P). Pauling first proposed the Keggin structure in 1929 [1] and then it was approved by Keggin in 1933 [38]. In the Keggin

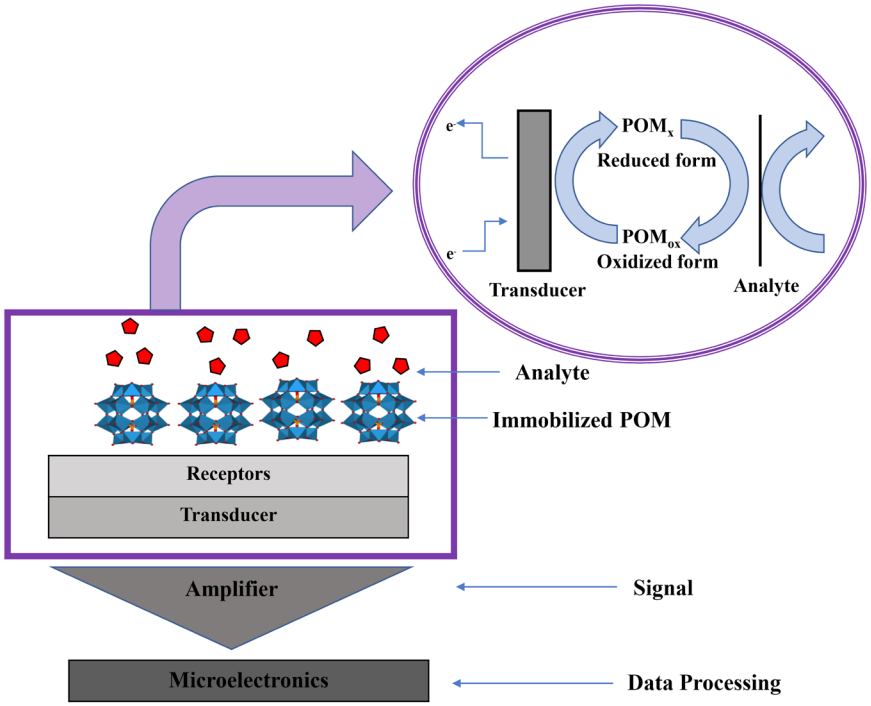

Fig. 2. Schematic design of the working process of a desirable POM-based electrochemical sensor.

structure, a tetrahedron is formed by the combination of the heteroatom X with four oxygen atoms and each metal atom with six oxygen atoms, makes an octahedral structure. The tri-metallic structures are linked to other networks and the typical place of M_3O_{13} is connected to the central heteroatom X [39].

Four oxygen atoms are bonded to the heteroatom X in the tetrahedron form of Keggin, and in the octahedron configuration, where every metal atom is bonded to six oxygen atoms. Because the Keggin type has three axes of symmetry, different rotations are also possible, resulting in more isomers. Although five types of Keggin structures are feasible theoretically, only three of them have been well identified, formed, and isolated. One or more metal centers would be lost by treating the Keggin structure of POMs with alkaline solvents under suitable laboratory settings including temperature, pH, and concentration [40, 41].

As a consequence, the lacunary POM species are achieved with the structure associated with the Keggin series. For instance, the decline of Keggin XM_{12} leads to both lacunary types of XM_9 and XM_{11}, having high stability and widely used in the following form. The produced lacunary types also possess multiple isomers. The lacunary Keggin structure of POMs can interact with transition metals (including NiII, MnII, ZnII, FeIII, and CoII) or other types of elements with close characteristics (MoV, WVI, VV) to complete the vacant positions and fabrication of the doped Keggin type of POMs [41, 42]. The reaction of transition metals (such as FeIII, NiII, MnII, CoII, and ZnII) or other close-aspect species (such as WVI, MoV, and VV) with lacunary Keggin POMs results in the formation of replaced Keggin POMs [1, 43].

Dawson POM dimer is constructed by combining two lacunary Keggin monomers $XW_9O_{34}{}^{z-}$, with X/M = 2/18. The first architectures of the Dawson structure were produced more than a century ago. For example, Souchay (1947) [44] proposed a dimer formation in Dawson as evidence of the proportion, X/M =2/18. Dawson POMs have two structures: (i) trimetallic groups (M_3O_{13}), which are shaped by the union of three octahedral WO_6 even though defined in the Keggin form, and (ii) the condensation of two octahedral with metal atoms in the centers and oxygen atoms in the vertices producing bimetallic groups (M_2O_{10}). Each group is connected to two $XW_9O_{34}z$ pieces and the heteroatom X to produce the Dawson structure. Other POMs are formed when lacunary types from the Keggin or Dawson series react, and their composite and structure variations depend on the experimental attitudes [45, 46]. Sandwich form POMs, which lead to the composition of two lacunary entities, for example, XW_9 for Keggin or H_4XW_{15} and X_2W_{15} for Dawson dissymmetrical and symmetrical, respectively, through transition metal cations, are excellent candidates among the recently developed new structures (e.g., FeIII, MnII, CoII, NiII, ZnII). Weakley et al. [47, 48] identified the first synthesized sandwich POM in 1973. $K_{10}Co_4(H_2O)_2(PW_9O_{34})_2$ is generated by two Keggin PW_9O_{34} moieties connected using four Co centers. Mbomekalle et al. [49] first announced the fabrication of a "banana" formation in the early 2000s, followed by Ritorto et al. [50]. This form resembles a sandwiched POM to make a banana formation of POM, with two Keggin structures, $XW_9M_2M_0O_{40}$ or $XW_9M_3O_{40}$ (M and M_0 are various metal species) being bound to an XW_6O_{16} component. Other POM formations with excellent multi-dimensions have been fabricated to extend their functionalities. Some POMs are synthesized by varying the bond lengths, such as $H_6B_3W_{39}O_{13215}$ and $H_6B_2W_{26}O_{90}$, which are made of trimers or dimers of $H_3BW_{13}O468$ [45, 46]. Lastly, more complicated designs have been created using self-assembly processes combining organic ligands and polyoxo-anions [45, 51].

POMs have a wide range of content, structure, size, and charge, resulting in a large number of characteristics. In an aqueous solvent, for example, the majority of POMs exhibit solubility trends and act as strong acids [46]. The Hammett acidity constants (Ho) of the dense media of $H_3PW_{12}O_{40}$ and $4SiW_{12}O_{40}$ using water solutions containing 94.5% acetic acid and 40% aqueous dioxane were determined by Khozhevnikov et al. [52]. The acidity of $H_3PW_{12}O_{40}$ is higher than that of H_2SO_4 or $HClO_4$, as can be shown. Mineral acids, such as H_2SO_4 and H_3PO_4 can be replaced by POMs in homogeneous catalytic processes. Inorganic media, POMs, for example, show medium-dependent insolubility [53].

POMs can be considerably altered when mixed with organic moieties including ionic liquids or quaternary ammonium salts [54]. Certain POMs exhibit luminous properties; others, which include ferromagnetic transition metal atoms with free electrons, display anomalous magnetic characteristics and are being studied as nano-computer storage systems. Certain possible green outlooks of POMs have been studied including a nonchlorine-based, way of decontaminating water, and the wood pulp

Table 1.
Some characteristics of POM composite-based sensor systems

Author/Ref.	Composite	Target Substance	Linear range (μM)	Detection limit (μM)
Qian et al. [74]	POM@mrGO	NADH	5.0 10^{-9} M-5.0 10^{-4} M	0.4 nM
Yokus et al. [75]	POM-rGO/GCE	l-tyrosine (l-Tyr) and l-tryptophan (l-Trp)	1.0×10^{-11}–1.0×10^{-9} M	2.0×10^{-12} M
Yola, et al. [75]	rGO/POM	triclosan	0.5–50.0 nM	0.15 nM
Li et al. [76]	MWNTs/PMo12	bromate	5 μM-15 mM	0.5 μM
Ertan et al. [77]	PtNPs/POM/MWCNs/GCE	simazine	1.0×10^{-10} - 5.0×10^{-9} M	2.0×10^{-11} M
Haghighi et al. [78]	GCE/MWCNTs/[C8Py][PF6]-PMo12	IO_3^-	2×10^{-5}-2×10^{-3} M	15 μM
		H_2O_2	2×10^{-5} -8×10^{-3} M	12 μM
Anwar et al. [79]	Cu2+/ POM- 2 mM	H_2O_2	up to 2 mM	0.3 μM
	Fe^{3+}/POM-doped polypyrrole			0.6 μM
Ayranci et al. [80]	POM/PAAC	glucose	0.1-10 mM	0.099 mM
Babakhanian et al. [81]	PPy–α-POM–AuNPs	folic acid	-	12 nM
Wang et al. [82]	Pd/POMs/NHCSs	acetaminophen	0.63 μM -0.083 mM	3 nM
Karimi-Maleh et al. [83]	PtNPs/POM/2D-hBN	N hydroxy succinimide	0.1-300 μM	60 nM
Zhang et al. [64]	$Ru(bpy)_3Cl_2{\cdot}6H_2O$ $H_7P_2Mo_{17}V_1O_{62}$ ($P_2Mo_{17}V$) ($Ru(bpy)_3$) /chitosan-palladium (Cs-Pd),	ascorbic acid	0.125–118 μM	0.1 μM
Zhou et al. [65]	$(P_2W_{16}V_2$-AuPd/PEI$)_8$	dopamine	2.1×10^{-6}-2.06×10^{-3} M	8.3×10^{-7} M
		ascorbic acid	1.2×10^{-6}-1.61×10^{-3} M	4.3×10^{-7} M

bleaching method. Numerous medicinal and biological characteristics of POM structures have been studied such as anti-bacterial, anti-viral, and anti-tumoral aspects [55, 56]. Fluorescent microspheres produced from Lindqvist POM covalently linked to pyrene groups, for example, have been used to detect foodborne illnesses [57, 58].

POMs, including inorganic molybdenum and/or tungsten with rare earth (RE) cores, were also demonstrated to be good illuminating probes. Cryogenic optic thermal probes made of polyoxomolybdate basic elements containing TbIII and EuIII ions, for example, have been explored. Moreover, the luminescence properties of RE-combining POMs are significantly delicate to the chemical media [59, 60].

Brown and blue POMs are formed when POMs are decreased. POMs in their oxidized form may adapt to and provide a specified quantity of electrons with no modification or disintegration in their construction. Except in rare circumstances where production is curtailed without adequate stability in the mixture, re-oxidation of reduction in POMs formation reforms oxidation structures. POMs-based redox systems are electrochemically quick in general. As a result, decreased POM formations can participate in numerous electrocatalytic cycles [61, 62].

To capitalize on these redox characteristics, POMs are selectively deposited on substances for heterogeneous electrocatalysis. Many researchers, who worked in the field of immobilized electrochemistry POM structures on solid surfaces, observed that the physicochemical features of POMs were frequently conserved after immobilization. Analytical devices, including a POM-based sensor that includes a POM rendered immobile on a solid surface are known as the transducer [61, 63]. Unless the POM's characteristics and structure after immobilization are preserved, this will catalyze and identify the analyte. The chemical process method caused by the distinction between both the analyte and then the immobilized POM would be converted to an electric signal, that will be amplified and transformed into a demonstration via a signal processing instrument (Fig. 2). The detection limit and stability, response time, sensitivity, linear range, and selectivity are all important properties of a POM-based sensor, the same as other sensors [64].

3. Insertion of dopant ions in POMs

Chemical modification of the POM formation, such as the incorporation of redox-active metal centers, can fine-tune the exact electrochemical characteristics including the number of electrons stored and redox potentials [65, 66]. Shi et al. [67] created polyoxometalates (POMs) and TiO_2 nanostructured materials by combining various POMs, including K_5 [$PW_{11}TiO_{40}$] and titanium-substituted POMs K_7 [$PW_{10}Ti_2O_{40}$] with TiO_2 nanoparticles to modify the crystalline structure of TiO_2 nanoparticles. In addition, the photoconductivity of TiO_2/POM nanocomposites is proportional to the difference in conduction bands between TiO_2 and POMs. Furthermore, TiO_2/PW_{11}Ti demonstrated excellent acetone gas sensing capabilities. These findings show that TiO_2/POM nanocomposites have excellent photoelectric characteristics as compared to pure TiO_2 nanoparticles, which is due to the interface modification with various POMs. Using cationic poly (diallyl dimethylammonium chloride) functionalized reduced polyoxometalates clusters $K_8P_2W_{16}V_2O_6$ combined with anionic Au nanoparticles ($P_2W_{16}V_2$-Au) and graphene oxide. Bai et al. [68] developed an accurate electrochemical biosensor for UA detection (PDDA-rGO). The effective combination of PDDA-rGO and $P_2W_{16}V_2$-Au offers several advantages in electrochemical detection, including more sensing sites, unimpeded diffusion pathways, and faster electric charge transfer. Under optimal circumstances, the amperometric i-t sensitivity of a modified PEI/[$P_2W_{16}V_2$-Au/PDDA-rGO] electrode was used to add different densities of UA to a swirling 0.2 M PBS (pH = 7.0) for 1700 s at 50 s former at a potential range of +0.43V, resulting in good analytical results for UA. The electrode has a consistent and well-defined amperometric response to the supplied UA, with the responsiveness of lefewerhan equal to 3 seconds. The calibration plot demonstrates a satisfactory linear correlation in the range of 2.5×10^{-7} - 1.025×10^{-4} M, with R_2 = 0.9912. I = -0.01406 + 0.24092 × CUA, which denotes the linear regression model. The limit of detection (LOD) is 1.4

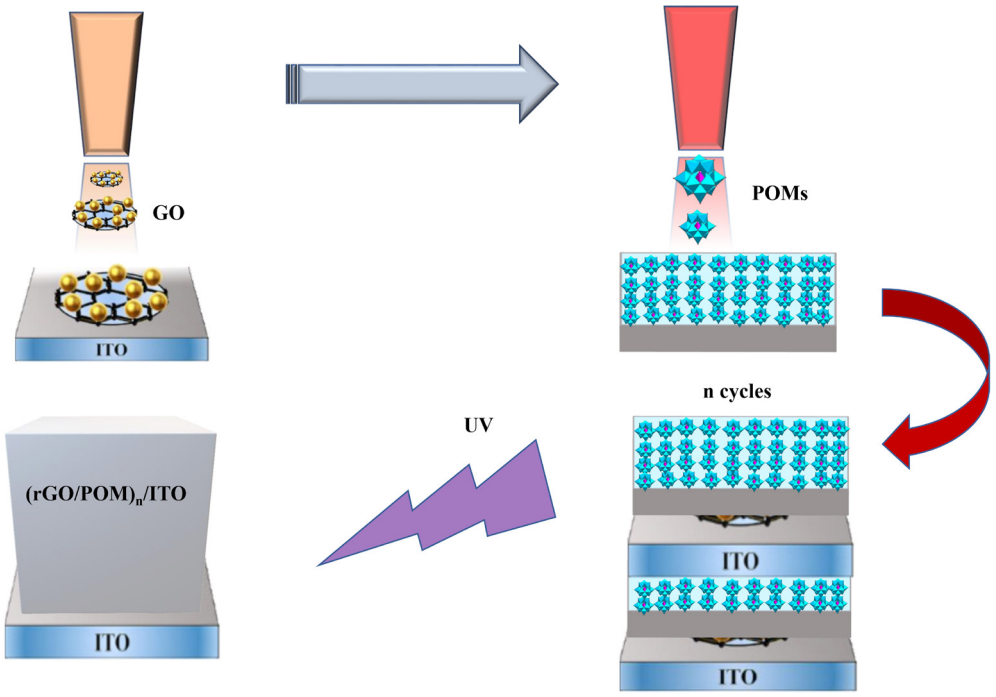

Fig. 3. The schematic of LbL growth via inkjet printing is used to fabricate (rGO/POM)n multi-layer films.

× 10^{7} M, and the responses are 0.24 A M1 based on a signal-to-noise ratio of 3 (S/N = 3).

Shen et al. [69] produced L-cysteine-doped tungstosilicate (Lcys-SiW_{12}) microtubes by altering them slightly. The ammonia gas sensitivity of synthesized Lcys-SiW_{12} microtubes is demonstrated by the unique color change of microtubes from a purple color after being exposed to ammonia gas turning to a dark blue color throughout the skin. The adsorbed ammonium molecules may raise the basicity of the Lcys-SiW_{12} microtubes, hence enhancing the redox process between L-cysteine and polyoxometalate, as a possible method for the coloration. The proton capture agent initiates a pH-dependent solid-solid redox process. Alkaline gas chemical sensors have been developed using Lays-SiW12 microtubes.

Sensitive analytical procedure enhancement, which is significant for a healthy lifestyle, was reported by Medetalibeyolu et al. [70]. The electrochemical behavior of electrodes was studied using hexagonal boron nitride (2D-hBN) nanosheets, molecularly/polyoxometalate (POM), and gold nanoparticles (AuNPs). Cyclic voltammetry (CV), differential pulse voltammetry (DPV), electrochemical impedance spectroscopy (EIS), and imprinted polymer (MIP) were also employed in their work. The DIA imprinted electrode had a highly sensitive response to DIA as-fabricated and presented a wide linear range. In addition, the LOD was 3.0×10^{-12} M. The modified detector was successful in detecting DIA in fruit juices [68].

Triacetone triperoxide (TATP), a homemade explosive, is simple to make and sensitive to the selection, but difficult for detection directly. Vapor sensing using arrays made up of only a few distinct sensor materials can differentiate TATP; however, manufacturing a stable sensor has always been difficult since each sensor may experience a device malfunction [71, 72]. To identify TATP from other explosives, a sensor array built on a single photonic TiO_2/PW_{11} sensor was created initially, with the excitation wavelength being controlled. Situ doping of $Na_3PW_{12}O_{40}$ on TiO_2 resulted in the production of a Keggin type of PW_{11}, which increased the sensor film detection sensitivity and response time, and facilitated photo-induced electron-hole separation, according to Lu et al. [72]. The TiO_2/PW_{11} sensor film has TATP sensitivity at 81, 37, and 42% under 365, 550, and 450 nm illumination, respectively. The TiO_2/PW_{11} sensor has TATP selectivity and can measure concentrations of less than 50 ppb. The amount of bending also demonstrates the stability and flexibility of the flexible sensor film. Moreover, ambient air with a relative humidity of less than 60% cannot influence the sensing response [73].

4. POM-based composites for sensor systems

Over the last decade, several PCM architectures have been developed under various preparation conditions. According to their various hybrid structures, PCMs are divided into three groups in this review: (1) POM-based conductive polymer composites, (2) POM-based nanocarbon composites, and (3) POM-based metal composites, which are all examples of POM-based composites. The characteristics of various POM composite-based sensors are indicated in Table1.

4.1. POM-nanocarbon composites

The enhancement of developed composition materials based on nanostructured carbons and POMs has garnered a lot of attention because they combine the incredible electronic properties of nanocarbon with the desirable chemical reactivity of POMs. The ability of POMs to initiate changeable multi-electron redox processes makes them appealing for amperometric sensor applications. Because of their capacity to trigger variable multi-electron redox reactions, POMs are intriguing for amperometric sensor usages. To achieve low selectivity, POMs must be immobilized or anchored on conductive substrates to maximize amperometric response while preserving molecular distribution. As a result, graphene and CNTs make excellent sensor substrates [25, 67, 84].

4.1.1. POM-graphene composites

Carbon compounds enhance the conductive surface area. Because of the strong electrical interactions among carbon materials and POMs, electrochemical features of carbon materials and POM compositions have been developed significantly [85-87]. Ji et al. [88] have recently proposed a highly advanced technique for nanocarbon layered electrodes/POM that could be used for automated and large-scale produc-

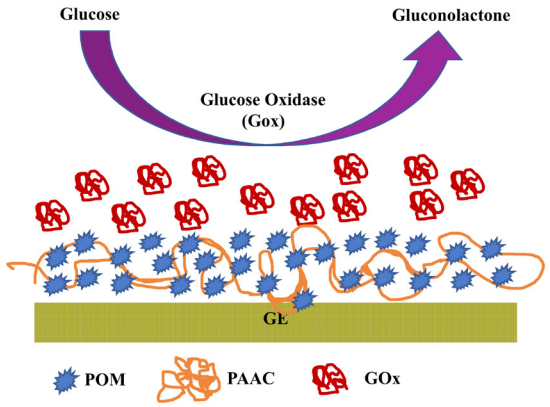

Fig. 4. Schematic design of a sensor platform contained metal/organic hybrid composite film based on POM/PAAC.

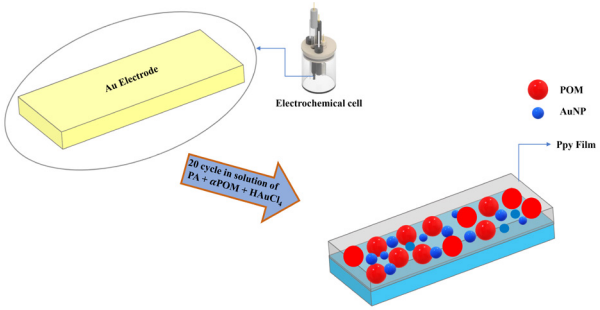

Fig. 5. The schematic of the synthesis of PPy–α-POM–AuNPs film; the Au electrode is shown schematically.

tion. The team used inkjet printing and a combination of layer-by-layer (LbL) processes for assembling the layered PW12/rGO composites (Fig. 3). LbL growth of a thin-film composition was linear, regular, and uniform. A POM-driven photo-reduction transformed GO to rGO under ultraviolet light, and the components were employed as high-response dopamine sensor devices.

Zhang et al. [89] used a layer-by-layer inkjet printing technique to make a multilayer film out of polyoxometalates such as $H_3PW_{12}O_{40}$ (PTA) and graphene oxide (GO) nanosheets. The composition of PTA/rGO film has an excellent electrocatalytic activity for the oxidized dopamine DA, according to cyclic voltammograms measurements. The oxidation peak current (Ipa), which can be used in electrochemical biosensors, increases gradually as the dopamine concentration rises.

The composition of polyoxometalate (POM) versatility coated reduced GO (POM@mrGO)/magnetic Fe_3O_4 as an embolization composite for the electrochemiluminescence (ECL) agent by bpy^{32+} was investigated by Qian et al. [90]. When compared to $Ru(bpy)^{32+}$ /Nafion@mrGO, which is increasing due to POMs high electro-catalytic interaction towards NADH oxidation, the efficient modification of POM@mrGO/$Ru(bpy)^{32+}$ hybrid easily implicated a magnetic electrode for about the equal density of nicotinamide adenine dinucleotide (NADH), which also resulted in a 10-fold increase in ECL intensity. The stable and ultrasensitive ECL monitoring of NADH at concentrations as low as 0.1 nM was made possible by this sort of finding. The manufactured biosensor has an extraordinarily decreased LOD of 0.4 nM and outstanding efficiency, with a linear curve range extending from 5.0 10^{-9} M to 5.0 10^{-4} M. This sensing technique may be defined as a biocompatible and novel substrate for dehydrogenase-based ECL biosensors since it combines facile sensor production with enzymatic selectivity. This research demonstrates a simple method for immobilizing ECL types within the versatile POM@mrGO support matrix and encourages the enhancement of magneto-controlled ECL biosensing for use in bioanalytical and analytical fields [32].

Yukos et al. [91] developed a polyoxometalate ($H_3PW_{12}O_{40}$, POM) and reduced graphene oxide (rGO) to change glassy carbon electrode (GCE) voltammetric sensor for concurrent determination of l-tryptophan (l-Trp) with l-tyrosine (l-Tyr). One of the developed methods was also used to successfully determine l-Tyr and l-Trp in spiked serum samples, with the LOD of 2.0×10^{-12} M and the linearity range of 1.0×10^{-11} - 1.0×10^{-9} M. Because of its widespread use in medical equipment, personal care products, and household cleaning products, triclosan (TCS) poses a significant risk to the environment and human health due to its toxic effects on aquatic organisms and leakage into groundwater supplies, surface water, and sediments.

Yola, et al. [76] invented a molecular-imprinted reduced GO/gold nanomaterials electrochemical sensor decorating polyoxometalate ($H_3PW_{12}O_{40}$). The functionalization of rGO using POM to produce a photocatalyst (rGO/POM) in an aqueous solution for detecting traces of TCS within wastewater via electrostatic interaction between rGO and POM nanosheets. Without using any reducing agent, gold nanoparticles (AuNPs) were deposited on the rGO/POM, and the synthesized nanomaterial (AuNPs/POM/rGO) was used for the modification of a glass carbon (GC) electrode (AuNPs/POM/rGO/GC) under infrared light. TCS-imprinted film was created on AuNPs/POM/rGO/GC using TCS and phenol polymerization and characterized using cyclic voltammetry (CV) and electrochemical impedance spectroscopy (EIS). TCS limit and linear detection range of the sensor were found to be 0.15 nM and 0.5 – 50.0 nM, respectively. When compared to other complicated methods, the molecularly imprinted sensor performed well on lake water samples and wastewater.

4.1.2. POM-carbon nanotube composites

Iodate and bromate are suspected carcinogens that are formed in drinking water as a result of ozone treatment. As a result, in situ detection is a hot topic in the industry. Li et al. [76] solved the problem by developing an MWNTs/PMO_{12} composite film based on an amperometric bromate sensor. The device feature has a 5-15 mM linear range, reaction times of less than 2 s, a sensitivity of 760.9 μA $mM^{-1}.cm^{-2}$, and a LOD of 0.5 M.

Based on this research, Qu et al. [77] conceived and developed MWNTs methyl silicone oil and a set of electrodes made of carbon nanotube paste (CNTP). Direct and indirect methods were used to assemble Keggin and Dawson types of POM anions on the CNTP electrode surface. The Dawson-anion of P_2MO_{18} structure proved to be a promising device, demonstrating effective bromate and iodate electrocatalytic reduction. A follow-up study used the LbL approach to create multilayered films of $(P_2Mo_{18}/PDDA)_n$ on CNTP electrodes, and comparative studies demonstrated that the LbL-assembled composites had higher electro-catalytic activity than the direct electrostatically generated composites.

Gue et al. [78] devised a chemically modified electrode with the distribution of CNTs in cationic chitosan films and applied it for electrostatically-immobilized Dawson anions of the P_2W_{18} structure. Electrochemical investigations showed that the P_2W_{18}/CNT/chitosan electrode had strong electrocatalytic activity, a fast response to reduce peroxodisulfate iodate, anions in acidic aqueous media. It was also stated that the sensor performed in acidic solutions, enhancing its application in different industries.

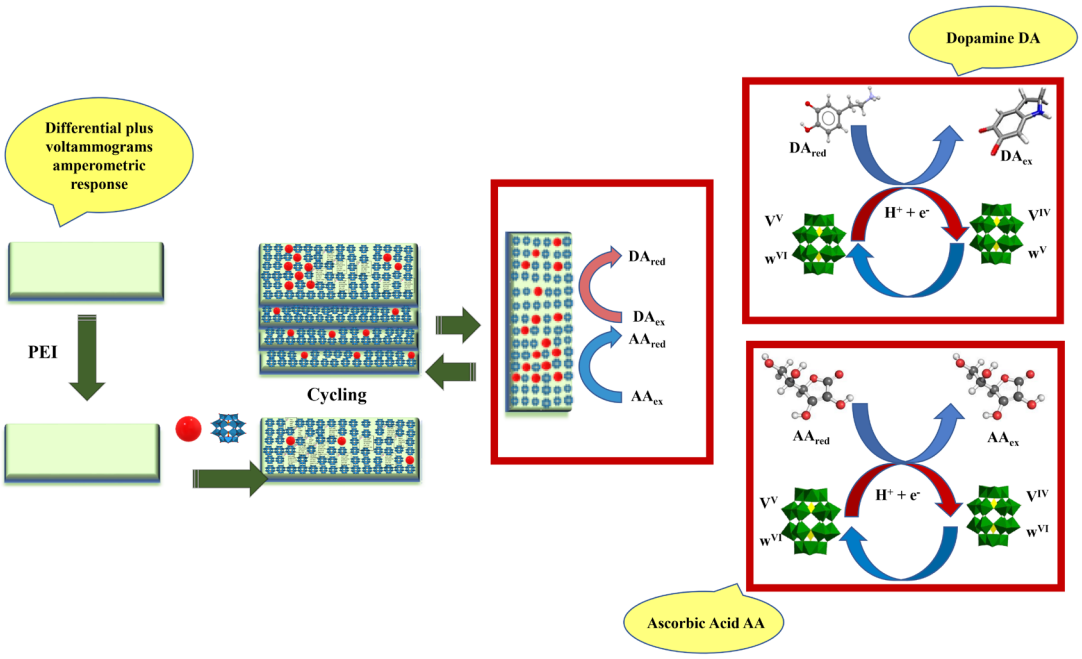

Fig. 6. The schematic design of the layer-by-layer self-assembly method.

To assess simazine (SIM), novel molecular imprinting voltammetric sensors are built on a glassy carbon electrode (GCE) altered with platinum nanoparticles (PtNPs) included in polyoxometalate ($H_3PW_{12}O_{40}$, POM) functionalized multi-walled carbon nanotubes (MWCNs) sheets as reported by Ertan et al. [79]. SIM imprinted GCE was synthesized by electro-polymerizing 100 mM pyrrole as the unit in 0.1 M acetate buffer (pH 4.0) with 25 mM SIM LOD. The linearity ranges of the developed method were determined to be 2.0×10^{-11} M and 1.0×10^{-10} - 5.0×10^{-9} M, respectively. Water samples were also tested using the voltammetric sensor.

Sahraoui et al. [92] successfully designed a Keggin-type metatungstate hybrid POMs ((APy) 6[$H_2W_{12}O_{40}$])/carboxylic acid-synthesized SWCNT-based amperometric sensor for hydrogen peroxide sensing. In the existence of SWCNTs, the sensitivity of hydrogen peroxide detection enhanced by a factor of 38.5, demonstrating their strong effect on peroxidase-like mimics of (APy) 6[H2W12O40]. Answer time, repeatability, and shelf life were 10 seconds, 4%, and 60 days, respectively. The LOD was 0.4 M in the presence of covalently bonded SWCNT. A linear plot was achieved in both aspects when the experimental data were viewed as Lineweaver-Burker plots, indicating Michaelis-Menten actions.

Dip-coating n-octyl pyridinium hexafluorophosphate ([C_8Py][PF_6]) and 1:12 phosphomolybdic acid (PMo_{12}) on glassy carbon electrodes modified using multiwall carbon nanotubes (GCE/MWCNTs) resulted in the formation of n-octyl pyridinium hexafluorophosphate ([C_8Py][PF_6], as reported by Haghighi et al. [93] who generated a robust and stable layer. The cyclic voltammograms of the GCE/MWCNTs/[C_8Py][PF_6]- PMO_{12} system exhibited three well-defined pairs of redox peaks attributable to the PMO_{12} system. The reduction of H_2O_2 and iodate was electrocatalyst with high efficiency by the GCE/MWCNTs/[C_8Py][PF_6]-PMO_{12}. With a correlation coefficient of 0.9999, the calibration plot for H_2O_2 determination is linear between 2×10^{-5} and 8×10^{-3} M. The LODs for H_2O_2 (signal to noise ratio = 3) and sensor sensitivity are 12 M and 73 A mM^{-1} cm^{-2}, respectively. Amperometric tests were also performed to determine IO_3^-. The IO_3^- detector calibration plot was linear between 2×10^{-3} M and 2×10^{-5} M, with LODs and sensibility of 190 A mM^{-1} cm^{-2} and 15 M, respectively.

4.2. POM-conductive polymer composites

The redox-active substrate binding sites of the molecularly scattered POMs signal the presence of substrates, whereas the CP translates the signal into electrical information for greater (quantitative) detection, making POM/CPs ideal composites for substrate sensing [80, 81, 94]. A composite film of Dawson anions trapped in electropolymerized PPy has recently been claimed by Anwar et al. [95]. With a 0.3 mM LOD, the compounds were employed as hydrogen peroxide amperometric sensors. In a pH range of 2–7, voltammetric analyses of redox processes were connected to all components, indicating highly stable redox reactions. Only transition-metal-functionalized Dawson anions (M = Fe^{3+}, Cu^{2+}, Co^{2+}) ([$P_2W_{17}O_{61}$M]n$^-$) were used to detect H_2O_2. Fe^{3+} and Cu^{2+} substituted in POM-doped polypyrrole films had LODs of 0.6 and 0.3 µM in order, with a linear region ranging from 0.1 - 2 mM H_2O_2. H_2O_2 was detected using only transition-metal functionalized Dawson anions (M =Fe^{3+}, Cu^{2+}, Co^{2+}) ([$P_2W_{17}O_{61}$M]n$^-$) . Cu^{2+} and Fe^{3+} substituted POM-doped polypyrrole films having a linear area extending from 0.1 to 2 mM for H_2O_2 had LODs of 0.3 and 0.6 µM, correspondingly.

Ammam et al. [96] reported using the composition of POM/CP for gas sensing, demonstrating that the nanostructured composition of POM/PPy can be utilized for the detection of NOx. The Dawson anion P_2Mo_{18} was used as an oxidant to polymerize pyrrole in situ. The resultant semiconducting composite had high selectivity for gaseous NOx detection and a wide NO_x-concentration-dependent linear response. They used a hybrid material made of polypyrrole and $K_6P_2Mo_{18}O_{62}.nH_2O$ to create sensitive and selective NO_x sensors with broad linearity (up to 5500 ppm NO_x).

Ayranci et al. [97] devised a new composite film-based amperometric glucose sensor, made via electrochemical polymerization of carbazole derivatives with free amino groups being of the Keggin kind of POM anion, (nBu$_4$N)$_3$[PW_9O_{34}(tBuSiOH)$_3$]. POM was entrapped in the produced PAAC polymer film during the electropolymerization process of 3-amino-9-ethyl carbazole (AAC) on the graphite electrode. Negatively charged POM structures were used to create a metal/organic conducting polymeric composite and a positively charged PAAC-based conducting polymer. The amperometric response of the POM/PAAC-GOx modified electrode was investigated by varying concentrations of glucose

at a potential of -0.7 V (Ag/AgCl). Among the composition structures synthesized at different ratios, the composite structure of POM/PAAC, owing to the best sensor response, had the lowest oxidation potential. The POM/PAAC sensor device had a sensitivity of 66.66μA $mM^{-1}cm^{-2}$ for actual glucose detections, with a LOD of 0.099 mm and a linear LOD of 0.1-10 mm. Because of the multiple redox reactions, rapid electron transfer, and high reactivity of POMs, the composition of POM/PACC possesses a desirable structure. This composite, in particular, showed a rapid response time with high electrocatalytic activity for amperometric glucose detection, reproducibility, and good sensitivity, as well as simple preparation as prepared and acceptable recovery (Fig. 4).

By using the cyclic voltammetry (CV) approach, Babakhanian et al. [82] electrochemically produced (-POM) (K7PMO2W9O39.H2O) and AuNPs doped into electropolymerized polypyrrole (PPy) film. The PPy–POM–AuNPs modified gold (Au) electrode was used to determine folic acid (FA) using square-wave voltammetry (SWV). With an electron transfer rate constant (ks) of 1.15 10^{19} s^{-1} at 0.3 V (vs. SCE), the improved electrode demonstrated better electrocatalytic capability in the reduction of FA. Common coexisting chemicals did not affect the changed electrode response to FA. The LOD and RSD measurements of the proposed method achieved 0.12 nM and 5.3%, respectively, for eight repeated measurements. During the experiments, the modified electrode demonstrated high-level stability and repeatable behavior, making it ideal for analytical applications (Fig. 5).

The synthesis of polypyrrole-polyoxometalate hybrid polymer films and their performance for resistive-type humidity sensors were reported by Miao et al. [98]. Co-electrodeposition of free pyrrole units with metal oxide groups resulted in hybrid polymer films of various thicknesses. A 59 nm-hick sample with a sensing range of 11-98% relative humidity revealed a sensing answer of 1.9 s and a healing process of 1.1 s at 98% humidity levels and a sensing range of 11-98% humidity. The physicochemical properties of the oxidation doping component and the proton acid doping component might be explained by considerable sensitivity in the polypyrrole chain. Even after two months, the nanocomposite-based humidity sensor was repeatable, with recovery times and good response. It was discovered that as the humidity level rose, the sensor conductance rose as well.

4.3. POM-metal composites

Because of their proton and electron storage and/or transfer abilities, POMs can emerge as effective acceptors or donors of numerous electrons in reduced forms without undergoing any structural changes. Reduced POMs have been shown to act with both capping and reductants for POMs, and noble-metal NPs have also been identified as green reduction/oxidation and environmentally friendly agents [64, 83, 99].

Wang et al. [100] synthesized Pd/POMs/NHCSs tri-component nanohybrids with the catalytic rate constant (kcat) of 2.34103 $M^{-1}s^{-1}$ and electrocatalytic activity for oxidized acetaminophen (AP) with a diffusion coefficient (D) of 6.1810^{-5} cm^2s^{-1} due to the synergistic actions of NPs, Pd, and NHCSs. They evaluated the usage of POMs/Pd/NHCSs as an effect on determining the template of AP for electrochemical detection, which demonstrated exceptional analytical performance, including a linear region of 0.02-0.63 μM with a sensitivity of 508.46 AmM^{-1}, a linear range of 0.63 M to 0.083 mM with a low LOD of 3 nM, and sensitivity of 154.27 μAmM^{-1}.

They produced a Pd/POMs/NHCSs-GCE-based sensitive electrochemical sensor for AP that had a broad linear range, superior sensitivity, low LOD, and high stability. Karimi-Maleh et al. [101] developed an N-hydroxysuccinimide sensor using a carbon paste electrode (CPE) amplified with a 1-hexyl-3-methylimidazolium chloride (HMICl) and tri-component nanohybrid composite (Platinum nanoparticle/Polyoxometalate/two-dimensional hexagonal boron nitride nanosheets) (PtNPs/POM/2D-hBN) as conductive mediators. HMIClPtNPs/POM/2D-hBN/POMBNS/CPE led to a remarkable reduction (110 mV) in oxidation overvoltage and a considerable increase (2.4 times) in the N-hydroxysuccinimide current. Moreover, the HMICl- PtNPs/POM/2DhBN/POMBNS/CPE showed high linearity from 0.1 to 300 μM and a LOD of 60 nM for N-hydroxysuccinimide determination. The ability to promote electron exchange between HMICl-PtNPs/POM/2D-hBN/POMBNS/CPE and N-hydroxysuccinimide demonstrated a novel analytical trend to fabricate a water pollutant sensor. In comparison to other electrodes, the PtNPs/POM/2D-hBN presented excellent characteristics such as great specific surface area and high electrical conductivity, as well as the role of HMICl as a conductive binder, helping to modify the oxidation signal of N-hydroxysuccinimide at the surface of HMICl-PtNPs/POM/2D-hBN/POMBNS/CPE.

Zhang et al. [102] developed a remarkably sensitive non-enzymatic electrochemical sensor based on an inorganic-organic nanocomposite film made up of chitosan-palladium (Cs-Pd) that was used to measure ascorbic acid (AA) and $H_7P_2Mo_{17}V_1O_{62}$ ($P_2Mo_{17}V$), $Ru(bpy)_3Cl_2{\cdot}6H_2O$ ($Ru(bpy)_3$). Because of the composition of three active components in the latest film, the non-enzymatic sensor has some benefits, including excellent sensitivity, simple production and operation, and good reproducibility, which overcome the disadvantages of enzyme-based sensors such as fast inactivation and limited immobilization. The sensor has excellent sensing performance for ascorbic acid detection with a low LOD of 0.1 μM (S/N = 3), a fast response time of 2 seconds, and a wide linear range of 0.125 – 118 μM. The sensor was also used to detect AA in juice with success. Zhou et al. [65] produced a new composite film based on Dawson-type phosphovanadotungstate $K_8P_2W_{16}V_2O_{62}{\cdot}18H_2O$ ($P_2W_{16}V_2$) decorated with Au–Pd alloy nanoparticles (Au–Pd) on quartz, ITO and silicon by the layer-by-layer self-assembly technique. The mixture film can be used to identify ascorbic acid and dopamine at biological pH in a simultaneous and sensitive determination (pH 7.0). Linear curves were achieved in the ranges of 1.2×10^{-6}-1.61×10^{-3} M and 2.1×10^{-6}-2.06×10^{-3} M for ascorbic acid and dopamine in order, by DPV procedures. Dopamine and ascorbic acid had low LODs of 8.3×10^{-7} M and 4.3×10^{-7}, respectively. Ascorbic acid and dopamine determinations in real samples were performed successfully using the composite film. The proposed electrochemical sensor has high selectivity and sensitivity, making it a simple method for determining ascorbic acid and dopamine simultaneously in practical applications (Fig. 6).

5. Conclusions and future insight

This literature review provided an overview of the promising performance of POMs and POM-based composites as well as their structures and properties. The structure of these materials varies from Keggin and Dawson to a variety of other structures such as wheels, sandwiches, bananas, and other forms. POMs-based composites have attracted much attention because of their multitudinous architectures and excellent redox activities as well as convenient proton and electron transport capacities, which are one of the candidates for functional components in a variety of functions, according to the findings. This review specifically highlighted the use of POM-based composites as sensors. A more detailed focus has been made on the combination of POMs and nanocarbon structures owing to the extensive availability and cost-effectiveness of POM/nanocarbon composites. A combination of nanostructured carbons and POMs, combining the excellent electronic properties of nanocarbon with the outstanding chemical reactivity of POMs, has led to its application in amperometric sensors mainly due to their alterable multi-electron redox behavior. The future growth of POM/nanocarbon compositions is not limited. There are joint projects that combine polyoxometalate chemists, device fabrication experts, and experience of nanocarbon expertise fo-

cusing on real-life technology that can produce self-assembled POM and nanocarbon components. As it can be seen, investigating novel materials with higher proton and electron conductivity, activity, and stability is always essential in promising technologies and is found to capture the way for future development of POM science, for which POMs are one of those promising materials.

REFERENCES

[1] M. Ammam, Polyoxometalates: formation, structures, principal properties, main deposition methods and application in sensing, Journal of Materials Chemistry A 1(21) (2013) 6291-6312.
[2] X. An, Q. Tang, H. Lan, H. Liu, J. Qu, Polyoxometalates/TiO_2 Fenton-like photocatalysts with rearranged oxygen vacancies for enhanced synergetic degradation, Applied Catalysis B: Environmental 244 (2019) 407-413.
[3] S. Li, G. Li, P. Ji, J. Zhang, S. Liu, J. Zhang, X. Chen, A Giant Mo/Ta/W Ternary Mixed-Addenda Polyoxometalate with Efficient Photocatalytic Activity for Primary Amine Coupling, ACS applied materials & interfaces 11(46) (2019) 43287-43293.
[4] L. Bazli, M.H. Bagherian, M. Karrabi, F. Abbassi-Sourki, H. Azizi, Effect of starch ratio and compatibilization on the viscoelastic behavior of POE/starch blends, Journal of Applied Polymer Science 137(29) (2020) 48877.
[5] A. Misra, K. Kozma, C. Streb, M. Nyman, Beyond Charge Balance: Counter-Cations in Polyoxometalate Chemistry, Angewandte Chemie International Edition 59(2) (2020) 596-612.
[6] N.I. Gumerova, A. Rompel, Polyoxometalates in solution: Speciation under spotlight, Chemical Society Reviews (2020).
[7] Z.-F. Chen, Y.-L. Yang, C. Zhang, S.-Q. Liu, J. Yan, Manufacture of non-aqueous redox flow batteries using sulfate-templated Dawson-type polyoxometalate with improved performances, Journal of Energy Storage 35 (2021) 102281.
[8] Q. Chen, C. Shen, L. He, Recent advances of polyoxometalate-catalyzed selective oxidation based on structural classification, Acta Crystallographica Section C: Structural Chemistry 74(11) (2018) 1182-1201.
[9] J. Xu, Z. Zhang, K. Yang, W. He, X. Yang, X. Du, L. Meng, P. Zhao, Z. Wang, Construction of new transport channels by blending POM-based inorganic-organic complex into sulfonated poly(ether ketone sulfone) for proton exchange membrane fuel cells, Journal of Membrane Science 596 (2020) 117711.
[10] D. Wang, L. Liu, J. Jiang, L. Chen, J. Zhao, Polyoxometalate-based composite materials in electrochemistry: state-of-the-art progress and future outlook, Nanoscale 12(10) (2020) 5705-5718.
[11] C. Boskovic, Rare earth polyoxometalates, Accounts of chemical research 50(9) (2017) 2205-2214.
[12] A. Al-Yasari, H. El Moll, R. Purdy, K.B. Vincent, P. Spence, J.-P. Malval, J. Fielden, Optical, third order non-linear optical and electrochemical properties of dipolar, centrosymmetric and C_{2v} organoimido polyoxometalate derivatives, Physical Chemistry Chemical Physics 23(20) (2021) 11807-11817.
[13] M. Guzel, Y. Torlak, E. Karatas, M. Ak, Optical and electrical properties of monolacunary Keggin-type polyoxometalate/star-shaped polycarbazole nanocomposite film, Journal of The Electrochemical Society 166(8) (2019) H313.
[14] J. Lei, J.J. Yang, T. Liu, R.M. Yuan, D.R. Deng, M.S. Zheng, J.J. Chen, L. Cronin, Q.F. Dong, Tuning Redox Active Polyoxometalates for Efficient Electron-Coupled Proton-Buffer-Mediated Water Splitting, Chemistry (Weinheim an der Bergstrasse, Germany) 25(49) (2019) 11432.
[15] X. Wei, K. Ma, Y. Cheng, L. Sun, D. Chen, X. Zhao, H. Lu, B. Song, K. Yang, P. Jia, Adhesive, Conductive, Self-Healing, and Antibacterial Hydrogel Based on Chitosan–Polyoxometalate Complexes for Wearable Strain Sensor, ACS Applied Polymer Materials 2(7) (2020) 2541-2549.
[16] Y. Xia, P. Wu, Y. Wei, Y. Wang, H. Guo, Synthesis, Crystal Structure, and Optical Properties of a Polyoxometalate-Based Inorganic− Organic Hybrid Solid,$(n\text{-}Bu_4N)_2$ $[Mo_6O_{17}$ (= $NAr)_2$](Ar= o-$CH_3OC_6H_4$), Crystal growth & design 6(1) (2006) 253-257.
[17] P. Ma, F. Hu, J. Wang, J. Niu, Carboxylate covalently modified polyoxometalates: From synthesis, structural diversity to applications, Coordination Chemistry Reviews 378 (2019) 281-309.
[18] S. Derakhshanrad, M. Mirzaei, C. Streb, A. Amiri, C. Ritchie, Polyoxometalate-based frameworks as adsorbents for drug of abuse extraction from hair samples, Inorganic Chemistry 60(3) (2021) 1472-1479.
[19] Y.-L. Zou, H.-Y. Li, W. Zhou, X.-G. Cui, G.-H. Zou, G.-Z. Shen, Introduction of the antibacterial drugs norfloxacin and Ciprofloxacin into a polyoxometalate structure: Synthesis, characterization, and antibacterial activity, Journal of Molecular Structure 1205 (2020) 127584.
[20] T.R. Bastami, A. Ahmadpour, Preparation of magnetic photocatalyst nanohybrid decorated by polyoxometalate for the degradation of a pharmaceutical pollutant under solar light, Environmental Science and Pollution Research 23(9) (2016) 8849-8860.
[21] H. Wu, M. Zhi, H. Chen, V. Singh, P. Ma, J. Wang, J. Niu, Well-tuned white-light-emitting behaviours in multicenter-Ln polyoxometalate derivatives: A photoluminescence property and energy transfer pathway study, Spectrochimica Acta Part A: Molecular and Biomolecular Spectroscopy 223 (2019) 117294.
[22] S.A. Alshehri, A. Al-Yasari, F. Marken, J. Fielden, Covalently Linked Polyoxometalate–Polypyrrole Hybrids: Electropolymer Materials with Dual-Mode Enhanced Capacitive Energy Storage, Macromolecules (2020).
[23] M.R. Horn, A. Singh, S. Alomari, S. Goberna-Ferrón, R. Benages-Vilau, N. Chodankar, N. Motta, K.K. Ostrikov, J. MacLeod, P. Sonar, Polyoxometalates (POMs): from electroactive clusters to energy materials, Energy & Environmental Science 14(4) (2021) 1652-1700.
[24] X. Xin, N. Hu, Y. Ma, Y. Wang, L. Hou, H. Zhang, Z. Han, Polyoxometalate-based crystalline materials as a highly sensitive electrochemical sensor for detecting trace Cr (VI), Dalton Transactions 49(14) (2020) 4570-4577.
[25] C. Zhou, S. Li, W. Zhu, H. Pang, H. Ma, A sensor of a polyoxometalate and Au–Pd alloy for simultaneously detection of dopamine and ascorbic acid, Electrochimica Acta 113 (2013) 454-463.
[26] C. Sabarinathan, M. Karthikeyan, R. Murugappan, S.P. Anthony, B. Shankar, K. Parthasarathy, T. Arumuganathan, Polyoxometalate based ionic crystal: dual applications in selective colorimetric sensor for hydrated $ZnCl_2$ and antimicrobial activity, New Journal of Chemistry 45(12) (2021) 5576-5588.
[27] J. Zhong, J. Pérez-Ramírez, N. Yan, Biomass valorisation over polyoxometalate-based catalysts, Green Chemistry 23(1) (2021) 18-36.
[28] M.A. Rezvani, M. Shaterian, M. Aghmasheh, Catalytic oxidative desulphurization of gasoline using amphiphilic polyoxometalate@ polymer nanocomposite as an efficient, reusable, and green organic–inorganic hybrid catalyst, Environmental technology 41(10) (2020) 1219-1231.
[29] N. Mizuno, K. Kamata, K. Yamaguchi, Green oxidation reactions by polyoxometalate-based catalysts: from molecular to solid catalysts, Topics in Catalysis 53(13-14) (2010) 876-893.
[30] C.G. Lin, J. Hu, Y.F. Song, Chapter Seven - Polyoxometalate-Functionalized Nanocarbon Materials for Energy Conversion, Energy Storage, and Sensor Systems, in: R. van Eldik, L. Cronin (Eds.), Advances in Inorganic Chemistry, Academic Press2017, pp. 181-212.
[31] Y. Ji, L. Huang, J. Hu, C. Streb, Y.-F. Song, Polyoxometalate-functionalized nanocarbon materials for energy conversion, energy storage and sensor systems, Energy & Environmental Science 8(3) (2015) 776-789.
[32] Q. Li, A. Tian, C. Chen, T. Jiao, T. Wang, S. Zhu, J. Sha, Anderson polyoxometalates with intrinsic oxidase-mimic activity for “turn on” fluorescence sensing of dopamine, Analytical and Bioanalytical Chemistry (2021) 1-11.
[33] J. Marignac, Recherches chimiques et cristallographiques sur les fluozirconates, Ann. Chim. Phys 60 (1860) 257-307.
[34] J. Du, Z.-L. Lang, Y.-Y. Ma, H.-Q. Tan, B.-L. Liu, Y.-H. Wang, Z.-H. Kang, Y.-G. Li, Polyoxometalate-based electron transfer modulation for efficient electrocatalytic carbon dioxide reduction, Chemical Science 11(11) (2020) 3007-3015.
[35] B. Huang, D. Ke, Z. Xiong, Y. Wang, K. Hu, P. Jiang, M. Liang, Z. Xiao, P. Wu, Covalent hybrid materials between polyoxometalates and organic molecules for enhanced electrochemical properties, Journal of Materials Science 55(13) (2020) 5554-5570.
[36] M.S. Nunes, P. Neves, A.C. Gomes, L. Cunha-Silva, A.D. Lopes, A.A. Valente, M. Pillinger, I.S. Gonçalves, A silicododecamolybdate/pyridinium-tetrazole hybrid molecular salt as a catalyst for the epoxidation of bio-derived olefins, Inorganica Chimica Acta 516 (2021) 120129.
[37] P. Liu, Y. Liang, X. Lin, C. Wang, G. Yang, A General Strategy To Fabricate Simple Polyoxometalate Nanostructures: Electrochemistry-Assisted Laser Ablation in Liquid, ACS Nano 5(6) (2011) 4748-4755.
[38] P. He, W. Chen, J. Li, H. Zhang, Y. Li, E. Wang, Keggin and Dawson polyoxometalates as electrodes for flexible and transparent piezoelectric nanogenerators to efficiently utilize mechanical energy in the environment, Science Bulletin 65(1) (2020) 35-44.
[39] L. Pauling, The molecular structure of the tungstosilicates and related compounds, Journal of the American Chemical Society 51(10) (1929) 2868-2880.
[40] J.F. Keggin, Structure of the molecule of 12-phosphotungstic acid, Nature 131(3321) (1933) 908-909.
[41] J. Macht, M.J. Janik, M. Neurock, E. Iglesia, Catalytic consequences of composition in polyoxometalate clusters with Keggin structure, Angewandte Chemie 119(41) (2007) 8010-8014.
[42] A. Kondinski, T.N. Parac-Vogt, Keggin structure, quō vādis?, Frontiers in chemistry 6 (2018) 346.

[43] W.A. Neiwert, J.J. Cowan, K.I. Hardcastle, C.L. Hill, I.A. Weinstock, Stability and Structure in α-and β-Keggin Heteropolytungstates,[$X^{n+}W_{12}O_{40}]^{(8-n)-}$, X= p-Block Cation, Inorganic chemistry 41(26) (2002) 6950-6952.
[44] J.M. Clemente-Juan, E. Coronado, A. Forment-Aliaga, J.R. Galán-Mascarós, C. Giménez-Saiz, C.J. Gómez-García, A new heptanuclear cobalt (II) cluster encapsulated in a novel heteropolyoxometalate topology: synthesis, structure, and magnetic properties of [Co_7 $(H_2O)_2(OH)_2P_2W_{25}O_{94}$]16-, Inorganic chemistry 43(8) (2004) 2689-2694.
[45] M. Ammam, B. Keita, L. Nadjo, I.M. Mbomekalle, M.D. Ritorto, T.M. Anderson, W.A. Neiwert, C.L. Hill, J. Fransaer, Cyclic Voltammetry Study of the Mn-Substituted Polyoxoanions [$Mn^{II4}(H_2O)_2$ $(H_4AsW_{15}O_{56})_2]^{18-}$ and [$((Mn^{II}OH_2)Mn^{II2}PW_9O_{34})_2(PW_6O_{26})]^{17-}$: Electrodeposition of Manganese Oxides Electrocatalysts for Dioxygen Reduction, Electroanalysis 23(6) (2011) 1427-1434.
[46] P. Souchay, Contribution a letude des phenomenes de condensation en chimie minerale. 1. Critique des mesures de diffusion et dialyse, bulletin de la societe chimique de france 14(9-10) (1947) 914-924.
[47] H. Wu, M. Zhi, C. Chen, Y. Zhu, P. Ma, J. Wang, J. Niu, Synthesis, characterization, and photoluminescence properties of three two-dimensional lanthanide-containing Dawson-type polyoxometalates, Dalton Transactions 48(36) (2019) 13850-13857.
[48] A. Iqbal, H.M. Asif, Y. Zhou, L. Zhang, T. Wang, F. Khurum Shehzad, X. Ren, From simplicity to complexity in grafting Dawson-type polyoxometalates on porphyrin, leading to the formation of new organic–inorganic hybrids for the investigation of third-order optical nonlinearities, Inorganic chemistry 58(13) (2019) 8763-8774.
[49] T.J. Weakley, H.T. Evans, J.S. Showell, G.F. Tourné, C.M. Tourné, 18-Tungstotetracobalto (II) diphosphate and related anions: a novel structural class of heteropolyanions, Journal of the Chemical Society, Chemical Communications (4) (1973) 139-140.
[50] I.M. Mbomekalle, B. Keita, M. Nierlich, U. Kortz, P. Berthet, L. Nadjo, Structure, Magnetism, and Electrochemistry of the Multinickel Polyoxoanions [$Ni_6As_3W_{24}O_{94}$ $(H_2O)_2]^{17-}$,[$Ni_3Na(H_2O)_2(AsW_9O_{34})_2]^{11-}$, and [$Ni_4Mn_2P_3W_{24}O_{94}(H_2O)_2]^{17-}$, Inorganic chemistry 42(17) (2003) 5143-5152.
[51] M.D. Ritorto, T.M. Anderson, W.A. Neiwert, C.L. Hill, Decomposition of A-Type Sandwiches. Synthesis and Characterization of New Polyoxometalates Incorporating Multiple d-Electron-Centered Units, Inorganic Chemistry 43(1) (2004) 44-49.
[52] S.T. Zheng, J. Zhang, G.Y. Yang, Designed synthesis of POM–organic frameworks from {Ni6PW9} building blocks under hydrothermal conditions, Angewandte Chemie 120(21) (2008) 3973-3977.
[53] Y. Zhang, L. Zhang, Z. Hao, F. Luo, Controlling the synthesis of novel chiral polyoxometalate-based compounds and racemic compounds from the same system, Dalton Transactions 39(30) (2010) 7012-7016.
[54] S. Zhang, Y. Lu, X.-W. Sun, Z. Li, T.-Y. Dang, Z. Zhang, H.-R. Tian, S.-X. Liu, Purely inorganic frameworks based on polyoxometalate clusters with abundant phosphate groups: single-crystal to single-crystal structural transformation and remarkable proton conduction, Chemical Communications 56(3) (2020) 391-394.
[55] I.V. Kozhevnikov, Catalysis by heteropoly acids and multicomponent polyoxometalates in liquid-phase reactions, Chemical Reviews 98(1) (1998) 171-198.
[56] N. Kashyap, S. Das, R. Borah, Chapter-9 A Brief Insight into the Polyoxometalate Based Organic-Inorganic Hybrid Systems and their Catalytic uses in Oxidation and Acid Catalyzed Organic Reactions, CHEMICAL SCIENCES 1 (2020) 167.
[57] I.M. Mbomekalle, B. Keita, L. Nadjo, K.I. Hardcastle, C.L. Hill, T.M. Anderson, Semi-vacant Wells–Dawson anions. Synthesis of tri-tungsten-vacant derivatives and crystallographic studies of [αββα-$(Cu^{II}OH_2)_2$ $(Cu^{II})_2(AsW_{15}(OH_2)_3(OH)O_{52})_2]^{12-}$, Dalton Transactions (24) (2004) 4094-4095.
[58] J. Lehmann, A. Gaita-Arino, E. Coronado, D. Loss, Spin qubits with electrically gated polyoxometalate molecules, Nature Nanotechnology 2(5) (2007) 312-317.
[59] B.S. Bassil, U. Kortz, 2.5 Polyoxometalates, Rare Earth Chemistry (2020) 171.
[60] W. Xu, J.-F. Cao, Y.-N. Lin, Y. Shu, J.-H. Wang, Functionalized polyoxometalate microspheres ensure selective adsorption of phosphoproteins and glycoproteins, Chemical Communications 57(27) (2021) 3367-3370.
[61] W. Salomon, A. Dolbecq, C. Roch-Marchal, G. Paille, R. Dessapt, P. Mialane, H. Serier-Brault, A Multifunctional Dual-Luminescent Polyoxometalate@ Metal-Organic Framework Composite as EuW Chemical 10@ UiO-67 Probe and Temperature Sensor, Polyoxometalates in Catalysis, Biology, Energy and Materials Science (2019).
[62] A. Kaczmarek, J. Liu, B. Laforce, L. Vincze, K. Van Hecke, R. Van Deun, Cryogenic luminescent thermometers based on multinuclear Eu^{3+}/Tb^{3+} mixed lanthanide polyoxometalates, Dalton Transactions 46(18) (2017) 5781-5785.
[63] D. Çimen, A. Denizli, Development of rapid, sensitive, and effective plasmonic nanosensor for the detection of vitamins in infact formula and milk samples, Photonic Sensors (2020) 1-17.
[64] A. Babakhanian, S. Kaki, M. Ahmadi, H. Ehzari, A. Pashabadi, Development of α-polyoxometalate–polypyrrole–Au nanoparticles modified sensor applied for detection of folic acid, Biosensors and Bioelectronics 60 (2014) 185-190.
[65] L. Wang, T. Meng, J. Sun, S. Wu, M. Zhang, H. Wang, Y. Zhang, Development of Pd/Polyoxometalate/nitrogen-doping hollow carbon spheres tricomponent nanohybrids: a selective electrochemical sensor for acetaminophen, Analytica chimica acta 1047 (2019) 28-35.
[66] N. Li, J. Liu, B.X. Dong, Y.Q. Lan, Polyoxometalate-Based Compounds for Photo-and Electrocatalytic Applications, Angewandte Chemie 132(47) (2020) 20963-20977.
[67] L. Zhang, S. Li, K.P. O'Halloran, Z. Zhang, H. Ma, X. Wang, L. Tan, H. Pang, A highly sensitive non-enzymatic ascorbic acid electrochemical sensor based on polyoxometalate/Tris (2, 2′-bipyridine) ruthenium (II)/chitosan-palladium inorganic-organic self-assembled film, Colloids and Surfaces A: Physicochemical and Engineering Aspects 614 (2021) 126184.
[68] Z. Bai, C. Zhou, H. Xu, G. Wang, H. Pang, H. Ma, Polyoxometalates-doped Au nanoparticles and reduced graphene oxide: a new material for the detection of uric acid in urine, Sensors and Actuators B: Chemical 243 (2017) 361-371.
[69] J. Zhang, Y. Huang, G. Li, Y. Wei, Recent advances in alkoxylation chemistry of polyoxometalates: From synthetic strategies, structural overviews to functional applications, Coordination Chemistry Reviews 378 (2019) 395-414.
[70] H. Shi, N. Li, Z. Sun, T. Wang, L. Xu, Interface modification of titanium dioxide nanoparticles by titanium-substituted polyoxometalate doping for improvement of photoconductivity and gas sensing applications, Journal of Physics and Chemistry of Solids 120 (2018) 57-63.
[71] Y. Shen, J. Peng, H. Zhang, C. Meng, F. Zhang, Preparation and application of L-cysteine-doped Keggin polyoxometalate microtubes, Journal of Solid State Chemistry 185 (2012) 225-228.
[72] H. Medetalibeyoğlu, M. Beytur, S. Manap, C. Karaman, F. Kardaş, O. Akyıldırım, G. Kotan, H. Yüksek, N. Atar, M.L. Yola, Molecular Imprinted Sensor Including Au Nanoparticles/Polyoxometalate/Two-Dimensional Hexagonal Boron Nitride Nanocomposite for Diazinon Recognition, ECS Journal of Solid State Science and Technology 9(10) (2020) 101006.
[73] H. Lin, K.S. Suslick, A colorimetric sensor array for detection of triacetone triperoxide vapor, Journal of the American Chemical Society 132(44) (2010) 15519-15521.
[74] A. Üzer, S. Durmazel, E. Erçağ, R. Apak, Determination of hydrogen peroxide and triacetone triperoxide (TATP) with a silver nanoparticles—based turn-on colorimetric sensor, Sensors and Actuators B: Chemical 247 (2017) 98-107.
[75] X. Lü, P. Hao, G. Xie, J. Duan, L. Gao, B. Liu, A Sensor Array Realized by a Single Flexible TiO_2/POMs Film to Contactless Detection of Triacetone Triperoxide, Sensors 19(4) (2019) 915.
[76] J. Qian, K. Wang, Y. Jin, X. Yang, L. Jiang, Y. Yan, X. Dong, H. Li, B. Qiu, Polyoxometalate@ magnetic graphene as versatile immobilization matrix of Ru $(bpy)_3^{2+}$ for sensitive magneto-controlled electrochemiluminescence sensor and its application in biosensing, Biosensors and Bioelectronics 57 (2014) 149-156.
[77] Ö.A. Yokuş, F. Kardaş, O. Akyıldırım, T. Eren, N. Atar, M.L. Yola, Sensitive voltammetric sensor based on polyoxometalate/reduced graphene oxide nanomaterial: application to the simultaneous determination of l-tyrosine and l-tryptophan, Sensors and Actuators B: Chemical 233 (2016) 47-54.
[78] M.L. Yola, N. Atar, T. Eren, H. Karimi-Maleh, S. Wang, Sensitive and selective determination of aqueous triclosan based on gold nanoparticles on polyoxometalate/reduced graphene oxide nanohybrid, Rsc Advances 5(81) (2015) 65953-65962.
[79] Z. Li, J. Chen, D. Pan, W. Tao, L. Nie, S. Yao, A sensitive amperometric bromate sensor based on multi-walled carbon nanotubes/phosphomolybdic acid composite film, Electrochimica Acta 51(20) (2006) 4255-4261.
[80] B. Ertan, T. Eren, İ. Ermiş, H. Saral, N. Atar, M.L. Yola, Sensitive analysis of simazine based on platinum nanoparticles on polyoxometalate/multi-walled carbon nanotubes, Journal of colloid and interface science 470 (2016) 14-21.
[81] B. Haghighi, H. Hamidi, L. Gorton, Formation of a robust and stable film comprising ionic liquid and polyoxometalate on glassy carbon electrode modified with multiwalled carbon nanotubes: Toward sensitive and fast detection of hydrogen peroxide and iodate, Electrochimica Acta 55(16) (2010) 4750-4757.
[82] N. Anwar, M. Vagin, F. Laffir, G. Armstrong, C. Dickinson, T. McCormac, Transition metal ion-substituted polyoxometalates entrapped in polypyrrole as an electrochemical sensor for hydrogen peroxide, Analyst 137(3) (2012) 624-630.

[83] R. Ayranci, Y. Torlak, T. Soganci, M. Ak, Trilacunary Keggin type polyoxometalate-conducting polymer composites for amperometric glucose detection, Journal of The Electrochemical Society 165(13) (2018) B638.
[84] H. Karimi-Maleh, F. Karimi, S. Malekmohammadi, N. Zakariae, R. Esmaeili, S. Rostamnia, M.L. Yola, N. Atar, S. Movaghgharnezhad, S. Rajendran, An amplified voltammetric sensor based on platinum nanoparticle/polyoxometalate/two-dimensional hexagonal boron nitride nanosheets composite and ionic liquid for determination of N-hydroxysuccinimide in water samples, Journal of Molecular Liquids 310 (2020) 113185.
[85] A. Proust, R. Villanneau, Functionalization of polyoxometalates: achievements and perspectives, Polyoxometalate Chemistry From Topology via Self-Assembly to Applications, Springer2001, pp. 23-38.
[86] P. Sun, S. Zhang, Z. Xiang, T. Zhao, D. Sun, G. Zhang, M. Chen, K. Guo, X. Xin, Photoluminescent sensing vesicle platform self-assembled by polyoxometalate and ionic-liquid-type imidazolium gemini surfactants for the detection of Cr^{3+} and MnO_4^- ions, Journal of colloid and interface science 547 (2019) 60-68.
[87] A. González, N. Gálvez, M. Clemente-León, J.M. Dominguez-Vera, Electrochromic polyoxometalate material as a sensor of bacterial activity, Chemical Communications 51(50) (2015) 10119-10122.
[88] D. Pan, J. Chen, W. Tao, L. Nie, S. Yao, Polyoxometalate-modified carbon nanotubes: new catalyst support for methanol electro-oxidation, Langmuir 22(13) (2006) 5872-5876.
[89] B. Iqbal, X. Jia, H. Hu, L. He, W. Chen, Y.-F. Song, Fabrication of redox-active polyoxometalate-based ionic crystals onto single-walled carbon nanotubes as high-performance anode materials for lithium-ion batteries, Inorganic Chemistry Frontiers 7(6) (2020) 1420-1427.
[90] H. Wei, J. Zhang, N. Shi, Y. Liu, B. Zhang, J. Zhang, X. Wan, A recyclable polyoxometalate-based supramolecular chemosensor for efficient detection of carbon dioxide, Chemical science 6(12) (2015) 7201-7205.
[91] H. Zhang, A. Xie, Y. Shen, L. Qiu, X. Tian, Layer-by-layer inkjet printing of fabricating reduced graphene-polyoxometalate composite film for chemical sensors, Physical Chemistry Chemical Physics 14(37) (2012) 12757-12763.
[92] J. Qu, X. Zou, B. Liu, S. Dong, Assembly of polyoxometalates on carbon nanotubes paste electrode and its catalytic behaviors, Analytica chimica acta 599(1) (2007) 51-57.
[93] W. Guo, L. Xu, F. Li, B. Xu, Y. Yang, S. Liu, Z. Sun, Chitosan-assisted fabrication and electrocatalytic activity of the composite film electrode of heteropolytungstate/carbon nanotubes, Electrochimica Acta 55(5) (2010) 1523-1527.
[94] Y. Sahraoui, S. Chaliaa, A. Maaref, A. Haddad, F. Bessueille, N. Jaffrezic-Renault, Synergistic Effect of Polyoxometalate and Single Walled Carbon Nanotubes on Peroxidase-like Mimics and Highly Sensitive Electrochemical Detection of Hydrogen Peroxide, Electroanalysis 32(4) (2020) 683-689.
[95] J. Hu, Y. Ji, W. Chen, C. Streb, Y.-F. Song, "Wiring" redox-active polyoxometalates to carbon nanotubes using a sonication-driven periodic functionalization strategy, Energy & Environmental Science 9(3) (2016) 1095-1101.
[96] A.D. Stergiou, M.D. Symes, Organic Transformations using Electro-Generated Polyoxometalate Redox Mediators, Catalysis Today (2021).
[97] M. Yang, S. Rong, X. Wang, H. Ma, H. Pang, L. Tan, Y. Jiang, K. Gao, Preparation and Application of Keggin Polyoxometalate-based 3D Coordination polymer Materials as Supercapacitors and Amperometric Sensors, ChemNanoMat 7(3) (2021) 299-306.
[98] M. Ammam, E.B. Easton, Advanced NO_x gas sensing based on novel hybrid organic–inorganic semiconducting nanomaterial formed between pyrrole and Dawson type polyoxoanion $[P_2Mo_{18}O_{62}]^{6-}$, Journal of Materials Chemistry 21(22) (2011) 7886-7891.
[99] J. Miao, Y. Chen, Y. Li, J. Cheng, Q. Wu, K.W. Ng, X. Cheng, R. Chen, C. Cheng, Z. Tang, Proton conducting polyoxometalate/polypyrrole films and their humidity sensing performance, ACS Applied Nano Materials 1(2) (2018) 564-571.
[100] M. Lechner, R. Güttel, C. Streb, Challenges in polyoxometalate-mediated aerobic oxidation catalysis: catalyst development meets reactor design, Dalton Transactions 45(42) (2016) 16716-16726.
[101] C. Si, P. Ma, Q. Han, J. Jiao, W. Du, J. Wu, M. Li, J. Niu, A Polyoxometalate-Based Inorganic Porous Material with both Proton and Electron Conductivity by Light Actuation: Photocatalysis for Baeyer–Villiger Oxidation and Cr (VI) Reduction, Inorganic Chemistry (2020).
[102] J. Xu, Z. Zhu, T. Su, W. Liao, C. Deng, D. Hao, Y. Zhao, W. Ren, H. Lü, Green aerobic oxidative desulfurization of diesel by constructing an Fe-Anderson type polyoxometalate and benzene sulfonic acid-based deep eutectic solvent biomimetic cycle, Chinese Journal of Catalysis 41(5) (2020) 868-876.

Available online at www.jourcc.com

Journal homepage: www.JOURCC.com

Journal of Composites and Compounds

Application of carbon allotropes composites for targeted cancer therapy: A review

Firooze Niazvand [a], Pushkaraj Rajendra Wagh [b], Elham Khazraei [c], Mahsa Borzouyan Dastjerdi [d], Chanakya Patil [e], Ishtiyaq Ahmad Najar [f]*

[a] School of medicine, Abadan Faculty of Medical Sciences, Abadan, Iran
[b] Department of Pharmaceutical Sciences, College of Pharmacy, Western University of Health Sciences, Pomona, CA, United States
[c] Department of Chemical Engineering, Faculty of Chemical Engineering, Tarbiat Modares University, Tehran, Iran
[d] Department of Stem Cells and Regenerative Medicine, National Institute of Genetic Engineering and Biotechnology, Tehran, Iran
[e] Department of Pharmaceutical Sciences, School of Pharmacy, Texas Tech University Health Sciences Center, Amarillo, TX, USA
[f] School Education Department, UT of Jammu and Kashmir, India

ABSTRACT

In recent years, various drug carrier nanomaterials have been investigated to improve drug delivery systems in cancer treatment. However, an ongoing requirement exists for more beneficial therapeutic materials, yielding rapid clearance, high capacity for reducing systemic toxicity via specific-tumor targeting, and superior drug solubility. Given that, carbon allotropes, including Active Carbon (AC), carbon nanotubes (CNTs), graphene and graphene oxides (GOs), nanodiamonds (NDs), fullerenes, carbon nanohorns, soporous carbons, and carbon dots, have been studied owing to their high thermal conductivity, rigid structure, flexibility for modification and functionalization, adequate surface-to-volume ratio, and high biocompatibility. This review aims to overview recent advances in applying different carbon allotrope composites in drug delivery-based cancer therapy systems.

Peer review under responsibility of jourcc

ARTICLE INFORMATION

Article history:
Received 18 April 2021
Received in revised form 10 June 2021
Accepted 29 June 2021

Keywords:
Carbon allotropes
Drug delivery
Cancer therapy
Nanocomposites
Nanomaterials

Table of contents

1. Introduction 140
2. Carbon allotropes-based drug delivery carriers for cancer therapy 141
2.1. Active Carbon (AC) 142
2.2. Carbon nanotube (CNT) 142
2.3. Graphene and graphene oxide 142
2.4. Nanodiamonds 143
2.5. Fullerene 144
2.5.1. Structures of the two fullerenes 1 and 2 144
2.6. Carbon Nanohorns 145
2.7. Soporous Carbons 146
2.8. Carbon Dots 146
2.8.1. Unmodified GQDs 147
2.8.2. Functionalized GQDs 147
3. Conclusions and future insights 148

1. Introduction

Cancer is a non-communicable disease recognized as the most worldwide deadly disease in humans, responsible for more than 9.6*10^6 mortalities in 2018 [1]. The common therapeutic strategies could not accomplish a beneficial cure for cancer [2, 3]. Bray et al. [4] believe that cancer is the main hurdle in retracting from an anticipated growth of life expectancy in the 21st century. However, consuming less than 5% support funding regarding the fundamental studies of cancer shows that

* Corresponding author: Mahsa Borzouyan Dastjerdi ; E-mail: Mahsaborzouyan@gmail.com
https://doi.org/10.52547/jcc.3.2.7

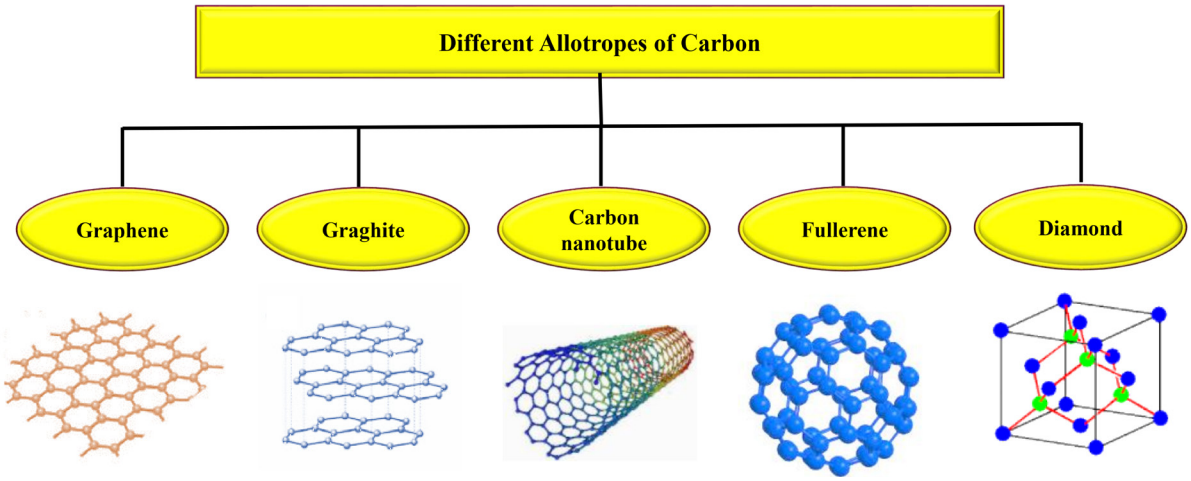

Fig. 1. The schematic illustration of the most common carbon allotropes.

the critical objective for cancer curing is impending.

The accumulation of somatic mutations in a normal cell progeny leads to an evolutionary process named cancer, which causes a discerning growth benefit and unrestrained cell propagation. The most critical cancers in humans are caused by epithelial tissues of the colon, breast, lung, prostate, stomach, and skin [5, 6].

Although there are enormous developments in the cancer disease understanding at the molecular scale, the high tumor heterogeneity and diversity limit to achieve modern treatment methods, which is a major challenge that should be addressed appropriately [7]. In addition, cancer cells are distinguished from normal cells by their different metabolic and genetic profiles. As a result, the development of novel anticancer handling approaches, which target the alterations of tumor cells, is another main challenge in pharmacology [8, 9]. There are many tumor handling strategies, including immunotherapy, chemotherapy, radiation, and surgery [10]. While the best operative treatment for metastatic cancers is chemotherapeutics [11], the potential of cancer cells to multidrug resistance, the concurrent resistance of tumor cells to altered drugs, is an important obstruction to chemotherapy success. In addition, their various side effects are defined mainly by their toxicity impacts, cancer repetition, and healthy cell-damaging due to their inability to target tumor locations appropriately [12, 13].

Thus, cancer investigation pursues treatments to minimize these undesirable side effects, touching to the excellent capable, innovative therapies, for example, nanomedicine and drug delivery [14].

Unique medication delivery methods targeted particularly to cancer cells can be used to reduce the detrimental and hazardous cytotoxicity on healthy organs and destroy malignant cells with minimal injury to normal tissue. In addition, using the right drug delivery system can help patients receive faster and better treatment [15]. Thus, finding innovative and effective drug delivery methods is one of the major challenges that academics are focusing on.

The present review intends to provide an overview of modern theragnostic applications of carbon allotropes and deliver a complete comparison concerning nanocarbon characteristics and their effects on theragnostic applications, particularly in drug delivery targeting cancer cells. Firstly, the different allotropes of carbon associated with their cancer theragnostic applications are introduced here. Then, their chemical and physical properties are explained, along with their production and surface functionalization methods. Finally, the theragnostic applications of different carbon allotropes associated with *in vivo* and *in vitro* systems are demonstrated by emphasizing the investigated biosystems and tumor drug delivery techniques.

2. Carbon allotropes-based drug delivery carriers for cancer therapy

Engineering, technology, and science are fused in the nanotechnology field, aiming to investigate, create, and use nanoparticles, which means any particle of materials with a dimension around 1-1000 nm [16]. The measurable physico-chemico-biological features of particles are granted by nanosize. As a result, their performance is improved in comparison with bulk materials. In concern to medicine, nanotechnology includes nanoparticle applications to improve new therapies and increase current methods. For example, the nanotechnology field has the incredible ability to play an important role in detecting, treating, and preventing cancer [10, 17].

Recently, materials chemistry is amid the fastest-growing fields in science and attains great worldwide attention. This severely emerging field contains either modifying the preexisting materials or producing new ones, chemically and/or physically, to develop their characterizations and applicability. For example, carbon nanomaterials (CNMs) are attractive because their unique properties involve large surface areas, tunable pore structures, rigid structures, post-chemical modifying, high thermal and electrical conductivity, wear and thermal resistance, chemical stability, and low friction coefficient [2, 18, 19]. Carbon nano allotropes have great potential for filling the gap between organic molecules and carbon materials [20]. Allotropes of carbon have great diversity in size and shape. Based on the morphology, carbon nanoallotropes are categorized into two classes, including nanostructures with inner cavities (carbon nanotubes (CNTs) [21] and fullerenes [22]) and not bearing inner voids (graphene [23], carbon dots (CDs) [24], and carbon nano onions (CNOs)). In addition to graphene nanoribbons [25], graphene oxides [26], and nanodiamonds [27], some macro and micro-structures are formed by carbon materials, for instance, 3-dimensional (D) microspheres, 2D films, and 1D nanowires.

Figure 1 shows the schematic of natural carbon allotropes (graphite and diamond) and synthetic examples (graphene, nanotubes, and fullerenes). Due to their distinctive chemical and physical properties, nano carbons remain high-attractive materials in many applications, including photovoltaics to sensing, optoelectronics, electronics, bioimaging, and therapeutics [28, 29].

The diagnostic and therapeutic applications of nanocarbons are intensively investigated as superb biosensors, capable fluorescent nano labels for imaging tissues and cells, operational photothermal nano reagents to tumor therapy, gene carriers, and being used in different types

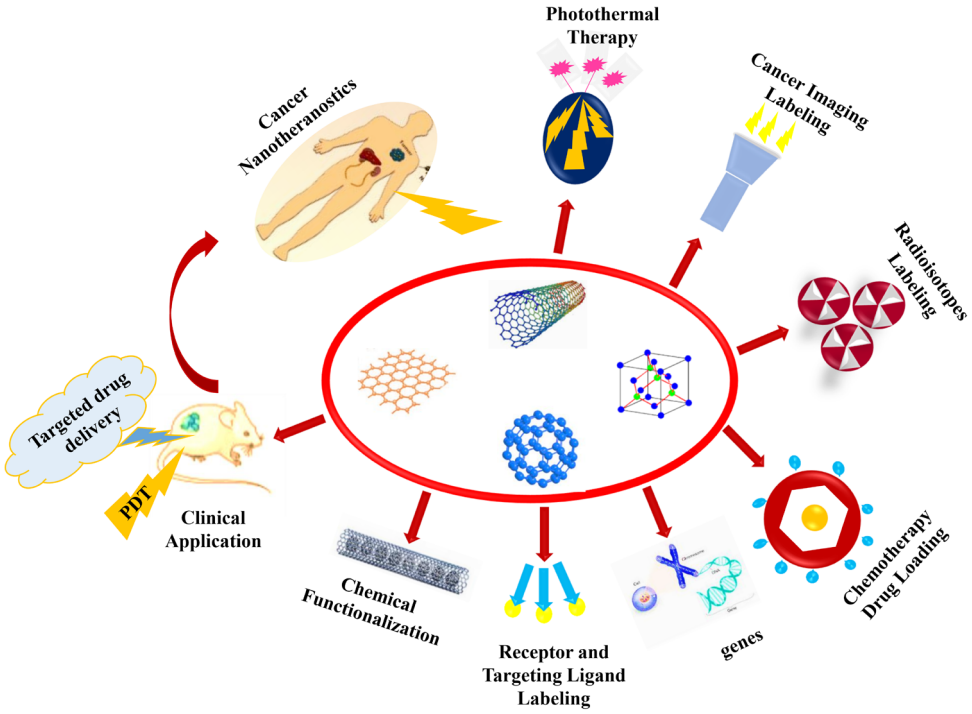

Fig. 2. Schematic diagram of using carbon allotropes in cancer theranostics.

of drug delivery systems [30, 31], particularly *in vivo* targeting cancer cells [28, 32, 33]. Among these, because of the unique physicochemical properties of nanostructured carbon materials such as graphene, nanodiamonds, fullerenes, and CNTs, they are highly investigated to tumor theranostics from the various aspects, for example, their engineering possibility for practical therapeutics matters and multi-function diagnostics [34, 35]. Within a live body, nanoparticles comprising carbon allotropes have a distinct behavior, distribution pathway, and toxicity [36, 37]. Some of these carbon allotropes show extremely photothermal impacts due to their capability to absorb the near-infrared radiation (NIR), a feature that can be applied to the in situ killing of cancer cells in a short time [38, 39]. Figure 2 shows the schematic diagram of using carbon allotropes in cancer theranostics.

2.1. Active Carbon (AC)

Well-known as charcoal, AC is one of the prominent participants in the carbon family. The structure of AC is amorphous and chemically stable. It is prepared from various carbonaceous resources, for instance, coal, wood, bamboo, and coconut shells [40]. This type of nanocarbon is a more interesting material for medical applications such as a therapeutic function for treating severe toxicity and/or overdoses through directly consumed drugs, such as acetaminophen and diethylcarbamazine, and even in acute poisoning cases. It can also be activated in drug delivery sets. AC could be a great alternative to carrier drugs in cancer therapeutic agents [41].

2.2. Carbon nanotubes (CNTs)

CNTs, attracting much attention during the last decade, contain unified rolling cylinders made of graphene sheets. These materials exhibit supreme chemical, mechanical, and physical characterizations [42, 43]. There are two classes of CNTs, including multiwalled (MWNTs) and single-walled (SWNTs) based on their graphene layer (that constitutes only one nanotube) number [44]. The rolled organization of graphene sheet layers could be formed as different-layered from single to multiple-layered, which are donated as numeral-walled nanotubes (NWCNTs), for example, multi- (MWCNTs), triple- (TWCNTs), double- (DWCNTs), or single-walled nanotubes (SWNTs) [42]. Figure 3 shows four major types of CNTs.

Functionalized CNTs have demonstrated excellent biocompatibility, making them attractive choices for anticancer treatment and diagnostic drug delivery [45]. For example, a novel nanoformulation including platinum nanoparticles (NPs) maintained on polybenzimidazole (PBI) functionalized polymers and MWCNTs were produced for cancer treatment [46]. This nanosystem exhibited potent inhibition on the epithelial-mesenchymal transition and cell cycle biomarkers of cancer stem cells, as well as specific cytotoxicity on breast cancer stem cells, though not on adult stem cells, according to quantitative gene expression assessments [46]. Singhai et al. [47] used hyaluronic acid and a-Tocopheryl succinate to functionalize MWCNTs and then loaded them with Doxorubicin hydrochloride (DOX) to achieve better cellular positioning and appropriately targeted CD44 receptor overexpressing triple-negative breast cancer cells (MDA-MB-231). The cellular absorption of the product was noteworthy, with strong proliferation inhibitory action and a significant overall apoptotic rate. Hyaluronic acid and DOX were employed as CD44 receptor targeting ligands and chemotherapeutic agents, respectively, in this nanoformulation, and a-Tocopheryl succinate was chosen because of its synergistic benefits. These chemicals exhibited the appropriate synergistic effects and were safe enough to be used in targeted anticancer treatment [47].

2.3. Graphene and graphene oxide

Graphene contains sp^2-bonded carbon atoms located in a two-dimension (2D) layer, in which each carbon atom fused to three carbons with a bond angle of 120 and arranged six-atom rings to construct a honeycomb network of one-atom thickness [48-50]. The sp^3-bonded graphene membranes are made up of two or three layers of known and novel in silico-designed carbon bulk architectures, with hydrogen passivated surfaces on both, one, or none of the surfaces. Many possible stable configurations of sp^3-bonded membranes exhibit varied electronic characteristics and transverse and longitudinal mechanical behaviors. In addition, carbon membranes rich in sp^3 bonds demonstrate mechanical qualities and optimum breaking strengths [51].

The graphene biomedical applications, such as drug delivery, were quickly developed a few years ago due to unique features of graphene, for example, noble biocompatibility, 2D planar structure, mechanical and chemical stability, large surface area, and excellent conductivity. As

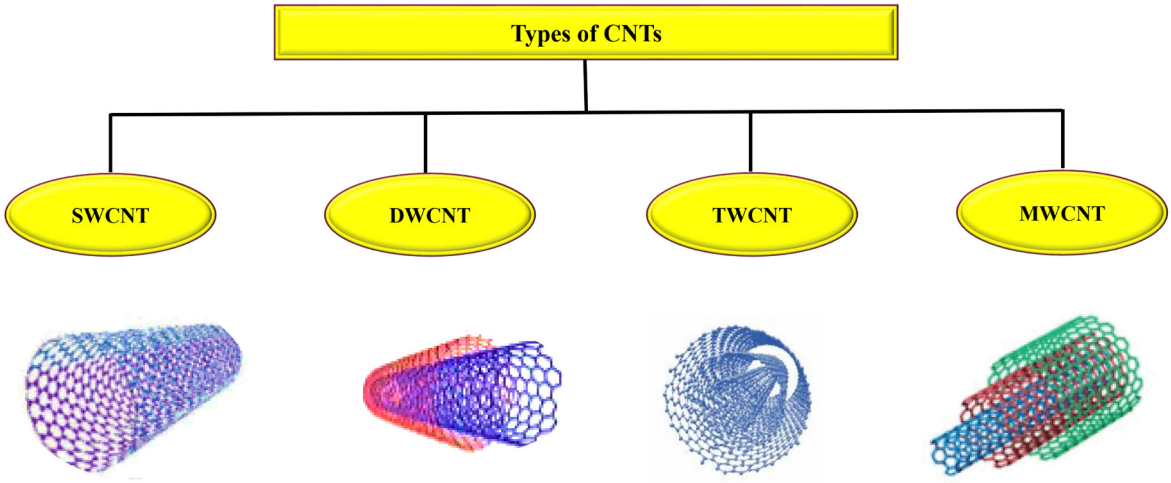

Fig. 3. The schematic of major types of carbon nanotubes.

a result, graphene-based materials have been widely investigated as high adequate biomaterials in biomedical applications, for instance, delivering a broad therapeutic series and designing innovative drug delivery structures [52].

Graphene oxide (GO), the main derivative of graphene, has great properties, including promising optical activity, cost-effectiveness, low toxicity, and good water solubility, making it a suitable candidate for bio probe developments [52]. Due to their typically large surface area, GO and GO-based nanoparticles can be used for combination chemotherapy and dual-drug delivery [53]. Supramolecular hydrogels of injectable graphene/GO composite were improved by Hu et al., aiming to carry anti-tumor drugs. GO and its reduced derivative (RGO) were stabilized in solution using Pluronic F-127. The storage modulus related to composite hydrogels of RGO or GO was higher than the native hydrogel, which gradually damaged and was unsteady in solution. The solubility of the water-insoluble anticancer drug camptothecin (CPT) in Pluronic F-127 solution, particularly the large drug-loaded sample, was improved by GO or RGO. In addition, the hydrogel of RGO or GO composite showed great potential to superior control and milder drug release (to both DXR and CPT) than native hydrogel [54].

There are few published studies concerning the anticancer activity of graphene or GO [55-57]. In this regard, the anticancer behavior studies of GO–hypocretin A in an aqueous media revealed its superior activity to free hypocretin [58]. A hybrid of GO-TiO_2 led to major promotion in the activity of caspase-3 involving apoptotic death [59]. Furthermore, the hybrid exhibited exceptional photodynamic activity as an anticancer due to the lack of dark cytotoxicity [60]. Wang et al. [60] and Hu et al. [59] established the double functional graphene quantum dots as carriers for anticancer drug targeting and savories for activating DNA cleavage, which was useful to cancer therapy. It was illustrated that polyethylene glycolated GO conjugated with transferrin as a proficient nanovector could target brain cancers *in vivo* and *in vitro* as an anticancer drug delivery system [61]. Gurunathan et al. [58] revealed that GO-CONH-Schiff base composite, as a nanostructured pH-sensitive antitumor drug, could be operated as a carrier of drug delivery and the inhibitor of cancer. Jagiello et al. [62] fabricated the composites RGO and GO with NPs such as AuNPs, AgNPs, Ag_2O, and TiO_2. These compounds displayed high vibrant surface regions and enabled adhesion to inorganic and organic molecules, which were proper to be applied in different biomedical applications involving anticancer therapy, bioimaging, or tissue regeneration.

Moreover, Su et al. [63] summarized that modifying the GO surface remarkably improved its physicochemical features, providing the applicant with a vaccine carrier and activating humoral and cellular immunity. The functionalized GO as a capable substrate to cancer treatment and chemotherapeutic drug delivery was deliberated by Gupta [64]. Generally, the studies indicate that new attempts in graphene and GO are concentrated in modifications, fabrications, and improvement of their characterizations. They were reviewed by Farjadian et al. [55], and the variation of oxidation degrees can change GO interactions with proteins.

2.4. Nanodiamonds

A new participant in the carbon nanoparticle family, nanodiamonds (NDs), is more attracted to biomedicine due to their superb chemical and physical features [65, 66]. Since their initial studies in Russia in 1960, nanodiamonds have extended global consideration because of their simplistic surface modification involving excellent biocompatibility and bio-conjugation, the small size of the prime particle (about 4-5 nm) having narrow size distribution, and economic large-amount production. They also appealed a lot of technological and scientific attention due to their distinctive optical, chemical, structural, mechanical, and biological properties [67]. Having a diameter of ~5 nm, along with highly tailorable surface chemistry and low cell toxicity, rendered them to be exciting materials for improving drug delivery structures summarized by Mochalin et al. [68]. NDs integrate numerous features, such as scalability, variety of impending conjugates, biocompatibility, and surface geometries, which facilitate the high-affinity release of therapeutics. NDs can also provide wide-ranging therapeutics, for instance, nucleic acids, proteins, and small molecules [67, 69]. In vitro biocompatibility of ND has been discovered by a wide series of assays [70, 71]. Additionally, the sides existing on the surface of ND possess burden characters that facilitate effective water-binding for sustained and dispersibility therapeutic release [72-74].

An apoptosis-making drug, DOX, extensively employed in chemotherapy, was reversibly and effectively anchored over the nanodiamonds (NDs, 2-8 nm) and hosted in alive cells. The observation of feasible and genetic interrogation research of DOX-functionalized ND composite confirmed this material applies to as a platform transport technology for a broad nanoscale medicine modality and multitude of therapeutic molecules [75].

The ND-C60 composite obtained from crushing nanodiamond (ND) with dry powder of C60 quickly adsorbed and oxidized organic contaminants using photogenerated ROS. Moreover, the photodynamic tumor therapy studies showed that ND-C60 without apparent toxicity could be internalized by tumor cells and made cell apoptosis. Besides, the treat-

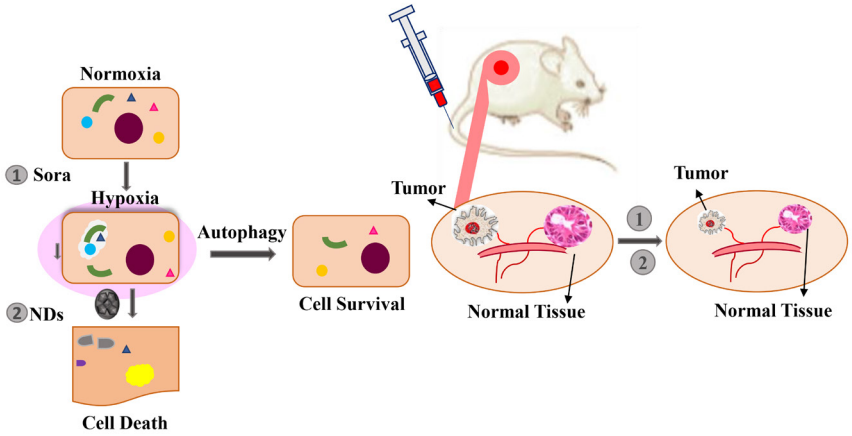

Fig. 4. Systematic diagram showing the experimental studies of NDs and Sora composite impacts on hypoxic tumor cells and the suggested mechanism.

ment of ND-C60 with mice cells bearing tumors along with light irradiation extended survival time by reducing cancer [22].

Furthermore, the study of NDs impacts on HIF activities and lysosomal agents displayed that NDs, in contrast to Baf A, successfully triggered autophagic flux obstruction without harming the lysosomal activities [76]. Besides, a combined system of NDs and Sorafenib, an anti-angiogenic drug, inhibited cancer growth via a synergistic impact. A suggested mechanism exhibited that the autophagic flux was blocked by NDs through a distinctive instrument from lysosomotropic reagents and might function as a targeted agent for tumor therapy while blending with oxygen scarcity [77]. Figure 4 illustrates experimental studies of NDs and Sorafenib (Sora) composite impacts on hypoxic tumor cells and the suggested mechanism.

2.5. Fullerene

After diamond and graphite, fullerene is the third allotrope of carbon, known as zero-dimensional nanostructure, which is a suitable and superb alternative to numerous applications in various fields due to its exclusive structural and electronic properties. After discovering C60 in 1985, this kind of nanostructures rapidly improved because of their remarkable physicochemical features [78]. Their most notable characters are the capacity to reversibly take several electrons, great thermal stability, large surface area, and wide absorption ranges [79, 80].

C60 is the most important member of fullerenes. This fullerene demonstrates both distinctive antioxidant behavior, biological activity, and physicochemical features, and has an important serving potential to be a nanocarrier for delivering drugs to tumor cells [81]. In nanotechnology, the biomedical application of C60 fullerene has recently attracted more attention due to its multipurpose biological activity and unique structure. The exploitation of double functional C60 as a photosensitizer demonstrated that C60 nano complexes showed an increased effect on chemotherapy of drugs, such as DOX, into leukemic cells of humans. It was also established that this strategy could be transferred to a potent alternative for delivering anticancer drugs, for instance, Berberine. In addition, the blend of photo- and chemo-dynamic treatments with drug nano formulated C60 opened promising synergistic strategies to drug delivery for tumor treatment [82].

Due to the low solubility in inorganic and organic solvents, original forms of non-modified carbon nanostructures (CNs) cannot be used in various fields [83]. The intermolecular van der Waals interactions between these materials cause their aggregation. Thus, functionalizing CNs is needed to increase their solubility and expand their applications in numerous fields [84].

The increased fullerene solubility by modifying chemical methods, such as anchoring hydroxyl or amino groups, leads to the broadly applying of C60 in the biomedical areas [85]. Naim et al. (1992) [86] reported the first hydroxylated fullerene C60(OH)n afforded through the heating of C60/C70 with the excess KOH in toluene under reduced pressure. Chiang et al. [87] obtained C60(-OCOR)x(OH)y through the electrophilic reaction of C60 with NO2BF4 using an aromatic acid mediator (RCOOH). C60 was also directly modified with 18 carboxylic functions and 24-26 hydroxyl functions. The highly water-soluble derivatives of malonic acid used to synthesize dendron fullerene and an aqueous NaOH and tetrabutylammonium hydroxide (TBAH) were applied to produce the multi-hydroxylated C60 [88, 89]. Moreover, Hu et al. [90] covalently modified C60 with an amino group to synthesize a series of folacin- and amino-fullerenes soluble in water.

There is evidence that the solubility improving C60 intensely affects the toxicological and physicochemical features of these compounds, therefore makes difficulties in the estimation of their therapeutic potential and toxicity. The in vitro studies concerning the impacts of two fullerenes (1 and 2) on the gene expression in the MCF7 cell line of humans showed that these compounds had null and cytotoxic impacts. The mechanisms of varied behaviors related to the many fullerene derivatives have still been unidentified in alive cells. The reactive oxygen species (ROS) generated along with the light-absorbing potential of fullerene (C60) was extensively investigated for cancer therapy and the water treatment of photosensitizer [22]. Fullerene displays superb capability to tumor therapy. However, the fullerene-lasting deposition and OH· generation have not been thoroughly explained in the literature. The mixed solutions of silk fibroin, water-soluble fullerene (SF-WSF), lead to fairly altered in vitro fullerene performance. It is established that SF can produce promising consequences, including 1) owing to hastening the fullerene degradation by SF, causing low deposition, and 2) the OH· of durable deposited water-soluble fullerene organization is scavenged in the attendance of SF. Hence, SF delivers an opportunity to OH· scavenged, which may be accessible for inhalation and intratracheal instillation applications. Researchers should consider the suitable mixture of different properties for nano n composites, including SF and fullerene, which would be favorable to reduce tissue injury and suppress the oxidative stress using the compounds. Moreover, the perfect separation of nanocomposite biomaterial varied property plays an essential role in updating new applications [91, 92]. The schematic diagram of some derivatives of fullerene applied to cancer therapy and diagnosis is illustrated in Figure 5 [93].

2.5.1. Structures of fullerenes 1 and 2

Proposing to design a smart carrier of drug based on the trimethyl chitosan (TMC) and fullerene, Maleki et al. [94] performed a simulation of molecular dynamics (MD). They found that the functionalized fullerene with carboxyl molecule and spending TMC might increase anticancer drugs such as PAX and DOX and biocompatibility, and reduce drug

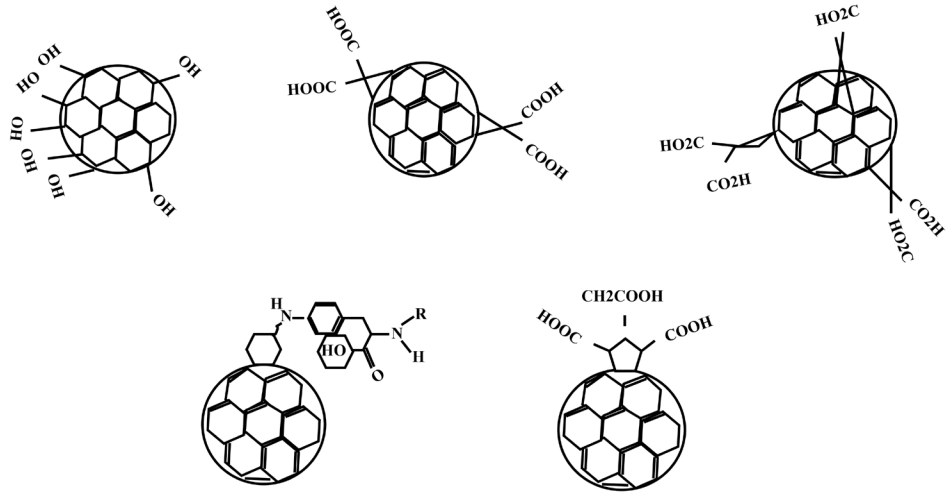

Fig. 5. The schematic diagram of some derivatives of fullerene applied to cancer therapy and diagnosis. 1) Gadolinium endohedral metallofullerenol $Gd@C_{82}(OH)_{22}$; 2) Carboxyfullerene $C60(C(COOH)_2)_2$; 3) C_3 (e,e,e-tris-malonic acid fullerene derivative); 4) Bucky amino acid (Baa); 5) Amino acid-type fullerene derivative.

side effects. Numerous anticancer drugs, such as PAX and DOX, can bring a set of side impacts through non-tumor cell damaging.

Lin et al. [95] designed and prepared a metal-organic photodynamic framework (PHF@ZIF-8). The PHF was loaded in the ZIF-8 to prevent aggregation and solve the solubility problems of fullerenes as photosensitizers. It was reported that the PHF@ZIF-8, under laser irradiation with 448 nm spectrum, showed great therapeutic affectivity, indicating the capability of this compound application to tumor treatment. Jiang et al. [96] prepared and determined a novel set of C60 derivatives with great water-solubility, using 1 H NMR, FTIR, 13C NMR, TGA, SEM, and UV–Vis. Since materials based on fullerene–glycine derivative are bioactive, the cell apoptosis and mortality were enlarged with enhancing the concentration of fullerene–glycine derivative in comparison to fullerene complex. Altogether, these results show that the new, extreme derivatives containing water-soluble C60 can be used for tumor therapy. Guan et al. [97] effectively synthesized the UCNP–PEG–FA/PC70 nanocomposite as a targeted theranostic platform and/or a NIR light-triggered for in vitro, in vivo, and PDT guided trimodal imaging. The following are benefits associated with improving nanocomposites of UCNP–PEG–FA/PC70. (1) Upon irradiation of NIR, UCNPs can make the conversion of NIR to UV-to-visible light for successfully activating PC70, which yields O2 to kill cancer cells under poor oxygen environments, (2) integrating three imaging techniques (FL/UCL/MR) into one set aims to afford the corresponding data of cancer directing treatment and careful diagnosis, and (3) leading superior retention and permeability impacts through passive targeting of folate activated with the PEG, which increases multifunctional nanoparticle accumulations in cancer. Notably, the produced UCNP–PEG–FA/PC70 might answer the two PDT blockage difficulties, including oxygen-poor microenvironment and depth-penetrated limitation. These outcomes emphasize the UCNP–PEG–FA/PC70 ability as multiple theranostic reagents to cancer PDT-guided imaging and a favorable alternative to overcome the drawback of deeply cancerous tissues existing PDT agents under complete deprivation of oxygen (hypoxic) conditions. Li et al. [98] used (PEG)-modified poly(amidoamine) dendrimers to develop supramolecular nanocomposites based on fullerene-dendrimer and reported that these nanoparticles were non-toxic and superbly water-soluble.

2.6. Carbon Nanohorns

A graphene-based nanostructure in horn shape, single-walled carbon nanohorns (SWCNHs), could be appropriate nanosystems to drug delivery targeting through assembly with multipurpose properties of an agent. These materials are simply prepared and modified to obtain the non-toxicological impacts and favorite physicochemical features. Some reports are referring *in vivo* administration of these properties [99].

From a topological and morphological viewpoint, CNH contains a narrowed front-tip unit (the angle of the cone is 120◦, and its critical diameter and length are 2–5 nm and 40–50 in size, respectively) collected of carbon atoms with sp^2 spin organized in five pentagons (found in F as well). CNT-like hexagon ramparts can also be formed by arranging a sixth pentagon around the axis [100]. Moreover, heptagons exist in the axis long to deliberate the usual CNH chemistry and counteract the variation associated with curving pentagons [101].

Depending on the morphologies formed from aggregating CNH assembles, some of these compounds are seed-, bud- or dahlia-like [102]. Notably, the dahlia-like type of CNH, commonly used in nano-oncology applications, has a spherical morphology, and its diameter changes in the range of 80–100 nm. This CHN collected almost 2000 tube-shaped units [103, 104].

Having properties such as “enriched permeation and retention” (EPR) impacts, SWCNHs, holes, high surface areas, lower intrinsic cytotoxicity, SWCNHs are attractive for use as delivery motors to successfully transport different molecules, for example drugs, contrast agent, photosensitizers, fullerene, small interfering RNA (siRNA), and proteins. Despite these favorable applications and features, the uses of oxSWCNHs as carriers of drugs have been limited due to their low dispersibility, which should be addressed appropriately [101].

Modification of CNHs could increase their aqueous solubility and extend their biological applications, such as photodynamic therapy, biosensors, and drug delivery sets (DDSs). It is reported that the dispersibility of oxSWCNHs in water is made using non-covalent and covalent functionalization. Among them, non-covalent modifications are easy and can reserve the natural features of oxSWCNHs. In addition, a natural polysaccharide, sodium alginate (SA), improves the biocompatibility and dispersibility of carbon nanomaterials through non-covalent functionalization [105].

Despite CNTs that forms large bundles, spherical conjugated SWCNHs only aggregate with small size, having < 100 nm in diameter. Hence, the SWCNHs minor size is extra appropriate in the physiological media to succeed a greater cell uptake and the efficacy of targeted delivery into the cancer cells. For instance, Ajimi et al. [106] synthesized nanocarriers of SWCNHs for cisplatin (CDDP) using a nanoprecipitation method. The efficiency of CDDP loading on SWCNHs can be nearly 46%, and the percentages of CDDP drug release for different solvents were 100-60% for water and dimethylformamide, respectively. Furthermore, its anticancer efficiency was enhanced by almost 4−6 folds in comparison to free CDDP drugs. *In vitro* delivery research of CDDP-loaded SWCNHs in lung tumor cells of humans using NCI- H460 as a model demon-

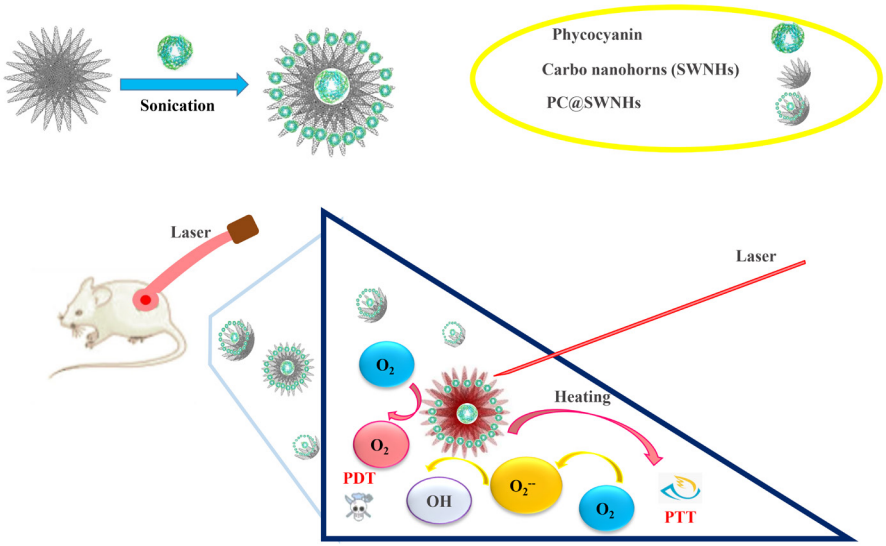

Fig. 6. Schematic diagram of the synthesis method of Phycocyanin @ Single-Walled Carbon Nanohorns.

strated an enhanced anticancer ability in inducing drug to cancer cells than the free CDDP samples. According to the authors, the attachment of the SWCNHs to the cells is responsible for the enhanced quantity of locally release related to CDDP-loaded SWCNHs drugs [107]. Figure 6 depicts a schematic diagram of the synthesis method of Phycocyanin @ SWCNHs and its application for near-infrared light-mediated photodynamic/photothermal cancer therapy [108].

2.7. Soporous Carbons

Nowadays, mesoporous carbon nanoparticles (MCNs), known as an intensifying star in material knowledge, prompt vast study activities, having superior chemical and physical features [109, 110]. MCNs are widely applied as supercapacitors, fuel cells, electrode materials for batteries, matrixes for highly critical catalytic procedures, and sorbents for gas storage and separation procedures [111]. Because of advantages associated with MCNs, including large pore volume, high specific surface area, well-defined surface properties, and tunable pore morphologies, these materials are predominantly more favorable for biomedical applications. The latest research discloses that MCNs can also be applied as nanomaterials with NIR-resonant capability combined with chemo-photo thermal therapy drug-loading [112]. Having such interesting properties, they are also used to construct a thermo-chemotherapy platform that can be answered to overwhelm the trials concerning releasing the carried drug and heterogeneous intracellular stimuli [113]. Newly, mesoporous nanoparticles, particularly silica nanoparticles (MSNs), are more attracted to DDSs as drug carriers because of their fascinating features such as low cytotoxicity, high surface area, large pore volume, biodegradability, and easy functionalization. MSN with a diameter < 200 nm, received great attention and could be successfully entreated to cells through intracellular endocytosis. Therefore, these materials are effectively studied with numerous groups as gene delivery vehicles, anticancer drugs, and protein. Despite mesoporous silica, the large quantity of drug charging is facilitated by ordered mesoporous carbons (OMCs) with higher pore volumes and surface areas. Moreover, it is found that carbon nanoparticle cytotoxicity is inferior to silica nanoparticles [110].

In addition, these materials with average particles (150 nm) can be proficiently endocytosed in cervical cancer cells of humans (HeLa). Besides, the reported information showed that MCN materials could act as a transmembrane delivery motor for releasing Fura-2 and a cell tissue resistant fluorescence dye in HeLa [114].

2.8. Carbon Dots

A novel kind of carbon nanomaterial, carbon quantum dots (CQDs), is appealed to significant interest due to their distinctive features, including low toxicity, better cell penetrability, facile production and modifying, exceptional biocompatibility, excellent water solubility, and higher optical characterizations. Therefore, these carbon nanomaterials have shown different favorable applications in sensing, optoelectronics, bioimaging, and theranostic fields [115-117].

Since a few years back, various CQDs have been synthesized using different approaches, for instance, electrochemical, thermal, microwave, and hydrothermal methods. Among these, the hydrothermal processes have broadly been investigated because of the green nature of hydrothermal precursor chemistry. Furthermore, having reasonable biocompatibility and worthy surface functions, CQDs can load platforms in numerous molecules. Especially, functionalized carbon dots with various chemical groups lead them to be engineered to different functionalized molecules, including protein, aptamer, and drug molecules, through noncovalent and/or covalent interaction useful to multipurpose biomedical applications [118]. For instance, Huang et al. (2012) [119] deliberated a new theranostic platform with photosensitizer-conjugated CQDs. The synthesized CQDs-Ce6, upon irradiation, exhibited greater photodynamic efficiency and more robust fluorescence emission than Ce6.

A kind of CQDs, known as Zero-dimensional graphene quantum dots (GQDs), consists of a few layers of graphene sheets with a thickness of < 10 nm in size. These materials are effectively made up by top-down methodologies such as electrochemical and chemical exfoliation, microwave/ultrasound-assisted exfoliation, and hydrothermal/solvothermal exfoliation, or via bottom-up methods, for example, chemical vapor deposition, stepwise cage opening/organic synthesis, and pyrolysis/carbonization [120-122]. They are employed in several bioimaging applications such as the magnetic resonance imaging (MRI), dual-modal and fluorescence, and two-photon fluorescence imaging [123, 124]. They can also be properly applied in electrochemical luminescence, photoluminescence, or the main neurotransmitter sensing (such as norepinephrine, tyrosine, dopamine, acetylcholine, serotonin, and epinephrine), and/or electrochemical sensors [125, 126]. In addition, due to the capability of GQDs for crossing the blood-brain barrier (BBB), these materials can be demonstrated as excellent drug delivery organizations over the bloodstream, up to the brain, and across the BBB. They are also successfully used in therapeutics and neuroscience diagnostics,

Table 1.
A variety of studies on different carbon allotropes in cancer therapy

Carbon allotropes	Study types (in vitro/in vivo)	Drug	Experimental model	Ref.
Nanodiamond	In-vitro & in-vivo	Fluorescein isothiocyanate	C6-Luc glioblastoma cells, U251MG-Luc human glioma bearing NIH nu/nu nude rats	[141]
Nanodiamond	In-vitro	Polyethylene glycol, transferrin	Human hepatoma (HepG2) cancer cell line	[142]
Graphene oxide	In-vitro and in-vivo	Polyethylene-glycol, 1,4,7- triazacy-clononane-1,4,7- triacetin acid, NOTA, 64Cu, and follicle-stimulating hormone receptor	Murine lung metastasis model of breast cancer	[143]
Graphene oxide	In-vitro and in-vivo	Polyethylene-glycol, folic acid	B16F0 melanoma tumors using a mouse model	[144]
Graphene oxide	In-vitro	Cyclic RGD chitosan, fluorescein isothiocyanate	Bel-7402, SMMC-7721, HepG2 cell line hepatocellular carcinoma	[145]
Graphene quantum dots	In-vitro	Carboxylic group	MCF 10A, SKBR3, MCF 7, MDA-MB-436, MDA-MB-468, MDA-MB-231, MDA-MB-157, MDA-MB-175VI, HCC1806, and Hs578T cells cancerous, and metastatic human breast cells	[146]
Graphene quantum dots	In-vitro	Folic acid	HeLa cell human cervical carcinoma cells, A549 adenocarcinomas human alveolar basal epithelial cells, and HEK293A normal human embryonic kidney cells	[147]
SWCNTs	In-vitro and in-vivo	Chitosan oligomer, folic acid	A549 cells lines, lung cancer cells, tumor-bearing mouse model [assisted through NIR pulsed laser irradiation (1064 nm)]	[34]
SWCNTs	In-vitro	Polyethylene glycol, folic acid	Breast cancer cell lines (MCF7) & mouse fibroblast cell lines (L929) (assisted through NIR laser irradiation (800 nm))	[148]
SWCNTs	In-vitro	Polyethylene glycol, sgc8 aptamers	Human leukemic lymphoblast cells (CCRF-CEM cells) [Assisted through NIR laser irradiation (808 nm)]	[149]
SWCNTs	In-vitro and in-vivo	Lipid molecule docosanol, folic acid	Human breast cancer, xenograft mouse model (MCF-7 breast cancer cells)	[150]
MWCNTs	In-vitro and in-vivo	Galactosylated chitosan	Hepatic tumor, HepG2 cells & mice bearing hepatocellular carcinoma H22 cells	[151]
MWCNTs	In-vitro and in-vivo	Polyethylene glycol, folic acid	HeLa cell line (human, cervix, epithelial-like, carcinoma)	[152]
MWCNTs	In-vitro and in-vivo	Polyethylene glycol, angiopep-2	Brain capillary endothelial cells (BCEC) & C6 glioma cells (xenograft mouse model)	[153]
MWCNTs	In-vitro and in-vivo	D-Alpha-tocopheryl, polyethylene gly-col 1000 succinate (TPGS), transferrin	Human lung cancer cells (A549 cells)	[154]
Fullerene	In-vitro and in-vivo	Diadduct malonic acid, micelles	HeLa cells, S180 tumor-bearing mouse models	[155]
Fullerene	In-vitro and in-vivo	Distearoyl-sn-glycero-3- phosphoe-thanolamine, polyethylene glycol, Asn-Gly-Arg (NGR)	4T1 cells (mouse breast cancer cell line)	[156]
Fullerene	In-vitro and in-vivo	Poly(lactic acid), L-phenylalanin	Melanoma tumor- bearing mouse models	[157]

for example, photodynamic therapy and photothermal, in combination with chemotherapy or alone [127-129]. Some examples of GQDs-based drug delivery-release modes are enriched retention and permeability, the delivery-release of ligand-pH, (EPR)-pH, and EPR-photothermal delivery-release. Besides, Levy et al. [130], Zhao et al. [131], and Jha et al. [132] reviewed the modes of magnetic thermal/core/shell-photothermal delivery-release.

2.8.1. Unmodified GQDs

The non-cytotoxic dose of GQDs (15 μg/mL) significantly changed the expression stairs of genes included in the metastasis and growth (PTEN, Bcl2, Box, miR-21, and miR-29a) of cells, breast cancer, and the activity of mitochondrial in the cellular stair, which suggests that the susceptibility and varied cell fate can have abnormality consequence in the GQDs application anticipated results. However, GQDs (50 nm) did not affect a significant diminution in the feasibility of KMBC/71, HUVEC, and MCF-7 cells [133].

In vivo investigations on type 2 diabetic mice displayed that the complications of GQD and vanadyl compounds presented a late glucose-lowering outline, and a three-week experiment showed a higher significant effect on β-cell protection and insulin development than only vanadyl component. Furthermore, these complexes, probably via the π–π stacking mechanism of GQD sheets, exhibited more *in vitro* membrane penetrability than GQDs and low toxicity related to GQDs [134].

2.8.2. Functionalized GQDs

It was found that Hydroxylated GQDs (OH–GQDs) could decrease the living colonic organoid size and normalize phosphorylated p53 at a three-dimension organoid culture produced via selected crypts [135]. It was also discovered that FA-PEG-GQD-COOH, as a smart drug motor, showed 97.5 % encapsulation efficacy (EE) along with 40.1% drug-loading measurements in mitoxantrone and entered cervical cancer cells of humans mainly through the macropinocytosis-related method. Besides, lower systemic toxicity and robust antitumor proficiency were shown by this nanomaterial [136].

The GQDs with a proper size infused in the biomembrane could

contribute to the drug delivery procedure via decreasing translocation free energy [137]. Water-soluble GQDs bearing DOX are prepared using exfoliation and acidic oxidation of MWCNTs, linked covalently to the module of biotin tumor targeting (BTN). Although both the QGD-BTNs and GQDs are identically low-toxic in concern to A549 cells, GQD-BTN-loaded DOX showed delayed and greater cell uptake than those of GQD-BTN and the free drug. The delayed nuclear internalization of the drug associated with removing the drug from the nano DDS was induced by the acidic environment of cancer cells [138]. Enzalutamide-functionalized GQDs when cross-linked with targeting tumor polyethylene glycol (PEG) and peptides exhibited high drug-loading efficiency by electron π-π interactions. Castration-resistant prostate cancer cells were quickly suppressed by modified GODs through endocytosis. Moreover, enzalutamide-loaded materials exhibited excellent cancer-targeting and reserved *in vitro* progression lines of LNCaP and C4-2B cells of prostate cancer. Additionally, nanocarriers of GQDs revealed an enriched ability of cancer-targeting, a measured drug release, and improved drug side impacts, proposing that it could be applied in the therapy of an intravenous related to this prostate tumor cell type[139]. A variety of different carbon allotropes applied in cancer therapy are provided in Table 1.

3. Conclusions and future insights

During the last few decades, immense attention is to developing cancer theragnostic agents. Many types of nanostructured materials have been investigated and advanced to theragnostic tumor applications. Among all nanostructured materials, carbon-based materials including graphene, carbon nanotubes (CNTs,), nanodiamonds, and fullerenes showed good advantages. In addition, due to their distinctive physicochemical features, they are extensively investigated for the theragnostic of cancer with the vast effective engineering possibility of multi-agent therapeutics and diagnostic functions. Carbon-based nanostructures demonstrate various excellent properties such as unique properties including small sizes, large specific surface areas, sp^2/sp^3 hybridized carbon atoms, tunable pore structures, rigid structures, post-chemical modifying, high thermal and electrical conductivity, wear and thermal resistance, chemical stability, and low friction coefficient. In addition, they could be modified using numerous bio-molecules through different surface coating approaches, possibility via covalent and non-covalent bonding, resulting in surface-functionalized carbon-based nanostructures with improving the regulation and biocompatibility properties within biological systems suitable for theranostic purposes. To provide a comprehensive overview of various types of carbon-based nanostructures and their application in cancer treatment, the current review is focused on introducing the substructures of carbon nanostructured materials, mentioning their physicochemical characterizations, and covering the biomedical applications associated with each carbon allotrope materials, highlighting their uses in targeted drug delivery for cancer therapy.

REFERENCES

[1] W. Chen, K. Sun, R. Zheng, H. Zeng, S. Zhang, C. Xia, Z. Yang, H. Li, X. Zou, J. He, Cancer incidence and mortality in China, 2014, Chinese journal of cancer research 30(1) (2018) 1.
[2] B. Hosnedlova, M. Kepinska, C. Fernandez, Q. Peng, B. Ruttkay-Nedecky, H. Milnerowicz, R. Kizek, Carbon nanomaterials for targeted cancer therapy drugs: A critical review, The Chemical Record 19(2-3) (2019) 502-522.
[3] J. Ferlay, M. Colombet, I. Soerjomataram, D.M. Parkin, M. Piñeros, A. Znaor, F. Bray, Cancer statistics for the year 2020: An overview, International Journal of Cancer (2021).
[4] F. Bray, J. Ferlay, I. Soerjomataram, R.L. Siegel, L.A. Torre, A. Jemal, Global cancer statistics 2018: GLOBOCAN estimates of incidence and mortality worldwide for 36 cancers in 185 countries, CA: a cancer journal for clinicians 68(6) (2018) 394-424.
[5] K.-S. Jeng, C.-F. Chang, S.-S. Lin, Sonic hedgehog signaling in organogenesis, tumors, and tumor microenvironments, International journal of molecular sciences 21(3) (2020) 758.
[6] S. Wang, Y. Liu, Y. Feng, J. Zhang, J. Swinnen, Y. Li, Y. Ni, A review on curability of cancers: more efforts for novel therapeutic options are needed, Cancers 11(11) (2019) 1782.
[7] Z.-F. Lim, P.C. Ma, Emerging insights of tumor heterogeneity and drug resistance mechanisms in lung cancer targeted therapy, Journal of hematology & oncology 12(1) (2019) 1-18.
[8] C.-N. Qian, Y. Mei, J. Zhang, Cancer metastasis: issues and challenges, Chinese journal of cancer 36(1) (2017) 1-4.
[9] E. Çömlekçi, C.V. Sezer, H.M. Kutlu, Handling a Novel Nanoscale D-erythro-MAPP in Lung Cancer Treatment: An in Vitro Cytotoxicity Research, Int. J. Sci. Res. in Biological Sciences Vol 7(4) (2020).
[10] S. Yan, P. Zhao, T. Yu, N. Gu, Current applications and future prospects of nanotechnology in cancer immunotherapy, Cancer biology & medicine 16(3) (2019) 486.
[11] A. El-Hussein, S.L. Manoto, S. Ombinda-Lemboumba, Z.A. Alrowaili, P. Mthunzi-Kufa, A review of chemotherapy and photodynamic therapy for lung cancer treatment, Anti-Cancer Agents in Medicinal Chemistry (Formerly Current Medicinal Chemistry-Anti-Cancer Agents) 21(2) (2021) 149-161.
[12] J.K. Vasir, V. Labhasetwar, Targeted drug delivery in cancer therapy, Technology in cancer research & treatment 4(4) (2005) 363-374.
[13] Y. Dang, J. Guan, Nanoparticle-based drug delivery systems for cancer therapy, Smart Materials in Medicine (2020).
[14] M. Sajjadi, M. Nasrollahzadeh, B. Jaleh, G.J. Soufi, S. Iravani, Carbon-based nanomaterials for targeted cancer nanotherapy: recent trends and future prospects, Journal of Drug Targeting (2021) 1-26.
[15] S. Liu, Epigenetics advancing personalized nanomedicine in cancer therapy, Advanced drug delivery reviews 64(13) (2012) 1532-1543.
[16] S. Gai, G. Yang, P. Yang, F. He, J. Lin, D. Jin, B. Xing, Recent advances in functional nanomaterials for light–triggered cancer therapy, Nano today 19 (2018) 146-187.
[17] P. Gao, W. Pan, N. Li, B. Tang, Boosting cancer therapy with organelle-targeted nanomaterials, ACS applied materials & interfaces 11(30) (2019) 26529-26558.
[18] S.H.K. Yap, K.K. Chan, S.C. Tjin, K.-T. Yong, Carbon Allotrope-Based Optical Fibers for Environmental and Biological Sensing: A Review, Sensors 20(7) (2020) 2046.
[19] L. Bazli, B. Eftekhari Yekta, A. Khavandi, Preparation and Characterization of Sn-Containing Glasses for Brachytherapy Applications, Transactions of the Indian Ceramic Society 76(4) (2017) 242-246.
[20] Y. Wang, P. Yang, L. Zheng, X. Shi, H. Zheng, Carbon nanomaterials with sp^2 or/and sp hybridization in energy conversion and storage applications: A review, Energy Storage Materials 26 (2020) 349-370.
[21] P.S.O. Ozgen, S. Atasoy, B.Z. Kurt, Z. Durmus, G. Yigit, A. Dag, Glycopolymer decorated multiwalled carbon nanotubes for dual targeted breast cancer therapy, Journal of Materials Chemistry B 8(15) (2020) 3123-3137.
[22] H. Lee, J. Seok Lee, K.J. Moor, H.-i. Kim, S.-R. Kim, G. Gim, J. Lee, H.-H. Kim, T.M. Fahmy, J.-H. Kim, C. Lee, Hand-ground fullerene-nanodiamond composite for photosensitized water treatment and photodynamic cancer therapy, Journal of Colloid and Interface Science 587 (2021) 101-109.
[23] R.M. Obodo, I. Ahmad, F.I. Ezema, Introductory chapter: graphene and its applications, Graphene and Its Derivatives-Synthesis and Applications, Intechopen2019.
[24] W. Fang, R. Jin, W. Mu, Near-infrared mediated polymer-coated carbon nanodots loaded cisplatin for targeted care management of lung cancer therapy, Process Biochemistry 99 (2020) 27-35.
[25] A.P. Johnson, H.V. Gangadharappa, K. Pramod, Graphene nanoribbons: A promising nanomaterial for biomedical applications, Journal of Controlled Release 325 (2020) 141-162.
[26] C. Martin, A. Ruiz, S. Keshavan, G. Reina, D. Murera, Y. Nishina, B. Fadeel, A. Bianco, A biodegradable multifunctional graphene oxide platform for targeted cancer therapy, Advanced Functional Materials 29(39) (2019) 1901761.
[27] K. Tjo, P. Varamini, Nanodiamonds and their potential applications in breast cancer therapy: a narrative review, Drug Delivery and Translational Research (2021) 1-12.
[28] N. Panwar, A.M. Soehartono, K.K. Chan, S. Zeng, G. Xu, J. Qu, P. Coquet, K.-T. Yong, X. Chen, Nanocarbons for biology and medicine: Sensing, imaging, and drug delivery, Chemical reviews 119(16) (2019) 9559-9656.
[29] K.M. Amin, H.M. Amin, Carbon Nanoallotropes-Based Anticorrosive Coatings: Recent Advances and Future Perspectives, Corrosion Protection of Metals and Alloys Using Graphene and Biopolymer Based Nanocomposites (2021) 81-98.

[30] E. Asadian, M. Ghalkhani, S. Shahrokhian, Electrochemical sensing based on carbon nanoparticles: A review, Sensors and Actuators B: Chemical 293 (2019) 183-209.
[31] J. Li, X. Deng, L. Wang, J. Liu, K. Xu, Clinical application of carbon nanoparticles in lymphatic mapping during colorectal cancer surgeries: A systematic review and meta-analysis, Digestive and Liver Disease (2020).
[32] M. Mirzaei, O. Gulseren, M. Rafienia, A. Zare, Nanocarbon-assisted biosensor for diagnosis of exhaled biomarkers of lung cancer: DFT approach, Eurasian Chemical Communications 3(3) (2021) 154-161.
[33] Z. Liu, X.-J. Liang, Nano-carbons as theranostics, Theranostics 2(3) (2012) 235.
[34] S. Augustine, J. Singh, M. Srivastava, M. Sharma, A. Das, B.D. Malhotra, Recent advances in carbon based nanosystems for cancer theranostics, Biomaterials Science 5(5) (2017) 901-952.
[35] G. Rajakumar, X.-H. Zhang, T. Gomathi, S.-F. Wang, M. Azam Ansari, G. Mydhili, G. Nirmala, M.A. Alzohairy, I.-M. Chung, Current Use of Carbon-Based Materials for Biomedical Applications—A Prospective and Review, Processes 8(3) (2020) 355.
[36] F. Menaa, Y. Fatemeh, S.K. Vashist, H. Iqbal, O.N. Sharts, B. Menaa, Graphene, an Interesting Nanocarbon Allotrope for Biosensing Applications: Advances, Insights, and Prospects, Biomedical Engineering and Computational Biology 12 (2021) 1179597220983821.
[37] D. Dai, Y. Li, J. Fan, Room-temperature synthesis of various allotropes of carbon nanostructures (graphene, graphene polyhedra, carbon nanotubes and nano-onions, n-diamond nanocrystals) with aid of ultrasonic shock using ethanol and potassium hydroxide, Carbon 179 (2021) 133-141.
[38] S. Pattnaik, Y. Surendra, J.V. Rao, K. Swain, Carbon family nanomaterials for drug delivery applications, Nanoengineered Biomaterials for Advanced Drug Delivery (2020) 421.
[39] N. Miriyala, D.J. Kirby, A. Cumont, R. Zhang, B. Shi, D. Ouyang, H. Ye, Synthesis of Carbon Onion and Its Application as a Porous Carrier for Amorphous Drug Delivery, Crystals 10(4) (2020) 281.
[40] K. Mitura, J. Kornacka, E. Kopczyńska, J. Kalisz, E. Czerwińska, M. Affeltowicz, W. Kaczorowski, B. Kolesińska, J. Frączyk, T. Bakalova, Active Carbon-Based Nanomaterials in Food Packaging, Coatings 11(2) (2021) 161.
[41] G.T. Pasaribu, T.K. Waluyo, G. Pari, N. Hastuti, The effectiveness of glucomannan and nano activated-carbon as hypercholesterol-lowering agents, Indonesian Journal of Forestry Research 7(2) (2020) 155-164.
[42] J. Sun, J. Zhu, M.A. Cooper, D. Wu, Z. Yang, Carbon Nanotubes: Preparation and Surface Modification for Multifunctional Applications, Functionalized Nanomaterials I: Fabrications (2020) 83.
[43] B.F. Dizaji, A. Farboudi, A. Rahbar, M.H. Azarbaijan, M.R. Asgary, The role of single-and multi-walled carbon nanotube in breast cancer treatment, Therapeutic Delivery 11(10) (2020) 653-672.
[44] M.I. Sajid, U. Jamshaid, T. Jamshaid, N. Zafar, H. Fessi, A. Elaissari, Carbon nanotubes from synthesis to in vivo biomedical applications, International journal of pharmaceutics 501(1-2) (2016) 278-299.
[45] M. Eskandari, S.H. Hosseini, M. Adeli, A. Pourjavadi, Polymer-functionalized carbon nanotubes in cancer therapy: a review, Iranian Polymer Journal 23(5) (2014) 387-403.
[46] M.R. Berber, H. Elkhenany, I.H. Hafez, A. El-Badawy, M. Essawy, N. El-Badri, Efficient tailoring of platinum nanoparticles supported on multiwalled carbon nanotubes for cancer therapy, Nanomedicine 15(08) (2020) 793-808.
[47] N.J. Singhai, R. Maheshwari, S. Ramteke, CD44 receptor targeted 'smart'multi-walled carbon nanotubes for synergistic therapy of triple-negative breast cancer, Colloid and Interface Science Communications 35 (2020) 100235.
[48] A. Bordbar-Khiabani, S. Ebrahimi, B. Yarmand, Highly corrosion protection properties of plasma electrolytic oxidized titanium using rGO nanosheets, Applied Surface Science 486 (2019) 153-165.
[49] G. Guday, Surface Chemistry of Low-Dimensional Carbon Materials: Synthesis and Functionalization of Graphene, 2020.
[50] S. Ebrahimi, A. Bordbar-Khiabani, B. Yarmand, Immobilization of rGO/ZnO hybrid composites on the Zn substrate for enhanced photocatalytic activity and corrosion stability, Journal of Alloys and Compounds 845 (2020) 156219.
[51] P.R. Niraula, T. Cao, A. Bongiorno, Mechanical properties of sp^3-bonded carbon and boron nitride 2D membranes: A first principles study, Computational Materials Science 179 (2020) 109635.
[52] K. Tadyszak, J.K. Wychowaniec, J. Litowczenko, Biomedical applications of graphene-based structures, Nanomaterials 8(11) (2018) 944.
[53] V.P. Jain, S. Chaudhary, D. Sharma, N. Dabas, R.S.K. Lalji, B.K. Singh, G. Jaiswar, Advanced functionalized nanographene oxide as a biomedical agent for drug delivery and anti-cancerous therapy: A review, European Polymer Journal (2020) 110124.
[54] X. Hu, D. Li, H. Tan, C. Pan, X. Chen, Injectable Graphene Oxide/Graphene Composite Supramolecular Hydrogel for Delivery of Anti-Cancer Drugs, Journal of Macromolecular Science, Part A 51(4) (2014) 378-384.
[55] T. Kavinkumar, K. Varunkumar, V. Ravikumar, S. Manivannan, Anticancer activity of graphene oxide-reduced graphene oxide-silver nanoparticle composites, Journal of colloid and interface science 505 (2017) 1125-1133.
[56] U.L. ABIA, A novel creatinine biosensor modified with pure silk fibroin based on pencil graphite electrode (PGE).
[57] A.V.A. Mariadoss, K. Saravanakumar, A. Sathiyaseelan, M.-H. Wang, Preparation, characterization and anti-cancer activity of graphene oxide--silver nanocomposite, Journal of Photochemistry and Photobiology B: Biology 210 (2020) 111984.
[58] S. Gurunathan, J.W. Han, J.H. Park, E. Kim, Y.-J. Choi, D.-N. Kwon, J.-H. Kim, Reduced graphene oxide–silver nanoparticle nanocomposite: a potential anticancer nanotherapy, International journal of nanomedicine 10 (2015) 6257.
[59] Z. Hu, Y. Huang, S. Sun, W. Guan, Y. Yao, P. Tang, C. Li, Visible light driven photodynamic anticancer activity of graphene oxide/TiO_2 hybrid, Carbon 50(3) (2012) 994-1004.
[60] L. Zhou, W. Wang, J. Tang, J.H. Zhou, H.J. Jiang, J. Shen, Graphene oxide noncovalent photosensitizer and its anticancer activity in vitro, Chemistry–A European Journal 17(43) (2011) 12084-12091.
[61] K. Yang, J. Wan, S. Zhang, Y. Zhang, S.-T. Lee, Z. Liu, In vivo pharmacokinetics, long-term biodistribution, and toxicology of PEGylated graphene in mice, ACS nano 5(1) (2011) 516-522.
[62] J. Jagiełło, A. Chlanda, M. Baran, M. Gwiazda, L. Lipińska, Synthesis and Characterization of Graphene Oxide and Reduced Graphene Oxide Composites with Inorganic Nanoparticles for Biomedical Applications, Nanomaterials 10(9) (2020) 1846.
[63] C.-Y. Su, Y. Xu, W. Zhang, J. Zhao, A. Liu, X. Tang, C.-H. Tsai, Y. Huang, L.-J. Li, Highly efficient restoration of graphitic structure in graphene oxide using alcohol vapors, ACS nano 4(9) (2010) 5285-5292.
[64] V. Gupta, N. Sharma, U. Singh, M. Arif, A. Singh, Higher oxidation level in graphene oxide, Optik 143 (2017) 115-124.
[65] Y. Zhang, K.Y. Rhee, D. Hui, S.-J. Park, A critical review of nanodiamond based nanocomposites: Synthesis, properties and applications, Composites Part B: Engineering 143 (2018) 19-27.
[66] P. Nowicki, E. Czarniewska, Nanodiamonds: unique nanoparticles for use in biomedicine and biotechnology, Postepy biochemii 65(4) (2020) 247-262.
[67] S. Kumar, M. Nehra, D. Kedia, N. Dilbaghi, K. Tankeshwar, K.-H. Kim, Nanodiamonds: Emerging face of future nanotechnology, Carbon 143 (2019) 678-699.
[68] V.N. Mochalin, A. Pentecost, X.-M. Li, I. Neitzel, M. Nelson, C. Wei, T. He, F. Guo, Y. Gogotsi, Adsorption of drugs on nanodiamond: toward development of a drug delivery platform, Molecular pharmaceutics 10(10) (2013) 3728-3735.
[69] C. Gaillard, H.A. Girard, C. Falck, V. Paget, V. Simic, N. Ugolin, P. Bergonzo, S. Chevillard, J.C. Arnault, Peptide nucleic acid–nanodiamonds: covalent and stable conjugates for DNA targeting, Rsc Advances 4(7) (2014) 3566-3572.
[70] J. Whitlow, S. Pacelli, A. Paul, Multifunctional nanodiamonds in regenerative medicine: recent advances and future directions, Journal of Controlled Release 261 (2017) 62-86.
[71] S. Chauhan, N. Jain, U. Nagaich, Nanodiamonds with powerful ability for drug delivery and biomedical applications: Recent updates on in vivo study and patents, Journal of pharmaceutical analysis 10(1) (2020) 1-12.
[72] G. Yang, W. Long, W. Yan, H. Huang, M. Liu, H. Ouyang, Y. Feng, L. Liu, X. Zhang, Y. Wei, Surface PEGylation of nanodiamond through a facile Michael addition reaction for intracellular drug delivery, Journal of Drug Delivery Science and Technology 57 (2020) 101644.
[73] M.V. Korobov, N.V. Avramenko, A.G. Bogachev, N.N. Rozhkova, E. Ōsawa, Nanophase of water in nano-diamond gel, The Journal of Physical Chemistry C 111(20) (2007) 7330-7334.
[74] E. Ōsawa, D. Ho, H. Huang, M.V. Korobov, N.N. Rozhkova, Consequences of strong and diverse electrostatic potential fields on the surface of detonation nanodiamond particles, Diamond and Related Materials 18(5-8) (2009) 904-909.
[75] H. Huang, E. Pierstorff, E. Osawa, D. Ho, Active nanodiamond hydrogels for chemotherapeutic delivery, Nano letters 7(11) (2007) 3305-3314.
[76] P. Moscariello, In vitro and in vivo investigation of dendronized streptavidin and fluorescent nanodiamonds, two flexible nanosystems efficiently crossing the blood-brain barrier to improve nanotheranostics in neurological disease treatment, 2019.
[77] M. Islam, L. Chen, J. Sisler, K. Tam, Cellulose nanocrystal (CNC)–inorganic hybrid systems: synthesis, properties and applications, Journal of Materials Chemistry B 6(6) (2018) 864-883.

[78] S.K. Tiwari, V. Kumar, A. Huczko, R. Oraon, A.D. Adhikari, G.C. Nayak, Magical Allotropes of Carbon: Prospects and Applications, Critical Reviews in Solid State and Materials Sciences 41(4) (2016) 257-317.
[79] V.M. Tyutyunnik, Graphene breakthrough into future technology: the 2010 Nobel Prize in Physics Laureate Sir Konstantin Sergeevich Novoselov.
[80] K. Andersson, The electronic spectrum of C60, Chemical Physics Letters 739 (2020) 136976.
[81] K.D. Patel, R.K. Singh, H.-W. Kim, Carbon-based nanomaterials as an emerging platform for theranostics, Materials Horizons 6(3) (2019) 434-469.
[82] A. Grebinyk, Synergistic Chemo-and Photodynamic Treatment of Cancer Cells with C_{60} Fullerene Nanocomplexes, Universität Würzburg, 2021.
[83] M. Lucafò, M. Gerdol, A. Pallavicini, S. Pacor, S. Zorzet, T. Da Ros, M. Prato, G. Sava, Profiling the molecular mechanism of fullerene cytotoxicity on tumor cells by RNA-seq, Toxicology 314(1) (2013) 183-192.
[84] M.E. Plonska-Brzezinska, Carbon Nano-Onions: A Review of Recent Progress in Synthesis and Applications, ChemNanoMat 5(5) (2019) 568-580.
[85] V.V. Sharoyko, S.V. Ageev, N.E. Podolsky, A.V. Petrov, E.V. Litasova, T.D. Vlasov, L.V. Vasina, I.V. Murin, L.B. Piotrovskiy, K.N. Semenov, Biologically active water-soluble fullerene adducts: Das Glasperlenspiel (by H. Hesse)?, Journal of Molecular Liquids 323 (2021) 114990.
[86] A. Naim, P.B. Shevlin, Reversible addition of hydroxide to the fullerenes, Tetrahedron letters 33(47) (1992) 7097-7100.
[87] L.Y. Chiang, R.B. Upasani, J.W. Swirczewski, S. Soled, Evidence of hemiketals incorporated in the structure of fullerols derived from aqueous acid chemistry, Journal of the American Chemical Society 115(13) (1993) 5453-5457.
[88] M. Brettreich, A. Hirsch, A highly water-soluble dendro [60] fullerene, Tetrahedron letters 39(18) (1998) 2731-2734.
[89] I. Lamparth, A. Hirsch, Water-soluble malonic acid derivatives of C60 with a defined three-dimensional structure, Journal of the Chemical Society, Chemical Communications (14) (1994) 1727-1728.
[90] Z. Hu, C. Zhang, Y. Huang, S. Sun, W. Guan, Y. Yao, Photodynamic anticancer activities of water-soluble C60 derivatives and their biological consequences in a HeLa cell line, Chemico-biological interactions 195(1) (2012) 86-94.
[91] Q. Liu, Y. Liu, H. He, F. Wang, D. Yao, F. He, H. Liu, Y. Fan, Silk fibroin scavenges hydroxyl radicals produced from a long-term stored water-soluble fullerene system, Journal of Materials Chemistry B 6(5) (2018) 769-780.
[92] L. Bazli, S. Eskandarinezhad, N. Kakur, V. Ramachandran, A. Bacigalupe, M. Mansilla, M. Escobar, Electrical properties of polymer blend composites based on Silicone rubber/EPDM/clay for high voltage insulators, Journal of Composites and Compounds 3(6) (2021) 18-24.
[93] Z. Chen, R. Mao, Y. Liu, Fullerenes for cancer diagnosis and therapy: preparation, biological and clinical perspectives, Current drug metabolism 13(8) (2012) 1035-1045.
[94] R. Maleki, A. Khoshoei, E. Ghasemy, A. Rashidi, Molecular insight into the smart functionalized TMC-Fullerene nanocarrier in the pH-responsive adsorption and release of anti-cancer drugs, Journal of Molecular Graphics and Modelling 100 (2020) 107660.
[95] W. Lin, J. Gong, W. Ye, X. Huang, J. Chen, Polyhydroxy Fullerene-loaded ZIF-8 Nanocomposites for Better Photodynamic Therapy, Zeitschrift für anorganische und allgemeine Chemie 646(23-24) (2020) 1900-1903.
[96] G. Jiang, F. Yin, J. Duan, G. Li, Synthesis and properties of novel water-soluble fullerene–glycine derivatives as new materials for cancer therapy, Journal of Materials Science: Materials in Medicine 26(1) (2015) 24.
[97] M. Guan, H. Dong, J. Ge, D. Chen, L. Sun, S. Li, C. Wang, C. Yan, P. Wang, C. Shu, Multifunctional upconversion–nanoparticles–trismethylpyridylporphyrin–fullerene nanocomposite: a near-infrared light-triggered theranostic platform for imaging-guided photodynamic therapy, NPG Asia Materials 7(7) (2015) e205-e205.
[98] X. Li, Y. Watanabe, E. Yuba, A. Harada, T. Haino, K. Kono, Facile construction of well-defined fullerene–dendrimer supramolecular nanocomposites for bioapplications, Chemical Communications 51(14) (2015) 2851-2854.
[99] A. Moreno-Lanceta, M. Medrano-Bosch, P. Melgar-Lesmes, Single-walled carbon nanohorns as promising nanotube-derived delivery systems to treat cancer, Pharmaceutics 12(9) (2020) 850.
[100] T. Azami, D. Kasuya, R. Yuge, M. Yudasaka, S. Iijima, T. Yoshitake, Y. Kubo, Large-scale production of single-wall carbon nanohorns with high purity, The Journal of Physical Chemistry C 112(5) (2008) 1330-1334.
[101] S. Zhu, G. Xu, Single-walled carbon nanohorns and their applications, Nanoscale 2(12) (2010) 2538-2549.
[102] D. Chen, C.A. Dougherty, K. Zhu, H. Hong, Theranostic applications of carbon nanomaterials in cancer: Focus on imaging and cargo delivery, Journal of controlled release 210 (2015) 230-245.
[103] B. He, Y. Shi, Y. Liang, A. Yang, Z. Fan, L. Yuan, X. Zou, X. Chang, H. Zhang, X. Wang, Single-walled carbon-nanohorns improve biocompatibility over nanotubes by triggering less protein-initiated pyroptosis and apoptosis in macrophages, Nature communications 9(1) (2018) 1-21.
[104] J. Guerra, M.A. Herrero, E. Vázquez, Carbon nanohorns as alternative gene delivery vectors, RSC advances 4(52) (2014) 27315-27321.
[105] X. Ma, C. Shu, J. Guo, L. Pang, L. Su, D. Fu, W. Zhong, Targeted cancer therapy based on single-wall carbon nanohorns with doxorubicin in vitro and in vivo, Journal of nanoparticle research 16(7) (2014) 1-14.
[106] K. Ajima, M. Yudasaka, T. Murakami, A. Maigné, K. Shiba, S. Iijima, Carbon nanohorns as anticancer drug carriers, Molecular pharmaceutics 2(6) (2005) 475-480.
[107] M. Curcio, G. Cirillo, F. Saletta, F. Michniewicz, F.P. Nicoletta, O. Vittorio, S. Hampel, F. Iemma, Carbon Nanohorns as Effective Nanotherapeutics in Cancer Therapy, C 7(1) (2021) 3.
[108] Z. Lin, B.-P. Jiang, J. Liang, C. Wen, X.-C. Shen, Phycocyanin functionalized single-walled carbon nanohorns hybrid for near-infrared light-mediated cancer phototheranostics, Carbon 143 (2019) 814-827.
[109] Y. Fang, D. Gu, Y. Zou, Z. Wu, F. Li, R. Che, Y. Deng, B. Tu, D. Zhao, A low-concentration hydrothermal synthesis of biocompatible ordered mesoporous carbon nanospheres with tunable and uniform size, Angewandte Chemie 122(43) (2010) 8159-8163.
[110] L. Zhou, Y. Jing, Y. Liu, Z. Liu, D. Gao, H. Chen, W. Song, T. Wang, X. Fang, W. Qin, Mesoporous carbon nanospheres as a multifunctional carrier for cancer theranostics, Theranostics 8(3) (2018) 663.
[111] Z. Wu, W. Li, P.A. Webley, D. Zhao, General and controllable synthesis of novel mesoporous magnetic iron oxide@ carbon encapsulates for efficient arsenic removal, Advanced Materials 24(4) (2012) 485-491.
[112] G. Xu, S. Liu, H. Niu, W. Lv, R.a. Wu, Functionalized mesoporous carbon nanoparticles for targeted chemo-photothermal therapy of cancer cells under near-infrared irradiation, RSC Advances 4(64) (2014) 33986-33997.
[113] L. Tian, L. Tao, H. Li, S. Zhao, Y. Zhang, S. Yang, J. Xue, X. Zhang, Hollow mesoporous carbon modified with cRGD peptide nanoplatform for targeted drug delivery and chemo-photothermal therapy of prostatic carcinoma, Colloids and Surfaces A: Physicochemical and Engineering Aspects 570 (2019) 386-395.
[114] Z. Li, Closed-Loop Molecular Release from Nanoporous Gold Thin Film Electrodes, University of California, Davis2018.
[115] E.P. Neustroev, Plasma Treatment of Graphene Oxide, Graphene Oxide: Applications and Opportunities (2018) 7.
[116] P. Marconcini, M. Macucci, The k• p method and its application to graphene, carbon nanotubes and graphene nanoribbons: The Dirac equation, La Rivista del Nuovo Cimento 34 (2011) 489-584.
[117] F. Wu, H. Su, K. Wang, W.-K. Wong, X. Zhu, Facile synthesis of N-rich carbon quantum dots from porphyrins as efficient probes for bioimaging and biosensing in living cells, International journal of nanomedicine 12 (2017) 7375.
[118] D. Du, K. Wang, Y. Wen, Y. Li, Y.Y. Li, Photodynamic graphene quantum dot: reduction condition regulated photoactivity and size dependent efficacy, ACS applied materials & interfaces 8(5) (2016) 3287-3294.
[119] P. Huang, J. Lin, X. Wang, Z. Wang, C. Zhang, M. He, K. Wang, F. Chen, Z. Li, G. Shen, Light-triggered theranostics based on photosensitizer-conjugated carbon dots for simultaneous enhanced-fluorescence imaging and photodynamic therapy, Advanced Materials 24(37) (2012) 5104-5110.
[120] L. Li, G. Wu, G. Yang, J. Peng, J. Zhao, J.-J. Zhu, Focusing on luminescent graphene quantum dots: current status and future perspectives, Nanoscale 5(10) (2013) 4015-4039.
[121] M.K. Kumawat, M. Thakur, R. Bahadur, T. Kaku, R. Prabhuraj, A. Ninawe, R. Srivastava, Preparation of graphene oxide-graphene quantum dots hybrid and its application in cancer theranostics, Materials Science and Engineering: C 103 (2019) 109774.
[122] A. Kalluri, D. Debnath, B. Dharmadhikari, P. Patra, Graphene quantum dots: Synthesis and applications, Methods in enzymology 609 (2018) 335-354.
[123] M.R. Younis, G. He, J. Lin, P. Huang, Recent advances on graphene quantum dots for bioimaging applications, Frontiers in Chemistry 8 (2020).
[124] S. Chung, R.A. Revia, M. Zhang, Graphene quantum dots and their applications in bioimaging, biosensing, and therapy, Advanced Materials (2019) 1904362.
[125] A. Lesiak, K. Drzozga, J. Cabaj, M. Bański, K. Malecha, A. Podhorodecki, Optical sensors based on II-VI quantum dots, Nanomaterials 9(2) (2019) 192.
[126] S. Tajik, Z. Dourandish, K. Zhang, H. Beitollahi, Q. Van Le, H.W. Jang, M. Shokouhimehr, Carbon and graphene quantum dots: a review on syntheses, characterization, biological and sensing applications for neurotransmitter determination, RSC Advances 10(26) (2020) 15406-15429.
[127] T. Henna, K. Pramod, Graphene quantum dots redefine nanobiomedicine,

Materials Science and Engineering: C 110 (2020) 110651.
[128] M. Zhang, B.P. Bishop, N.L. Thompson, K. Hildahl, B. Dang, O. Mironchuk, N. Chen, R. Aoki, V.C. Holmberg, E. Nance, Quantum dot cellular uptake and toxicity in the developing brain: implications for use as imaging probes, Nanoscale advances 1(9) (2019) 3424-3442.
[129] M.-X. Zhao, B.-J. Zhu, The research and applications of quantum dots as nano-carriers for targeted drug delivery and cancer therapy, Nanoscale research letters 11(1) (2016) 1-9.
[130] M. Levy, P.P. Chowdhury, P. Nagpal, Quantum dot therapeutics: a new class of radical therapies, Journal of biological engineering 13(1) (2019) 1-12.
[131] C. Zhao, X. Song, Y. Liu, Y. Fu, L. Ye, N. Wang, F. Wang, L. Li, M. Mohammadniaei, M. Zhang, Synthesis of graphene quantum dots and their applications in drug delivery, Journal of Nanobiotechnology 18(1) (2020) 1-32.
[132] S. Jha, P. Mathur, S. Ramteke, N.K. Jain, Pharmaceutical potential of quantum dots, Artificial cells, nanomedicine, and biotechnology 46(sup1) (2018) 57-65.
[133] M.S. Hashemi, S. Gharbi, S. Jafarinejad-Farsangi, Z. Ansari-Asl, A.S. Dezfuli, Secondary toxic effect of graphene oxide and graphene quantum dots alters the expression of miR-21 and miR-29a in human cell lines, Toxicology in Vitro 65 (2020) 104796.
[134] J. Du, B. Feng, Y. Dong, M. Zhao, X. Yang, Vanadium coordination compounds loaded on graphene quantum dots (GQDs) exhibit improved pharmaceutical properties and enhanced anti-diabetic effects, Nanoscale 12(16) (2020) 9219-9230.
[135] L. Yu, X. Tian, D. Gao, Y. Lang, X.-X. Zhang, C. Yang, M.-M. Gu, J. Shi, P.-K. Zhou, Z.-F. Shang, Oral administration of hydroxylated-graphene quantum dots induces intestinal injury accompanying the loss of intestinal stem cells and proliferative progenitor cells, Nanotoxicology 13(10) (2019) 1409-1421.
[136] Z. Li, J. Fan, C. Tong, H. Zhou, W. Wang, B. Li, B. Liu, W. Wang, A smart drug-delivery nanosystem based on carboxylated graphene quantum dots for tumor-targeted chemotherapy, Nanomedicine 14(15) (2019) 2011-2025.
[137] Z. Xue, Q. Sun, L. Zhang, Z. Kang, L. Liang, Q. Wang, J.-W. Shen, Graphene quantum dot assisted translocation of drugs into a cell membrane, Nanoscale 11(10) (2019) 4503-4514.
[138] D. Iannazzo, A. Pistone, M. Salamò, S. Galvagno, R. Romeo, S.V. Giofré, C. Branca, G. Visalli, A. Di Pietro, Graphene quantum dots for cancer targeted drug delivery, International journal of pharmaceutics 518(1-2) (2017) 185-192.
[139] W. Jiang, J. Chen, C. Gong, Y. Wang, Y. Gao, Y. Yuan, Intravenous delivery of enzalutamide based on high drug loading multifunctional graphene oxide nanoparticles for castration-resistant prostate cancer therapy, Journal of nanobiotechnology 18(1) (2020) 1-12.
[140] G. Xi, E. Robinson, B. Mania-Farnell, E.F. Vanin, K.-W. Shim, T. Takao, E.V. Allender, C.S. Mayanil, M.B. Soares, D. Ho, Convection-enhanced delivery of nanodiamond drug delivery platforms for intracranial tumor treatment, Nanomedicine: Nanotechnology, Biology and Medicine 10(2) (2014) 381-391.
[141] D. Wang, Y. Li, Z. Tian, R. Cao, B. Yang, Transferrin-conjugated nanodiamond as an intracellular transporter of chemotherapeutic drug and targeting therapy for cancer cells, Therapeutic delivery 5(5) (2014) 511-524.
[142] D. Yang, L. Feng, C. Dougherty, D. Chen, Z. Liu, H. Hong, Tumor vasculature-targeted nano-graphene as a multimodality imaging guidable drug delivery platform for metastatic breast cancer, Journal of Nuclear Medicine 57(supplement 2) (2016) 193-193.
[143] P. Kalluru, R. Vankayala, C.-S. Chiang, K.C. Hwang, Nano-graphene oxide-mediated In vivo fluorescence imaging and bimodal photodynamic and photothermal destruction of tumors, Biomaterials 95 (2016) 1-10.
[144] C. Wang, B. Chen, M. Zou, G. Cheng, Cyclic RGD-modified chitosan/graphene oxide polymers for drug delivery and cellular imaging, Colloids and Surfaces B: Biointerfaces 122 (2014) 332-340.
[145] C. Wang, Y. Chen, Z. Xu, B. Chen, Y. Zhang, X. Yi, J. Li, Fabrication and characterization of novel cRGD modified graphene quantum dots for chemo-photothermal combination therapy, Sensors and Actuators B: Chemical 309 (2020) 127732.
[146] X. Wang, X. Sun, J. Lao, H. He, T. Cheng, M. Wang, S. Wang, F. Huang, Multifunctional graphene quantum dots for simultaneous targeted cellular imaging and drug delivery, Colloids and Surfaces B: Biointerfaces 122 (2014) 638-644.
[147] P. Jeyamohan, T. Hasumura, Y. Nagaoka, Y. Yoshida, T. Maekawa, D.S. Kumar, Accelerated killing of cancer cells using a multifunctional single-walled carbon nanotube-based system for targeted drug delivery in combination with photothermal therapy, International journal of nanomedicine 8 (2013) 2653.
[148] Y. Yang, J. Liu, X. Sun, L. Feng, W. Zhu, Z. Liu, M. Chen, Near-infrared light-activated cancer cell targeting and drug delivery with aptamer-modified nanostructures, Nano Research 9(1) (2016) 139-148.
[149] W. Shao, A. Paul, B. Zhao, C. Lee, L. Rodes, S. Prakash, Carbon nanotube lipid drug approach for targeted delivery of a chemotherapy drug in a human breast cancer xenograft animal model, Biomaterials 34(38) (2013) 10109-10119.
[150] X. Qi, Y. Rui, Y. Fan, H. Chen, N. Ma, Z. Wu, Galactosylated chitosan-grafted multiwall carbon nanotubes for pH-dependent sustained release and hepatic tumor-targeted delivery of doxorubicin in vivo, Colloids Surf B Biointerfaces 133 (2015) 314-322.
[151] N.M. Dinan, F. Atyabi, M.-R. Rouini, M. Amini, A.-A. Golabchifar, R. Dinarvand, Doxorubicin loaded folate-targeted carbon nanotubes: preparation, cellular internalization, in vitro cytotoxicity and disposition kinetic study in the isolated perfused rat liver, Materials Science and Engineering: C 39 (2014) 47-55.
[152] J. Ren, S. Shen, D. Wang, Z. Xi, L. Guo, Z. Pang, Y. Qian, X. Sun, X. Jiang, The targeted delivery of anticancer drugs to brain glioma by PEGylated oxidized multi-walled carbon nanotubes modified with angiopep-2, Biomaterials 33(11) (2012) 3324-3333.
[153] M.A. Koch, G.L. Reiner, K.A. Lugo, L.S. Kreuk, A.G. Stanbery, E. Ansaldo, T.D. Seher, W.B. Ludington, G.M. Barton, Maternal IgG and IgA antibodies dampen mucosal T helper cell responses in early life, Cell 165(4) (2016) 827-841.
[154] X. Guo, R. Ding, Y. Zhang, L. Ye, X. Liu, C. Chen, Z. Zhang, Y. Zhang, Dual role of photosensitizer and carrier material of fullerene in micelles for chemo–photodynamic therapy of cancer, Journal of pharmaceutical sciences 103(10) (2014) 3225-3234.
[155] J. Shi, B. Wang, L. Wang, T. Lu, Y. Fu, H. Zhang, Z. Zhang, Fullerene (C60)-based tumor-targeting nanoparticles with “off-on” state for enhanced treatment of cancer, Journal of Controlled Release 235 (2016) 245-258.
[156] R. Yin, M. Wang, Y.-Y. Huang, H.-C. Huang, P. Avci, L.Y. Chiang, M.R. Hamblin, Photodynamic therapy with decacationic [60] fullerene monoadducts: effect of a light absorbing electron-donor antenna and micellar formulation, Nanomedicine: Nanotechnology, Biology and Medicine 10(4) (2014) 795-808.